UNIVERSITEIT VAN PRETORIA
UNIVERSITY OF PRETORIA
YUNIBESITHI YA PRETORIA
Denkleiers • Leading Minds • Dikgopolo tša Dihlalefi

Sensitivity study of dynamic features to monitor the condition of vibrating screen isolators

Simeon Pienaar
12019420

Submitted in Partial Fulfilment of the Requirements for the Degree

Masters of Engineering (Mechanical Engineering)

In the
Department of Mechanical and Aeronautical Engineering
Faculty of the Engineering, Built-environment and Information Technology

University of Pretoria

November 2023

Abstract

Sensitivity study of dynamic features to monitor the condition of vibrating screen isolators.

Author	:	Simeon Pienaar
Student Number	:	12019420
Supervisor	:	Prof. P.S. Heyns
University	:	University of Pretoria
Department	:	Mechanical and Aeronautical Engineering
Degree	:	Master of Engineering, MEng (Mechanical Engineering)

Vibrating screens form an integral part in the processing of bulk materials. The major components of a vibrating screen are purposefully designed and selected to contribute to the operational parameters required. The monitoring of each components function is essential to guarantee optimal performance and reduce downtime through predictive maintenance. This is the premise of a condition-based maintenance strategy which is becoming increasingly popular with the advent of new, affordable technology and advanced signal processing and classification algorithms. For vibrating screen components such as motors, gearboxes, and bearings there exist several validated monitoring strategies. However, for components such as vibrating screen isolators very few working strategies exist. The isolators are a notoriously difficult component to monitor due to the operating environment, limited access, isolator geometry and material composition. Each of these factors restrict the use of conventional non-destructive testing (NDT) and visual inspection. Another monitoring strategy is a static compression or displacement technique which suffers practical relevance for very large vibrating screens with numerous isolators.

The most promising techniques for isolator condition monitoring are vibration-based approaches. One such approach is the evaluation of modal parameters by experimental modal analysis (EMA) and modal parameter extraction. The premise for this approach is that a deterioration of isolator condition will manifest as a change in stiffness which directly influences modal natural frequencies, particularly for the rigid body modes (RBM). Another approach is the use of signal processing to extract features directly from operational vibration measurements. These features need to be sensitive to faults such that their change will be indicative of a fault developing. The difficulty of the latter approach is that the evaluation of feature sensitivity is expensive when done experimentally. It is therefore common to use a model-based approach for feature evaluation. This implies the use of simulated measurements from which the feature sensitivity can be established. However, this does not excuse the use of some experiments to validate both the numerical model as well as the feature sensitivity results.

The purpose of this dissertation is to evaluate the sensitivity of identified features to known faults in isolators using both numerically simulated and experimentally obtained measurements. The same premise as for an EMA approach is used to evaluate isolator deterioration (i.e. as a change in stiffness only). A numerical model of a vibrating screen is developed which uses linear approximations for the exciters and isolators. However, the experiments were performed on a vibrating screen with different isolator types considered (spring steel and rubber-based isolators). This was done to demonstrate the generic use of the features for isolators condition monitoring in that they are not coupled to only one

isolator type. The features identified for this study are exploratory as research has yet to identify the most appropriate features for isolator condition monitoring. The entire operating envelope (startup, steady operation and coast down) of a vibrating screen, with no material on the deck, is considered. An EMA is also conducted to evaluate the behaviour of modal parameters for changes in isolator condition.

The sensitivity results from both the simulated and experimental measurements are compared to one another. It was found that the features that undergo the highest percentage change and are the most sensitive to changes in isolator stiffness are those obtained from the transient startup and coast down envelopes. The steady operating orbit features underwent considerably smaller changes. The rigid body mode natural frequencies obtained by EMA and those extracted from the transient startup and coast down envelopes are comparable in magnitude and behaviour. However, from the experimental results the features and how they change are dependent on the type of isolator used, the temperatures of the isolators and exciters as well as the sensor locations.

Keywords: Vibration-based condition monitoring, Modal analysis, Sensitivity study, Feature extraction, Multi-body dynamics

Acknowledgements

SOLI DEO GLORIA

I would like to thank and acknowledge the following people for their contribution, patience, guidance, and motivation during the completion of this work:

- Prof. P.S. Heyns, it is an absolute privilege to have your name on this dissertation as my supervisor. Firstly, thank you for your patience, this has taken quite some time to complete, and the number of hurdles encountered were crippling. Thank you for your continuous enthusiasm and passion as well as your invaluable inputs towards this study.
- Kenny Mayhew-Ridgers and the team from Kwatani. I thoroughly enjoyed working alongside you during this study. I was privileged to have the opportunities that you provided and to ask the questions with your guidance and support. Thank you for all the conversations, gleaning from your expertise in this field and having fun while working to get it done. I truly hope this study can also provide you with answers to questions and provide a spark to your genius for innovation and future developments.
- The staff in the C-AIM Sasol Laboratory, Dr Abrie Oberholster, Mr George Breytenbach and Mr Herman Booysen. Thank you or all the support regarding test equipment and helping on short notice. It was an absolute pleasure working with you all.
- To my wife and son, thank you for your endless patience and motivation. For believing in me and keeping my spirits up during some challenging times. This thank you can be extended to my parents and close friends who somehow never stopped believing I could finish this, but also took the opportunity to prod me along with some necessary humour amidst tuff opposition.
- Also, there are numerous other friends and colleagues that gave me timeous advice, strokes of genius and some necessary perspective on this study. Thank you for taking the time to sit down with me, listen to my complaining and sometimes lack of reason, and for patiently and gently asking me all the right questions.

TABLE OF CONTENTS

LIST OF ABBREVIATIONS

CAD	Computer aided design
CG	Centre of gravity
CM	Condition monitoring
CSAC	Cross signature assurance criterion
CSF	Cross signature scale factor
DAQ	Data acquisition device
DEM	Discrete element modelling
DFT	Discrete Fourier transform
DOF	Degrees of freedom
EMA	Experimental modal analysis
FBM	Flexible body mode
FDD	Fault detection and diagnosis
FEA	Finite element analysis
FEM	Finite element model
FFT	Fast Fourier transform
FRF	Frequency response function
ICP	Integrated Circuit-Piezoelectric
MAC	Modal assurance criterion
MBD	Multi-body dynamics
MEMS	Microelectromechanical systems
MISO	Multi-input single output
NDT	Non-destructive testing
OEM	Original equipment manufacturer
PSD	Power spectral density
PSP	Phase space plot
RBM	Rigid body mode
RMS	Root means square
RPM	Rotations per minute
SIMO	Single input multi-output
STFT	Short time Fourier transform
SVM	Support vector machine
WM	Working moment

NOMENCLATURE

General: (for the numerical model)

$[C]$	Damping matrix
$[K]$	Stiffness matrix
$[M]$	Mass matrix
$\vec{F}$	Force vector
F_c	Centrifugal force
x	Horizontal displacement
y	Lateral displacement
z	Vertical displacement
w	Screen width between isolators
a	Longitudinal distance between the vibrating screen CG and the F2 isolators
b	Longitudinal distance between the vibrating screen CG and the F1 isolators
c	Perpendicular distance between CG and line joining the F1 and F2 isolators
m	Vibrating screen mass
K	Isolator stiffness
C	Isolator damping
J	Mass moment of inertia
r	Distance of weight CG to centre of rotation for eccentric weights
m_{ub}	Mass of unbalance weights
WM	Working moment of exciters ($2 \times m_{ub} \cdot r$)
WS	Weight setting
$N_{exciters}$	Number of exciters
g_{acc}	Gravitational acceleration
e	Vertical distance of exciter centre to CG of the vibrating screen
f	Horizontal distance of exciter centre to CG of the vibrating screen
g	Lateral distance of exciter centre to CG of the vibrating screen

Greek Symbols:

ω	Exciter weights rotating speed in radians per second
β	Screen angle
α	Drive angle
θ	Pitch angle
ϕ	Roll angle
δ_i	Phase difference between exciters

Subscripts:

CG	Centre of gravity
$F1$	F1 isolator (at the feed end of the vibrating screen)
$F2$	F2 isolator (at the discharge end of the vibrating screen)
L	Left side
R	Right side
x	X direction (horizontal) component
y	Y direction (lateral) component
z	Z direction (vertical) component

1 BACKGROUND

1.1 INTRODUCTION

Vibrating screens form an integral part in the processing of bulk mining materials, whether it be coal, platinum, copper, iron ore, diamonds, chrome, or mineral sand [1]. The primary use of vibrating screens in the mining industry is the classification of bulk ore based on size, shape, density, and friction coefficients that constitute the ore body [2]. Major applications of vibrating screens include [1] [3] [4]:

- Scalping - the first screen in a mining process which involves the removal of fines prior to secondary crushing within a comminution circuit.
- Classification or sizing – separating the crushed ore into different size categories.
- Washing and screening – washing the crushed ore to remove fines and classify according to particle size.
- Dewatering – removal or recovery of water from wet processed bulk materials.
- Depulping or drain and rinse – recovery of dense media such as magnetite or ferrosilicon.
- Desliming or deslurrying – removing fine particles of size <1mm.
- Trash removal – removal of unwanted debris from ore product.

The role of vibrating screens in bulk mineral processing is essential and their efficient operation is crucial to most mining operations. Vibrating screen components are specified, designed, and built to meet the demands of the application requirements. Due to the harsh environmental conditions of the mining operation, the condition of the machine does deteriorate with time. Maintenance is therefore required to increase the longevity of the machine and ensure safe and optimum performance is retained.

To mitigate operational disturbances leading to productivity loss, decline in quality and deterioration of performance, it is important for each mining site to have an effective maintenance strategy in place [5]. For machinery, one of the following maintenance strategies is typically adopted [6]:

1. Run-to-failure:
   For machines not critical to production i.e., where machine failures are unlikely to be catastrophic, the machine is run and only replaced upon failure. This strategy is only feasible for inexpensive machinery running in parallel with other machines to reduce the risk of production loss.
2. Preventative Maintenance:
   An estimated replacement date can be derived if machine components tend to wear at predictable rates. This maintenance strategy can be costly if maintenance is erroneously performed too frequently. Another possible downside to preventative maintenance is secondary failures due to components regularly being disassembled and reassembled resulting in undesirable wear and tear. The original equipment manufacturer (OEM) of the machine or component is typically relied upon for guidance regarding a time or usage-based replacement schedule.
3. Condition-Based Maintenance:
   Also known as predictive maintenance, this strategy makes use of condition monitoring at regular intervals to diagnose the current condition of the machine, as well as provide a prognosis as an estimate of the remaining useful life. Determining an accurate prognosis

allows for maintenance at the optimum time, mitigating the risk of over-maintenance as well as preventing breakdowns leading to loss of production.

Run-to-failure is an unplanned or reactive maintenance strategy whereas preventative and condition-based maintenance are planned or proactive maintenance strategies [5].

Although all three of the abovementioned maintenance approaches have their place and application, the use of condition-based maintenance is undeniably superior in critical applications. Whether a vibrating screen forms part of a single or parallel line plant layout, it is beneficial to adopt a predictive maintenance approach. Not only does monitoring and signal processing contribute to accurate fault diagnostics, deviations in machine performance are also indicative of fault developments [6].

Studies have shown that the vibrating screen's performance is dependent on the correct adjustment of its operating parameters, screening panel selection and the ore properties [7] [8] [9] [10]. The vibrating screen operating parameters are easily monitored using vibration sensors. Operating parameters are adjusted using different excitation and isolators as well as adopting different screen body designs.

Numerous research studies have been done on gearbox and bearing vibrations which relate to the exciters of a vibrating screen but most of the recent research in condition monitoring of vibrating screens focus on isolators. When isolators deteriorate, the performance of the vibrating screen and that of the structure on which is stands is negatively affected. This is due to the isolators directly influencing the motion of the vibrating screen both during operation as well as during start-up and shutdown [11].

What follows is a literature survey which outlines the relevant research relating to the monitoring of vibrating screens. Within the scope of work following the literature survey is a problem statement as well as a description of what this study entails. The development and validation of a numerical model for sensitivity analysis is discussed followed by a description of experiments. The results from the experiments and numerical study are evaluated. Finally, conclusions are drawn and recommendations for future work are discussed.

1.2 LITERATURE SURVEY

The purpose of this survey is to provide background and justification for the dissertation problem statement. It is necessary to present the relevant research conducted in the field of condition monitoring of vibrating screens as a foundation for this study. The literature is grouped into the following categories:

1. Vibrating screens
   1.1. Mechanics
   1.2. Vibrating screen condition monitoring
   1.3. Vibrating screen modelling
2. Vibration-based condition monitoring
   2.1. Sensors
   2.2. Fault detection and feature extraction

1.2.1 Vibrating screens

This section provides background regarding the design and operation of a vibrating screen as well as current research in the field of condition monitoring and modelling. Included in this section are references to documents of vibrating screen OEMs in South Africa and around the world. This is

included to understand the applications and types of vibrating screens typically used in current mining applications.

1.2.1.1 Mechanics

A vibrating screen is characterized as a high throughput, low operating cost machine that requires a low technical effort to construct [12]. Key attributes necessary for application of a vibrating screen include ease of use, assembly, and maintenance. Vibrating screens comprise four major components, as illustrated in Figure 1: a screen body, an exciter, screening media and liners and isolators. These components are further discussed below.

1. Screen body – typically a steel body or frame with a size designed to contain a specific number of screening panels. The screen body is a combination of welded and bolted assemblies which allows for the mounting of exciters and screening media. The side plates are tied together by the exciter and deck beams; these major components are the most stressed components on the screen body.
2. Exciter – typically swinging (mostly counter rotating), unbalanced weights causing a centrifugal force which acts on the vibrating screen body. The centrifugal force is responsible for exciting the vibrating screen at a predetermined g-force. Other types of excitation mechanisms include the use of CAM shafts or eccentric shafts as well as electromagnets.
3. Screening media and liners – screening media refers to the panels with apertures or perforations sized to allow a specified size and shape of ore to pass through the vibrating screen. Liners are used to protect the screen body from corrosion due to ore abrasion or water corrosion. Since these components experience the most wear, they are designed to be easily replaceable.
4. Isolators – typically coil springs or rubber isolators used to isolate the vibrating screen from the structure on which it stands.

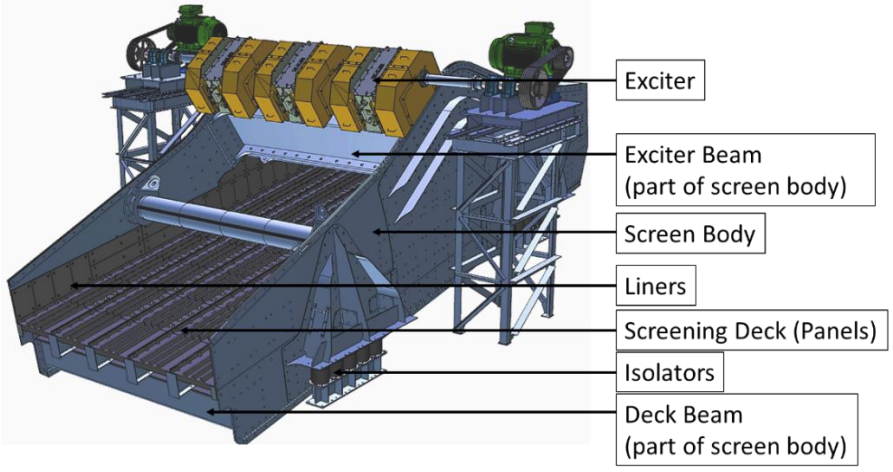

Figure 1: Vibrating screen illustration with major components labelled (Kwatani)

A vibrating screen is built with a specific application in mind, therefore the screen body, exciter, screening panels and isolators are selected based on design calculations and simulations to ensure the most effective design. The process of vibrating screen component design and selection is followed not only to identify the best design, but also to manufacture the most cost-effective screen. The design and selection of each component seen in Figure 1 above contributes to the optimal operation and the performance efficiency.

1.2.1.1.1 Types of vibrating screens

Vibrating screens are designed for a variety of different applications in a mining operation. The shape, size and orientation of the screen is specifically designed to meet the process requirements. The most common types of vibrating screens include horizontal and multi-slope screens; the characteristics of each are discussed below:

1. Single, double, and triple deck horizontal screens, as seen in Figure 2, are used for scalping and sizing bulk minerals. They are referred to as horizontal screens due to the decks all being at the same constant angle. These screens can be placed at incline or decline angles to improve process efficiency [13].

(a) *(b)* *(c)*

Figure 2: Horizontal screens a) single, b) double and c) triple deck [3]

2. Single and double deck multi-slope screens also known as 'banana' screens due to their shape as seen in Figure 3. These screens are popular due to their ability to screen larger feed quantities of material, compared to equivalently sized horizontal screens. Multi-slope screens can also handle high contents of fine particles in the feed [14].

(a) *(b)*

Figure 3: Multi-slope banana screens a) single, b) double deck [3]

One method adopted to improve screening efficiency is using multiple decks on top of one another. This allows for more efficient screening by splitting large particles from the product thereby increasing the statistical probability of the product particles screening through the panels [15].

Using bolted connections for the assembly of vibrating screens is preferred over welded connections due to the higher fatigue limits of bolted connections. Furthermore, Huck bolts are favoured over conventional bolts to reduce assembly time.

1.2.1.1.2 Types of motion

The vibratory motion of a vibrating screen is responsible for the stratification and conveying of the bulk material. Stratification refers to the process of sorting or splitting fine and coarse particles by

agitating the bulk ore. By vibrating the ore, the finer particles move down in the material bed increasing the likelihood of them screening through the deck whereas the coarse particles remain on top of the material bed and are conveyed and discharged over the screen [8].

The motion of the vibrating screen can be altered by the excitation type, direction, and position with respect to the centre of mass of the vibrating screen. The most common types of motions include linear, elliptical, and circular. Figure 4 illustrates each of these motions and their interaction with a particle on the screen deck. For a horizontal deck screen with 0° inclination, a linear or elliptical motion can be used. Notice the angle of the linear and elliptical motion is directed to convey the material forwards. For circular motion no such conveying direction of motion exists and therefore the screen deck must be placed at a steep inclination angle to convey the material forward.

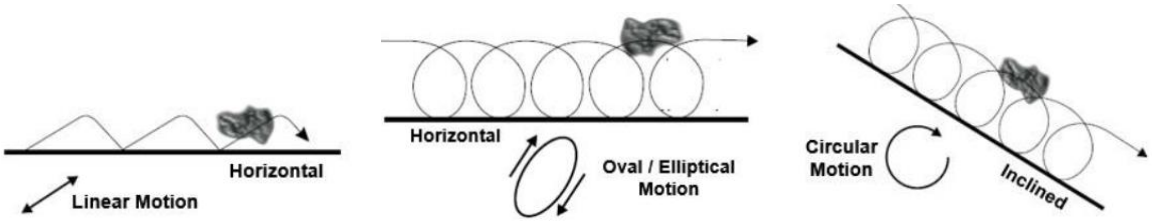

(a) *(b)* *(c)*

Figure 4: Types of screening motion a) linear, b) elliptical, c) circular [15]

1.2.1.1.3 Excitation types

As mentioned, the selection of an excitation type is responsible for the resulting type of motion of the vibrating screen. Rotating eccentric weights is mostly responsible for vibrating motion [16]. The eccentric weights are mounted to either a motor or gearbox for rotation to occur. Unbalanced motors and exciter gearboxes are commonly used in industry for vibrating screen excitation, as illustrated in Figure 5.

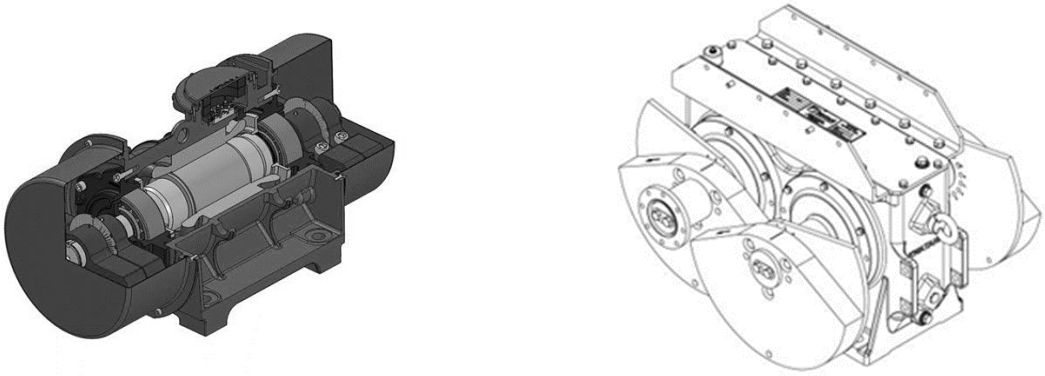

(a) *(b)*

Figure 5: Common exciters a) unbalanced motors and b) gearbox exciter [17]

The unbalanced weights exert a centrifugal force when rotating at speed. The magnitude of the centrifugal force is directly proportional to the mass and radius of unbalance and is quadratically proportional to the rotating speed of the weights. The equation for the computation of centrifugal force is as follows:

$$F_c = m \times r \times \omega^2 \qquad \text{Eq. 1}$$

where m is the excitation mass in kilograms, r is the radius from the center of rotation to the center of mass of the excitation mass in meters, and ω is the operating speed in radians per second for the computation of a centrifugal force expressed in Newton, as illustrated in Figure 6.

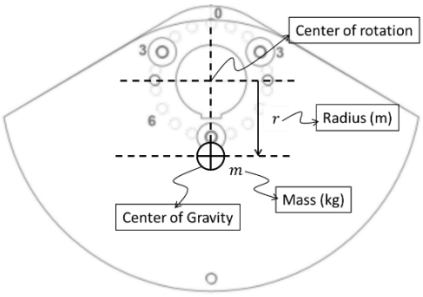

Figure 6: Illustration of an unbalanced weight [17]

The summation of $m \times r$ for all weights on an exciter is referred to as the static moment of the exciter and is expressed as $kg \cdot cm$ (kilogram centimeter) in an exciter catalogue [18] [17]. An estimation of the operating stroke or throw (2 x amplitude of vibration) of the vibrating screen with a mass m_{screen}. can be made using the static moment:

$$stroke\ [cm] = 2 \times \frac{m \times r}{m_{screen}} \times N_{exciters} \qquad \textit{Eq. 2}$$

where $N_{exciters}$ is the number of exciters. Note that in some exciter catalogues a working moment (WM) is given. The working moment is the static moment multiplied by 2 for the calculation of the stroke [17].

The working moment can be adjusted to change the centrifugal force and therefore the amplitude of the vibration. This adjustment is done using a weight setting which is a percentage of the maximum unbalance ($m \times r$). For example, a 100% weight setting is 100% unbalance, and 50% weight setting is 50% unbalance. The change in unbalance is possible because of weight pairs used where one weight is loosened and rotated to a different relative angle to the other fixed weight. This is illustrated in Figure 7.

The operating speed of the exciters can also be adjusted by selecting either a 2, 4, 6, or 8 pole motor or by adjusting pulley sizes for gearbox exciters. Motor speed is also adjustable using a variable speed drive (VSD).

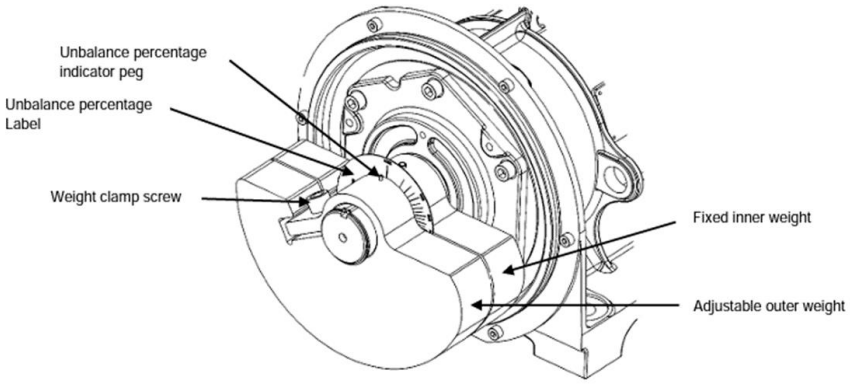

Figure 7: Unbalanced motor weight pair adjustment illustration [18]

Having the ability to adjust the unbalance and operating speed allows for optimization of the vibrating screen operation. According to Cleary, et al. [8] the g-force (or acceleration) exerted by the vibrating screen on the bulk material directly influences the stratification of the material. Therefore, having the ability to adjust the g-force allows for screening performance optimization. The magnitude of the g-force is directly proportional to the vibration amplitude and quadratically proportional to the operating speed of the vibrating screen. The g-force magnitude (in m/s^2) is calculated as:

$$g_{force} = A \cdot \omega^2 \qquad \textit{Eq. 3}$$

where A is the vibration amplitude ($stroke/2$) in meters and ω is the operating speed in radians per second.

1.2.1.1.4 Isolator types

Vibration isolation is a procedure whereby the unwanted effects of vibration on the support structure are mitigated or reduced to avoid damage or fatigue failure [19]. In the case of vibrating screens, the static support structure on which the screen rests is isolated from the unbalanced motion of the vibrating screen by inserting a resilient member or isolator between the vibrating screen and the main structure. Figure 8 illustrates a rigid body diagram of a vibration isolator, where the vibrating mass m is isolated from the base using an isolator with stiffness coefficient k and damping coefficient c.

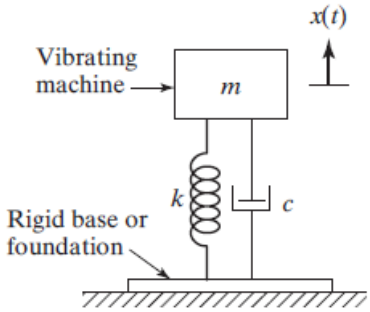

Figure 8: Single degree of freedom model for vibration isolation [19]

An isolator is selected based on a transmissibility ratio (T_f). The transmissibility ratio is the ratio of the force transmitted to the static structure and the excitation force. For a single degree of freedom (SDOF) system, T_f is calculated as follows [19]:

$$T_f = \frac{F_T}{F_0} = \left\{\frac{k^2 + \omega^2 \cdot c^2}{(k - m \cdot \omega^2)^2 + \omega^2 \cdot c^2}\right\}^{0.5} = \left\{\frac{1 + (2 \cdot \zeta \cdot r)^2}{[1 - r^2]^2 + (2 \cdot \zeta \cdot r)^2}\right\}^{0.5} \qquad \textit{Eq. 4}$$

where $r = \frac{\omega}{\omega_n}$, ω_n is the natural frequency, ω is the excitation frequency of the SDOF system and ζ is the damping ratio of the isolators. For isolation to be effective, the transmitted force needs to be less than the excitation force, therefore $T_f < 1$. The forcing frequency is therefore required to be at least $\sqrt{2} \times \omega_n$, as illustrated in Figure 9. The diagram in Figure 9 further demonstrates the transmissibility of an SDOF system and regions where vibration amplification and isolation occur, as well as the effect of damping on the transmissibility ratio. An increase in damping attenuates the response to excitation frequencies at or near the natural frequency of the system.

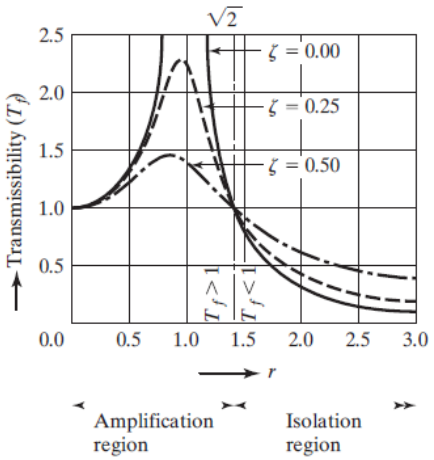

Figure 9: Transmissibility ratio illustration for SDOF system

Passive vibration isolators, such as metal coil springs and rubber springs, are commonly used for vibrating screen applications. Although both metal and rubber springs perform the same function, they have different characteristics:

- Coil springs have linear stiffness and damping characteristics within a certain working range. This is however only applicable to the vertical stiffness; lateral stiffness is non-linear due to its relation to the vertical stiffness [20].
- Rubber springs or isolators offer the advantage of higher internal friction compared to coil springs. Rubber springs absorb vibration or friction energy internally and dissipates the energy in the form of heat [21]. Consequently, rubber has more damping than coil springs. In contrast to coil springs, rubber isolators exhibit non-linear deformations under load and therefore have non-linear stiffness and damping associated to them [22].

1.2.1.2 Vibrating screen condition monitoring

Due to the relevance of condition monitoring to this study, an in-depth review on existing studies on the subject as well as the usefulness of the results obtained for condition monitoring of vibrating screens, is included. Existing studies, experiments and the results obtained have been taken into consideration to ensure that the same research is not repeated and enabling this study to build on existing methodologies. To explore the progression of condition monitoring over time, a chronological order of dates is used in this section.

The combination of high cycle fatigue and a corrosive environment means that failures due to fatigue of vibrating screens, are common [16]. The rate at which the failure occurs is further aggravated if operation is within close proximity to the structural natural frequency of the machine. For this reason, the condition monitoring of vibrating screens using sensors is necessary for early fault detection before failures occur.

In 1984, Fry & Greenway [16] addressed the issue of fatigue cracks in the welded structure of a vibrating screen body. When designing a structure for fatigue and structural integrity, an appropriate design methodology is necessary. Standards and codes exist for welded and bolted structures; this standardisation addresses the problem of fatigue by using an S-N curve which is a graphical indication of the number of cycles to failure (N) with respect to the dynamic stress ranges (S) [23]. However, there is no standardisation for vibrating screen designs. Codes written for other structures, such as bridges, can be used as guideline in an attempt at standardising vibrating screen designs. The

generation of S-N curves requires extensive testing typically resulting in validation extending only to endurance limits of up to 10^7 cycles; endurance limits thereafter are yet to be verified experimentally. High cycle endurance limits are imperative as a vibrating screen typically reaches 10^7 cycles within a month of operation.

Fry & Greenway propose that fatigue life prediction is accurately made by measuring the stress ranges on a vibrating screen body. The stress range on the screen body can be estimated using strain gauges and comparing the results with the S-N curves in appropriate standards relating to fatigue in welded and bolted steel structures. Steyn came to a similar conclusion in 1995 [23] when investigating the fatigue failure of deck beam supports of vibrating screens and used strain gauges to validate assumptions, regarding boundary conditions and loading, made when creating a model for fatigue life prediction. The deck beams are main cross members in a vibrating screen and experience high dynamic stress loads. The high stress load is due to the g-force and the bulk material load that is conveyed on the screen deck.

In 2010, Guanghui, et al. [24] also investigated the detection of deck beam cracks. Because the machine used is critical to a coal preparation production line, the catastrophic failure of a deck beam resulting in unplanned shutdowns have negative financial implications for the plant. This is motivation for an investigation into quick crack detection methods on deck beams that are more reliable than visual inspections. Visual inspections on vibrating screens are not a reliable technique for the monitoring of deck beams due to access restrictions. Deck beams are situated below the screening panels and the beam surfaces may have liners bolted or cured to the deck beam surface restricting faults to be detected visually.

Consequently Guanghui, et al. recommend the use of a combined method of metal magnetic memory testing (MMMT) and eddy current testing (ET) for the monitoring of deck beam cracks. Both of these techniques are non-destructive testing techniques. The combination of these techniques successfully detects crack existence, location and even the depth of the crack on a deck beam. The above-mentioned monitoring techniques can effectively detect cracks through rubber lining of up to 14mm thick. This is of benefit as rubber lining of this thickness is a common form of deck beam protection. A limitation of the use of MMMT and ET is that specialized and expensive equipment is required and the machine is to be stationary for fault detection.

In 2011 Guanghui & Guorui [25] revisited their earlier work [24] and proposed a different approach to the early detection of cracks in deck beams. A vibration-based method was proposed by which the response to a given force is measured and a transfer function or frequency-response function (FRF) determined. Accelerometers measure the response at the ends of a deck beam and a modal hammer is used to excite the beam with an impulse, exciting a band of frequencies simultaneously. By dividing the cross-spectrum of the response and force with the auto-spectrum of the force, a transfer function is calculated. The final transfer function is the average of several transfer functions (responses to impulse) measured.

With the emergence of a crack, what is referred to in the study as a ‘down shift evolution regularity’ occurs and the response amplitude at characteristic frequencies (i.e. natural frequencies) decrease gradually. The characteristic frequencies shift gradually to lower frequencies and the emergence of new characteristic frequencies occur below the original characteristic frequency. Monitoring this gradual down shift evolution allows for the early diagnosis of cracks in deck beams.

When exploring the field of isolator condition monitoring in 2011, Liu, et al. [26] examined numerous signal processing techniques for vibrating screen fault diagnosis. The signal processing methods are

categorised as stationary or non-stationary signal processing techniques. The statistical properties of stationary signals are constant with time [6]. Stationary signal processing techniques identified are discrete frequency spectrum analysis (i.e. a Fast Fourier Transform (FFT)), and denseness spectrum analysis. A denseness spectrum analysis refers to a zoom spectrum analysis or Zoom FFT where a limited frequency range within the zero to Nyquist frequency range is analysed in more detail.

For non-stationary signals Liu, et al. identify a Wigner-Ville time-frequency distribution and Wavelet Transform as relevant techniques for vibration-based condition monitoring. A Wigner-Ville time-frequency distribution is similar to a Short Time Fourier Transform (STFT) but with better time and frequency resolution and less interference. A wavelet transform adopts a sliding window along the signal length decomposing the signal in terms of a group of related wavelets.

The work by Liu, et al. [26] also considers a 3-DOF (degree of freedom) vibrating screen model seen in Figure 10 for dynamic and static studies of defects in coil springs at corners of a vibrating screen. This model is an undamped rigid body model.

The model shown in Figure 10 was used in 2014 by Peng, et al. [27] as a basis for a theoretical study of a novel technique for coil spring isolator fault diagnosis on vibrating screens. The technique, known as twice-suspended-mass method (TSMM), is a static deformation method detecting isolator faults at a corner of a vibrating screen. Implementing TSMM requires an external weight of known mass to be added to a stationary vibrating screen body. The weight is placed on each corner of the vibrating screen sequentially and the static deformation of isolators is measured for each corner. The procedure is repeated at regular intervals during the machine's life. A fault is indicated by a difference between the original static deformation and the most recent deformations.

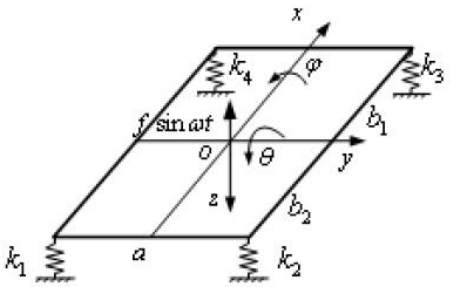

Figure 10: 3-DOF model [26]

The change in static deformation directly correlates with a change in stiffness of the isolator. The model in Figure 10 is used to establish the relationship between the roaming weight and the deformations of coil springs at each corner. Changes in deformation of a coil spring is sensitive to the position of the roaming weight as well as the stiffness of each coil spring per corner. Moving the weight to each corner of the vibrating screen indicates at which corner the highest deformation takes place and therefore the highest stiffness change.

The TSMM method does carry merit for the determination of stiffness change in isolators, however, the weight required for the TSMM method needs to be significant to cause measurable changes in deformation per corner. The mass of the weight could be impractical for large vibrating screens and could require special lifting equipment to move around on site. If the mass of the weight, and therefore the displacements, are too small, expensive measurement equipment sensitive to small displacements can be used. Also, this method can only be applied when the machine is stationary.

As mentioned, the efficient performance of a vibrating screen is directly dependent on its operating parameters [8] [9]. The isolators influence the operation of the vibrating screen therefore, changes in isolator conditions influence operating parameters which in turn could negatively influence the screening performance [11]. For this reason, Rodriguez, et al. [11] developed a 3-DOF model for the 2-dimensional analysis of a vibrating screen's operating motion, as seen in *Figure 11*.

The three degrees of freedom include horizontal and vertical bounce in the x and y directions respectively and pitching rotation about the z axis. This model considers large angular displacements and is therefore non-linear. Large angular rotations could potentially occur during transient start-up and coast-down phases of a vibrating screen. The model also considers damping as well as the inclination angle between front and rear isolators.

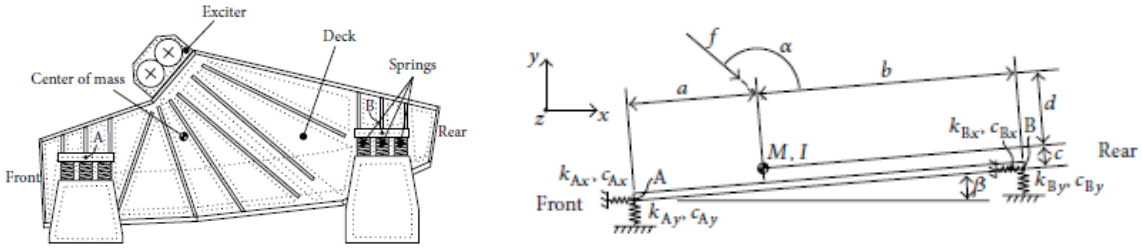

Figure 11: 2 Dimensional 3-DOF model [11]

The 3-DOF model is used to determine the effect of changes in stiffness on the amplitude and inclination angle of the screen's vibration. *Figure 12* is a schematic demonstration of amplitude and angle of inclination. The OEM of a vibrating screen can provide limits for both amplitude and angle deviations to ensure optimum screening efficiency. A vibrating screen operating outside these limits performs poorly with low screening efficiency. This study only considers steady-state operation; studying how changes in stiffness of isolators influence the amplitude and angle of vibration allows for the determination of limits on spring deterioration.

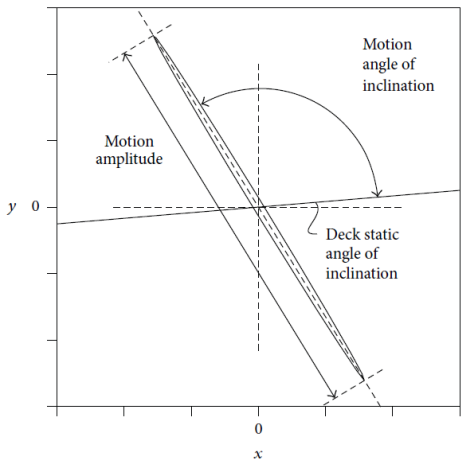

Figure 12: Schematic of orbit plot with amplitude and angle [11]

From the results it is evident that amplitude changes are negligible for changes in isolator stiffness. However, the operating or inclination angle does deviate outside of OEM limits for a notable change in isolator stiffness. Therefore, the model can predict the amount of stiffness change allowed before isolators need to be replaced to ensure optimum screening performance. The results from the model

are not experimentally verified, however, the study is useful in proving that monitoring the angle of inclination on a vibrating screen is a useful metric for determining screen performance.

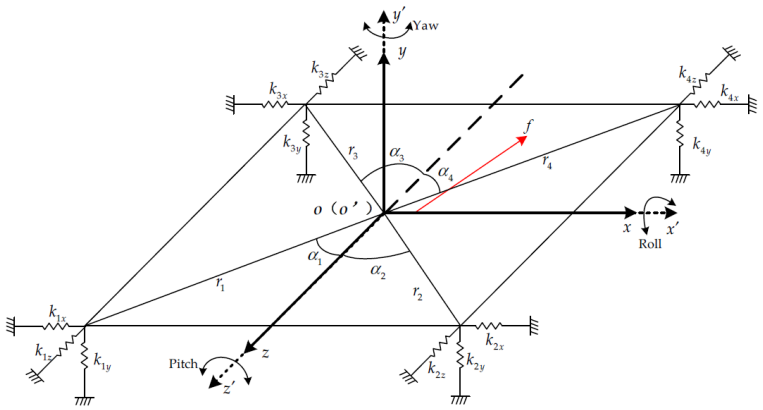

Figure 13: 6-DOF model of a vibrating screen [28]

In a similar study to Rodriguez, et al. [11], Liu, et al. [28] also developed a numerical model for studying the effect of spring failures on the dynamics of a vibrating screen. The model is a 3-dimensional 6-DOF model seen in *Figure 13*. This model does consider damping (as proportional to the mass and stiffness matrices) and is linearized for small angular displacements. The degrees of freedom considered include the six rigid body degrees of freedom about the centre of gravity, namely vertical, lateral, and horizontal (y, z and x) displacements and yaw, pitch and roll rotations about the y, z and x axes respectively.

Using the 6-DOF model, simulations are used to determine how changes in coil spring stiffness influence the amplitude or displacement of vibration at the respective corners. To visualize the effect of stiffness change to displacement change, two normalized variables are compared. The first variable is a stiffness variation coefficient (SVC); the percentage change in stiffness of a coil spring from its initial stiffness. The second variable is an amplitude variation coefficient (AVC) which is the percentage change in vibration amplitude (in all three displacement directions for each corner) from its initial undisturbed amplitude before spring "failure" is introduced. Comparing these two variables provides an indication of which displacement (the dependent variable) is the most sensitive to a specific stiffness variation (the independent variable). The vertical y direction of the AVCs is the most sensitive to stiffness changes in coil springs, as deduced from simulations.

In a further study conducted in 2019 by Liu, et al. (2019) [29] a finite element model (FEM) of a vibrating screen is used instead of the 6-DOF model seen in *Figure 13*. An FEA model is used to take into consideration the flexible (or elastic) deformation, which is present during the operation of a vibrating screen. The rigid body model in *Figure 13* does not take flexible deformation into consideration. The FEA model is compiled in ANSYS comprising solid 3D elements and shell 2D elements for the screen body as well as beam elements for all bolted connections. The coil springs are modelled using linear spring elements (one in each displacement direction) at each corner of the screen. Of note in the coil spring model is that damping is not considered.

Initial simulation results show an increase in steady state lateral z displacement when spring failure is introduced. Performing multiple simulations with different stiffness variations, the SVCs and AVCs indicate that lateral z vibration amplitudes are most sensitive to coil spring stiffness variations. This is followed by the vertical y amplitude and lastly the horizontal x amplitude, which is the least sensitive.

The simulated results are validated using experimental results whereby a coil springs of 20% less vertical stiffness are used to represent "spring faults". Only steady state vibration amplitudes are used.

The experimental results also indicate that lateral z vibration amplitude is the most sensitive to spring stiffness variation. Also, the experimental and simulation results correlate well, with minor differences attributed to simulation modelling simplifications made. The proposed method, using SVCs and AVCs for coil spring failure diagnosis proves promising, specifically studying lateral vibration sensitivity to spring stiffness variations. However, using this methodology assumes that only coil spring stiffness changes will result in the higher lateral z vibrations. There are however several simultaneous changes occurring during the operating of a vibrating screen to take into consideration. These changes include feed bulk material load changes and wear on liners and screening panels, to name but two.

When surveying vibrating screen images it is evident that the use of helical coil springs as vibrating screen isolators is very common. Continuous cyclic loading of coil springs leads to permanent deformation in the pitch of helical coil springs [30]. The physical phenomenon, in which helical coil springs experience slow plastic deformation under constant and/or cyclic loads, is known as creep. This change or reduction in pitch results in a change in the stiffness of the coil spring which influence the vibrating screen.

In 2017 Chandravanshi and Mukhopadhyay [30] studied the influence of the reduced pitch coil springs on the dynamic behaviour of a vibrating feeder using modal analysis. Both simulated modal analysis (using FEA) and experimental modal analysis (EMA) are used in this study. Using modal analysis to analyse the dynamic behaviour of a vibrating machine allows for the detection of variations in modal parameters including natural frequencies, damping and mode shapes. Identifying variations in modal parameters is useful for fault diagnosis and prognosis. A force is transmitted to the base frame structure on which the feeder rests using a shaker and the response of the discharge of the feeder is measured using accelerometers. The measured force and responses are used to compute the FRFs.

EMA findings during this study by Chandravanshi and Mukhopadhyay show that multiple natural frequencies of the vibrating feeder increase with a reduction in helical coil pitch. This implies that the coil spring increases in stiffness as its pitch reduces. Due to creep, the stiffness of a coil spring increases as the active coils collapse under compression; reducing the number of active coils increases the stiffness, as seen in equation Eq. 5.

$$K_v = \frac{G \cdot d^4}{8 \cdot D^3 \cdot N} \qquad \textit{Eq. 5}$$

where G is the shear modulus of elasticity, d is the wire or bar diameter, D is the mean coil diameter and N is the number of active coils [30].

Changes in the mode shapes also accompany changes in natural frequencies. Changes in damping ratio are also observed, although the changes are not as noteworthy as the changes in natural frequency.

The simulated modal analysis is performed using ANSYS and a finite element model of the feeder body and coil springs uses solid 3-Dimensional tetrahedral shape elements. The simulated modal analysis indicates that the natural frequencies increase with coil spring pitch reduction; changes in mode shapes are also observed. No changes in damping are noted during the FEA analysis as damping was not considered in this model.

When comparing the FEA with EMA results, differences are observed. The source of these differences is the presence of damping in the actual test set-up and other non-linearities not accounted for in the

FEA model. However, the experiments prove useful for fault diagnosis as results indicate the possibility of using modal parameters for identifying changes in dynamic behaviour.

A thorough study of coil spring failure or crack detection was performed by Krot and Zimroz in 2019 [31]. Using the knowledge that isolators exhibit a gradual decrease in stiffness over time, it is necessary to evaluate the effect on the amplitude and frequency of a vibrating screen. It is difficult to implement traditional non-destructive tests (NDT) for coil spring fault diagnosis due to the spring geometry. Another disadvantage of NDTs is that they require the removal of the isolators from under the screen for close-up visual inspection. Therefore, vibration monitoring is the most logical for diagnosis of isolator faults. However, the vibration signature or signal of an operating vibrating screen has a stochastic component present due to bulk material excitation [31].

Krot and Zimroz suggested that coil spring vibration can be monitored by detecting changes in natural frequency from a nominal or initial value or by detecting changes in displacements on the four corners of the vibrating screen. The last mentioned, however, requires sensors on each corner of the vibrating screen. The study by Krot and Zimroz [31] recommended the use of vibration measurements from sensors already measuring bearing vibrations on the vibrating screen exciters and extracting features based on a phases space plot (PSP) method relating to the deterioration of coil springs. The PSP method does not require long sampling times as it is a time-based method that compares the displacement and velocity of the measured vibration in a particular direction.

A non-linear 6-DOF dynamic model, seen in *Figure 14*, was used for this study. The model considers deterministic and stochastic force excitation for the exciter forces and the bulk material forces on the screen deck respectively. Coil spring defects are introduced through stiffness reductions and crack initiation which is characterized by bilinear stress-strain characteristics. These bilinear characteristics of cracked coil springs produce harmonics of the excitation frequency which can be measured using vibration sensors.

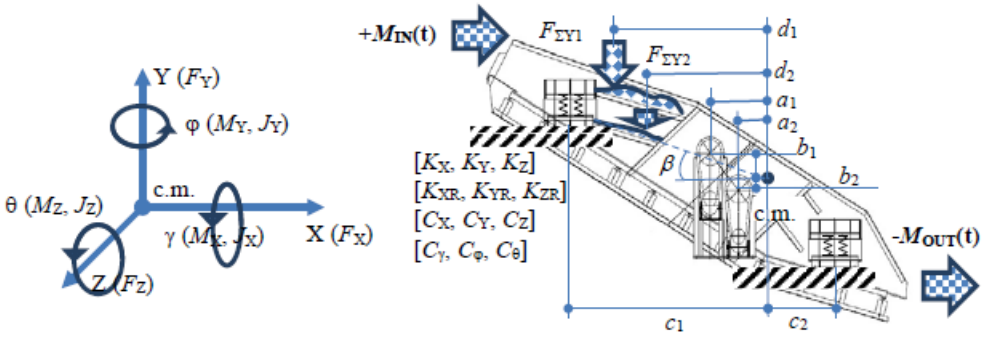

Figure 14: 6DOF model for coil spring deterioration study [31]

Using the model to introduce coil spring defects, a clear distinction is made between PSP results for the faultless and damaged spring case. However, further research is required to identify qualitative metrics for the analysis of PSP results.

In a further study in 2020 Krot, et al. [32] continued to use a model-based approach for evaluating features. Features extracted from measured signals using signal processing techniques for spring stiffness reduction and crack initiation diagnostics were evaluated. The model described in *Figure 14* is used along with a deterministic force excitation for the periodic motion as well as an alpha-stable stochastic impulsive force excitation as previously used [31]. The stochastic force component is

expanded to include both impacts of material on the screen deck, due to input flow and material impacts which occur due to the periodic motion of the vibrating screen.

A sensitivity study is performed using the model whereby bilinear stiffness change in coil springs are related to the following metrics:

- orbit amplitudes,
- orbit angles,
- the form factor (dV_y/dy i.e., phase space plot height divided by width) of the phase space plot (PSP) (The PSP is the velocity in a direction with respect to the displacement in the same direction),
- the change in velocity in a particular direction, and
- changes in amplitude and frequency of respective natural frequencies.

The results indicate that a near-perfect linear relationship exists between changes in metrics and respective changes in stiffness. However, the sensitivity of the changes is weak making it unclear whether these metrics are useful for real life application. Therefore, on-site tests were conducted and vibration measurements on an operating vibrating screen used to understand the metrics used.

The vibrating screen was instrumented with sensors on each corner as well as on the exciters measuring bi-axial acceleration (vertical y and horizontal x). Measurements were made while the screen was operating with material on the deck. From the test results it was observed that the orbit plots show significant difference in orbit angle between the left and right side of the screen and differences in PSPs per corner between the left and right side are apparent. This points towards the potential usefulness of PSP for fault diagnosis. Also, impacts on the screen deck from large ore particles excited the rigid body modes of the vibrating screen. Although not examined in detail, the impact response may be useful for fault detection by extracting the modal parameters and monitoring changes over time.

In conclusion, the motion trajectory metrics, such as orbit plots and PSP, show promising use in determining isolator stiffness decrease. However, more research is necessary for reliable qualitative metrics which are less sensitive to non-Gaussian noise.

The presence of non-Gaussian noise is prevalent in measured vibration signals of vibrating screens. This is particularly evident when largely impulsive vibration is exerted on the screen deck due to large, unpredictable ore particles landing on the screen deck. Common diagnostic techniques used, for example, for bearing fault detection depend on the reliable detection of cyclic impulses in the measured signal. However, if the signal is dominated by non-cyclic impulses, these classic diagnostic techniques are ineffective [33]. For this reason, it is necessary to identify and extract both the deterministic and random impulses in a vibrating screen's vibration signal.

In 2020 Gąsior, et al. [33] proposed the use of statistical analysis, envelope analysis and curve fitting to identify random impulsive behaviour in vibration measurements. A simple four-stage algorithm was used to iteratively remove the deterministic components from the measured signal. The algorithm then identifies the number of impulses present in the signal as well as recognizing their respective start and stop times. The identified non-cyclic, high amplitude or energy impulses can now be studied for properties relating to damage detection or are simply removed from the original measurement. Removing the non-cyclic impulses allows for the use of conventional diagnostic techniques.

Although the algorithm proposed by Gąsior, et al. shows promising results for simulated and real-life vibration measurements on vibrating screens, there are limitations to its use. The algorithm is only

applicable to vibration signals from a machine operating in quasi-stationary conditions. Also, impulses which occur before a previous impulse has dissipated can also cause the algorithm to be ineffective.

Michalak, et al. [34], in 2020, performed an in-depth decomposition of the vibration signal from a vibrating screen which leads to the identification and parameterization of the key signal components present which contain valuable information related to fault diagnosis. In an attempt at model-based diagnostics, Michalak, et al. set out to create a model of the vibration signal. This was done by reconstructing the signal considering the deterministic components (related to the excitation frequency of rotating weights), stochastic Gaussian component (related to external noise), stochastic α-stable component (as a model of impulses caused by large falling ore particles), and identified machine responses to unitary excitations (i.e. impulse excitations from falling ore particles).

Removing the main deterministic excitation frequency allows for the segmentation of the signal based on the presence of apparent impulse disturbances, then clustering the spectra of these impulses and finally fitting an autoregressive model. Although the signal model assumes stationary conditions (i.e. stationary excitation), it has the potential to be used in fault detection as it is constructed from the vibration signals of a "healthy" vibrating screen. Whereafter any additional future components in the vibration signal can be attributed to specific component faults.

In a similar study in 2021, Duda-Mróz, et al. [35] proposed the use of a wavelet-filtering technique to denoise the vibration signal measured on a vibrating screen. If one considers $s(n)$ to be the true vibration signal, which is a summation of the main drive frequency $sm(n)$ and fault frequencies $sf(n)$ and $e(n)$ the additive noise which corrupts the signal, then the observed or measured signal is $x(n)$=$s(n)$+$e(n)$. Denoising a signal reduces the magnitude of $e(n)$ allowing for the isolation of the main component $sm(n)$ and the study of the fault frequencies $sf(n)$ [36].

Duda-Mróz, et al. [35] proposed signal denoising using a wavelet filter which shows improved representation of the original signal as well as conserves the magnitude of the original signal and orbit trajectory after the filter is applied. This is the case when comparing the result to conventional moving average and low-pass filters. Filtering the vibration signal also shows improved convergence to an orbit trajectory compared to the unfiltered signal. A recommendation made during this study is to fit an ellipse to the measured orbit of the vibrating screen. The orbit parameters such as orbit length, width and angle can be extracted from the ellipse equation. The following equations are used for a 2D ellipse fit on horizontal and vertical vibration measurements:

$$x_t = x_c + a \cdot \cos(\theta) \cdot \cos(t) - b \cdot \sin(\theta) \cdot \sin(t) \quad \textit{Eq. 6}$$

$$y_t = y_c + a \cdot \sin(\theta) \cdot \cos(t) + b \cdot \cos(\theta) \cdot \sin(t) \quad \textit{Eq. 7}$$

$$d = \sqrt{(x - x_t)^2 + (y - y_t)^2} \quad \textit{Eq. 8}$$

where (x_t, y_t) is the closest point on the ellipse to the measured point (x, y) and therefore d is the shortest distance from the point to the ellipse. The objective function to be minimize is d. The hypothesis proposed is that this may be useful for long term analysis.

1.2.1.3 Vibrating screen modelling

Controlled experiments are considered the most effective and accurate method for measuring, monitoring, and studying features relating to the condition of a machine and its components. However, experiments can be expensive and time consuming. Therefore, developing a numerical model that has been validated within a defined working scope is a fast, cost-effective method for

studying features pertaining to the condition of the machine and its component. A validated numerical model can be useful for:

1. Interpreting experimental data
2. Predicting machine performance under known conditions

Vibrating screen modelling is useful for the prediction of screening performance and prognosis of its components. The numerical model can be developed and validated for known operating conditions using experimental data. Thereafter it can be used to predict changes in features for vibrating screens. Using the model, it is possible to estimate thresholds for features identified in the monitoring of the component condition. The model can also continuously be verified and improved with time as more test data is made available.
There are three main vibrating screen modelling approaches:

1. Discrete element modelling (DEM) using commercial software such as EDEM, ROCKY or open source LIGGGHTS software.
2. Finite element modelling (FEM) using commercial software such as ANSYS.
3. Multi-body dynamics (MBD) modelling using commercial software such as MSC ADAMS.

Models of vibrating screens mostly focus on separation [9], particle motion [37], screen component design [38] and failure investigations on component structures [23]. In some cases, coupled models are used combining DEM and FEA [38] or MBD and DEM [39]. The models generated for these analyses are computationally expensive and, in most cases, require expensive commercial software to compile and solve the simulations.

As seen in several studies [11] [26] [27] [28] [31] [39], making use of a numerically integrated mathematical MBD model for isolator analysis is both common and useful. These models have the benefit of being easy and efficient to set-up and perform simulations. However, there is the risk that the model over-simplifies the real-life problem. This shortcoming must be quantified to know the useful limits of the model.

1.2.2 Vibration-based condition monitoring

In the field of condition monitoring several techniques exist ranging from oil analysis in gearboxes to acoustic emissions from crack growth, temperature monitoring of bearings and the most common being vibration measurements. Vibration based condition monitoring has the advantage over other techniques in that it reacts immediately to changes in condition and there are numerous and powerful signal processing techniques which can be applied to a vibration signal to extract even very weak fault indications [6].

Using different signal processing techniques in combination with one another may prove more beneficial in that the advantage of each technique is used to strengthen the diagnosis of faults. In a practical study, Makua, et al., in 2019 [12] proposed the implementation of a monitoring system for the reduction of machine failures and improved preventative maintenance. The proposed system is based on the sensing of noise and vibration levels to detect abnormalities and faults. A fault or abnormality would be an audible noise or vibration level that is higher than normal or above a specified threshold for healthy operation which is a potential indication of a developing fault.

When the system detects a fault, it then informs the control room of the plant and can trip the vibrating screen to reduce the risk of catastrophic failure. However, this system does not specify a fault, but provides an indication that an anomaly has been detected. Once the vibrating screen has come to a standstill after being tripped, the potential fault needs to be investigated. This system,

although basic, can be expanded to include other sensors and algorithms to detect specific faults such as bearing defects and temperatures. The work by Makua, et al., considers some important practical considerations for the development of any condition monitoring system's integration into a mining environment where safety and clear visual communication is a necessity for quick response times to faults.

1.2.2.1 Sensors

Accelerometers, laser Doppler vibrometers and image-based stereo-photogrammetry are widely accepted as valid measurement techniques for measuring structural dynamics [40]. Each technique has its limitations such as laser Doppler vibrometers being sensitive to large displacements and accelerometers only able to measure a discrete point and adding mass to the structure. Laser Doppler vibrometers and image-based techniques are non-intrusive, however they do require line of site of the structure being monitored.

In 2017 Baqersad, et al. [41] performed a detailed review of full field measurement methods (i.e. Laser Doppler Vibrometer and Photogrammetry) compared to conventional point-wise sensors such as accelerometers and strain gauge. Their findings indicate that point-wise sensors, although being intrusive and having low spatial resolution, are substantially cheaper and allow for faster signal processing than full field techniques. Also, their calibration is not sensitive to changes in set-up conditions such as rigid body modes causing large displacements.

It is probable that due to these advantages, accelerometers have been widely accepted in the mining industry for vibrating screen monitoring. There are several vibration-based condition monitoring vendors available which have products advertised for application in vibrating screen monitoring. A short web survey identified the following available products:

- Schenk Process's CONIQ monitor [42] which is a wireless vibration condition monitoring system that makes use of Parker Lords' wireless node technology and methodology for online monitoring [43]. This product provides synchronized triaxial acceleration measurements between multiple nodes wirelessly enabling the measurement of operational deflection shapes (ODS). The wireless sensors use MEMS accelerometers that are battery powered. From a video [44] showcasing the monitoring solution there is also the opportunity for modal hammer impact tests to identify modes and mode shapes of the screen. Also, the ability to measure bearing vibrations is possible but then using other sensors than the wireless MEMS accelerometers described.
- Haver & Boecker Niagara's Pulse Vibration Condition Monitoring [45] is a wireless monitoring solution for either continuous or intermittent monitoring. There are no details regarding the sensors used, but the brochure indicates the possibility of ODS measurement as well as modal hammer impact tests being possible. Also, the inclusion of bearing condition monitoring is also available.
- IFM's Solution for Vibrating Screen and Feeder Monitoring [46] includes wired acceleration, speed, and temperature sensors in combination with diagnostic modules which interpret the data and have programmable limits built in. This solution is advertised for catastrophic failure detection, improving response time to the failure before other secondary failures occur. The accelerometers recommended are capacitive MEMS sensors. This is an application package as the sensors and modules recommended are useful for several other monitoring applications.
- PCB Piezotronics also recommends an application package for vibrating screen monitoring [47]. Because of the high levels of vibration in this application low sensitivity high range sensors are recommended. The accelerometers recommended are Ceramic ICP sensors able

to measure the low frequencies of vibrating screen applications. This solution package is also primarily applicable for catastrophic failure detection.

The earlier two-monitoring solutions above make use of wireless sensors for operational deflection shape measurements and experimental modal analysis through modal hammer impact testing. Due to advances in wireless sensor technology, using Bluetooth or Wi-Fi to transmit vibration data is becoming widely accepted in industry [48]. Bluetooth data transmission is low energy but has limited transfer speeds whereas Wi-Fi data transmission can handle high data transfer rates but has been known to have high power consumption compared to Bluetooth. However, there are now Wi-Fi products available with comparable power consumption to Bluetooth [48].

Wireless sensor solutions have the advantage of not requiring cables, which simplifies installation. However, they make use of batteries which imply a limited battery lifetime. For the CONIQ wireless sensors, a battery life of approximately 365 hours is obtained for triaxial measurements at a 256Hz sample rate [43]. This means a battery life of a little over 2 weeks for continuous monitoring. Typically, these sensors will be triggered for measurement either at regular intervals or when some sort of measurable event occurs such as a threshold exceeded. To extend the battery life sensors are developed which harvest energy from the vibration of the screen to recharge the sensors [49]. The drawback is that the energy harvesting technology in these sensors make them more expensive. Even with the drawbacks mentioned, the adoption of wireless sensors for the monitoring of vibrating screens is a trending topic in industry.

Wired solutions such as the latter two options mentioned above make use of commercially available industrial MEMS and ICP accelerometers. These sensors are comparable in price and are commonly used in industrial monitoring applications. The use of MEMS sensors for condition monitoring rather than ICP sensors has been a topic for research for many years due to noted benefits of MEMS sensor technology.

1.2.2.1.1 MEMS vs Piezoelectric Accelerometers

According to Varanis, et al. (2018) [50] and Koene (2022) [51] microelectromechanical systems (MEMS) sensors are known for their low price, low power consumption and small size in comparison with conventional ICP sensors which are known to be more accurate than MEMS sensors. However, they are also more expensive, consume more power and are bigger in size limiting their application, particularly with Internet of Things (IOT) technologies such as wireless sensors [51].

MEMS technology being small and efficient enables its use in IOT applications and wireless sensing which further reduces costs and eliminates complex installations for Condition Monitoring (CM) systems. The mechanism of measurement for MEMS accelerometers can be either piezoresistive or capacitive. Both piezoresistive and capacitive MEMS accelerometers can measure static (0Hz) and dynamic motion. MEMS sensors are known to be more suitable for low frequency applications than conventional piezoelectric accelerometers [50].

According to PCB Piezotronics [52] a capacitive MEMS accelerometer sensor is suitable for lower range, high sensitivity applications such as structural monitoring and constant (DC) acceleration measurements whereas a Piezoresistive MEMS accelerometer is suitable for higher range, low sensitivity applications such as shock and blast applications.

Studies showing comparisons between low-cost MEMS and conventional Piezoelectric accelerometers have indicated the suitability of MEMS accelerometers for Condition Monitoring (CM) and Structural Health Monitoring (SHM). Albarbar, et al. (2008) [53] performed tests comparing the performance of 3 different low-cost MEMS accelerometers with that of an ICP accelerometer for condition monitoring

of a CNC machine. Two of the MEMS sensors tested gave results comparable to that of the piezoelectric sensor however the results indicated that there is still room for improvement for low-cost MEMS sensor technology and more tests are required before this sensor type will be accepted in practice for CM.

1.2.2.2 Fault diagnostics and feature extraction

Based on a review by Park, et al. in 2020 [54] fault detection and diagnosis (FDD) is the process of developing an effective fault indicator which allows for timeous corrective action to avoid failure. FDD concerns the monitoring of the behaviour of variables within a process with the goal of revealing the presence of a fault, its characteristics and possible root cause. FDD is not concerned merely with the failure of a component but how a component's failure affects the entire process. The implementation procedure of a conventional FDD method is seen in Figure 15.

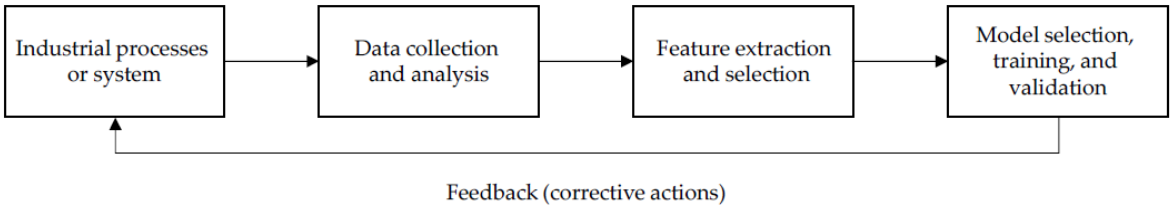

Figure 15: Fault detection and diagnosis implementation procedure [54]

A similar approach can be used for condition monitoring of faults on machinery whereby data is collected in the form of sensor measurements, features are extracted from the data using robust signal processing techniques. Thereafter a suitable model is developed which, after validation, can be used to study the sensitivity of the features extracted to developing faults and other changes in the system. The model is used to gain confidence in the ability of extracted features to isolate and identify faults in a system. A trained model, using machine learning algorithms, can provide further insight into the possible abnormal operation of the machine and is useful for the isolation and identification of the fault.

A model is trained using either supervised or unsupervised methods [54]. In a supervised method, data or information relating to known faults are used to establish a subspace or region of abnormal operation based on the fault status. Unsupervised methods isolate faults from data without prior knowledge. Using controlled experiments whereby faults are introduced to a system and the response is measured allows for extracting features relating to the specific fault introduced while simultaneously minimizing external noise [55]. The features extracted can therefore be confidently classified to a known fault and can now be further analysed. In such a case supervised learning methods such as Support Vector Machines (SVM) can be adopted to establish the fault subspace relating to a specific fault.

Using controlled experiments is essential for building the knowledge necessary for damage identification and isolation. This was emphasised by Daga and Garibaldi in 2019 [56] who identified steps or levels of depth for damage identification in measured signals as,

1. Detection: identifying the indicators given by the presence of damage within a signal with reasonable confidence.
2. Localization: identifying the location of the damage based on prior knowledge.
3. Classification: identifying the typed of damage that has occurred based on prior knowledge.
4. Assessment: quantify the magnitude of the damage.
5. Consequence: determine a prognosis of the damage.

Feature extraction using reliable and efficient signal processing techniques is critical for the identification of faults in machinery [57]. Signal processing techniques for feature extraction can be categorized into various categories. Yang, et al. [57] use three main categories in which to group signal processing techniques for rotating machinery fault diagnosis. Time domain, frequency domain and combined time-frequency domain categories are used. An overview of time domain signal processing techniques is shown in Figure 16.

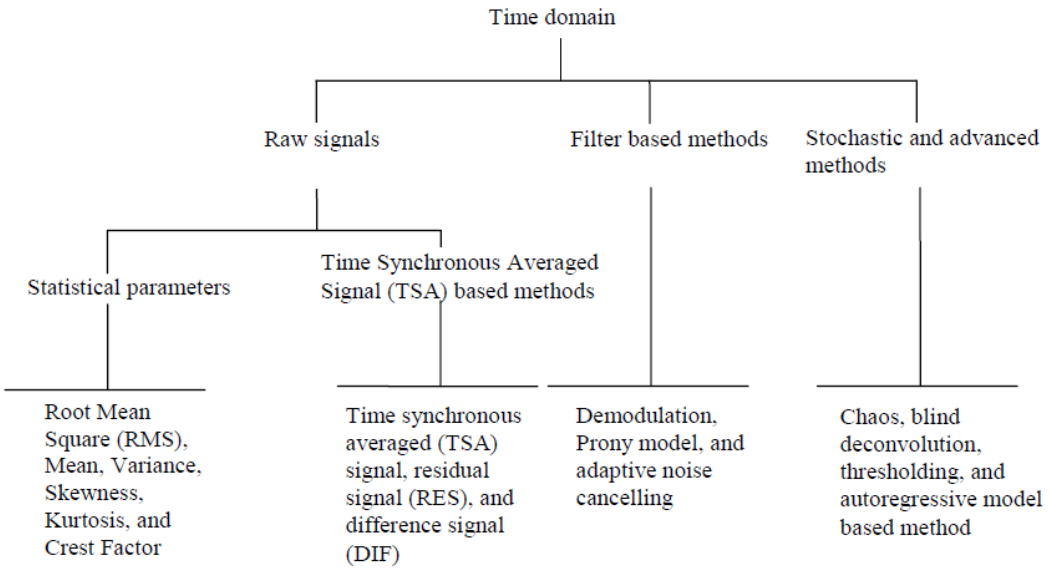

Figure 16: Overview of time-domain techniques [57]

According to Yang, et al., statistical parameters are considered the most basic analysis on time domain data and have proven to be useful for machine fault detection, particularly for bearing defects. Time synchronous averaging and filter-based methods are useful for effectively separating the fault component of vibration from other irrelevant components such as noise. Stochastic and advanced time domain methods are useful for denoising the signal by decomposing the vibration signal into deterministic components allowing for the enhancement of the fault signals.

An overview of frequency and time-frequency domain techniques can be seen in Figure 17 which shows a table of techniques. These techniques are grouped according to an increasing order of frequency or time frequency transformation parameters. Increasing the order of transformations allows for the computation of different coefficients for fault detection.

Frequency domain techniques are preferred over time-domain techniques due to their consistency [57]. The Fast Fourier Transform (FFT) is the base technique for the higher order power spectrum and cepstrum and bicoherence frequency domain techniques all of which are useful for stationary time signal analysis [6]. The time-frequency domain techniques (CWT, DWT, DWPA, TAWS, TFS, Spectrogram, Scalogram, Wigner distribution and Wigner bi and tri spectra) are useful for creating a map indicating how frequency content varies with time and is useful for analysis of time varying transient signals. The more clearly this variation is mapped out, i.e., the higher the resolution, the easier it is to identify faults in transient signals. According to the review by Yang, et al. [57] in 2003, these techniques have been effectively applied in the diagnosis of faults in rotating machinery.

A more recent review by Zhang, et al. in 2022 [55] identified the signal processing techniques that have become invaluable for structural health monitoring (SHM). Zhang, et al. describe the basic goal of signal processing as identifying the changes or damages indicative in a vibration signal for the

detection, location and quantifying of any damage existing in the system. The signal processing techniques are classified in two major categories (i) Time and (ii) Frequency domain techniques.

Table 1. Overview of frequency techniques and time-frequency techniques

First order	Second order	Third order	Fourth order
Spectrum (FFT)	Power spectrum	Bicoherence spectrum	
	Power cepstrum (logarithm of Power spectrum)		
Correlation of spectrum, signal averaging	Cyclostationarity	bilinearity	
Short time Fourier transform (STFT)	Spectrogram		
	Wigner distribution	Wigner bi spectra	Wigner tri spectra
Continuous wavelet transform(CWT)	Scalogram		
Discrete wavelet transform(DWT)			
Discrete wavelet packet analysis (DWPA)			
time-averaged wavelet spectrum (TAWS)			
time-frequency-scale domain (TFS)			

Figure 17: Table 1 from [57] showing frequency and time-frequency domain techniques

Time domain signal processing for SHM primarily focusses on linear statistical time series models. Linear statistical time series models can be categorised as stationary methods, such as autoregressive (AR) and moving average (MA) models, or non-stationary methods such as vector autoregressive (ARV) models. Autoregressive models make use of time series features extracted from historic measurements as well as the quantified residual errors to make predictions of the future values of these features [55].

The use of frequency domain techniques such as FFT for SHM are primarily focused on measuring variations in modal parameters such as natural frequency, mode shapes and damping ratio. Changes in these parameters are considered indicative of changes in structural mass or stiffness. Variation in natural frequency is the most utilized approach as only a single sensor is required to detect the changes. Taking the FFT of both the responses of the structure and the measured excitation forces allows for the computation of a linear frequency-based transfer functions also referred to as frequency response functions (FRFs). There are numerous techniques available for the extraction of modal parameters from measured FRFs using both single degree of freedom (SDOF) and multiple degree of freedom (MDOF) analyses [58].

The basis for modal parameter extraction methods consists of curve fitting a theoretical expression of a system of FRFs to actual measured FRFs obtained by EMA. The coefficients of the theoretical FRF receptance model ($\alpha_{jk}(i\omega)$) comprise of the mode shapes ($_r\theta$ with modal constants a_r), natural frequencies (ω_r) and damping ratios (ζ_r) as seen in equation Eq. 9 [58]. The theoretical model is the starting point for modal analysis.

One of the earliest methods of modal analysis of MDOF systems is the complex exponential method [58]. This method is a time domain method utilizing impulse response functions (IRFs), derived from the measured FRFs, and fitting a series of complex exponential components to the IRFs. Comprised in

the properties of the complex exponential components are the eigenvectors (mode shapes) and eigenvalues (natural frequencies and damping ratios) of the modes. The principal advantage of this method is that it does not rely on initial estimates of modal parameters.

$$\alpha_{jk}(i\omega) = \sum_{r=1}^{N} \left(\frac{{}_r\theta_j \, {}_r\theta_k}{a_r \left(\omega_r \zeta_r + i \left(\omega - \omega_r \sqrt{1-\zeta_r^2} \right) \right)} + \frac{{}_r\theta_j^* \, {}_r\theta_k^*}{a_r^* \left(\omega_r \zeta_r + i \left(\omega - \omega_r \sqrt{1-\zeta_r^2} \right) \right)} \right) \qquad \textit{Eq. 9}$$

Each signal processing technique has application limitations, advantages, and disadvantages over other techniques. Zhang, et al. [55] describe some of these advantages and disadvantages as well as limitations in more detail. The most noteworthy are the limitations of frequency domain techniques which are primarily useful for stationary discrete time sampled signals making their application on non-stationary signals from nonlinear structures less effective. For this reason, time-frequency domain techniques are adopted for analysis of non-stationary signals and using artificial intelligence techniques such as Artificial Neural Networks can minimize the errors made on non-linear signals. Also, limitations on the use of FRFs, although effective for analysis of response signals, are not able to efficiently identify damage types, magnitude, and locations. This drawback can however be mitigated by combining the FRF technique with other numerical models or simulations such as finite element analysis (FEA) models.

1.3 SCOPE OF WORK

For condition-based maintenance to function effectively it is necessary to have robust and reliable monitoring techniques. The purpose of this study is not to develop new techniques, but to evaluate existing techniques for determining the condition of vibrating screen isolators. Techniques considered involve the processing of measured vibration signals for the extraction of interesting features. It is necessary to identify which of these features are most sensitive to changes in the condition of the component being investigated.

The difficulty of deciding whether changes in the responses measured are due to changes in excitation, mass, inertia, stiffness etc. of components comprising a vibrating screen is the basic problem of condition monitoring [6]. Therefore, evaluating each deviation separately removes ambiguity in the classification of changes of features in the measured responses. Evaluating the changes in operation (i.e. dynamic motion and/or functional performance) can be directly related to specific changes in condition of vibrating screen components (assuming the operating conditions are unchanged). Based on the most recent literature for condition monitoring of vibrating screens it is both relevant and necessary to study how changes in isolator characteristics influence the operation of a vibrating screen.

From the literature it is clear that the effect of isolator deterioration on the operation of a vibrating screen is not clearly known, and no generic metrics or approach has shown to be universally applicable in determining the isolator condition. Static displacement techniques seen in literature [27] may prove useful for identifying large stiffness changes but become impractical for the diagnosis of specific failures if multiple isolators are present per corner of large vibrating screens.

Non-destructive testing (NDT) techniques cannot be used for crack detection on coil springs due to their geometry [31]. Also there exists no NDT techniques for rubber isolators. Visual inspections are not practical or effective for fault development detection due to limited access which may require the isolators be removed from under the vibrating screen for thorough inspection. This is a very time-consuming process and there is the obvious risk of a misdiagnosis based on misleading visual cues.

A promising method for isolator monitoring is vibration-based monitoring. A major benefit of vibration-based monitoring is that there exist many robust signal processing techniques to extract features relating to fault diagnosis and prognosis. Literature surveyed indicate the features of most practical relevance for isolator monitoring involve the use of experimental modal analysis (EMA) [30] and operational features [32] [35]. Although mentioned [11], the transient startup and coast down have not been considered for studies relating to vibrating screen condition monitoring.

A common approach to evaluating how features change with changes in isolator condition is a model-based approach [32] [11] whereby a dynamic model of a vibrating screen is developed and used for a sensitivity study to evaluate how the features are expected to change with faults introduced. Although this method is useful for feature evaluation, if not validated, the model cannot be assumed to be representative of the actual system under test, which in this case is a vibrating screen of any size and for any application. The model needs to be generic, able to be adapted to represent a particular vibrating screen with reasonable accuracy. Also, although most models developed only consider the "steady" operation of the vibrating screen, the transient startup and coast downs portions of the operating envelope should also be considered.

It is necessary to sieve through different techniques and identify promising features which may be used generically to indicate isolator changes and faults independent of the isolator type being used. To cement the application of these features for monitoring of isolators, a numerical model simulating rigid body motion of a vibrating screen will be developed. This implies an MBD model which can be modified to introduce isolator faults and ignores the effects of the vibrating screen structural flexion as well as the effects of material on the deck of the screen. The model shall be validated for the entire operating envelope (startup, steady operation and coast down) using experimental results after which a sensitivity study will be performed to evaluate features for the monitoring of deviations in isolator parameters (i.e. stiffness).

Although no generic model or algorithm for feature extraction exists, it is the purpose of this study to identify interesting features and evaluate their relation to the condition of isolators. Following the sensitivity study from the developed MBD model the quantitative predictions of feature behaviour are to be compared with empirical investigation of the effect of change of isolator characteristics on the vibrating screen's operation. Correlation between the simulated and empirical feature behaviour builds confidence in the usefulness of the model for further study. Also, features exhibiting high sensitivity and predictability will be indicative of a starting point for deciding how to monitor the condition of isolators.

For sensor selection, considering the comparisons in literature between optical (full field) and point wise sensors, due to their low cost, ease of use and insensitivity to external changes in the working environment, accelerometers are more suitable for vibration monitoring of vibrating screens. A supplementary evaluation is performed in this study using conventional ICP (integrated circuit Piezoelectric) and comparable MEMS (microelectromechanical systems) based accelerometers for vibrating screen monitoring. This evaluation is more qualitative than quantitative. Both ICP and MEMS accelerometers are suitable for vibrating screen applications which are low frequency applications and

require high sensitivity and resolution within the working range. However, a direct comparison is performed in this study to evaluate their suitability.

1.3.1 Final considerations

This research forms part of an ongoing study at the University of Pretoria into the use of response measurements, numerical models, and signal processing techniques for condition monitoring of vibrating screens. In the study by Harat [59] the problem of isolator condition monitoring was supported by developing a finite element analysis (FEA) model of an existing vibrating screen with rubber isolators. The rubber isolators were modelled as linear spring elements. The FEA model was validated by comparing the rigid body natural frequencies and mode shapes from simulated modal analysis to those obtained from an EMA of the actual vibrating screen.

As a secondary study Harat extracted time domain features from transient tests performed on a real vibrating screen. Several test cases are performed with damage induced onto the isolators as well as loose mass added to the deck to force a change in dynamic behaviour. Finally, the features extracted were classified using a Support Vector machine model. The model indicated clear classification for several feature combinations. The classification of features from simulated data in the FEM environment was also performed.

In conclusion it was found that the FEM model, although having similar modal frequencies to the physical vibrating screen, was not able to determine the dynamics of the physical vibrating screen for different isolator stiffness configurations. Also, classifying features from the FEM environment do not correlate well with the feature classification from the experimental data. The FEM model was limited in its application to feature extraction for changes in isolator stiffness due to its oversimplification of the vibrating screen. The real vibrating screen exhibited a non-linear response in that inconsistent transient behaviour was observed during successive tests.

For the purpose of this study, and considering the conclusion made by Harat [59] regarding the perceived limitations of the FEM model, an MBD model is selected as a suitable alternative. The benefit of an MBD model over a FEM model is the reduction of complexity by not including flexible modes in the dataset thereby reducing ambiguity when interpreting results. This also has the benefit of time saving in that an MBD model (only considering the rigid body modes) is faster to compile and modify to account for different vibrating screens where a FEM model requires a meshed geometry for each vibrating screen which is very time consuming. Reducing the model to only considering rigid body motion enhances the contribution of the isolators to the dynamics as no energy is lost/absorbed by the flexion of the vibrating screen structure.

Lastly, it is desirable to first identify interesting features which are sensitive to the condition of the isolators before attempting to classify the data by training and validating an appropriate model. Therefore, this study attempts to determine which interesting features are most sensitive to isolator conditions as classification models may benefit the most by including these features to their datasets.

1.4 DOCUMENT OVERVIEW

In Section 2 an MBD model of a vibrating screen is developed. Equivalent results from similar MBD models developed in commercial software as well as experimental results are used to validate the model for its usefulness in representing the entire operating envelope of a vibrating screen. The validated model is then used for a sensitivity analysis whereby the operation of the vibrating screen is predicted for varying faults introduced on the isolators.

In Section 3 an overview is given of an experimental investigation into the changes in dynamic response to artificial faults introduced to the isolators of an existing vibrating screen. Three different types of isolators are used and installed in different configurations to introduce controlled faults. Each isolator type is first characterized to assess their vertical stiffness with compression. Three different types of accelerometers and two different data acquisition devices are used to perform the measurements. Each are evaluated qualitatively for accuracy and practicality. Preliminary results are presented as well as a description of the interesting features identified, and the signal processing used for feature extraction.

Section 4 shows details regarding the results obtained from the numerically simulated and experimentally derived sensitivity study of each identified feature. A discussion regarding the comparison between the simulated and empirical results is provided whereby similarities and differences are described and possible reasons for discrepancies given. Finally, the conclusions and recommendations are presented in Section 5.

2 NUMERICAL MODEL

This section describes the methodology used in developing a 4 degree of freedom vibrating screen model. After validation and calibration, the mathematical model is used to make significant predictions of the systems behaviour to changing isolator parameters.

2.1 INTRODUCTION

A vibrating screen has 6 rigid body modes associated with it. To simplify the model only 4 major degrees of freedom are considered. The 4 degrees of freedom considered for this model are:

1. Vertical (up and down in the z direction) bounce of the centre of gravity (CG),
2. Horizontal (forward and backwards in the x direction) bounce of the CG,
3. Pitching (rotation about the lateral y axis) about the CG and
4. Rolling (rotation about the horizontal x axis) about the CG.

Figure 18 shows an illustration of the vertical and horizontal bounce. Take note of the z and x axes. These directions are considered because they are associated with the primary motion of a vibrating screen. The lateral y direction bounce is not considered in the model. The reason is because the lateral direction motion is significantly less than the vertical and horizontal directions due to the excitation forces direction being primarily vertical and horizontal.

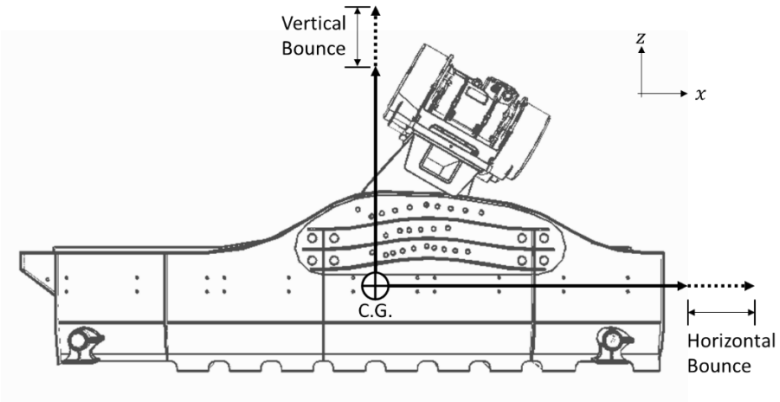

Figure 18: Illustration of bounce degrees of freedom

Figure 19 shows the rotation about the lateral y axis. The illustration shows a negative rotation or pitch as the opposite rotational direction is taken to be the positive pitch or θ direction. Figure 20 illustrates the rolling degree of freedom which is the rotation about the horizontal x axis. The rotation illustrated is in the positive rolling direction.

The yaw degree of freedom, which is the rotation about the vertical z axis, is not considered in this model for the same reason that the lateral displacement is not considered. The yaw degree of freedom is primarily associated with lateral displacements.

The degrees of freedom selected correlate with the degrees of freedom measured during the experiments where sensors on each corner measure both the vertical and horizontal motion of the actual vibrating screen. The 4 degrees of freedom considered are useful in predicting the steady state operation of the vibrating screen as well as the transient start-up and shutdown or coast down.

The numerical model is developed mathematically using Newtons second law $(\sum F = m \times a)$. The mathematical equations are scripted in Python. Standard Python libraries such as Numpy and Scipy

are used to compile a system of first order differential equations. These equations are numerically integrate using a Runge-Kutta 4th order integration algorithm to predict the displacement, velocity, and acceleration of the vibrating screen.

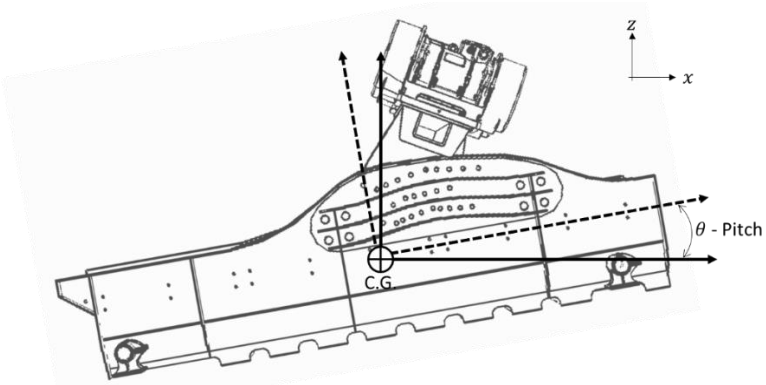

Figure 19: Illustration of the pitch degree of freedom

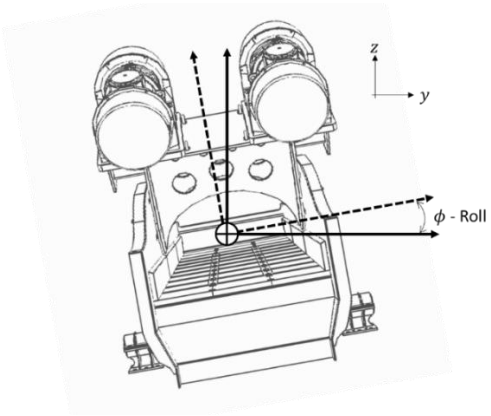

Figure 20: Illustration of the roll degree of freedom

2.2 MODEL ASSUMPTIONS

To simplify the model and avoid complex and computationally expensive simulations, assumptions are made. These assumptions are mostly aimed at linearizing non-linear behaviour inherent in vibrating screen dynamics. The following assumptions are applicable to the model:

1. The motors are driven using experimentally measured or numerically generated rpm curves per motor. This implies that motors are not modelled. Rather, as in the case of unbalanced motors, a linearized force vector model is used which estimates the necessary force vectors for the respective axes. The force vector is estimated by considering the position and orientation of the unbalanced motors, the unbalance ($m \times r$) of the motor weights and the measured or assumed rpm profile of each motor. The problem of self-synchronization of unbalanced motors does not fall within the scope of this study. The unbalanced motors are assumed to be in sync unless otherwise measured during experiments or numerically generated.
2. The isolators are modelled as a spring and dashpot damper combination per corner. Constant stiffness and viscous damping are assumed in all directions. However, the vertical and horizontal component of stiffness and damping are not the same and can be adjusted. The

stiffness and damping values per corner are initially assumed from catalogues, calculations or estimated values. The experiment data will be used to calibrate each corners stiffness and damping to get the most reasonable response. Defects in isolators are introduced by simply modifying the respective stiffness and damping value(s).

3. The vibrating screen body is modelled as a completely rigid frame. Although this is relevant to the current study, it is not safe to assume that this is the case for other vibrating screens. As mentioned, the vibrating screen considered in this study has no structural or flexible modes below the operating frequency of ≈16.4Hz or 985rpm. Only rigid body modes exist within the stationary to operating frequency range. The assumption of a rigid body also implies that the effect of non-linear structural materials such as polyurethane and rubber panels or liners are ignored.
4. All dimensions including dimensions measured or referenced from the centre of gravity of the machine are assumed from the CAD model of the vibrating screen. A critical assumption is the position of the centre of gravity (CG) relative to the isolation corners as well as the mass and respective mass moments of inertias. The mass is assumed to be a lumped mass placed on the CG position. The CG position, mass and mass moments of inertia are hard coded and are not calibrated after implementation. However, the ability to change the model's mass and mass moments of inertia about the CG allows for a study into the influence of these parameters on noted features in the transient and operating dynamics.
5. The pitch and roll degrees of freedom, being angles, introduce nonlinearities to the model. However, it is possible to linearize the angles for small angles. For linear vibrating screens a small angle assumption may be more reasonable whereas for an orbital or circular motion vibrating screen the small angle assumption may result in errors due to large oscillating motion especially during startup/ramp-up and shutdown/coast-down. A nonlinear model is more intuitive to build using sine and cosine geometric relations for pitch and roll angles. Thereafter the model can be linearized for small angles. The small angle equivalents are,

$$\cos(\theta) \approx 1$$
$$\sin(\theta) \approx \theta$$

Small angles are assumed to be angles less than or equal to $5°$. This is a reasonable assumption as an angle of $5°$, for the screen in question, results in $\approx 88mm$ of vertical displacement at the discharge of the screen and $\approx 175mm$ of vertical displacement at the feed of the screen. With these displacements the isolators are either over compressed (in the case of coil springs they will bottom out) or the screen is no longer making contact with the isolator due to a vertical displacement amplitude being above the initial steady state compression under gravity.

For larger vibrating screens the rotation angles of pitching and rolling will be much less due to the displacement limitations. For example, a vibrating screen of 6 meter length and rotations of $5°$ about the centre will result in a vertical displacement of $\approx 260mm$ which is not only impractical but should such displacement actually occur there is a safety risk in that it is possible for the machine to jump off its isolation positions on site. Therefore, a small angle assumption is a reasonable assumption for vibrating screens even though transient displacements may be significantly more than the operating displacements. The displacements are not such that large rotational angles are experienced.

The small angle assumption introduces errors. Figure 21 shows the relative errors for linearizing $\sin(\theta)$ and $\cos(\theta)$. The largest error lies with the linearization of $cos(\theta) \approx 1$ which is a $\approx 0.4\%$ error at $5°$. For smaller angles such as $1°$ the error is such that the difference between the nonlinear and linearized values are negligible.

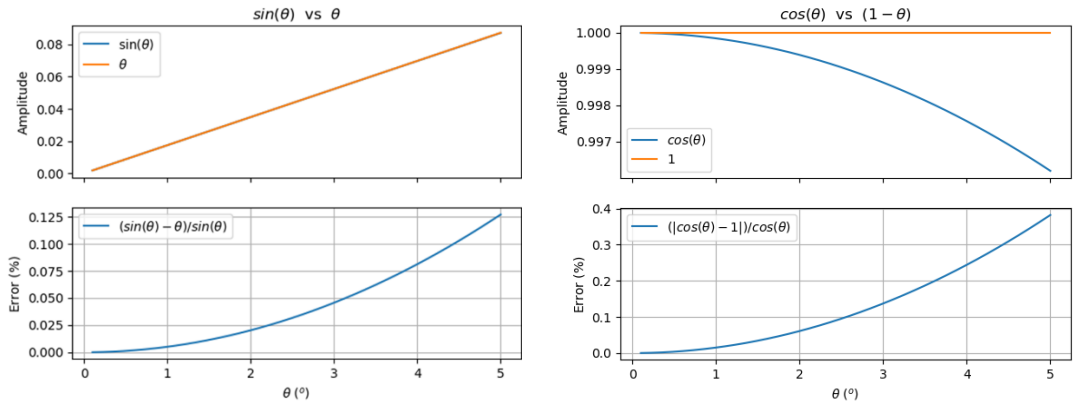

(a) *(b)*

Figure 21: Linearization Error a) Error using $sin(\theta) \approx \theta$ b) Error using $cos(\theta) \approx 1$

6. Gravity is introduced as an initial condition for all the degrees of freedom. The benefit of this is that the isolators compress to an initial condition whereafter it is possible to determine if the vibrating screen jumps out of the isolators during transient behaviour. However, if during transient simulation the displacement of a corner should increase to above zero displacement then that corner is assumed to have jumped beyond the uncompressed length of the isolator. This is an important prediction as a vibrating screen that jumps beyond isolator limits is considered unsafe.
7. The isolators to be considered are Resatecs, coil springs and rubber isolators, the latter two being compressive elements only and the Resatec being able to exert both a compressive and tensile force. Therefore, for large displacements above steady state compression under gravity large errors will occur due to a tensile stiffness assumed. The model does not consider the case when the vibrating screen is no longer in contact with the isolators.

2.3 MODEL DEVELOPMENT

The model is based on a 3 degree of freedom (DOF) model found in literature [11]. The 3DOF model is a 2-dimensional model that includes vertical and horizontal bounce along with pitching about the CG. The 4th degree of freedom we are introducing is the rolling about the CG. This implies that the new model is 3-dimensional in that it requires information relating to the height, length, and width of the vibrating screen.

The model is built in two distinct steps:

1. A rigid body of the vibrating screen is modelled with respect to the CG. This includes modelling the stiffness and damping elements per corner.
2. Modelling the excitation forces exerted on the vibrating screen with respect to the CG and respective degrees of freedom.

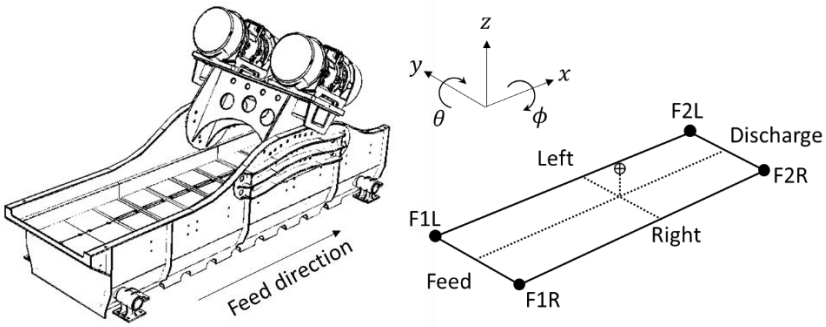

Figure 22: Vibrating screen with equivalent rigid body model

Figure 22 shows the sign convention adopted along with an equivalent free body diagram of a rigid vibrating screen. The sign convention shows the positive axis directions which will be used for the model. Take note of the labelled left and right side of the screen as well as the feed and discharge of the screen. The feed of the screen is the side where ore is fed onto the screen deck and the discharge is where the ore is conveyed over the screen deck into the next process. F1 refers to the feed side and F2 refers to the discharge. L and R refer to the left and right side of the screen respectively.

2.3.1 Vibrating screen rigid body model development

To relate the four corners of the vibrating screen to the CG the rigid body is parameterized using variables that can be adjusted accordingly for any screen body. Figure 23 shows the dimensional variables with reference to the CG of the machine. Variables a, b and w are measured from the centre of the isolation bracket or the centre most isolator on each corner. The dimension c is measured perpendicular to the line between isolator centres which is not necessarily perpendicular to the screen deck.

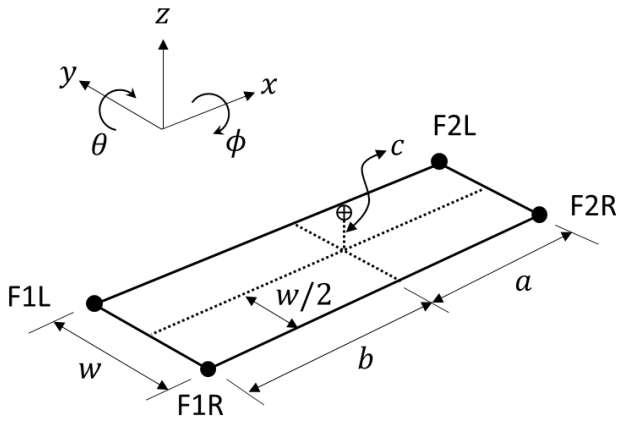

Figure 23: Variables used to build the rigid body of the screen.

As mentioned, each corner, namely F1R, F1L, F2R and F2L, each have stiffness and damping in both the z and x directions. Figure 24 shows a spring and dashpot damper element for corner F1R in both the vertical (z) and horizontal (x) directions.

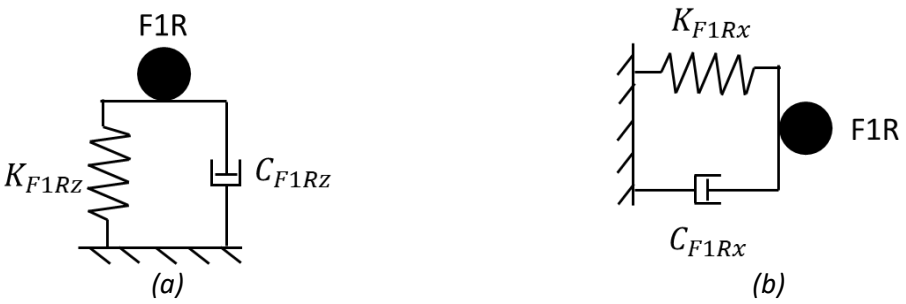

Figure 24: Stiffness and damping elements in the a) Vertical and b) Horizontal directions

The deck or screen angle (β) from F1 to F2 is also considered in the model in the same way that the 2-dimensional model [11] incorporated the deck/screen angle. Figure 25 shows how the deck angle is accounted for. The deck angle β is an initial condition of the geometry to determine the datum of the vibrating screen. It is also used to update the moment arms at supports such that the reaction forces at the corners will exert the correct moment arm about the CG. Although the moment arms are not altered significantly at small angles, they are altered significantly at screen angles of $5°$ to $35°$ which is not uncommon for a vibrating screen [8] [9].

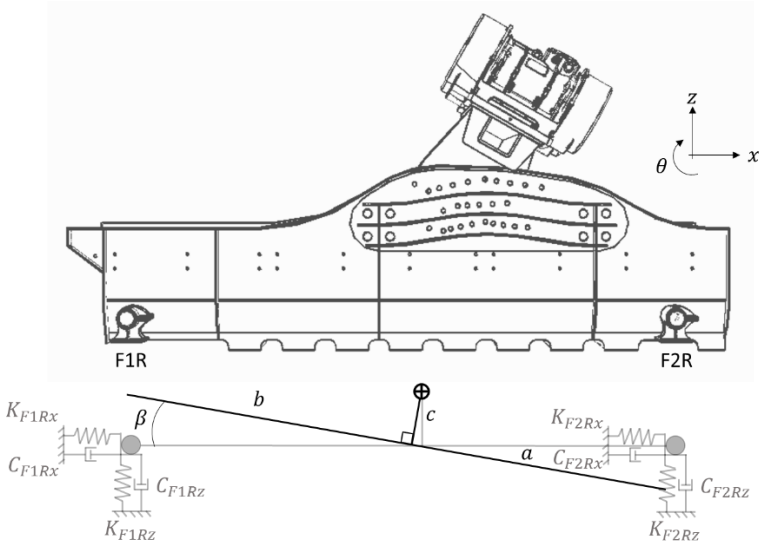

Figure 25: 2-dimensional view of XZ plane with deck angle

Parameterizing the z and x displacements per corner requires that the geometric variables (a, b, c, β) be linked to the displacements per corner. Figure 26 shows how the rotation through the screen angle β and pitch angle θ influence the vertical displacement at F1 and the horizontal displacements at F2. The equations shown are nonlinear as the sine and cosine of θ is used. The sine and cosine of β result in constants because β is known. Similar geometric relations as seen in Figure 26 can be used to get the equations for the horizontal displacement at F1 and vertical displacement at F2.

The datum for the equations in Figure 26 is the zero/initial state where $\beta = \theta = 0°$. Once a β of greater than or less than zero is introduced the new zero/initial state is where $\beta \neq 0°$ and $\theta = 0°$.

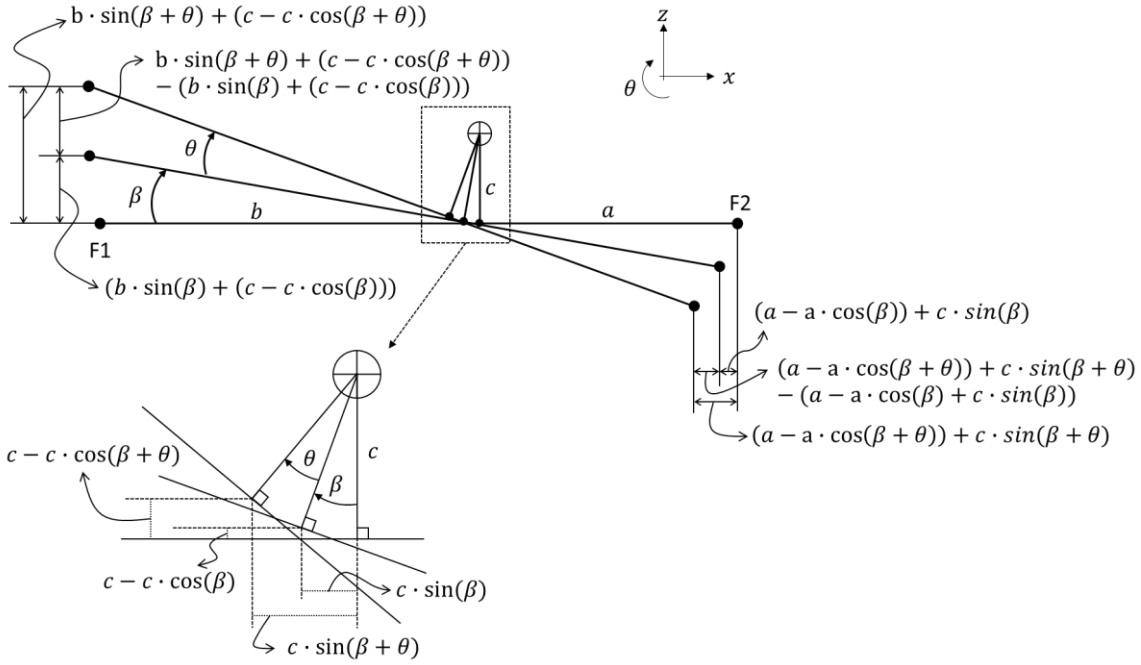

Figure 26: Derivation of equations linking geometry and degrees of freedom to corner displacements.

The equations relating the vertical (z_{CG}) and horizontal (x_{CG}) bounce degrees of freedom as well as the nonlinear pitching angle (θ) to the x and z displacements for F1 and F2 are as follows,

$$\begin{aligned} x_{F1} &= x_{CG} + \cos(\theta) \cdot A + \sin(\theta) \cdot B - A \\ x_{F2} &= x_{CG} + \cos(\theta) \cdot C + \sin(\theta) \cdot D - C \\ z_{F1} &= z_{CG} + \cos(\theta) \cdot B - \sin(\theta) \cdot A - B \\ z_{F2} &= z_{CG} + \cos(\theta) \cdot D - \sin(\theta) \cdot C - D \end{aligned} \qquad \textit{Eq. 10}$$

where,

$$\begin{aligned} A &= (a \cdot \cos(\beta) - c \cdot \sin(\beta)) \\ B &= (-a \cdot \sin(\beta) - c \cdot \cos(\beta)) \\ C &= (-b \cdot \cos(\beta) - c \cdot \sin(\beta)) \\ D &= (b \cdot \sin(\beta) - c \cdot \cos(\beta)) \end{aligned} \qquad \textit{Eq. 11}$$

The coefficients A, B, C and D are derived by expanding the equations seen in Figure 26 with the trigonometric identities $\sin(\beta + \theta) = \sin(\beta) \cdot \cos(\theta) + \sin(\theta) \cdot \cos(\beta)$ and $\cos(\beta + \theta) = \cos(\beta) \cdot \cos(\theta) - \sin(\beta) \cdot \sin(\theta)$.

The z and x velocities are derivatives of equations Eq. 10. The velocities are as follows,

$$\begin{aligned} \dot{x}_{F1} &= \dot{x}_{CG} - \dot{\theta} \cdot \sin(\theta) \cdot A + \dot{\theta} \cdot \cos(\theta) \cdot B \\ \dot{x}_{F2} &= \dot{x}_{CG} - \dot{\theta} \cdot \sin(\theta) \cdot C + \dot{\theta} \cdot \cos(\theta) \cdot D \\ \dot{z}_{F1} &= \dot{z}_{CG} - \dot{\theta} \cdot \sin(\theta) \cdot B - \dot{\theta} \cdot \cos(\theta) \cdot A \\ \dot{z}_{F2} &= \dot{z}_{CG} - \dot{\theta} \cdot \sin(\theta) \cdot D - \dot{\theta} \cdot \cos(\theta) \cdot C \end{aligned} \qquad \textit{Eq. 12}$$

Considering the roll DOF, only the vertical z direction is influenced and the x direction remains unchanged. This implies that corners at F1 have the same horizontal displacement in the model, and the same is true for F2. Therefore, the following equations are applicable for both the nonlinear (Eq. 10) and the linear (Eq. 37) horizontal x direction equations.

$$\begin{aligned} x_{F1R} &= x_{F1} \\ x_{F1L} &= x_{F1} \\ x_{F2R} &= x_{F2} \\ x_{F2L} &= x_{F2} \end{aligned} \qquad \textit{Eq. 13}$$

Figure 27 shows how the rolling angle (ϕ) effects the vertical displacements at the left and right corners. The datum is the initial zero state where $\phi = 0°$. Also note the positive sign convention for the y direction and the rolling angle ϕ.

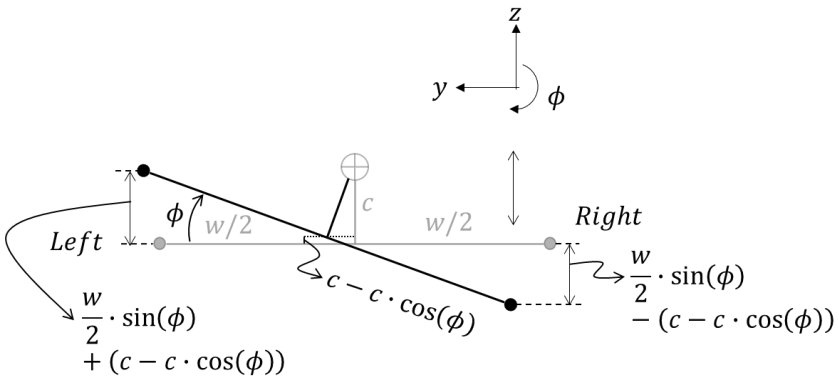

Figure 27: Equations showing the influence of roll on the vertical displacement.

To get the equations of the vertical displacement per corner the equations for z_{F1} and z_{F2} from Eq. 10 are expanded to include the influence of the rolling. This is done through the addition of the equations seen in Figure 27. The right-side corners of the screen have a component added to them and the left-side corners have a component subtracted from them. This is consistent with the positive sign convention used for rolling.

$$\begin{aligned} z_{F1R} &= z_{F1} - \frac{w}{2} \cdot \sin(\phi) - c \cdot \cos(\phi) + c \\ z_{F1L} &= z_{F1} + \frac{w}{2} \cdot \sin(\phi) - c \cdot \cos(\phi) + c \\ z_{F2R} &= z_{F2} - \frac{w}{2} \cdot \sin(\phi) - c \cdot \cos(\phi) + c \\ z_{F2L} &= z_{F2} + \frac{w}{2} \cdot \sin(\phi) - c \cdot \cos(\phi) + c \end{aligned} \qquad \textit{Eq. 14}$$

The nonlinear vertical velocities per corner are,

$$\dot{z}_{F1R} = \dot{z}_{F1} - \frac{w}{2} \cdot \phi \cdot \cos(\phi) + c \cdot \dot{\phi} \cdot \sin(\phi)$$
$$\dot{z}_{F1L} = \dot{z}_{F1} + \frac{w}{2} \cdot \phi \cdot \cos(\phi) + c \cdot \dot{\phi} \cdot \sin(\phi)$$
$$\dot{z}_{F2R} = \dot{z}_{F2} - \frac{w}{2} \cdot \phi \cdot \cos(\phi) + c \cdot \dot{\phi} \cdot \sin(\phi)$$
$$\dot{z}_{F2L} = \dot{z}_{F2} + \frac{w}{2} \cdot \phi \cdot \cos(\phi) + c \cdot \dot{\phi} \cdot \sin(\phi)$$

Eq. 15

For the roll and pitch equations of motion it is necessary to identify the moment arm of the reaction forces at the isolation corners about the CG. The moment arm is used for the completion of the roll and pitch equations of motion. Figure 28 illustrates how the moment arm for the reaction force are computed for the pitching degree of freedom.

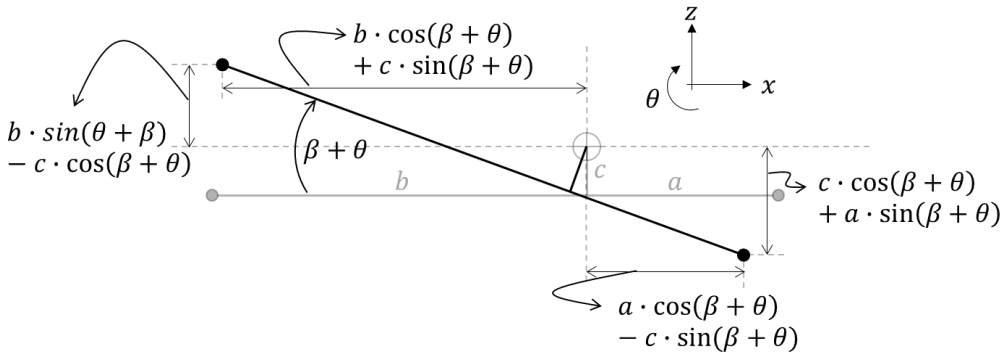

Figure 28: How the pithing moment arm of the reaction force are calculated.

These moment arms are introduced in the pitching equation of motion as variables a', b', c_1' and c_2' shown in Figure 29. Figure 29 also shows the reaction force directions for positive displacements in the x and z directions. The moment arm equations shown in Figure 28 are either positive for a positive pitching moment or negative for a negative pitching moment. This is dependent on the angle $\beta + \theta$ which changes the position of the isolation corners to above or below the CG of the vibrating screen as seen in Figure 29b.

The moment arm equations therefore ensure that a positive sign convention is used for the reaction force moments. This same logic is applied to the roll degree of freedom.

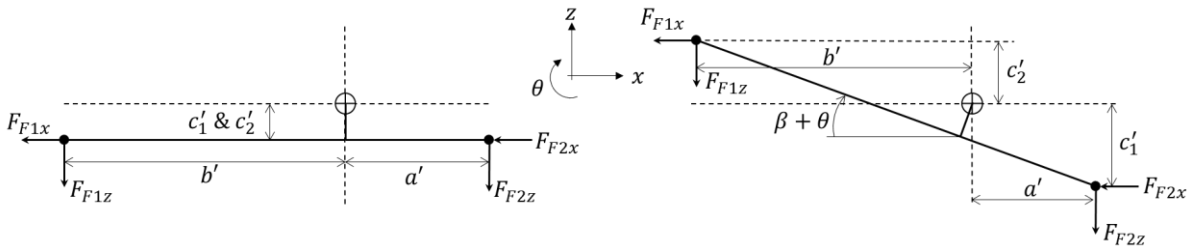

(a) *(b)*

Figure 29: Illustration of moment arms for reaction forces about the pitch degree of freedom for a) a horizontal machine and b) a machine at angle $\beta + \theta$.

The equations for the reaction force moment arms in the pitch θ direction are,

$$a' = A \cdot \cos(\theta) + B \cdot \sin(\theta)$$
$$b' = C \cdot \cos(\theta) + D \cdot \sin(\theta)$$
$$c_1' = -B \cdot \cos(\theta) + D \cdot \sin(\theta)$$
$$c_2' = -D \cdot \cos(\theta) + C \cdot \sin(\theta) \qquad \textit{Eq. 16}$$

where A, B, C and D are the same as in Eq. 11. Similar equation can be used to compute the reaction force moment arms for the roll degree of freedom. There are two moment arms, one for the left side of the screen and the other for the right side of the screen. The moment arm variable names are w_L' and w_R' respectively and are calculated as follows,

$$w_L' = \frac{w}{2} \cdot \cos(\phi) - c \cdot \sin(\phi)$$
$$w_R' = -\frac{w}{2} \cdot \cos(\phi) - c \cdot \sin(\phi) \qquad \textit{Eq. 17}$$

2.3.1.1 Equations of motion

Both the linearized and nonlinearized model displacement and velocity equations can now be substituted into the respective equations of motion. Because there are 4 degrees of freedom and there are also 4 equations of motions. For the x and z displacements the equations of motion are as follows,

$$m\ddot{x} = \boldsymbol{X} = -K_{F1Rx} \cdot x_{F1R} - K_{F1Lx} \cdot x_{F1L} - K_{F2Rx} \cdot x_{F2R} - K_{F2Lx} \cdot x_{F2L} - C_{F1Rx} \cdot \dot{x}_{F1R} - C_{F1Lx} \cdot \dot{x}_{F1L} - C_{F2Rx} \cdot \dot{x}_{F2R} - C_{F2Lx} \cdot \dot{x}_{F2L} \qquad \textit{Eq. 18}$$

$$m\ddot{z} = \boldsymbol{Z} = -K_{F1Rz} \cdot z_{F1R} - K_{F1Lz} \cdot z_{F1L} - K_{F2Rz} \cdot z_{F2R} - K_{F2Lz} \cdot z_{F2L} - C_{F1Rx} \cdot \dot{z}_{F1R} - C_{F1Lz} \cdot \dot{z}_{F1L} - C_{F2Rz} \cdot \dot{z}_{F2R} - C_{F2Lz} \cdot \dot{z}_{F2L} \qquad \textit{Eq. 19}$$

where variable K refers to spring stiffness in N/m and variables C refers to viscous damping in Ns/m for each corner in the x and z directions. m is the static mass of the vibrating screen.

For the θ and ϕ angles the equations of motion are as follows,

$$J_y\ddot{\theta} = \boldsymbol{\theta} = K_{F1Rx} \cdot x_{F1R} \cdot c_2' + K_{F1Lx} \cdot x_{F1L} \cdot c_2' + K_{F2Rx} \cdot x_{F2R} \cdot c_1' + K_{F2Lx} \cdot x_{F2L} \cdot c_1' + C_{F1Rx} \cdot \dot{x}_{F1R} \cdot c_2' + C_{F1Lx} \cdot \dot{x}_{F1L} \cdot c_2' + C_{F2Rx} \cdot \dot{x}_{F2R} \cdot c_1' + C_{F2Lx} \cdot \dot{x}_{F2L} \cdot c_1' + K_{F1Rz} \cdot z_{F1R} \cdot b' + K_{F1Lz} \cdot z_{F1L} \cdot b' + K_{F2Rz} \cdot z_{F2R} \cdot a' + K_{F2Lz} \cdot z_{F2L} \cdot a' + C_{F1Rx} \cdot \dot{z}_{F1R} \cdot b' + C_{F1Lz} \cdot \dot{z}_{F1L} \cdot b' + C_{F2Rz} \cdot \dot{z}_{F2R} \cdot a' + C_{F2Lz} \cdot \dot{z}_{F2L} \cdot a' \qquad \textit{Eq. 20}$$

$$J_x\ddot{\phi} = \boldsymbol{\phi} = K_{F1Rz} \cdot z_{F1R} \cdot w_R' + K_{F1Lz} \cdot z_{F1L} \cdot w_L' + K_{F2Rz} \cdot z_{F2R} \cdot w_R' + K_{F2Lz} \cdot z_{F2L} \cdot w_L' + C_{F1Rx} \cdot \dot{z}_{F1R} w_R' + C_{F1Lz} \cdot \dot{z}_{F1L} \cdot w_L' + C_{F2Rz} \cdot \dot{z}_{F2R} \cdot w_R' + C_{F2Lz} \cdot \dot{z}_{F2L} \cdot w_L' \qquad \textit{Eq. 21}$$

where J_y and J_x are the mass moments of inertia of the vibrating screen about the y and x axes respectively.

Equations Eq. 18, Eq. 19, Eq. 20 and Eq. 21 can be written in matrix form as,

$$\boldsymbol{M}\begin{Bmatrix}\ddot{x}\\ \ddot{z}\\ \ddot{\theta}\\ \ddot{\phi}\end{Bmatrix} = \vec{F} \qquad \textit{Eq. 22}$$

where,

$$\boldsymbol{M} = \begin{bmatrix} m & 0 & 0 & 0\\ 0 & m & 0 & 0\\ 0 & 0 & J_y & 0\\ 0 & 0 & 0 & J_x \end{bmatrix} \qquad \textit{Eq. 23}$$

and

$$\vec{F} = \begin{Bmatrix}\boldsymbol{X}\\ \boldsymbol{Z}\\ \boldsymbol{\theta}\\ \boldsymbol{\phi}\end{Bmatrix} \qquad \textit{Eq. 24}$$

Note that for a linear model it is possible to have the mass(M), stiffness(K) and damping (C) matrices completely decoupled in the form,

$$[M]\{\ddot{x}\} = -[K]\{x\} - [C]\{\dot{x}\} \qquad \textit{Eq. 25}$$

For nonlinear equations of motion (those relating to the sine and cosine of angles such as the pitch and roll degrees of freedom) the stiffness and damping are coupled, and it is not possible to get the form as in equation Eq. 25.

2.3.2 Force vector models

The linear force vector models are based on three types of excitations typically used on vibrating screens. Each is considered for the model's excitation to expand the model's usefulness in future studies. The three exciter configurations considered are,

1. Exciter Gearbox. (Section 2.3.2.1)
2. Unbalanced motor top mounted. (Appendix F Section 6.3)
3. Unbalanced motor side mounted. (Appendix F Section 6.2)

The working principle behind the excitation force is centrifugal force. The centrifugal force of the swinging weights of the exciters are computed using the following equation,

$$F_c = m_{ub} \cdot r \cdot \omega^2 \qquad \textit{Eq. 26}$$

where m_{ub} is mass of the unbalanced weights per exciter, r is the shortest distance from the center of rotation to the CG of the weights. Together $m_{ub} \cdot r$ is the total unbalance and is also known as the static moment. An exciter is typically specified with a working moment (WM) which is two times the static moment (i.e. $2 \times m_{ub} \cdot r$). ω is the rotating speed in radians per second.

2.3.2.1 Exciter gearbox force model

As mentioned, an exciter gearbox has 4 weight pairs that rotate together such that a linear reciprocating force is exerted. The weights are linked together by shafts and gears to transfer the rotation. The exciter is mounted on a beam that is angled such that a specific drive angle (α) to the horizontal is achieved. Figure 30 provides an illustration of how the rotating weights result in a linear reciprocating force at a drive angle α. The weight pairs rotate in opposite directions to ensure a

balanced linear force. Note the z and x axes which correlate with the axes of the vibrating screen model.

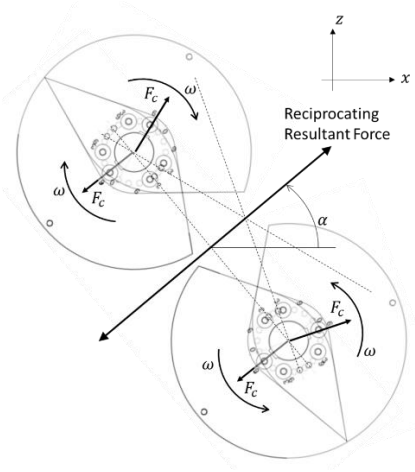

Figure 30: Gearbox exciter force vector illustration

The freebody diagram of a vibrating screen with exciter gearbox force vector(s) is seen in Figure 31. The force vector in the zx-plane shows a resultant force which is the sum of the amplitudes of reciprocating forces from multiple exciter gearboxes. Figure 31 shows the variables used to geometrically locate each force vector to the CG of the machine. This is useful for the computation of the forces acting on respective degrees of freedom. Variables e, f, g_1, g_2 and g_3 as well as α are dimensions taken from the CAD of the vibrating screen. Variable d is calculated by rotating the zx axis by the drive angle α using the following equation,

$$d = e \cdot \cos(\alpha) - f \cdot \sin(\alpha) \qquad \textit{Eq. 27}$$

Variables g_1, g_2 and g_3 are used to position each exciter along the y direction. This is necessary as the model allows for the phase of the forcing function per exciter to be adjusted with a phase difference (δ). Exciter gearboxes are linked together by mechanical couplings which are more rigid than flexible couplings. More rigid couplings are necessary as all the gearboxes must rotate at the same phase. However, it is possible that a slight phase difference be present in the coupling attachments resulting in an exciter leading or lagging the others. It is also possible that, due to wear, a coupling will degenerate causing a larger phase difference between gearboxes.

This phase difference will result in a net unbalanced force which will excite the rolling degree of freedom. Also, as indicated in Figure 31 an offset angle can also be applied to the resultant of the exciters that will excite the rolling degree of freedom with a moment arm of e. This offset angle is a hardcoded value which accounts for imperfections in the actual vibrating screen by ensuring that the rolling degree of freedom has some moment force acting on it.

The resultant forces computed for the xz and yz planes are as follows,

$$F_{xz} = \sum_{i=1}^{N} WM/2 \cdot \omega^2 \cdot \sin(\omega \cdot t + \delta_i) \cdot \cos\,(offset°)$$
$$F_y = \sum_{i=1}^{N} WM/2 \cdot \omega^2 \cdot \sin(\omega \cdot t + \delta_i) \cdot \sin\,(offset°) \qquad \textit{Eq. 28}$$

where N is the number of exciters, WM is the working moment, ω is the operating speed, δ_i is the phase difference per exciter. An important observation is that the working moment (WM) and ω and the $offset°$ are the same for all the exciters.

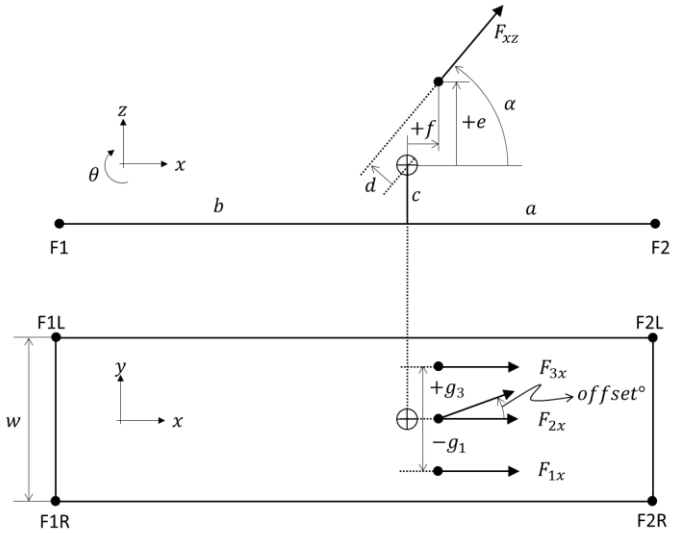

Figure 31: Freebody diagram of rigid screen with exciter gearbox force vector

The excitation of the pitch (θ) and roll (ϕ) degrees of freedom are moments acting about the CG and are calculated as follows,

$$M_\theta = \sum_{i=1}^{N} WM/2 \cdot \omega^2 \cdot \sin(\omega \cdot t + \delta_i) \cdot \cos(offset°) \cdot d$$

$$M_\phi = \sum_{i=1}^{N} WM/2 \cdot \omega^2 \cdot \sin(\omega \cdot t + \delta_i) \cdot \cos(offset°) \cdot \sin(\alpha) \cdot g_i + \sum_{i=1}^{N} WM/2 \cdot \omega^2 \cdot \sin(\omega \cdot t + \delta_i) \cdot \sin(offset°) \cdot e \qquad \text{Eq. 29}$$

Note that the sign of g_i is important as it determines the direction of the moment exerted about the x axis. From the free body diagram in Figure 31 it can be deduced that a positive vertical force of F_{1z} with moment arm g_1 will result in a negative moment about the x axis. This is countered by $F_{3z} \times g_3$ which exerts a positive rolling moment. Therefore, for an exciter positioned to the left of the CG (in the positive y direction) g_i is positive and to the right is negative.

2.3.3 Numerical integration

The equations of motion consider the acceleration, velocity, and displacement of each degree of freedom. Therefore, numerical integration is required to get a reasonable prediction of the solution. The Runge-Kutta 4th order method is a numerical technique or algorithm that allows one to solve for ordinary differential equations with initial conditions. To solve for multiple coupled differential equations simultaneously, it is necessary to get the equations in the form of a system of first order differential equations. Eq. 22 shown previously is a representation of a system of differential equations. Expanding Eq. 24 to include the forcing functions results in the following,

$$\vec{F} = \begin{Bmatrix} \boldsymbol{X} \\ \boldsymbol{Z} \\ \boldsymbol{\theta} \\ \boldsymbol{\phi} \end{Bmatrix} + \begin{Bmatrix} \boldsymbol{F_X} \\ \boldsymbol{F_Z} \\ \boldsymbol{F_\theta} \\ \boldsymbol{F_\phi} \end{Bmatrix} \qquad \textit{Eq. 30}$$

Because there are 4 degrees of freedom with their first and second derivatives it is necessary to include the derivatives in our system of differential equations, otherwise we have to many unknowns and too few equations. Therefore, the system of first order differential equations takes the following form,

$$\ddot{\vec{X}} = \begin{Bmatrix} \ddot{x} \\ \ddot{z} \\ \ddot{\theta} \\ \ddot{\phi} \end{Bmatrix} \qquad \textit{Eq. 31}$$

$$\boldsymbol{M}\ddot{\vec{X}} = \vec{F}$$

$$\ddot{\vec{X}} = \boldsymbol{M}^{-1} \cdot \vec{F} \qquad \textit{Eq. 32}$$

Now,

$$let, \qquad \vec{y} = \begin{Bmatrix} \dot{\vec{X}} \\ \vec{X} \end{Bmatrix}$$

$$\dot{\vec{y}} = \frac{d}{dt}\begin{Bmatrix} \dot{\vec{X}} \\ \vec{X} \end{Bmatrix} = \begin{Bmatrix} \boldsymbol{M}^{-1} \cdot \vec{F} \\ \dot{\vec{X}} \end{Bmatrix} = \vec{G}(\vec{y}, t)$$

$\vec{G}(\vec{y}, t)$ is the step function for the Runge-Kutta algorithm. Starting with an initial state at an initial time t_0 the Runge-Kutta 4th order algorithm numerically integrates as follows,

$$\vec{y}_{t+1} = \vec{y}_t + \frac{\Delta t}{6} \cdot \left(\vec{K}_1 + 2 \cdot \vec{K}_2 + 2 \cdot \vec{K}_3 + \vec{K}_4\right)$$

where,

$$\vec{K}_1 = \vec{G}(\vec{y}_t, t)$$

$$\vec{K}_2 = \vec{G}\left(\vec{y}_t + \vec{K}_1 \cdot \frac{\Delta t}{2}, t + \frac{\Delta t}{2}\right)$$

$$\vec{K}_3 = \vec{G}\left(\vec{y}_t + \vec{K}_2 \cdot \frac{\Delta t}{2}, t + \frac{\Delta t}{2}\right)$$

$$\vec{K}_4 = \vec{G}\left(\vec{y}_t + \vec{K}_3 \cdot \Delta t, t + \Delta t\right)$$

This Runge-Kutta 4th order algorithm is scripted in Python. The time step Δt is constant for the calculation of the solution. The time step needs to be sufficiently small to ensure convergence of the algorithm to a unique solution [60].

2.4 MODEL VALIDATION

Validation of the model is required to ensure confidence in the results obtained and identify the limitations of its use. Several limitations can already be deduced from the assumptions made such as the absence of flexible body modes, only 4 degrees of freedom considered and the use of linear stiffness and viscous damping. Another outcome of the validation is whether a small angle assumption gives useful results when compared to the non-linear angles.

Two forms of validation are performed. The first being a mathematical validation whereby the model is compared to similar numerical model developed in commercial software. The second is an experimental validation whereby the model is compared to experimental results obtained from an actual vibrating screen.

2.4.1 Mathematical validation

An ADAMS model is developed in close likeness to the screen model used in this study. The ADAMS model considers all 6 DOF for rigid body modes and accounts for large pitch, roll and yaw angles. The vibrating screen considered for this validation has top mounted unbalanced motors and has been designed and manufactured by Kwatani[1]. Figure 32 is an illustration of the screen considered. According to representatives at Kwatani the coil springs of this vibrating screen tend to bottom out during shutdown. The ADAMS numerical model is used to replicate the shutdown and determine if this occurrence is observed.

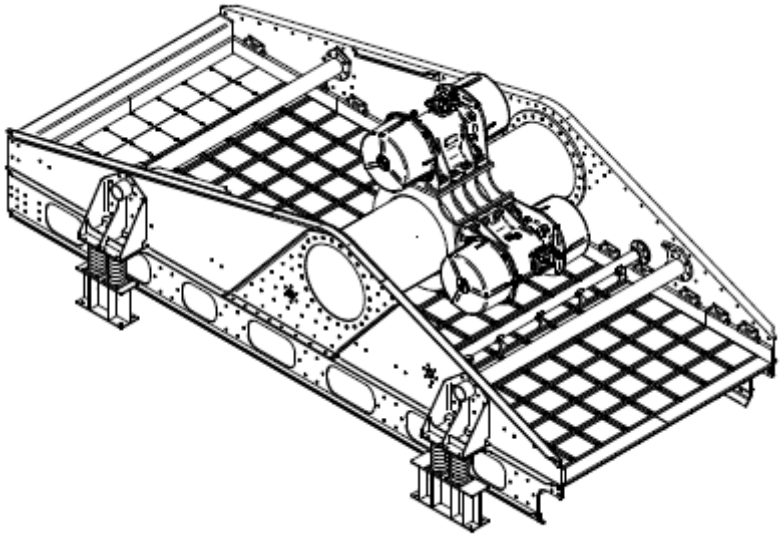

Figure 32: Vibrating screen used for mathematical validation

For both the Python and ADAMS models the respective variables are assigned the values shown in Table 1. Because top mounted unbalanced motors are used there are two e and f variables. The stiffness values of the coil springs are calculated, and the damping values are chosen to be 1% of the stiffness of a coil spring.

[1] KWATANI, 18 Belgrade Avenue Aeroport Spartan Ext. 2 Kempton Park, 1619, Johannesburg, South Africa

Table 1: Numerical model parameters for mathematical validation

Variables	Symbol	Units	Value
Distance CG to F2	a	m	1.835
Distance CG to F1	b	m	2.13
Perpendicular distance CG to line F1-F2	c	m	0.418
Vertical distance CG to exciter(s)	e_1, e_2	m	1.155, 0.384
Horizontal distance CG to exciter(s)	f_1, f_2	m	0.239, 1.158
Lateral distance CG to exciter(s)	g_1, g_2	m	0, 0
Distance F1L to F1R (= distance F2L to F2R)	w	m	2.916
Mass moment of inertia about pitching (y) axis	J_y	$kg.m^2$	21444.88
Mass moment of inertia about pitching (x) axis	J_x	$kg.m^2$	9288.72
Mass of vibrating screen	m	kg	8347
Drive angle	α	°	50
Screen angle	β	°	0
Gravitational acceleration	g_{acc}	m/s^2	9.81
Number of exciters	$N_{exciters}$		2
Working moment (unbalance $(\boldsymbol{m} \cdot \boldsymbol{r})$) per exciter	WM	Kg.cm	4462
Weight setting	WS	%	100
Vertical stiffness per corner	K_z	N/m	590 000
Horizontal stiffness per corner	K_x	N/m	300 000
Vertical damping per corner	C_z	$\frac{N}{m}/s$	2950
Horizontal damping per corner	C_z	$\frac{N}{m}/s$	1500
Zeta (damping scaling factor)			1.00

The variables and values in Table 2 are provided to the solvers (for Python this is a written script containing the Runge-Kutta algorithm) to generate the RPM curves to calculate the force,

Table 2: Mathematical validation parameters for solver

Variables	Symbol	Units	Value
Time step	h	s	0.001
Initial time	t_0	s	0
Total time	T	s	200
Ramp up time	T_{up}	s	3
Coast down time	T_{down}	s	120
Machine stationary time	T_{stat}	s	5
Operating Speed	rpm_{op}	rpm	985

The time variables T_{up} and T_{down} are determined from observations on site. The machine has 6-pole motors which means the operating speed is 985rpm. The variable T_{stat} refers to a period at the beginning and end of the simulation where no unbalanced force is applied to the model. This allows the model time to settle at its initial state after gravity is introduced and allows the machine to settle at the end when the excitation force is zero.

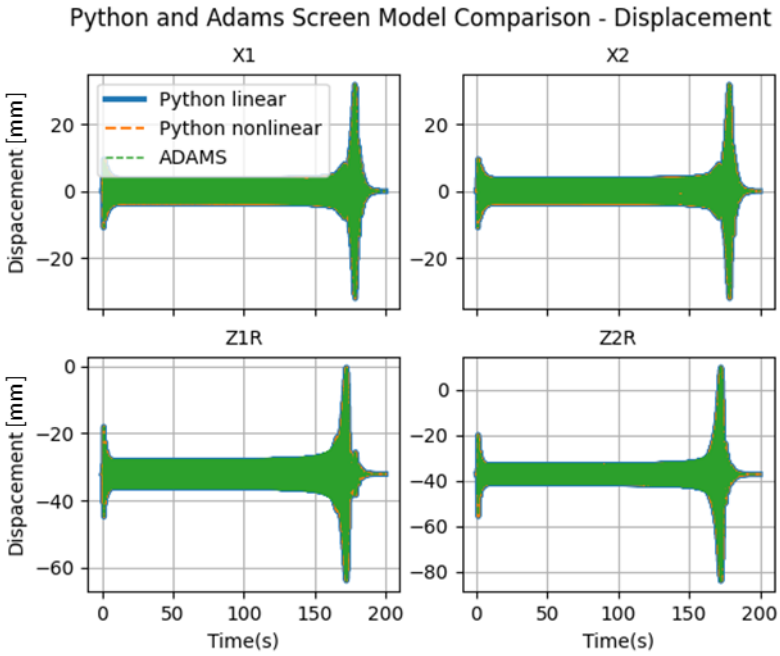

Figure 33: ADAMS and Python model displacement comparison

The ADAMS model makes use of a simplified exciter gearbox force model, so the e and f variables above were replaced with the values 0.77 and 0.668 respectively. These values are also used for the linear and nonlinear models in Python. Figure 33 shows the results obtained for the X directions at F1 and F2 as well as the vertical displacement at F1R and F2R. The results from the ADAMS and the Python linear and non-linear models are identical with negligible magnitude discrepancies during the transient start-up and shutdown phases. These differences could be due to the ADAMS model utilizing 6 DOF as opposed to the 4 DOF Python model.

Notice that the discharge (Z2R) vertical displacement is considerably more than the feed (Z1R) during shutdown. The maximum and minimum amplitudes at the discharge indicate the potential for loss of contact with the coil springs (i.e. vertical displacement > 0) as well as to bottoming out of the coil springs with 85mm compression. Based on the geometry of the coil springs (i.e. the wire diameters, the number of turns and the squared and ground coil ends) $\pm$90mm of compression can occur before being considered fully bottomed out. Although this is interesting, it was observed that the peak amplitude simulated during shutdown is dependent on the damping which was an assumed value.

Considering the start-up (first 6 seconds) of the simulated data, the power spectral density (PSD) of the displacements, seen in Figure 34, indicate a peak at a frequency of $\pm$2.6Hz, which is the vertical bounce natural frequency, and 16.5Hz which is the operating speed. These frequencies and amplitudes are identical for the linear and nonlinear models, but the ADAMS model has a noticeably lower amplitude at 2.6Hz. The PSD is estimated using the FFT squared and a Hanning window is used to ensure the start-up is periodic for the computation of the FFT.

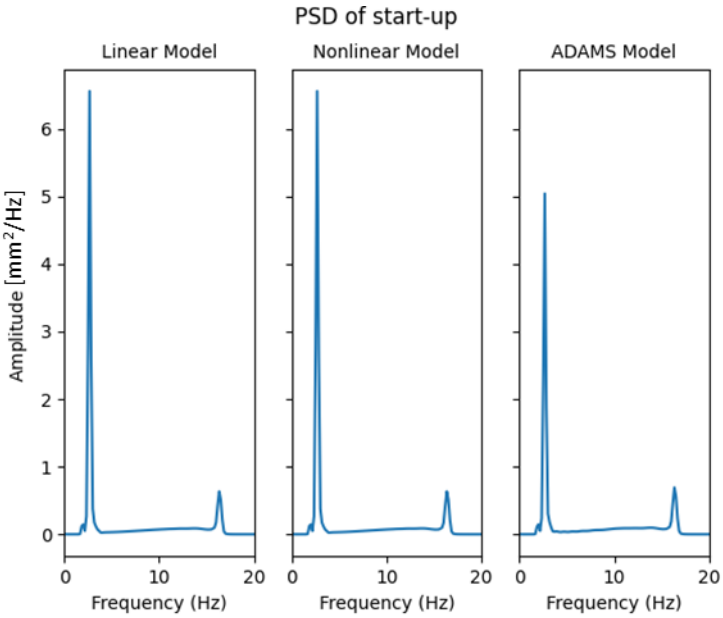

Figure 34: PSD of start-up for mathematical validation

It is understood that the area under the PSD is equal to the mean square value of the time signal. Taking the square root of the mean square result in the root mean square or RMS value of the time signal. The RMS computed from the PSD for each model is,

- Linear model: 4.46387mm
- Nonlinear model: 4.46388mm
- ADAMS model: 4.20853mm

The ADAMS model has a 5.7% lower RMS value during start-up than the other models which are essentially identical. For shutdown a similar analysis can be made whereby the PSD is taken for a much larger portion which contains the high amplitude transient motion. For this model the rigid body modes were all below 5Hz. The shutdown is 120seconds long, and the last 40 seconds contain the most interesting high amplitudes. Although a PSD is not a common analysis tool for transient data, prominent features are observed when using a moving window with a suitable block size. Along with the use of overlapping windows, to ensure no interesting features are missed, result in minimum smearing of frequencies and clearly defined peaks. The PSD for the shutdown can be seen in Figure 35 which shows that all three models have noticeable peaks of the same magnitude at ± 1.8Hz, ± 2.6Hz and a noticeable feature at $\pm 3.4Hz$ which are the horizontal and vertical bounce as well as pitching natural frequencies respectively. The area under the PSD (RMS values) for each model's response are as follows:

- Linear model: 9.67180mm
- Nonlinear model: 9.67178mm
- ADAMS model: 9.65153mm

The ADAMS model has a 2.9% lower RMS value than the other two models which, once again, are negligibly different.

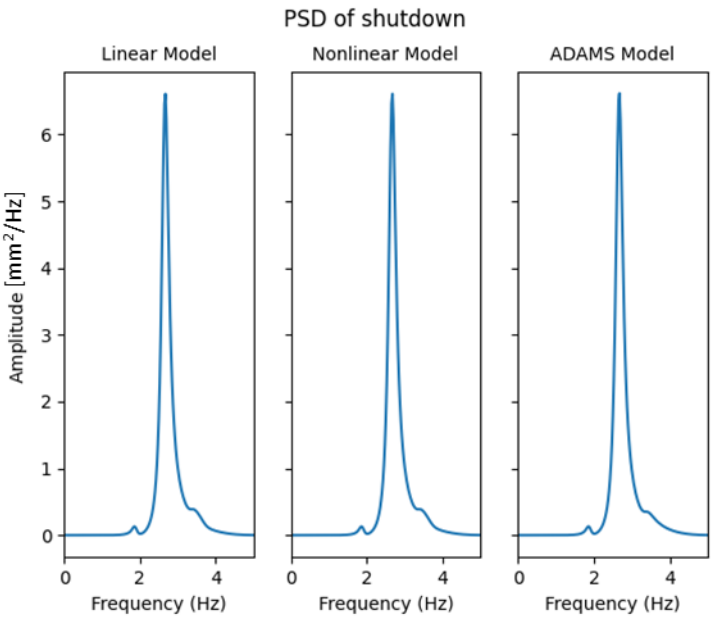

Figure 35: PSD of shutdown for mathematical validation

Considering the steady-state operating portion of the vibrating screens operating envelope the orbit plots in Figure 36 show the orbits with orbit parameters (i.e. orbit length or stroke, orbit width, and orbit angle). The differences observed between all three models are negligibly small.

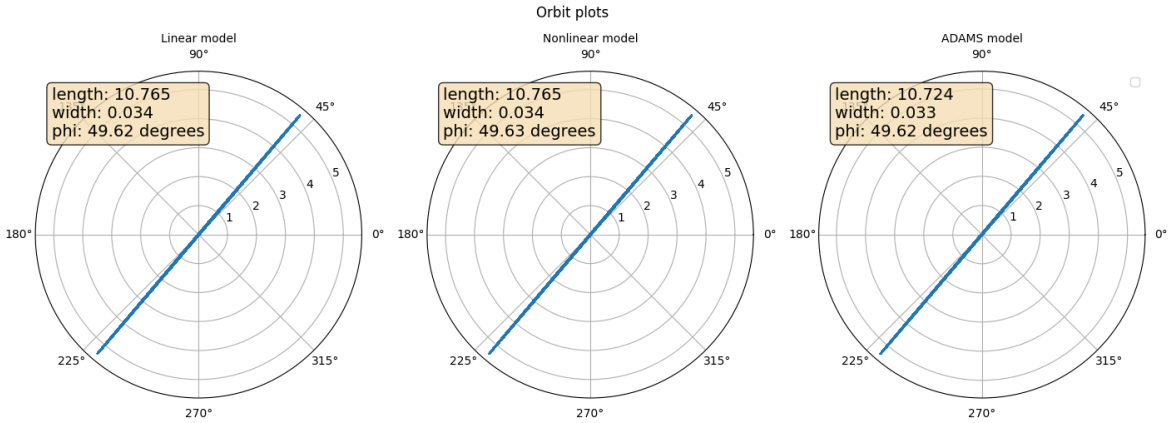

Figure 36: Orbit plots for mathematical validation

The comparison between the Python and ADAMS model shows that for both frequency and amplitude of the vibration during start-up, steady state operation, and shutdown the models compare well. Also, the potential for isolators bottoming out is noticed in both models. The mathematical validation indicates that both the vibrating screen and force excitation models are correct and useful. But the question remains how the models compare with real life measured vibrations.

2.4.2 Experimental validation

The experimental validation makes use of a vibrating screen with three top mounted exciter gearboxes and 7 coil springs per corner for isolation. An illustration of this vibrating screen can be seen in Figure 37. This vibrating screen is designed and manufactured by Kwatani[2]. A simulation driven design methodology was used. This entails the use of a finite element analysis (FEA) for modal analysis and

[2] KWATANI, 18 Belgrade Avenue Aeroport Spartan Ext. 2 Kempton Park, 1619, Johannesburg, South Africa

dynamic (frequency response) analysis of the vibrating screen. A modal analysis and frequency response evaluate the screen for natural frequencies at or near the operating speed as well as indicate stresses on the structure which are near the material fatigue limits. After assembly a factory acceptance test was performed using biaxial accelerometers per corner. The FEA modal results as well as the transient tests can now be used to validate the linear and nonlinear models for this study.

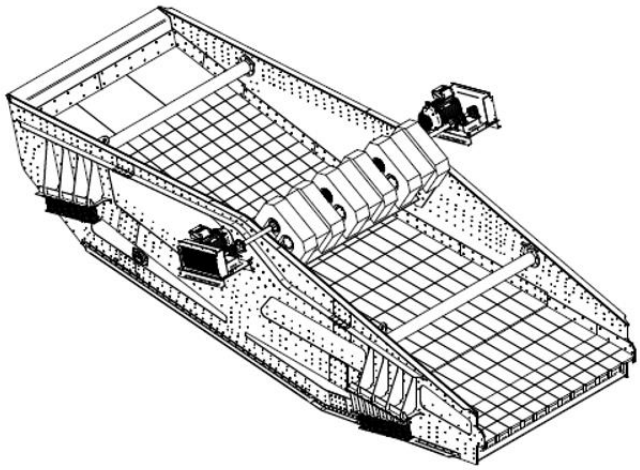

Figure 37: Vibrating screen for experimental validation

Table 3 shows the variables and values used to model this vibrating screen. The damping is manipulated using the zeta damping factor which increases or decreases the damping. In this case the initial guess for the damping results in a very lightly damped response. The damping is therefore increased by a factor of 3 (zeta) to improve the response.

Table 3: Numerical model parameters for experimental validation

Variables	Symbol	Units	Value
Distance CG to F2	a	m	3.845
Distance CG to F1	b	m	3.847
Perpendicular distance CG to line F1-F2	c	m	0.432
Vertical distance CG to exciter(s)	e	m	1.135
Horizontal distance CG to exciter(s)	f	m	1.192
Lateral distance CG to exciter(s)	g_1, g_2, g_3	m	1.279, 0, -1.279
Distance F1L to F1R (= distance F2L to F2R)	w	m	4.350
Mass moment of inertia about pitching (y) axis	J_y	$kg.m^2$	303935.64
Mass moment of inertia about pitching (x) axis	J_x	$kg.m^2$	94084.46
Mass of vibrating screen	m	kg	34250
Drive angle	α	°	45
Screen angle	β	°	21
Gravitational acceleration	g_{acc}	m/s^2	9.81
Number of exciters	$N_{exciters}$		3
Working moment (unbalance $(\boldsymbol{m} \cdot \boldsymbol{r})$) per exciter	WM	Kg.cm	12371
Weight setting	WS	%	100
Vertical stiffness per corner	K_z	N/m	7x 230 500
Horizontal stiffness per corner	K_x	N/m	7x 92 000

Vertical damping per corner	C_z	$\frac{N}{m}/s$	2305
Horizontal damping per corner	C_x	$\frac{N}{m}/s$	920
Zeta (damping factor)			3.00

The variables and values in Table 4 are provided to the solvers (for Python this is the Runge-Kutta algorithm) to generate the RPM curves to calculate the force,

Table 4: Mathematical validation parameters for solver

Variables	Symbol	Units	Value
Time step	h	s	0.001953125
Initial time	t_0	s	0
Total time	T	s	302
Ramp up time	T_{up}	s	5
Coast down time	T_{down}	s	40
Machine stationary time	T_{stat}	s	17
Operating Speed	rpm_{op}	rpm	750

The Python models can be excited using an artificial impulse which is used to calculate the FRFs shown in Figure 38. The impulse is a unit force at F2R and is orientated such that all 4 degrees of freedom are excited. Solving the system of equations for the linear model yield the same results as seen in Figure 38.

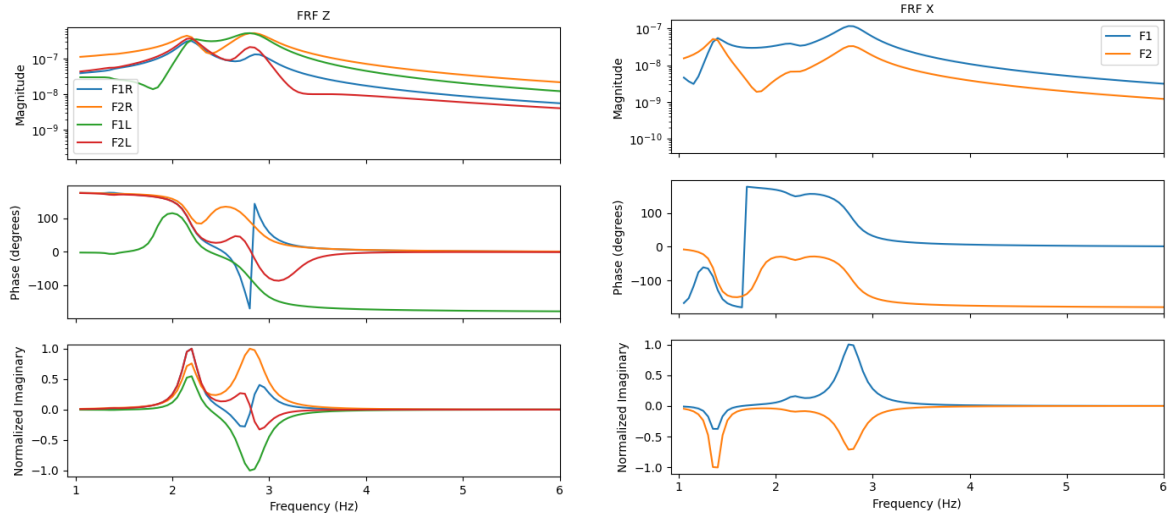

(a) *(b)*

Figure 38: Frequency response functions in a) vertical and b) horizontal directions from nonlinear model for validation

From the vertical FRF (Figure 38a) it is seen that 2 prominent frequencies exist at ± 2.15Hz, ± 2.8Hz. Looking at the normalized imaginary values of the FRF it appears there are two frequencies present, but which are closely coupled. These frequencies are ± 2.7Hz and ± 2.9Hz. The horizontal FRF (Figure 38b) also shows two prominent peaks at ± 1.4Hz and $\pm 2.8Hz$. The mode shapes and corresponding natural frequencies estimated from the model are as follows:

- Horizontal Bounce: 1.38Hz

- Vertical Bounce: 2.15Hz
- Pitching: 2.72Hz
- Rolling: 2.90Hz

Comparing the frequencies and mode shapes above to those from the FEA's modal results (seen in Appendix G) show good correlation which further validates the model.

Now considering the experimental data, only the measured and simulated data at F2R is considered for this validation. Figure 39 shows the experimental results and Figure 40 shows the simulated results using the linear model. The simulation model with linear and non-linear angles gave the same results. The acceleration, velocity, displacement, and rpm or operating speed are shown. The rpm is estimated from the time differences between peaks of the displacement.

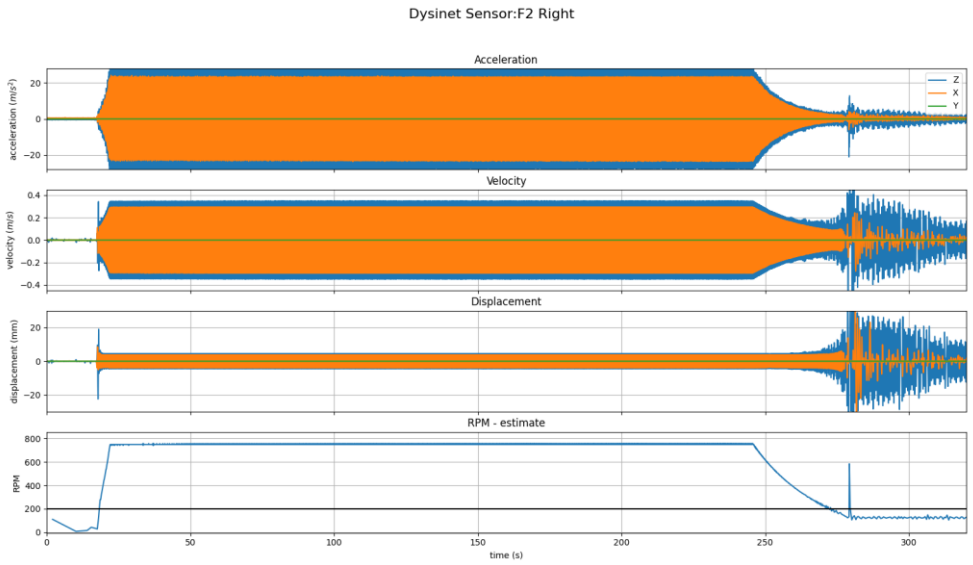

Figure 39: Experiment results for model validation

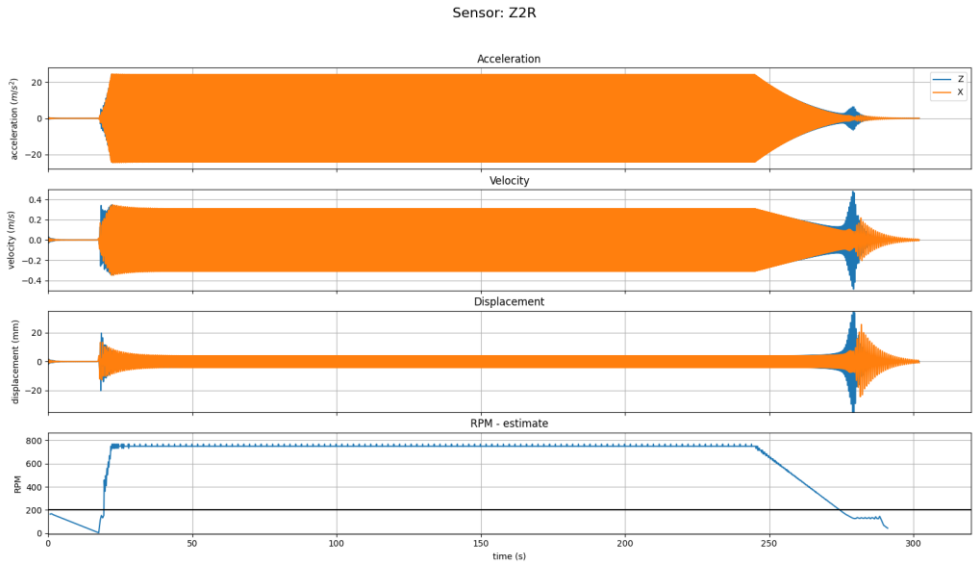

Figure 40: Simulated results for model validation

Taking a closer look at the comparison between Figure 39 and Figure 40, the following can be deduced:

- The acceleration of the simulated results shows that X direction has a higher amplitude of vibration during steady operation than the Z direction. This is because, in the model, the CG is closer to the discharge F2, slightly tilting the screen such that the excitation angle acts at an angle less than the drive angle of $45°$. However, from the experiment results the Z direction has a higher amplitude than the X direction during steady operation. This can be seen in the orbit plots in Figure 41 where the angle of the orbit is also different. The orbit angle is 49.9° and 44.5° for the experiment and simulated results respectively.
- During shutdown, the locations and magnitudes of the rigid body modes are easily discernible. Figure 42 shows the shutdown period from 370rpm till the oscillations are considered unforced. An FFT of the respective shutdown signals shows the frequency content of both the experimental and simulated signals. These signals are conditioned using a Hanning window to avoid frequency leakage. Prominent peaks occur at ± 1.3 Hz, 2.1 Hz and 2.7 Hz in the experiment signal and 1.38 Hz and 2.18 Hz in the simulated results. These frequencies correspond with those from the simulated impulse response as well as the FEA results in Appendix G. The amplitude discrepancies in the time and frequency domain during shutdown are attributed to non-linear forces at coast down speeds.
- Below an RPM of ± 200rpm the swinging weights of the vibrating screen do not immediately slow down to a stop but continue in a “see-saw” back and forth motion which continues to excite the vibrating screen. In the simulation the decay is mostly forced resulting in a shorter decay. The simulation does not account for the ‘see=saw’ oscillation of the exciter weights at the lower coast down speeds. For both the simulation and experimental results, the vibration continues to decay slowly to zero at the frequency of ± 2Hz and ± 1.3Hz for the Z and X displacements respectively. Figure 43 shows the decay which occurs while the weights are in the “see-saw” motion (280s to 295s in the vibration signals). An FFT is taken of the decay. An exponential window is used to enhance the frequencies and amplitudes of the FFT. No obvious leakage is observed. Note the similarities between the simulation and experiment for both the frequencies and amplitudes observed for the X and Z directions.
- The start-up potion of the signals has high amplitudes at frequencies which are less prominent and obvious when compared to those obtained during shutdowns. The start-up time is considerably less than the shutdown time and therefore the modes have less time to develop. This is true for the experiment and simulated results as seen in Figure 44.
- From the experimental results the RPM during shutdown decays exponentially, whereas the simulation makes use of a linear decay.

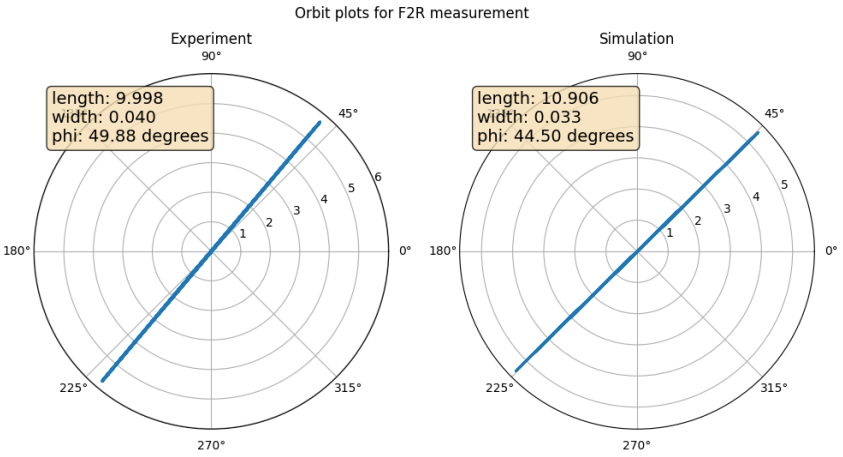

Figure 41: Orbit plots at F2R for experimental validation

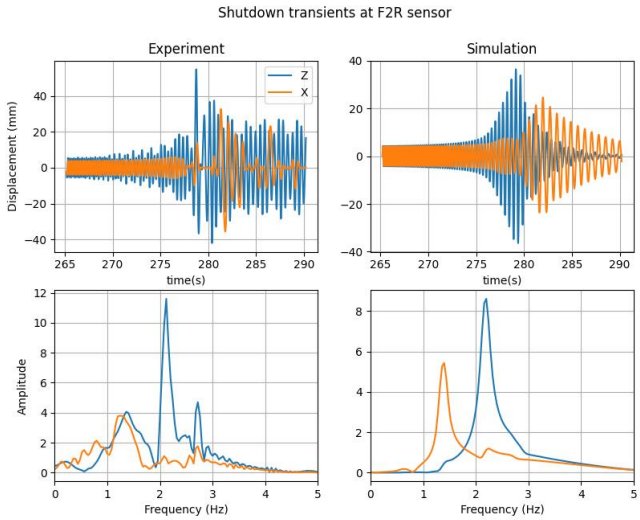

Figure 42: Experimental and simulated transients during shutdown (top) and FFT (bottom) for model validation

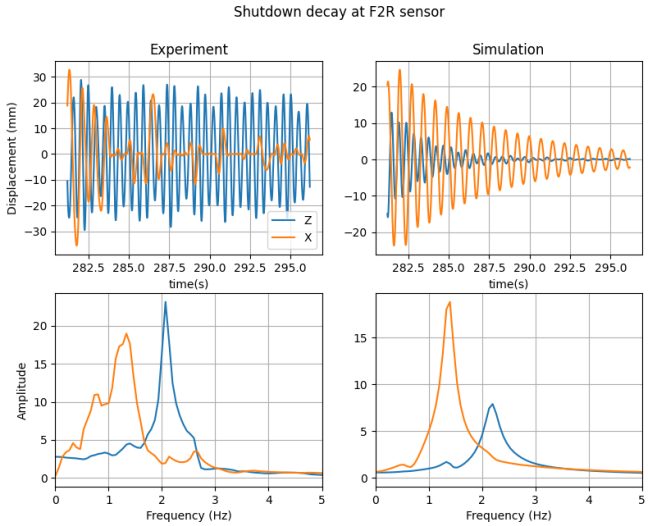

Figure 43: Experimental and simulated "unforced" decay (top) and FFT (bottom) for model validation

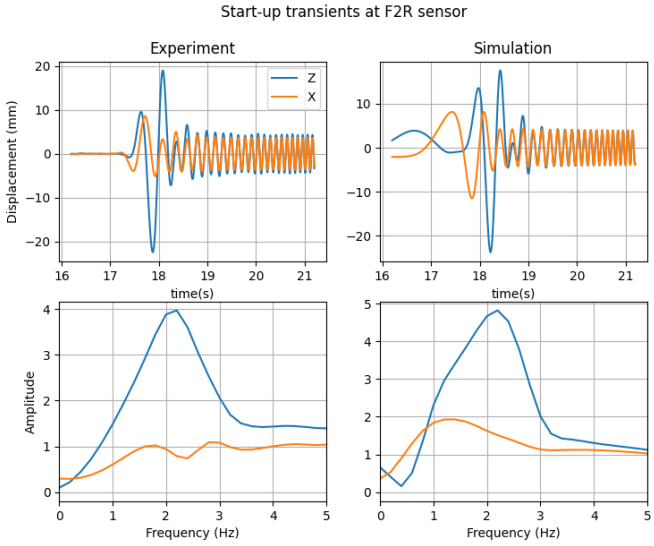

Figure 44: Experimental and simulated transients (top) and FFTs (bottom) during start-up for model validation

Although not exact, the numerical model compares well with the experimental results with comparable features in all phases of operation. There are discrepancies in amplitudes during operating and transient periods which may be attributed to non-linearities (particularly of the excitation) as well as geometric and inertial differences between the model and the real machine.

2.5 CONCLUSION

In conclusion, based on the mathematical and experimental validation, the numerical models developed in Python represent the dynamics of a real vibrating screen. Both the linear and non-linear models give results which are comparable to the experimental results with negligible differences. This refutes the argument that a non-linear angle must be considered for vibrating screen models, particularly for the transient startup and coast down envelopes of the vibrating screen. There are discrepancies in magnitudes between the models and experiments, however a high degree of accuracy is not necessary for this study. It is only important that the model can simulate responses with reasonable accuracy and that the responses predicted are as interpretable as real measurements.

The developed and validated model allows for other changes that could possibly influence the features to be considered. Some of these changes include:

1. Changes in excitation weight setting and speed.
2. Changes in mass and mass moment of inertias of the vibrating screen due to material build up and wear of liner components.
3. CG position changes relative to isolators and excitation force.
4. Combinations of various stiffness changes of isolators.

Based on the success of the validation, the model is useful for a sensitivity study. The sensitivity study is concerned with how parameters or features change with changing conditions or faults introduced. For this study it is necessary to know how features in the dynamics of the vibrating screen model behave with changes in isolator condition (simulated as stiffness changes). The signal processing and features extracted are discussed in Section 3.9.

3 EXPERIMENTAL INVESTIGATION

3.1 INTRODUCTION

For this study, experiments are planned and performed to evaluate the following,

1. Vibrating screen condition monitoring techniques with specific emphasis on isolator monitoring. Experimental modal analysis (EMA) and operational tests are performed. Signal processing techniques are used to extract features that are characteristic of the dynamic behaviour of the screen for different combinations of isolators.
2. The use of commercially available industrial sensors and data acquisition devices are evaluated for their application to condition monitoring of vibrating screens. This entails the use of common ICP sensors in conjunction with modern MEMS based accelerometers. Also, the use of low-cost data acquisition devices is used in parallel with expensive high end DAQs.

The experiments were performed at Kwatani [3] where a test facility with a vibrating screen and measurement equipment is readily available for the purpose of testing.

In this section a brief overview of the test screen and its major components is given. Thereafter the sensor arrangement, data acquisition devices and their setup are discussed. The experiment procedure and the signal processing methodology for feature extraction is discussed. Also, the experiment proceedings and some preliminary results are given.

3.2 TEST SCREEN

An illustration of the test screen assembly can be seen in *Figure 45*. The screen has the designation "SUE 915x3355" which means it is a single deck horizontal screen with unbalanced motors and a screen deck that is 915mm wide and 3355mm long. The support frame rests on a flat concrete floor.

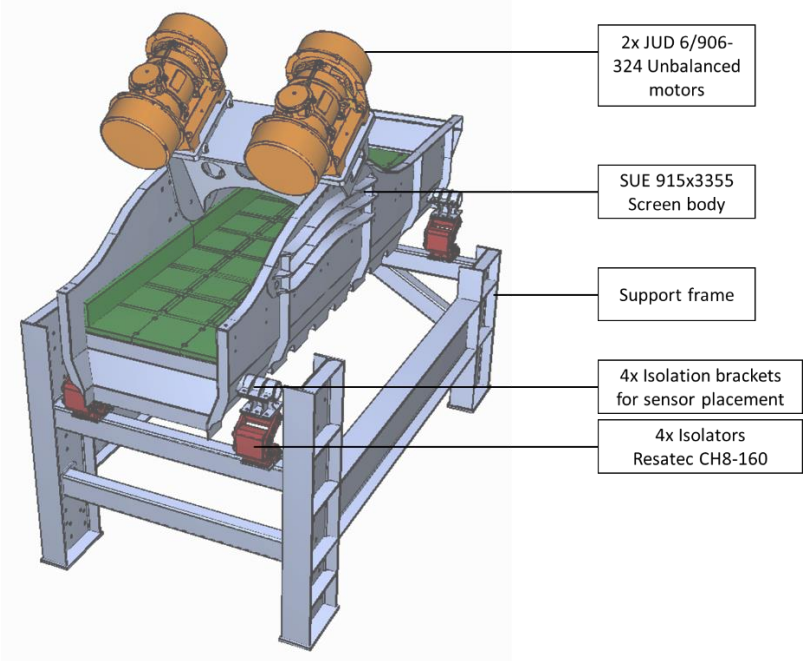

Figure 45: Test screen set-up

[3] KWATANI, 18 Belgrade Avenue Aeroport Spartan Ext. 2 Kempton Park, 1619, Johannesburg, South Africa

The test screen was designed by Kwatani with the following mechanical specifications:

- Screen weight: ±1740kg (based on the CAD).
- Operating speed: 750 RPM to 1500 RPM (12.5Hz to 25Hz) using a Variable Speed Drive (VSD).
- Maximum acceleration G-force: 15G.
- Stroke/throw: 1 to 12mm by adjusting the weight setting of the unbalanced motor weights.
- Drive angle: configurable between 40° to 60° (angle of the force drive line to the horizontal).
- Deck angle: configurable between 0° to 17.5° (angle of the screen deck to the horizontal).
- The screen is designed for linear vibration meaning that, during operation, the reciprocating force vector passes through the centre of mass of the screen assembly. The result is a straight-line orbit plot with minimal elliptical width.
- The screen body comprises of a welded assembly where the traverse or exciter beam is bolted in. Due to this design, the screen body has no structural modes below 25Hz (i.e. only rigid body modes are expected between 0 and25Hz).

3.2.1 Motor specifications

The JUD 6/906 324 UO1 is a 6-pole motor designed to operate at a nominal speed of 960rpm when excited by a 50Hz 3-phase supply. According to the motor data sheet the maximum centrifugal force at 100% weight setting and 960rpm is 45 780kN with a working moment (unbalance) of 906kg.cm. A copy of the motor data plate and motor specifications from the catalogue can be seen in Appendix A.

3.2.2 Isolation specifications

For this experiment three types of isolators are used,

1. Resatec torsional spring isolators (Figure 46a)
2. Rubber isolators (Figure 46b)
3. Coil springs (Figure 46c)

(a) *(b)* *(c)*

Figure 46: Isolators a) Resatec, b) Rubber Isolator, c) Coil Spring

Each isolator type introduces unique characteristics which directly influence the dynamics of the vibrating screen. For rubber isolators and coil springs the stiffness values are provided by the supplier for the vertical direction only. The lateral or shear stiffness is not given by suppliers, and neither are estimates of damping. For coil springs the shear force can be estimated through calculation. However, for rubber isolators this data it to be estimated from the experimental results. A description of each isolator used follows.

3.2.2.1 Resatec Oscillating Mounts

The Resatec used is a CH 8-160 oscillating mount. The catalogue (seen in Appendix B Figure 88) indicate a static stiffness of ± 90N/mm at 60mm static compression and the dynamic stiffness in the vertical and horizontal directions are 266N/mm and 138N/mm respectively (seen in Appendix B Figure 87). Figure 47 shows the static stiffness from the catalogue in the form of a force-displacement curve in the compressed direction for a new and one year old Resatec.

Notice that the graph in Figure 47 starts at a compression of approximately 30mm. Although this graph is relatively linear the stiffness of this element is known to be non-linear due to the complex geometry [61] [62] of the element as well as the rubber inserts used for torsional stiffness [63]. This is particularly true for large displacement in bi-axial loading as the horizontal and vertical stiffness are coupled to one another through the torsional rubber spring [62].

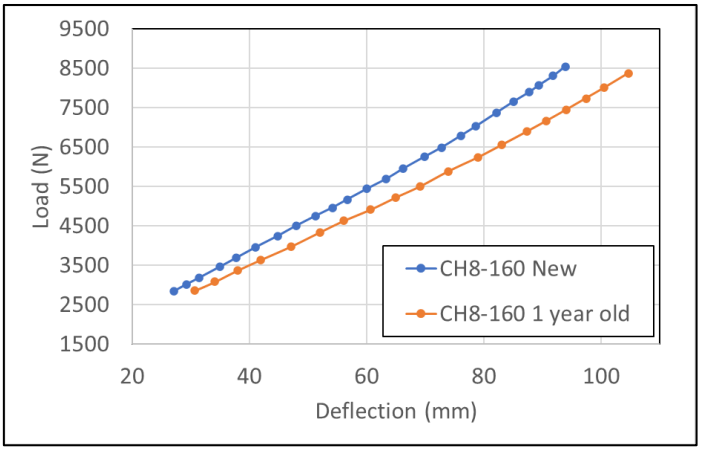

Figure 47: Force deflection curves for CH8-160 Resatec from the catalogue

To capture the non-linear stiffness accurately, a quasi-static test was performed on a hydraulic press at Delta Rubber[4]. A load cell measured the load while a linear displacement sensor measures the compression (photos seen in Appendix C). To get an idea of how the stiffness changes with time a new Resatec is compared to an old/used Resatec (approximately 4 years used).

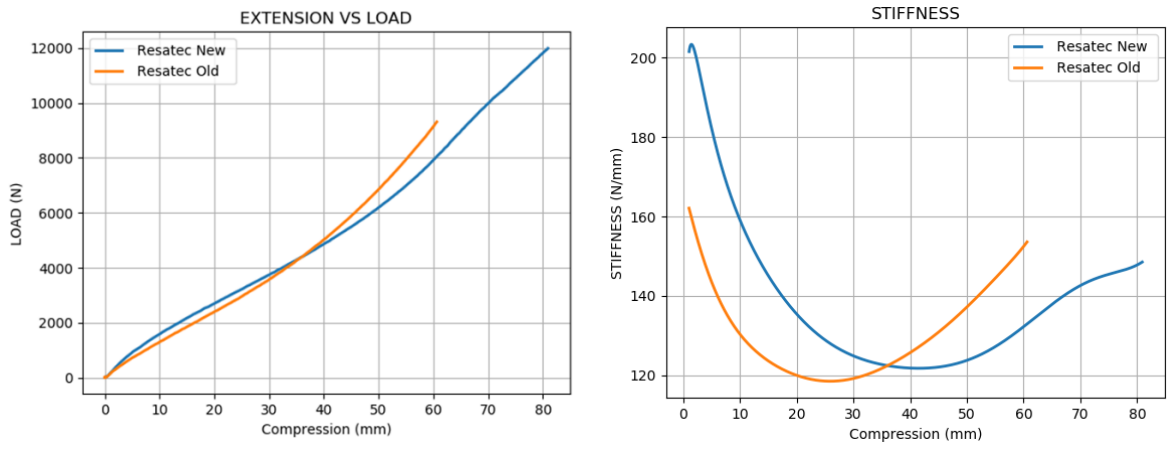

Figure 48: Force deflection curves and stiffness from CH8-160 Resatecs quasi-static test

[4] DELTA RUBBER (Pty) Ltd, 10 Diagonal Rd, Eastleigh, Edenvale, 1609, South Africa

Figure 48 shows the resulting graphs from the quasi-static tests. The loading is purely vertical during the tests. The stiffness shown in Figure 48a is less linear than indicated on Figure 47. Figure 48b shows an estimate of the stiffness (load divided by compression). Comparing the new and old Resatec stiffnesses shows that for compressions below 35mm the old Resatec is less stiff and for compressions above 35mm the old Resatec is stiffer than the new.

3.2.2.2 Rubber isolators

The rubber isolators used have an estimated vertical stiffness of $263N/mm$. Rubber is an inherently nonlinear material with varying stiffness and damping values. The stiffness and damping values are also known to change with temperature [64]. The rubber isolators used are manufactured and supplied by Delta Rubber[5]. The vertical stiffness of the rubber isolator according to the test certificate can be seen in Figure 49.

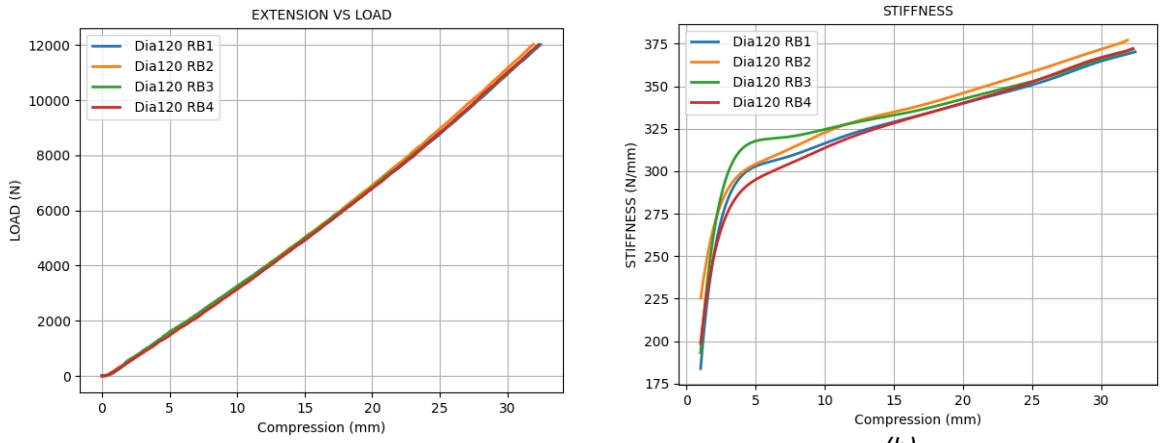

Figure 49: Force deflection curves (a) and stiffness (b) from Rubber isolators quasi-static test

The vertical stiffness in Figure 49b shows a larger stiffness than $263N/mm$ and the stiffness is considerably non-linear as it continues to increase with the compression. At 15mm compression a stiffness of $\pm 330N/mm$ is expected. The shear stiffness of the rubber isolators is not tested by the manufacturer.

3.2.2.3 Coil Springs

Coil springs are commonly used for vibration isolation. The vertical and horizontal stiffness of the coil spring is dependent on the geometric parameters of the coil spring such as the wire diameter used, the nominal coil diameter, the uncompressed length as well as the number of active turns. The two coil springs identified as being suitable for this experiment are:

1. Ø 20x124x260 coil spring ($Ø20$ wire diameter, $124mm$ nominal coil diameter, $260mm$ uncompressed length) with a calculated vertical and horizontal stiffness of 140N/mm and 90N/mm respectively.
2. Ø 19x123x250 coil spring ($Ø19$ wire diameter, $123mm$ nominal coil diameter, $250mm$ uncompressed length) with a calculated vertical and horizontal stiffness of 115N/mm and 80N/mm respectively.

Both coil springs have closed and ground ends on the top and bottom, so the coil sits flat on a horizontal surface. The implication is a reduced number of active turns in the coil when calculating the

[5] DELTA RUBBER (Pty) Ltd, 10 Diagonal Rd, Eastleigh, Edenvale, 1609, South Africa

vertical and horizontal stiffnesses. The calculated vertical stiffnesses correlate with quasi-static compression tests performed, the results of which can be seen in Figure 50. The stiffness shows approximately linear behaviour after 8mm of compression.

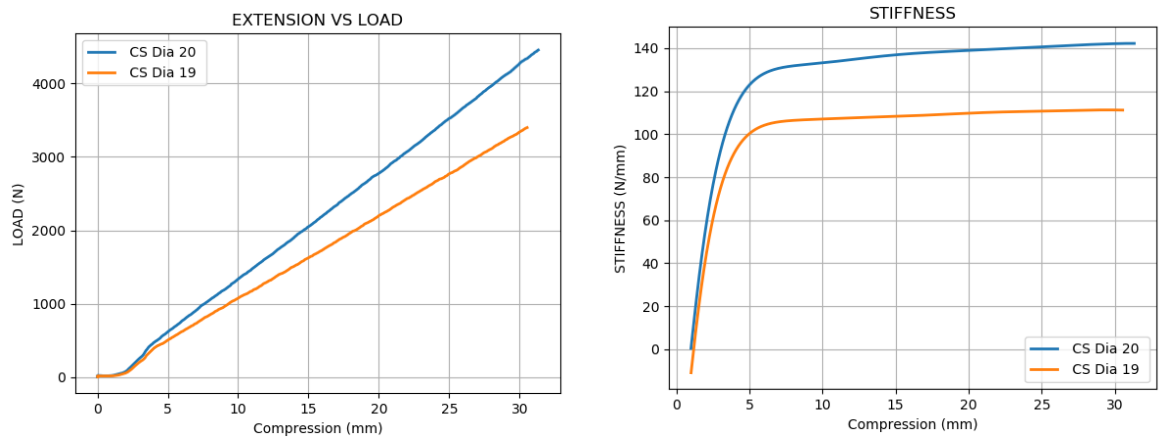

(a) *(b)*

Figure 50: Force deflection curves (a) and stiffness (b) from coil springs quasi-static test

3.3 TEST SET-UP

The screen is mechanically set up with a specific performance in mind. This performance requirement is typically linked to the required operating parameters to achieve the most efficient screening of ore particles. Screening efficiency is linked to the ability to stratify the bulk material and convey the ore therefore reducing the bed depth [8] [9]. The performance specifications for the tests are kept constant and are set to the following:

- Operating speed: 960rpm @50Hz (according to motor catalogue) supply from VSD
- Stroke: 8-9mm @ weight setting of 90% (see Figure 6)
- Resultant G-force: ±4.4g
- Drive angle (i.e., the slope at which the exciters are mounted): 50°
- Deck angle (i.e., the slope of the deck panels): 0°

Figure 51: Weight setting of left motor

Both motors are confirmed to have the same weight setting. This is a requirement for the structural integrity and dynamics of linear vibrating screens. Figure 52 shows the terminology adopted to refer to positions and directions on the vibrating screen during tests and signal processing.

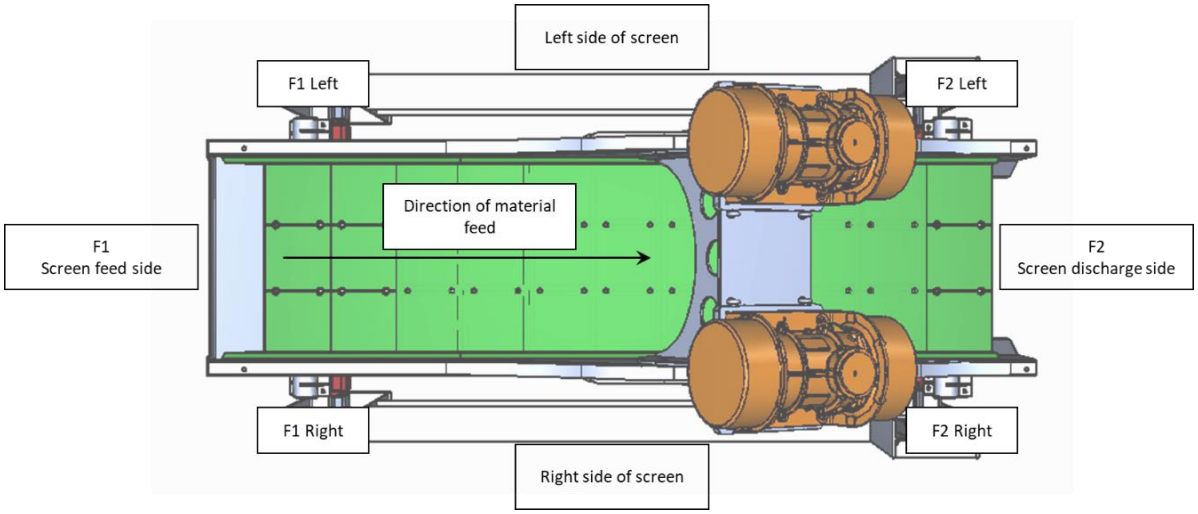

Figure 52: Screen position terminology

3.4 SENSORS

Different accelerometers are used for this experiment to ensure consistency/repeatability in results and evaluate the suitability of different accelerometers for vibrating screen vibration measurements. The accelerometers chosen are commercially available sensors with applications in automotive, industrial, and mining sectors for monitoring and control systems feedback. MEMS Capacitive sensors are considered more affordable than ICP sensors, however ICP sensors are more sensitive with less electrical noise and a wider frequency bandwidth. Table 17 shows the accelerometers used for this experiment. A summary of the accelerometers used are as follows:

- 4x Dysinet DA 2202-050
- 8x IFM VSA 004
- 8x PCB ICP

The IFM and ICP sensors are comparable in price where the Dysinet sensor is considerably cheaper. The Dysinet sensor is a biaxial sensor measuring 2 orthogonal axes simultaneously whereas the other sensors only measure single axes.

In conjunction with the accelerometers there are also two IFM Inductive sensors used to pick up the zero-passing time of the swinging weights of each unbalanced motor. Table 18 shows the information related to the inductive sensors.

A modal hammer is used for experimental modal analysis. The hammer is calibrated to measure the impact force and is fitted with a rubber tip for the excitation of a broad band of frequencies simultaneously. A rubber tip ensures most of the impact energy is concentrated on the frequency range of 0 to $100Hz$. This is seen in Figure 53 which shows the FFT of impulse forces using a rubber tip as well as the FFT of the responses measured from accelerometers. After 100Hz the force starts to decay more noticeably, and the response shows less prominent features. The modal hammer specifications can be seen in Table 19.

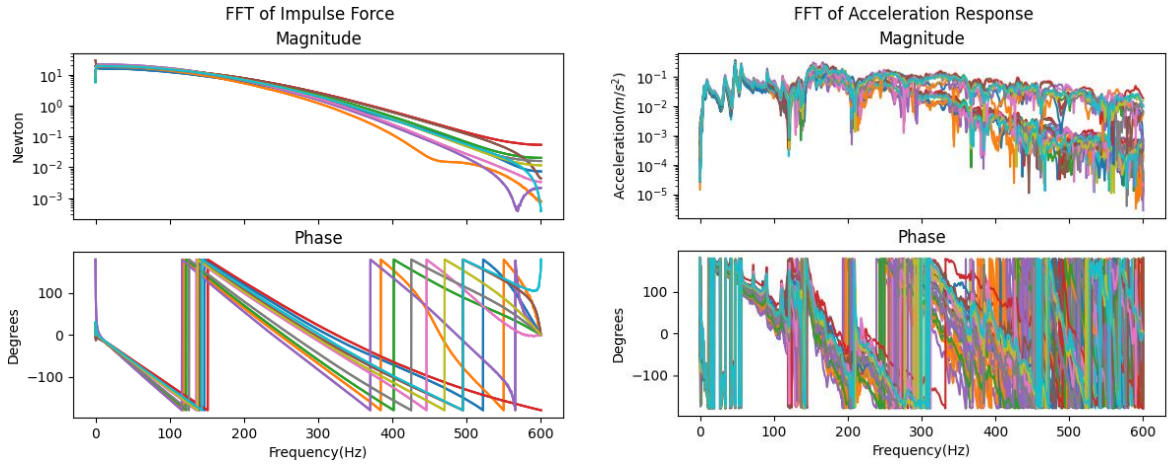

Figure 53: FFTs of a) impulse forces with a rubber tip and b) acceleration responses

3.4.1 Sensor placement

Figure 54 shows the sensor placement for the accelerometers as well as respective sensor serial numbers and the directions in which sensors are orientated (either z or x directions). The speed pick-up labels are also shown (i.e Left Motor and Right Motor). Accelerometers of each type will be placed on each isolation bracket. The sensors are orientated such that they measure vertical vibration (z-axis) as well as horizontal vibration (x-axis). Their sensing directions will be in the positive reference axes unless otherwise stated.

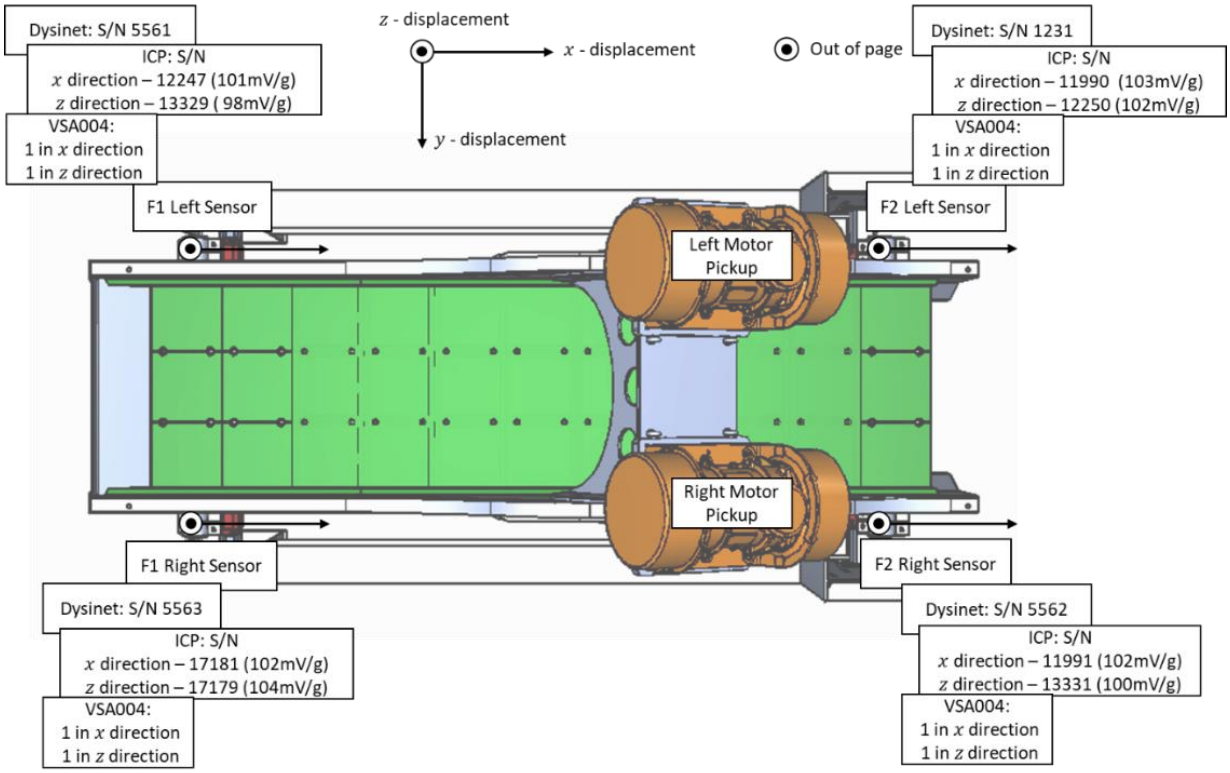

Figure 54: Sensor positions and orientations

The lateral (y-axis) vibration is not measured as it is known that the resultant force from the two unbalanced motors is the least in the lateral direction. This is because the swinging weights (for the left and right motors) rotate in opposite directions, thereby cancelling the lateral force during

operation. The only time during which there could be a major lateral force would be during start-up and/or shutdown/coast down of the screen where the swinging weights are not rotating in synchronously. This will be measured as a rolling motion whereby the vertical motion of the left-hand side (LHS) of the screen is 180° out of phase with the right-hand side (RHS) of the vibrating screen.

Figure 55 shows the accelerometers on an isolation bracket along with positive sensing directions. Two IFM VSA 004 sensors are bolted onto a clamp bracket at right angles to one another (for measurement of positive z and x directions). The bracket is clamped with a bolt onto the isolation bracket. The Dysinet sensor is mounted on the isolation bracket with a high strength rare-earth magnet. It is orientated such that its respective sensing axes are in the same directions as the IFM sensors. The Piezoelectric sensors are mounted at the rear of each isolation bracket using super glue for a rigid connection. The vertical sensor measures the positive z direction and the horizontal sensor is mounted to measure in the negative x direction. This negative sensing direction of the horizontal ICP sensor is corrected during signal processing.

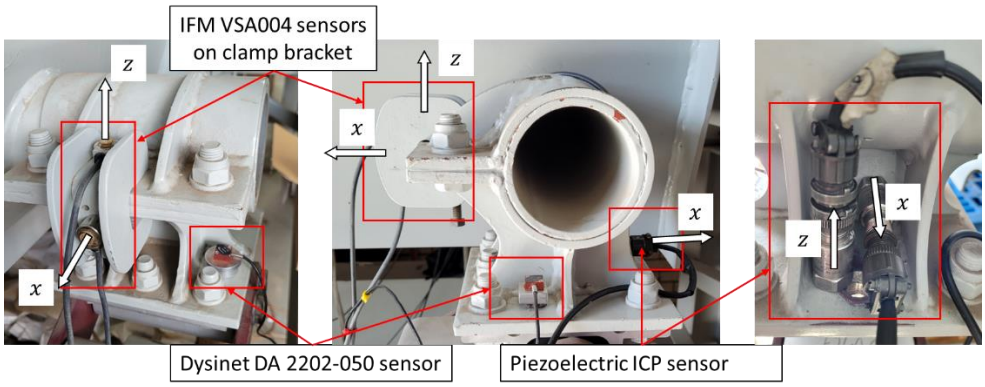

Figure 55: Photos of sensor placement on an isolation bracket

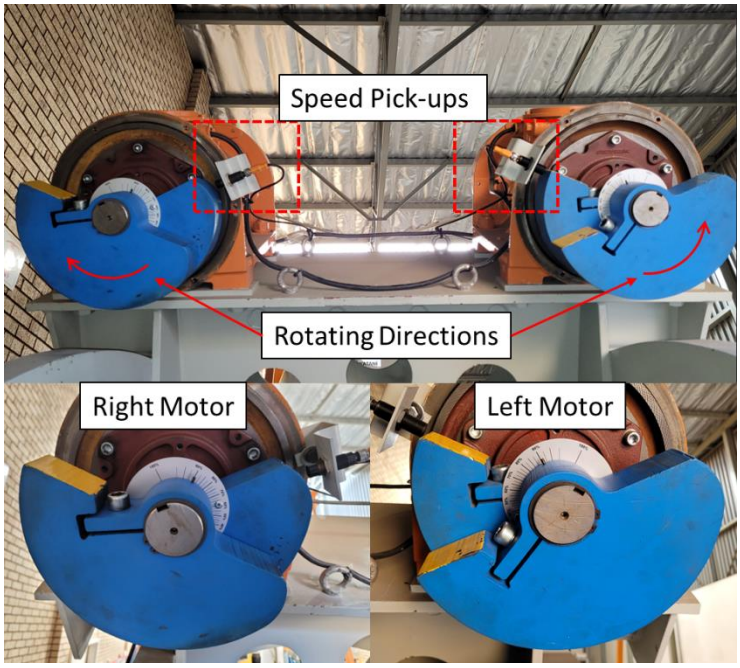

Figure 56: Motor speed pick-ups

Figure 56 shows the inductive sensors (speed pick-ups) placed on each motor as well as each weights geometry and weight setting. The inductive sensors are mounted to a bracket which clamps onto the motor housing ensuring a rigid connection. Also notice the weight setting is set to 90% for both left and right weight pairs. Because the weights rotate in opposite directions, as shown, the speed pickups are orientated such that they give a pulse when the respective weights are positioned down and therefore on the falling edge of the pulse.

In summary for vibration tests a total of 20 accelerometers (4 Dysinet, 8 IFM and 8 ICP accelerometers) are used along with 2 inductive sensors for speed pickup on the unbalanced motor weights and 1 modal hammer with rubber tip. A thermal camera is also used to measure the unbalance motor and isolator temperatures as independent parameters and a tape measure is used to measure the static compressions of the isolators.

3.5 DATA ACQUISITION

As with the accelerometers, different data acquisition devices (DAQs) are used for comparison purposes. The acquisition or measurement of sensor data is done in three “streams” as seen in Figure 57. Stream 1, furthest to the left, shows the IFM sensors, data acquisition modules (VSE 002) and software required to communicate with the modules and retrieve measurements (using IFM AnReSa firmware and API). The VSE 002 modules are flashed with the AnReSa firmware which enables synchronous measurements of up to 4 sensors. Stream 2, in the middle, shows the Dysinet sensors, HBM QuantumX DAQ and the HBM Catman software installed on a PC. Catman is required to set-up the QuantumX and retrieve data.

The piezoelectric sensors along with the modal hammer are also measured using a QuantumX DAQ. The modal hammer will only be used during the modal hammer tests. Notice that two computers are used, one running Catman for triggering of measurements for the Dysinet and ICP sensors, the other running a Python script that concurrently triggers measurements on two IFM VSE modules for measurement of the IFM accelerometers and inductive sensors.

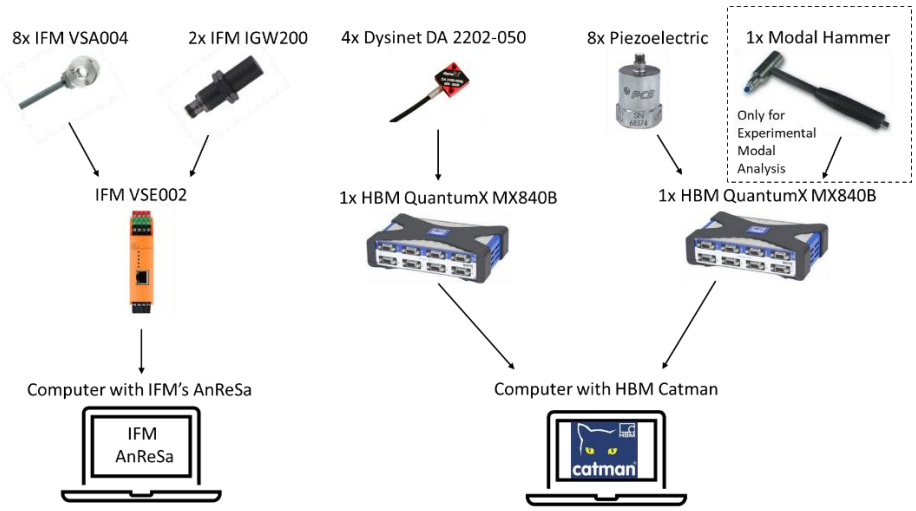

Figure 57: Data acquisition

Due to there being 20 accelerometers and 2 inductive sensors, it is necessary for multiple data acquisition devices (DAQs). As seen in Figure 57, the ICP sensors are all connected to a QuantumX DAQ

and the Dysinet sensors to another QuantumX DAQ. The IFM sensors are connected to separate IFM VSE002 modules. Table 20 in Appendix D shows a comparison between the DAQs used.

Because the IFM VSE 002 can only measure 4 accelerometers the sensors are divided between two VSE modules, with sensors measuring the horizontal x direction connected to the one module and sensors measuring the vertical z direction connected to the other. This is set-up as illustrated in Figure 58 which also shows the configured IP addresses of the computer and modules used, as well as which inductive sensor is connected to which module. Also note the names given to the modules. These names will be used from here on to describe the IFM modules.

As mentioned, the separate IFM modules are not synchronized by default but receive a trigger from the computer to measure. In theory because they receive a trigger at the same time from the same PC the measurements should be in sync. Because two PCs are used to trigger the two DAQ types, the ICP and Dysinet sensors are in sync with each other but are not in sync with the IFM sensors. This requires correction during signal processing to synchronize the sensors. This is not considered to be difficult as the sensors are measuring the same directions and therefore it is possible to cross-correlate the sensors to a particular event that occurs during measurement, for example a transient peak or impulse response.

The two Quantum DAQs are configured to measure at a sampling rate of 1200Hz. The IFM modules with AnReSa can, at the date of the experiments, only sample at 100kHz. The IFM sensors are to be decimated to a 1200Hz sampling rate and thereafter synchronized with the ICP and Dysinet sensors using cross-correlation.

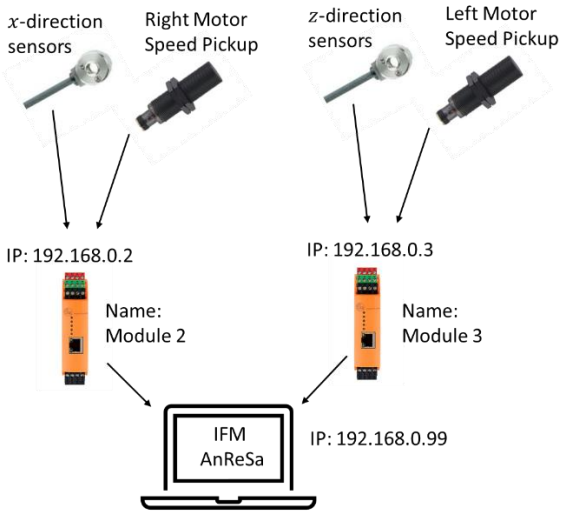

Figure 58: IFM sensors and modules configuration

3.6 EXPERIMENTAL PROCEDURE

Before testing can commence it is necessary to ensure all sensors are correctly calibrated. The only sensors that need calibration before testing are the Dysinet sensors. Being sensors capable of DC (0Hz) acceleration measurements they are calibrated using gravity as a reference. The sensors are rotated 90 degrees until all sensing directions are calibrated using the Catman software. Careful consideration is required during calibration so that when the acceleration measured is double integrated it gives a positive displacement vertically. This is illustrated in Figure 59 showing the positive acceleration ($\ddot{x}$

and $\ddot{z}$) directions for positive displacement (x and z) directions. The inductive sensors are also checked to ensure they give pulses at the correct weight angles.

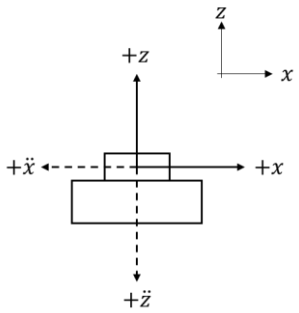

Figure 59: Dysinet sensor calibration directions

Figure 60 illustrates the test procedure for the experiment. There are two conditions under which the tests are conducted. The first set of tests are performed when the machine is cold (motors at room temperature) and the second set of tests are performed when the machine is hot (motors at near operating temperature). This is done to determine to what extent the modal and operational features are coupled to the temperature of the motors and/or isolators.

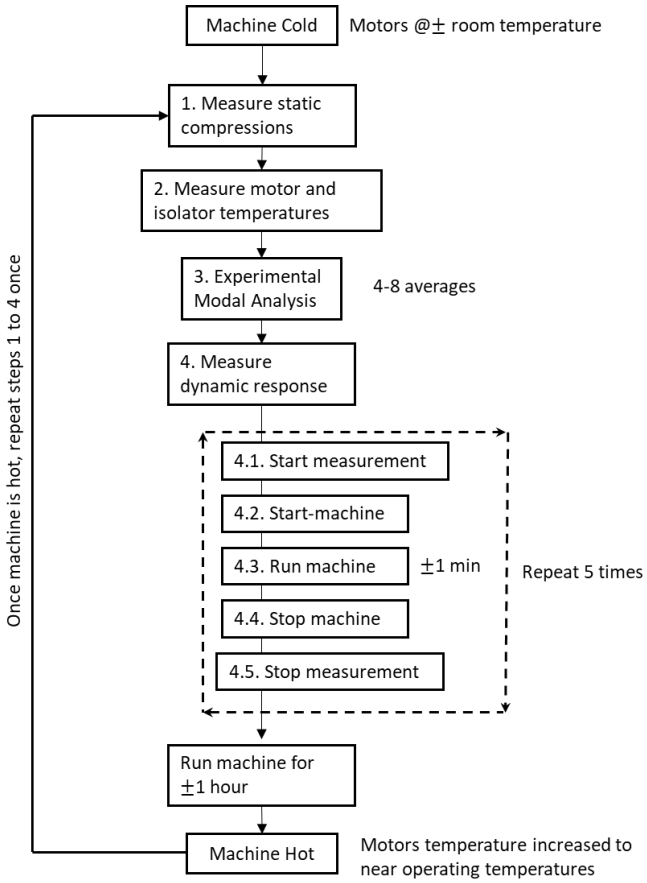

Figure 60: Experimental procedure

In the case of rubber isolators, because of the internal resistance of rubber some energy is lost (damping) in the form of heat and therefore the temperature is expected increase. Changes in temperature of rubber elements are also expected to change the stiffness and damping characteristics of the rubber [64] which in turn influences the modal and transient behaviour of the vibrating screen.

The extent to which the screening parameters are influenced by temperature changes in isolators is not clearly known before the experiments.

Step number 1 in the test is the measurement of the static compression of each isolator. This is a simple check to ensure that the compressions make sense and that no major discrepancies are present. Major discrepancies in static compressions per corner may occur due to stiffness differences for isolators, machine mass imbalance or the screen stand not being level. Step 2 is the measurement of the isolator and motor temperatures using a thermal camera.

Step number 3 is an experimental modal analysis (EMA). EMA is concerned with the determination of modal parameters such as natural frequencies, damping ratios and mode shapes. Modal parameters are considered as global parameters for a system. The first step in determining the modal parameters is to measure the response(s) of a system to an excitation force and compute the frequency response functions (FRFs) of the system. The FRFs are transfer functions satisfying the following condition [65],

$$Responses = FRF \times Forces$$

There are several methods available to perform an EMA on vibrating screens including a sine sweep using a shaker, step relaxation and hammer impact response [65]. The most popular method for vibrating screens is a hammer impact response modal analysis [42] [45]. Hammer impact tests require minimal set-up and are efficient to execute. In this method a modal hammer with a rubber tip is used to excite the vibrating screen's natural frequencies between 0-100Hz. This is confirmed in Figure 61 showing the averaged accelerance FRF from each sensor at F2R (vertical response only). The coherence can be seen to decay after approximately 100Hz.

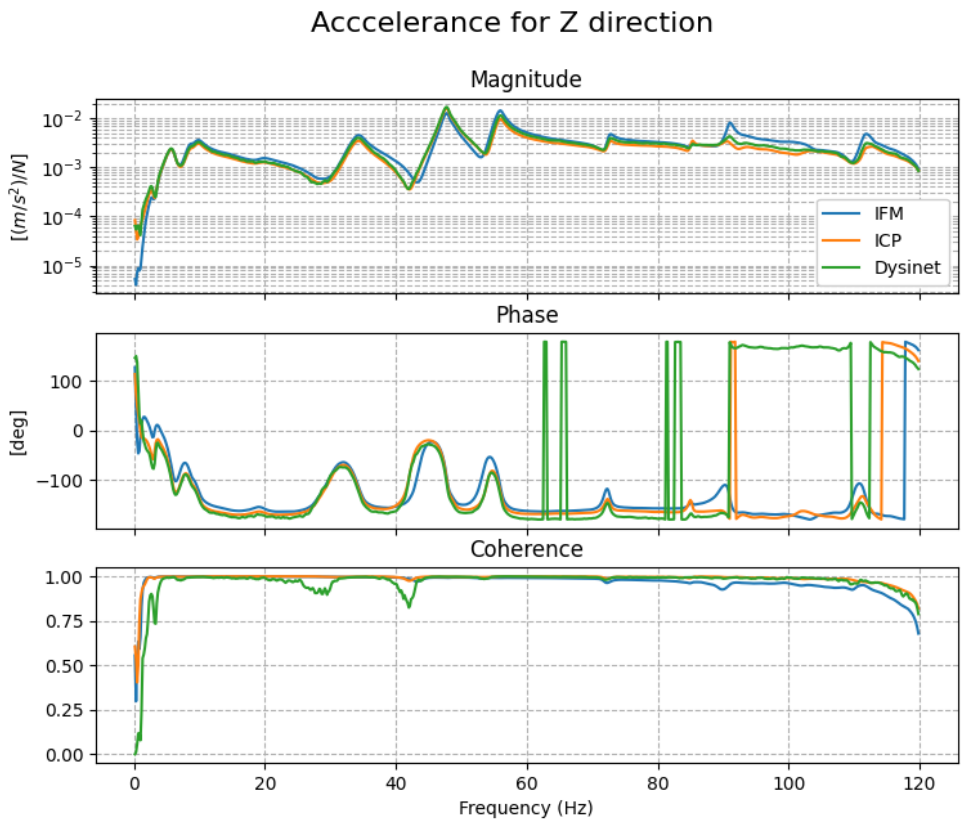

Figure 61: FRF Accelerance for sensor responses at F2R in the z-direction

The position, direction and magnitude of the impact force is harder to control compared to other methods as it is directly dependent on the skill of the tester. Also, skill is required to ensure that no

successive multiple impacts occur which negatively influence the impact force measurement and the response. The measured response must originate from a single impact.

Although there is some skill required, the major benefit of this method over others is the ease of changing the impact position and the speed at which modal analyses can be performed. The advantage of easily changing the impact position implies that, using the theory of reciprocity, a single accelerometer and modal hammer can be used to determine all modal parameters (including mode shapes) of a vibrating screen. Reciprocity during modal tests can also be used as an indication of the quality and linearity of measurements [65].

The impact method can be either a SIMO (single input, multiple output) test method or a MISO (multiple input, single output) modal test method. Multiple forces and/or multiple responses need to be measured at different locations to determine the mode shapes of the system and ensure repeatability, reliability, and consistency of the FRFs [65].

To ensure that the most energy is transferred to the modes of interest, several positions of the hammer impact are evaluated at different locations before deciding on a final location. The excitation position chosen should produce a large measurable response in both the vertical and horizontal directions, exciting all the modes and ensuring a high coherence within the frequency band of interest in the X and Z directions.

The results of the position evaluation can be found in Appendix E. Because the model hammer tip is large, only a limited number of positions are practical. Impact on the F1 and F2 isolation brackets gave the best response, particularly in the Z direction. However, it is difficult to get consistent impacts in these areas due to welded ribs on the isolation brackets making it impossible for the impact to occur on a flat surface. The perimeter stiffeners gave the next highest modal response when compared to excitation on the traverse or exciter beam. Although the left and right perimeter stiffeners gave similar response amplitudes the left side is selected over the right side as it is the easier to hit with the hammer.

The impact area on the perimeter stiffener is slightly angled such that the impact force acts in both the vertical and horizontal direction. The perimeter stiffener is also laterally off-centre ensuring that the pitching and rolling modes are also excited.

Several averages of the computed FRFs are taken to reduce noise and ensure the coherence is as close to unity across the frequency spectrum possible. Coherence is the measure of the statistical reliability of measured data based on averages of a random process. A unity coherence is required to have confidence in the usefulness of the FRFs measured. The main source of low coherence in modal tests is leakage errors (due to non-periodic force and response), nonlinearities in the system being tested or high noise levels in the response signal. Leakage is mitigated by selecting using an appropriate window and the nonlinearities and noise are reduced by taking the average of several FRFs [65].

For the experimental modal analysis in step 3 the modal hammer is connected to the same Quantum DAQ as the ICP sensors. There are 8 available channels on the Quantum DAQ and 8 ICP sensors, therefore the ICP sensors at F1 Left measuring the horizontal direction (S/N 12247) is not measured during the modal analysis to allow for the measurement of the modal hammer. After the modal hammer test is completed, the modal hammer is removed from the Quantum and replaced with the F1 left horizontal sensor.

Step number 4 is the measurement of the dynamic response of the vibrating screen to the forced excitation of the unbalanced motors. The measurements are to capture the start-up, operating

(approximately 1min) and coast down of the vibrating screen. This is repeated 5 times. The repetition of the test is a check for consistency or repeatability of the transient behaviour. The more repeatable the tests are the more linear and predictable they are. Also, this allows for averages to be taken of the metrics or features extracted during signal processing.

Lastly the machine is started again and left running for approximately an hour. By then the motors will have warmed up close to their operating temperatures. After a temperature increase is confirmed steps 1 to 4 are repeated. This is referred to as a "Hot" condition test whereas the former is a "Cold" condition test.

The experiment procedure is repeated for several isolator combinations or configurations. The following configurations are planned:

1. CH8-160 Resatec – Old
2. CH8-160 Resatec – New
3. Resatec combination of Old and New
4. Ø19x123x250 coil spring
5. Ø20x124x260 coil spring
6. Coil spring combination Ø19 and Ø20
7. Ø120x50x140 rubber isolator – New
8. Ø120x50x140 rubber isolator – Old
9. Rubber isolator combination New and Old or Damaged

The experiment procedure in Figure 60 was repeated 9 times, once for each isolator combination above. For the isolation combinations (configuration number 3, 6 and 9 above) the old, damaged, or less stiff isolator was placed at the F2 Right isolator position only. The other isolation positions had new "healthy" isolators.

3.7 EXPERIMENT CONSIDERATIONS

During the experiments some unexpected situations were encountered.

3.7.1 Sensor saturation

The first challenge encountered was that the ICP sensors saturated during start-up and shutdown of the machine only when only coil springs were used as isolators. This is due to high frequency impulsive shock waves from coil springs knocking on the steel spring cups. Spring cups are used to seat the coil springs into position.

The shock waves exceed the threshold of the sensors shock limit and sensor saturation occurs. It was observed that the coil springs do not bottom out which can occur during start-up or shutdown. The impulsiveness occurred during the erratic motion when sweeping through the rigid body modes. Figure 62 illustrates the effect of the ICP sensor saturation on the measured signal (Figure 62 is for illustrative purposes only, therefore the axes labels and values are not shown). It is not possible to filter the saturation effect from the signal.

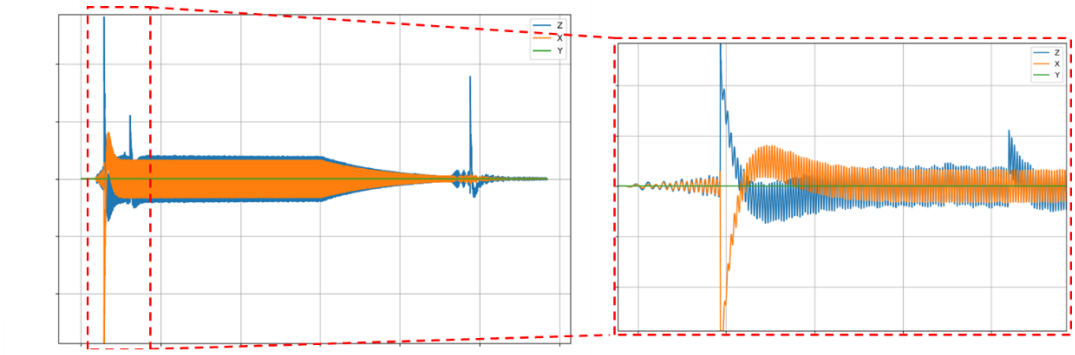

Figure 62: Illustration of the effect of sensor saturation

The saturation was mitigated by introducing a "mechanical filter" between the sensor and the mounting position. Something as simple as a thin sheet of rubber placed between the sensor and the isolation bracket could attenuate the high frequency impulsive shock waves. However, adding a medium between the sensor and the structure can introduce non-linearities. It is therefore important to select the right material and evaluate its effect on the measured response. Wooden blocks were stuck onto the isolation brackets using super glue and the ICP sensor was then stuck to the wooden blocks. The wooden blocks were laminated chipboard. Wooden blocks were used due to their availability and the fact that they can be considered rigid for the frequency range of interest.

An EMA was performed before and after the wooden blocks were introduced to ensure there was no influence on the modal parameters (results seen in Appendix L). The introduction of the wooden blocks did not alter the FRFs obtained. The ICP sensor measurements were checked to ensure saturation no longer occurred during start-up and shutdown. Immediately after introducing the wooden blocks several start-ups and shutdowns were performed and no sensor saturation occurred.

The issue of sensor saturation is a practical consideration when gluing ICP sensors on isolation brackets where coil springs are present. The MEMS sensors do not indicate instabilities or erratic non-linearities.

3.7.2 Damaged or used rubber isolators unavailable

A final challenge was encountered during the final experiment. This was where a combination of new and old or damaged rubber isolators was to be used. An attempt to source used rubber isolators suitable for this test was not successful and the option to physically damage a new rubber isolator to cause significant change in stiffness was considered a safety risk. There is a real risk of the rubber isolator failing catastrophically due to high strain experienced during shutdown.

However, it is important to understand how rubber isolators change after a period of use. Therefore, other larger used rubber isolators were sourced. These isolators have a larger diameter and height and are suitable for larger vibrating screens. Their desired stiffness is 1020N/mm. These buffers are too large to be installed on the test screen.

To understand how the stiffness between new and old rubber isolators differ, quasi-static tests were performed at Delta Rubber. The resulting graphs are shown in Figure 63. The load-compression graphs show clear differences between the two used rubber isolators and two new rubber isolators. Like the Resatecs, within the initial compression window (0-10/15mm compression) the used rubber isolators are less stiff when compared to the new. However, beyond 10/15mm compression the used rubber isolators are considerably stiffer than the new.

Similar behaviour as described can be expected from rubber buffers with similar geometry and rubber compound used. The stiffness change with age/use is not linear and compression regions with higher and lower stiffness will develop. If the change in stiffness is significant enough it may have a noticeable impact on the overall dynamics of a vibrating screen.

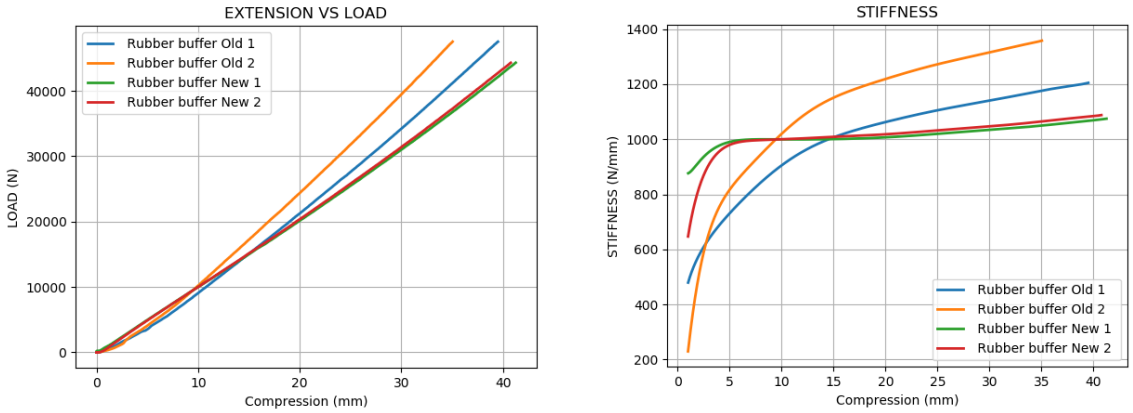

Figure 63: Load compression and stiffness curves of 1020N/mm rubber isolators from quasi-static tests

3.8 PRELIMINARY RESULTS

The isolator configurations tested are shown in Table 5. All tests were performed over a period of 6 days. Time was limited due to the availability of the measurement equipment as well as the vibrating screen. The preliminary results include measurements and observations made for each configuration tested which include the static compressions, temperatures of isolators and unbalanced motors as well obvious anomalies seen in the EMA and transient tests results. Measurements and observations were recorded on a test card, an example of which can be seen in Appendix H.

Table 5: Configurations tested

Config No.	Description
1	Old/Used Resatec isolators on all 4 corners.
2	New Resatec isolators on all 4 corners.
3	New Resatec isolators on 3 corners and old/used Resatec on F2R corner.
4	Ø19 coil springs on all 4 corners.
5	Ø20 coil spring on all 4 corners.
6	Ø20 coil springs on 3 corners and Ø19 coil springs on F2R corner (test cancelled due to ICP sensor saturation).
7	Ø20 coil springs on 3 corners and Ø19 coil springs on F2R corner (ICP sensors placed on wooden blocks).
8	New Ø120 Rubber isolators on all 4 corners (with ICP sensors on wooden blocks).
9	New Ø120 Rubber isolators on all 4 corners (with wooden blocks removed).

3.8.1 Isolator static compression and temperature results

Table 6 shows the static compression and respective temperatures recorded for each configuration and condition. As per the test procedure, each configuration is evaluated in a cold and hot condition. The cold condition refers to tests while components are at room temperatures and hot conditions are directly after the machine has been operating for approximately 1 hour.

The uncompressed lengths of the isolators as well as the ambient room temperatures are also shown. The room temperatures are estimated using a thermal camera but are not exact. Also, static compression differences of less than ±2mm are not considered significant as a tape measure is used for this measurement which is not precise.

Table 6: Isolator static compression and temperature results per configuration

Config. & Cond.	Static Compressions					Temperatures				
	F1R	F1L	F2R	F2L		F1R	F1L	F2R	F2L	
1	Uncompressed length: 351mm					Ambient Temp. 10-12 °C				
Cold	43	55	66	65	mm	11.2	10.9	10.9	11.7	°C
Hot	45	52	63	62	mm	33.1	34.5	39.2	38.8	°C
2	Uncompressed length: 368mm					Ambient Temp. 10-12 °C				
Cold	43	45	64	58	mm	11.3	11.1	10.5	10.6	°C
Hot	44	45	63	56	mm	28.9	27.5	29.5	32.9	°C
3	Uncompressed length: 368mm					Ambient Temp. 14 °C				
Cold	48	44	*75	59	mm	17.8	17.6	11.4	18.7	°C
Hot	49	43	*77	63	mm	32.9	30.2	35.4	36.3	°C
4	Uncompressed length: 255mm					Ambient Temp. 14 °C				
Cold	28	33	47	44	mm	14.2	14.1	14.2	13.9	°C
Hot	27	35	47	45	mm	14.1	14.7	14.5	14.8	°C
5	Uncompressed length: 255mm					Ambient Temp. 10-12 °C				
Cold	25	29	40	36	mm	12.2	12.3	11.6	12.7	°C
Hot	27	30	41	37	mm	12.8	14.1	12.5	14.2	°C
6	Uncompressed length: 255mm					Ambient Temp. 16 °C				
Cold	30	27	45	39	mm	15.6	17.1	16.6	16.6	°C
Hot	30	27	47	40	mm	15.5	16.5	15.8	16.2	°C
7	Uncompressed length: 255mm					Ambient Temp. 16 °C				
Cold	30	28	46	40	mm	14.4	16.3	15.1	16.2	°C
Hot	30	27	47	40	mm	16	17.2	15.4	16.8	°C
8	Uncompressed length: 140mm					Ambient Temp. 14 °C				
Cold	10	14	16	12	mm	14.8	15	14.7	15.9	°C
Hot	10	13	15	10	mm	31.0	28.1	31.7	33.5	°C
9	Uncompressed length: 140mm					Ambient Temp. 10-12 °C				
Cold	11	14	17	13	mm	11.6	12.1	10.4	12.6	°C
Hot	10	14	17	12	mm	27.9	30.6	31.1	33.8	°C

* Uncompressed length actually 351mm because isolator was shorter to begin with.

From Table 6 the following is observed:

- F2 (discharge) isolators compress more than the F1(feed) isolators. This is an indication that the CG of the screen is closer to the discharge end. This is expected as the motors, which are the heaviest single components of the vibrating screen, are positioned closer towards the discharge end.
- Configurations with Resatecs and rubber isolators (Config. 1, 2, 3, 8 & 9) show that after the machine has operated for an hour the isolator temperatures increase. This is expected as rubber dissipates internal friction energy as heat. Figure 64 shows the thermal images of Resatecs and rubber isolators after one hour of operation. The highest temperatures occur

where the strain is the most. For rubber isolators the highest strain occurs at the centre of the isolator and for Resatecs the top torsional element experiences the highest strain. In this study it is not important to know how isolator characteristics are affected by changes in temperature, however its effect on the dynamics shall be considered.

- In the hot condition the Resatec and rubber isolators at the discharge have a higher temperature than those at the feed end. This correlates with the static compression which is also higher at the discharge which seems to imply that the temperature is higher due to the higher initial strain on the rubber elements. But this could also be due to dynamic differences between the feed and discharge during operation.
- The coil springs did not experience temperature changes due to operation but rather due to ambient temperature changes.
- The old Resatec in Test 1 have a lower uncompressed length than the new Resatecs in Test 2. But the static compressions from the respective uncompressed heights are similar.
- The isolator temperature does not appear to influence the static compression observed.
- The static compressions for the configurations where a combination of old and new Resatecs (Config. 3) as well as where different stiffness coil springs (Config. 6 & 7) are used indicate greater compressions where the “less stiff” isolator is present. The isolator at F2R shows a significantly greater compression than the other isolators. For the other configurations, where similar isolators are used per corner, the compressions are more uniform.

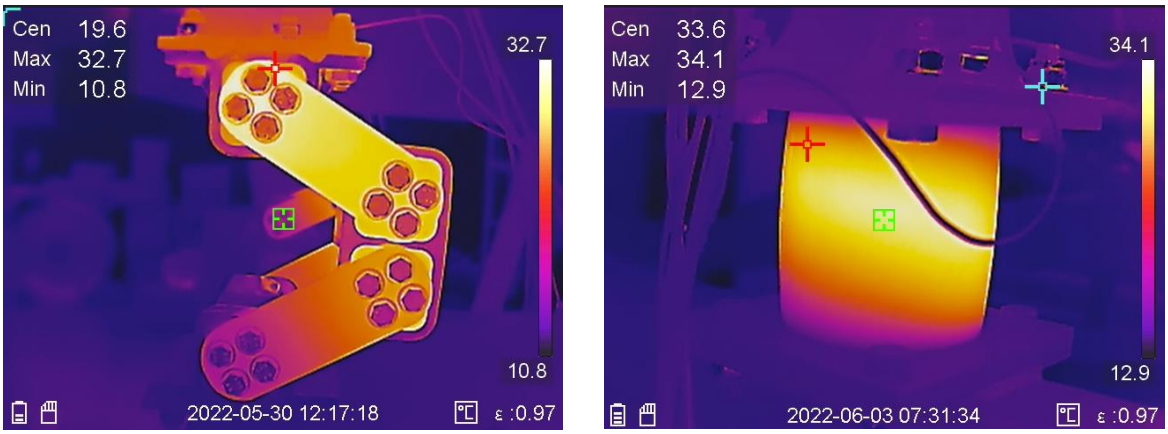

(a) *(b)*

Figure 64: Thermal images of a) Resatec and b) Rubber isolator after 1 hour of operation

Beside the results in Table 6 there are other temperature related observations made during testing. During the cold transient tests, the temperatures of the Resatecs and rubber isolators increased such that by test repetition number 5 the temperature was 2-4°C higher. During the warm transient tests, the temperatures of the Resatecs and rubber isolators gradually decreased per test.

Figure 65 shows a thermal image of the left and right motors after 1 hour of operation. The temperatures are observed to increase to between 30 and 40°C. The maximum temperature attained is dependent on the ambient temperature. The temperature of the LHS motor is also consistently higher than the RHS motor by 2-3°C. This can be due to differences in physical internal friction or motor slip between the two motors.

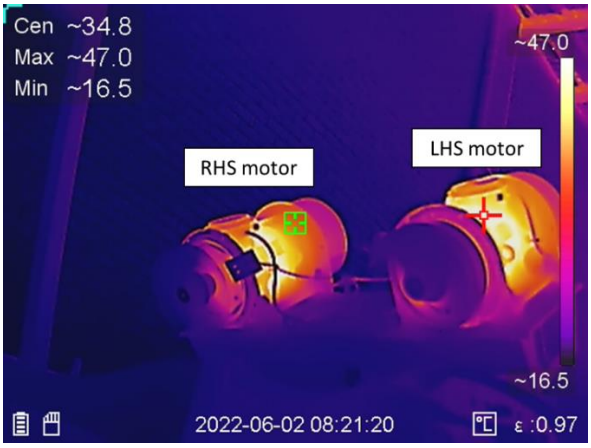

Figure 65: Thermal image of left and right motor after 1 hour of operation

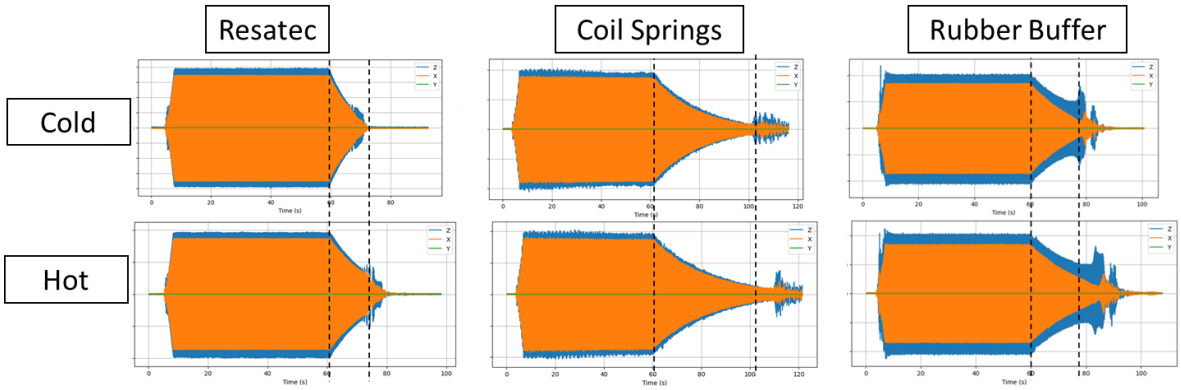

Figure 66: Observation of increased shutdown time of hot conditions for all three isolator types

During the hot condition, the coast down time was noticeably longer than during the cold condition. This occurs irrespective of which isolator is used as seen in Figure 66 where an occurrence in the cold condition measurements is compared to that of the hot condition (Figure 66 is for illustrative purposes only, therefore the axes labels and values are not shown). Although the coil springs did not change temperature a longer coast down time is still observed for the hot condition. This implies that the exciter temperature is the major contributor to this phenomenon.

Another observation is that the isolator type used also influenced the coast down time of the test. This can be seen in Figure 67 where the shutdown time with Resatec isolators is considerably shorter compared to the coil spring isolators (Figure 67 is for illustrative purposes only, therefore the axes labels and values are not shown). Both these observations indicate that there exists a strong coupling between the shutdown dynamics, the type of isolator used and the test condition (i.e. exciter temperature).

Lastly, an anomaly was observed in all measured IFM sensor signals. Details of the anomaly can be seen in Appendix M. The anomaly is suspected to originate in the VSE measurement module and could be either hardware or software related. It was however not deemed detrimental to the measurements as the anomaly occurred at predictable times after a measurement was triggered and it never occurred in a critical phase of the operation.

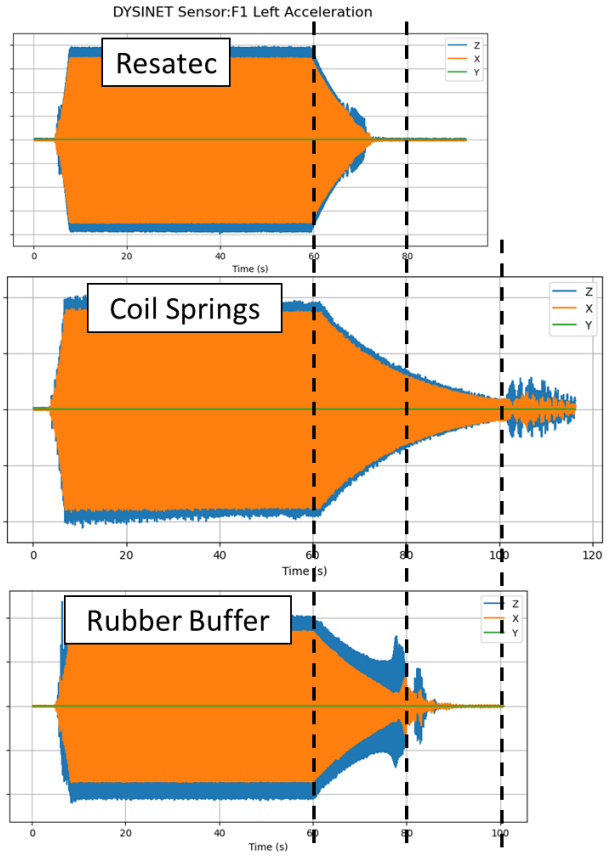

Figure 67: Observation of shutdown time difference for each isolator type

3.9 SIGNAL PROCESSING

Signal processing techniques can be used to condition the measurements and extract interesting features with application to isolator condition monitoring. For both the experimental modal analysis as well as the transient tests different techniques are available. Figure 68 shows a high-level overview of the signal processing steps taken.

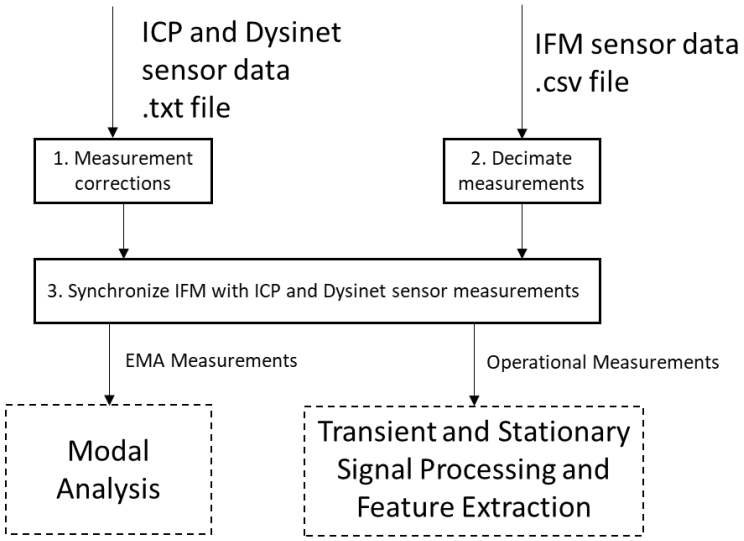

Figure 68: High level overview of signal processing

The ICP and Dysinet sensor data is stored in .txt files and the IFM sensor data is stored in .csv files. Before the EMA and transient signal processing can commence a few alterations need to be made to the sensor data. A Python script is used to perform the following corrections,

1. Measurement corrections entail unit and direction corrections such that all sensor data is scaled to the same units of m/s^2 and their sensing directions are positive in the same directions.
2. Down-sample IFM sensors from 100kHz to 1200Hz.
   A Butterworth lowpass filter with cut-off frequency at 600Hz and an order 6 is used to remove all high frequency content. The filter is designed and applied using Python's 'scipy.signal.butter' to get the filter coefficients which are passed to 'scipy.signal.filtfilt' to apply the filter twice to the measured data. Filtering twice (i.e. forwards and backwards) implies that the filter has zero phase and double the order of the original Butterworth filter.
   After filtering a linear interpolation of the filtered signal is performed at new timestamps for a 1200Hz sample rate. The interpolations is performed using the Python package Scipy and its 'interp1d' method which interpolates a 1-Dimensional function.
   Finally, the decimated IFM measurements are saved in a .txt file. The down sampled file is $\pm$85 times smaller than the original .csv file which enables faster loading and processing.
3. Synchronize the IFM sensor measurements with the ICP and Dysinet sensors. The indices of a common event (such as an impulse) in both the IFM and ICP sensors are used for the synchronization. The measured responses at the events are isolated and cross-correlated to get an offset or lag between the events. The cross correlation is performed using Python's 'scipy.signal.correlate' method. The cross-correlation is normalized to the maximum and the lags or differences in indices for the highest correlation is used as an indication of the offset between the two signals.
   The offset is then removed from the IFM sensor measurements. A negative offset means that the IFM sensors lead the ICP sensors and vice versa. The IFM measurement is offset by padding zeros at the beginning of the measurement and removing indices from the end or vice versa for a positive offset. This method is illustrated in Figure 69 which shows the IFM measurement leading the others, the offset is then removed, and the signals are now synchronized. The impulse force is also shown and has an impact contact time of $\pm$0.005s. (Figure 69 is for illustrative purposes only, therefore the axes labels and values are not shown).

3.9.1 Modal analysis

During the experiments a Python script was used to compute the FRFs for viewing between successive experiments to monitor the FRF quality. MATLAB is used for the final signal processing of the EMA measurements. MATLAB has up to date and validated tools available for FRF computation and modal parameter extraction. The following MATLAB tools, available in the signal processing toolbox, are used,

- *[frf,f,coh] = modalfrf(forces,responses,fs,window, 'Sensor', 'acc')*
  - This function returns FRFs computed using the H_1 estimator with Welch's method. This estimator assumes that there is no noise on the force/input signal and that all the noise is contained in the response signals [60].
  - Also, the returned FRFs are in receptance format (with the response in displacement units) and not in accelerance format (with response as acceleration). The receptance is simply the double time integration of the accelerance [60]. For modal parameter extraction in MATLAB the receptance model is used.

- A window function is applied to the measured force and response signals to ensure they are periodic and thereby avoiding leakage errors [60]. To avoid altering the measured signals, an exponential window is used for hammer impact experimental measurements. The window used is generated in Python using the following script (requires the *scipy.signal* package be imported),

  M = window_length
  tau = -(M-1) / np.log(0.001)
  window = signal.windows.exponential(M, 0, tau, False)

  The '*window_length*' refers to the product of the sampling rate and response length and '*tau*' controls the rate of the exponential decay in the window.

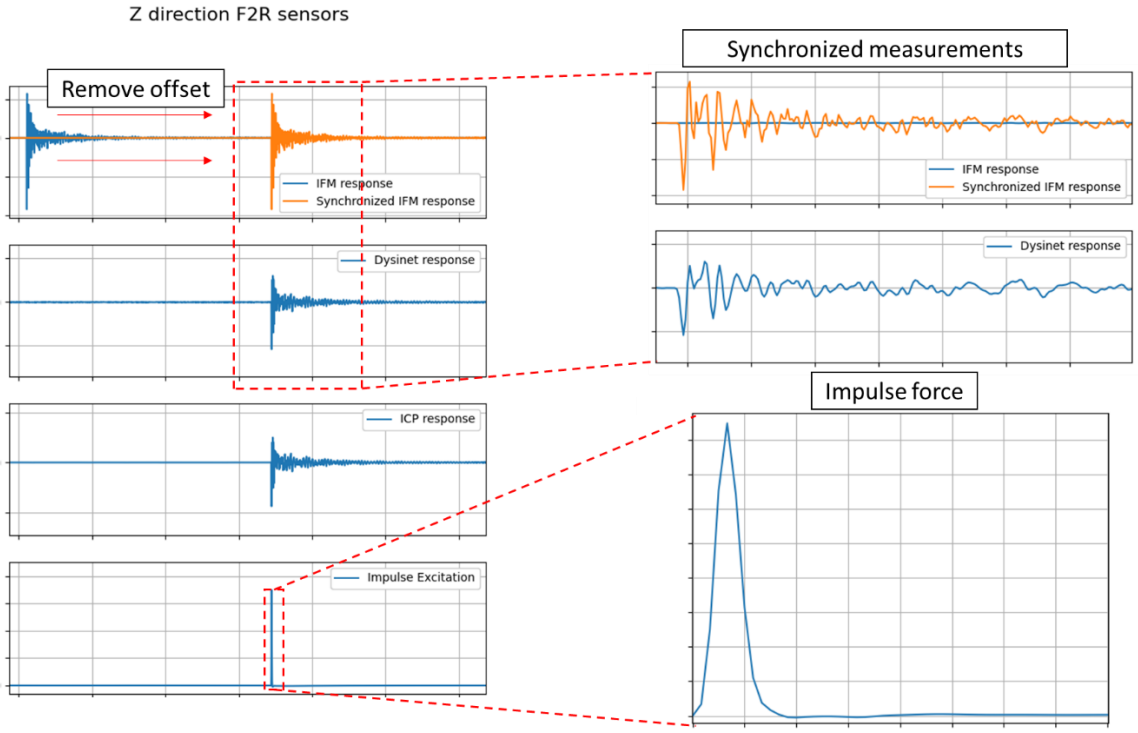

Figure 69: IFM measurement synchronization and impulse force

- *modalsd(frf,f,fs,'MaxModes',27,'FreqRange',[1 100], 'FitMethod','lsce')*
  - This function plots a stabilization diagram using the receptance FRFs. A stabilization diagram allows for the selection of physical modes by indicating points on the FRF where estimated natural frequencies and damping ratios computed from models of varying order remain within a specific tolerance. The natural frequencies and damping ratios are estimated by fitting models of increasing order on the FRFs using least-square complex exponential method. The maximum model order is also the maximum number of modes expected in the frequency range of interest. Care must be taken when choosing the maximum model order as there is the risk of overfitting which introduces spurious computational modes.
- *[fn,dr,ms,ofrf] = modalfit(frf,f,fs,12,'PhysFreq',fn_est,'FreqRange',[1 100], 'FitMethod','lsce')*
  - This function uses the receptance FRFs to fit a receptance model which is used to estimate the modal parameters (i.e. natural frequencies, damping ratios and mode shapes) of the system being evaluated. The model order is set as the number of

expected modes within the frequency range specified. Also, an array containing estimated frequencies (*fn_est*) can be passed to the function to assist with the fit. The fit method used is a least squares complex exponential method.

The process followed for performing the modal analyses of measured impact forces and responses can be seen in Figure 70. This is a similar procedure for modal analysis described by commercial software such as Siemens Testlab [66] and Matlab [67].

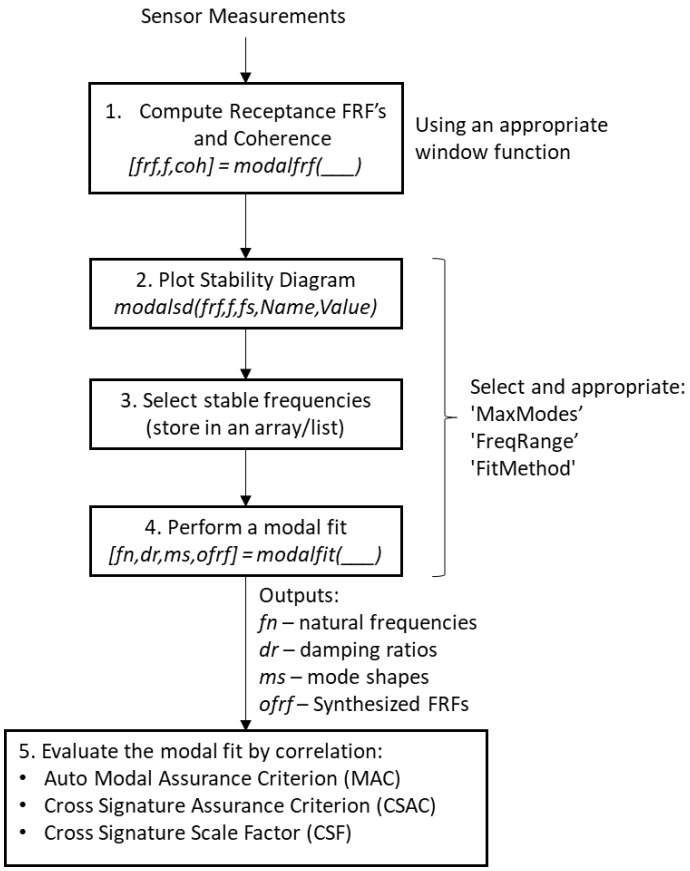

Figure 70: Modal analysis procedure

An example of a stabilization diagram plotted using MATLAB's '*modalsd*' function can be seen in Figure 71 which shows the stabilization diagram obtained using the receptance FRFs for Test 3 in the hot condition. After the stable modes have been identified they are placed in an array as initial guesses for MATLAB's *modalfit* function. The stabilization diagram in Figure 71 indicates stable modes at the following locations,

fn_est = [6, 9, 19, 34, 47, 56, 72, 85, 91];

Some spurious modes are present at higher model orders. These modes are not included in the modal fit and only frequencies where a peak is observed are considered. An example of the FRF fit ('ofrf') returned from the 'modalfit' method can be seen in Figure 72 where the FRF fit (red) is superimposed onto the original FRF (blue) to show their similarities.

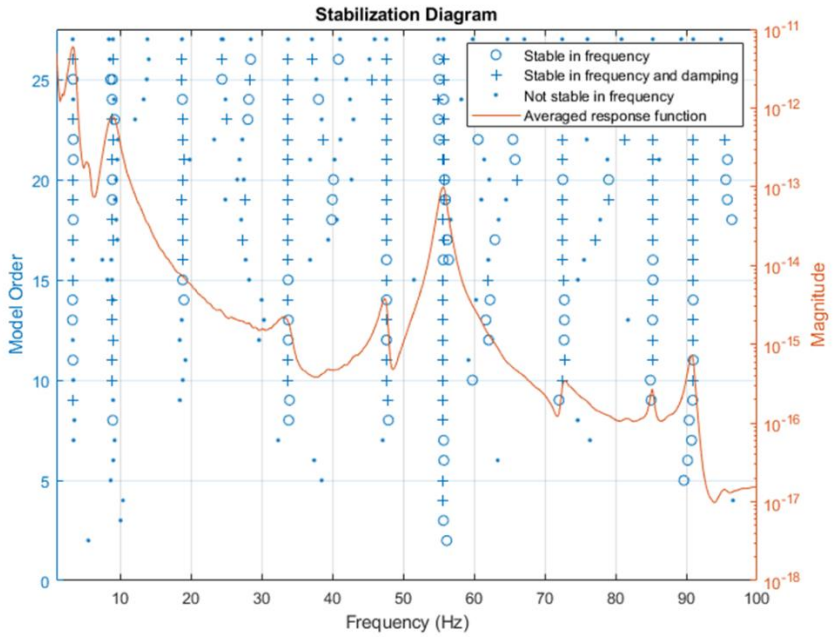

Figure 71: Stabilization diagram using MATLAB's 'modalsd' function

The final step in the modal analysis process is the evaluation of the modal parameters returned by the '*modalfit*' function using correlation techniques. These techniques include:

- Auto Modal Assurance Criterion (AutoMAC) which evaluates the orthogonality of the mode shapes [58]. An auto MAC ensures orthogonality within a single mode set and is important as no two modes in the same set should be the same. An example of the auto MAC can be seen in Figure 73. The MAC values can either be scaled from 0 to 1 or shown as percentage magnitude. The high off diagonal values indicate that some modes appear to be similar in shape. In this example, the third mode is an "out of plane" mode and therefore the sensing direction was not able to show the mode sufficiently. Also, the higher modes suffered from spatial aliasing due to lack of sufficient sensors.

- Cross Signature Assurance Criterion (CSAC) of Frequency Domain Assurance Criterion [58] which evaluates the shape (not amplitude) of the derived FRFs with the original measured FRFs [68]. As with the AutoMAC, the CSAC is either calculated as a value between 0 and 1 or as a percentage value. The higher the CSAC the higher the degree of correlation between the FRFs.

- Cross Signature Scale Factor (CSF) which evaluates both the phase and the amplitude of the derived FRFs with the original measured FRFs [68]. The CSF is evaluated the same as the AutoMAC and CSAC. The higher the value the higher the correlation.

For brevity the equations for calculating each of the correlation criterion mentioned are not included in this document.

An example of calculated CSAC and CSF values can be seen in Table 7. Note that the values correspond to the FRFs shown in Figure 72. The F1L correlation values are significantly lower than for the other FRFs. The FRFs obtained at the F1L position are of lower quality. This may be attributed to its position being the furthest from the excitation position (being closer to F2R).

For the stabilization diagram and the modal fit there are parameters which can be altered (i.e. 'MaxModes' or model order, 'FreqRange' which is the frequency range of interest and 'FitMethod' where several different modal fit methods can be selected). These parameters are selected to provide orthogonal modes (MAC) and high CSAC and CSF correlation percentages.

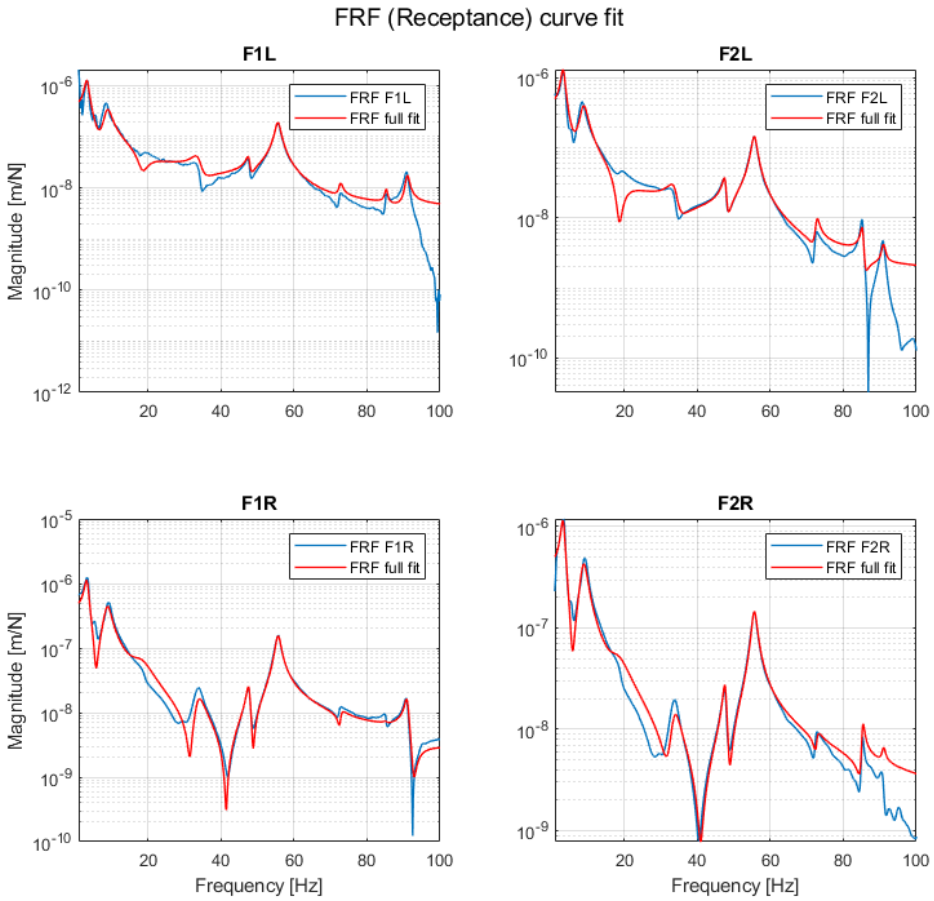

Figure 72: 'modalfit' returned FRF example from test 3 hot ICP sensor response

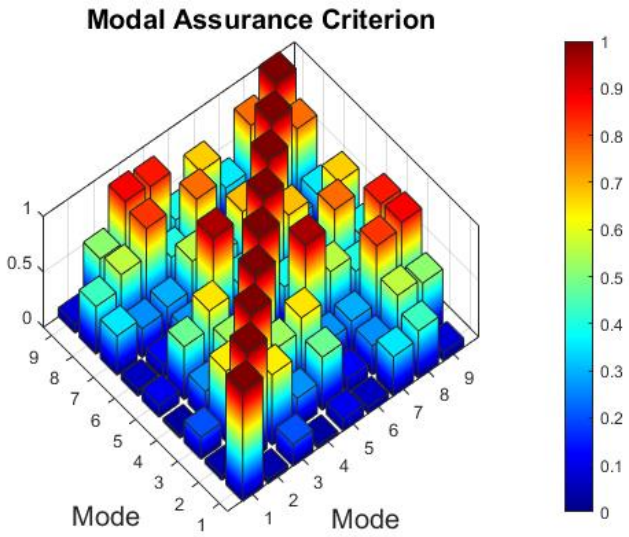

Figure 73: Auto MAC from config 3 hot ICP 'modalfit' returned mode shapes

Table 7: CSAC and CSF for config 3 hot ICP sensor FRFs

	F1R	F1L	F2L	F2R
CSAC [%]	95.63	59.41	92.36	97.29
CSF [%]	96.96	77.07	95.87	98.56

3.9.2 Transient signal processing

For transient signals there are numerous useful signal processing techniques available. The most popular techniques are time-frequency techniques which map how the amplitude of the vibration signal changes with time and frequency. The simplest time-frequency method is the Short Time Fourier Transform (STFT) where a short time window is moved along the record and a Fourier spectrum is obtained for each time window as a function of time shift. The STFT is typically plotted in spectrogram form whereby the square of the amplitude is plotted on a time-frequency map [6].

The spectrogram form of the STFT is also referred to as the power spectrum variation with time. The average of all short time power spectra is equal to the power spectrum of the whole record. In the power spectrum the mean square value is shown for each frequency and has the unit U^2 where U represent the record's units. Normalizing the power spectrum to the frequency resolution (assuming it is constant) gives the power spectral density (PSD) which has the units U^2/Hz. Integrating over a finite bandwidth of the PSD gives the finite power or mean square value within that bandwidth. Taking the square root of the integral of the PSD gives the root mean square (RMS) value of the signal.

The PSD of a signal is typically calculated by taking the Fourier transform (FFT) of the autocorrelation function. However, a PSD of a transient signal can also be estimated using Welch's PSD estimate [6]. This method follows a similar procedure to the STFT but ignores the time axis. First the signal is divided into multiple overlapping segments or blocks after which a modified periodogram (squared magnitude of a discrete Fourier transform (DFT)) is calculated for each segment. An average is taken of all the segments resulting in an estimated PSD. A window function is typically applied to the overlapping segments to avoid leakage errors. Also, the segments overlap each other by a percentage of the segment of block size. The percentage overlap is usually large (>50%) when a widow is used to guard against the loss of information at the ends of each window/segment. The advantage of taking the average of several segments also reduces noise or variability in the PSDs.

A PSD is not a conventional method for evaluating a transient signal as it can be susceptible to smearing of frequencies resulting in an inability to identify peaks. However, using Welch's PSD estimate on a vibrating screen measurement, where the change in speed is gradual, is almost equivalent viewing a spectrogram from the frequency axis. This is clearly illustrated in Figure 74 which shows a spectrogram (with light colours representing high magnitude) and PSD of a shutdown measurement made during testing of configuration 1. The PSD and spectrogram share the x axis. From the PSD and spectrogram, it is clear that the peak amplitude occurs at the same frequency.

For this study a PSD is not required to be accurate but consistent. This study requires the identification of features which change due to changes in isolator condition. As faults are introduced the PSD is expected to change in shape as an indication. From the PSD of each vibration measurement there are several features which can be extracted to describe the PSD's shape. The most prominent and interesting feature are the peaks in the PSD. During a transient operating envelope, peaks in the STFT occurs when the rigid body modes of the vibrating screen are excited. This occurs during both startup and coast down envelopes.

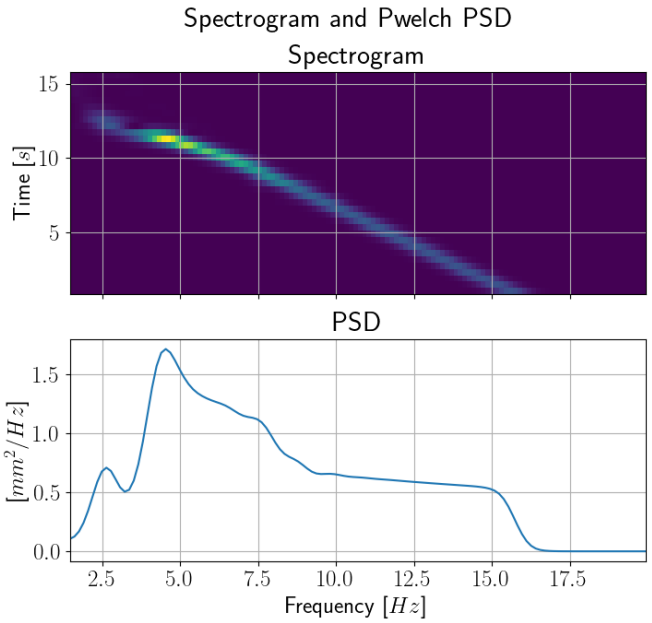

Figure 74: Spectrogram vs PSD

Peaks in the PSD are expected at particular frequencies and can be recognized by a prominent magnitude and width. The width of the peak in Hz is an indication of the peak prominence. There is no convention for measuring the width of a peak in a PSD however for modal analysis of single degree of freedom systems the width of a peak in a receptance FRF is measured at a "half-power point" which is a line cutting the peak at the peak magnitude divided by $\sqrt{2}$. For modal analysis the peak width at the "half-power point" is used to estimate the damping ratio of the mode [58]. In the PSD however, it is a good reference point at which to measure the peak's width. Figure 75 shows the same PSD as in Figure 74 with the addition of red vertical and horizontal lines at the recognized peaks. The vertical red line is an indication of the peak's magnitude prominence, and the horizontal red line is the peak's width at the "half-power point". A final feature of the PSD is its resultant area which includes the areas under respective peaks within their respective band widths.

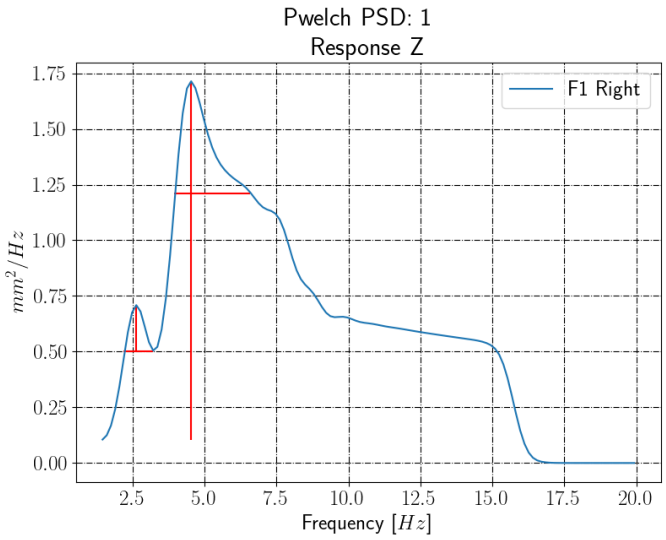

Figure 75: PSD with peak prominence and width indicated.

3.9.3 Stationary signal processing

There are several signal processing methods available for stationary signals. These comprise of both time and frequency domain methods for extracting features from a measured signal. Several of these techniques have proved useful for numerous applications of vibration-based monitoring (see Section 1.2.2.2). Frequency domain techniques such as the fast Fourier transform (FFT) provide an indication of the operating magnitude and frequency which is not significantly influenced by the isolators but are determined by the exciters used. Because of this a frequency domain technique applied to a stationary portion of the vibration measurement is not expected to show significant change with isolators.

Time domain techniques may prove useful but not in the conventional sense. Vibrating screens are designed to operate according to a required orbit or elliptical motion (i.e. a combination of vertical and horizontal vibration). The magnitude, frequency and shape of the motion is determined by the excitation type. However, the isolators may influence the orbit shape due to changes in stiffness. As mentioned, the magnitude and frequency of the motion is primarily influenced by the exciters and is not expected to change considerably with isolators. Conventionally, an orbit is visualized by plotting the vertical and horizontal vibration components on the vertical and horizontal axes respectively (see Figure 76a). However, not much can be seen from this plot, and it is necessary to extract features describing the shape of an orbit. These features are:

1. Orbit length
2. Orbit width
3. Orbit angle

These features can be extracted by fitting an ellipse to the combination of vertical and horizontal vibration as recommended by Duda-Mróz, et al. [35]. An ellipse fit adds an additional feature which is the location of its centre. However, if the vibration signals are detrended then the orbit centre is located at (0, 0) in the (x, z) plot. While attempting an ellipse fit method it was found that fitting an ellipse result in accurate orbit angle and width, but the ellipse length was often shorter than the actual orbit length. Therefore another, simpler method, was chosen which is to convert the measured vertical and horizontal data from rectangular coordinates to polar coordinates. This requires the calculation of the radius of the orbit as well as the angle of each radius point. The radius (r) is calculated by taking the magnitude of the vertical (z) and horizontal (x) vibration as seen in the following equation,

$$r = \sqrt{x^2 + z^2} \qquad \textit{Eq. 33}$$

The angle of each radius (θ) is calculated by taking the inverse tangent of the vertical to horizontal ratio as seen in the following equation,

$$\theta = \tan^{-1}\left(\frac{z}{x}\right) \qquad \textit{Eq. 34}$$

Visualizing the orbits in a polar plot eases interpretation as the orbit length, width and angle are clearly discernible (see Figure 76b). From the polar coordinates the orbit features can be calculated. The orbit length is equal to the sum of successive maximum peaks in the radius array. The orbit width can be estimated by taking the sum of successive minimum peaks in the radius array. The orbit angle is the acute angle at which the orbit radius is at a maximum peak value.

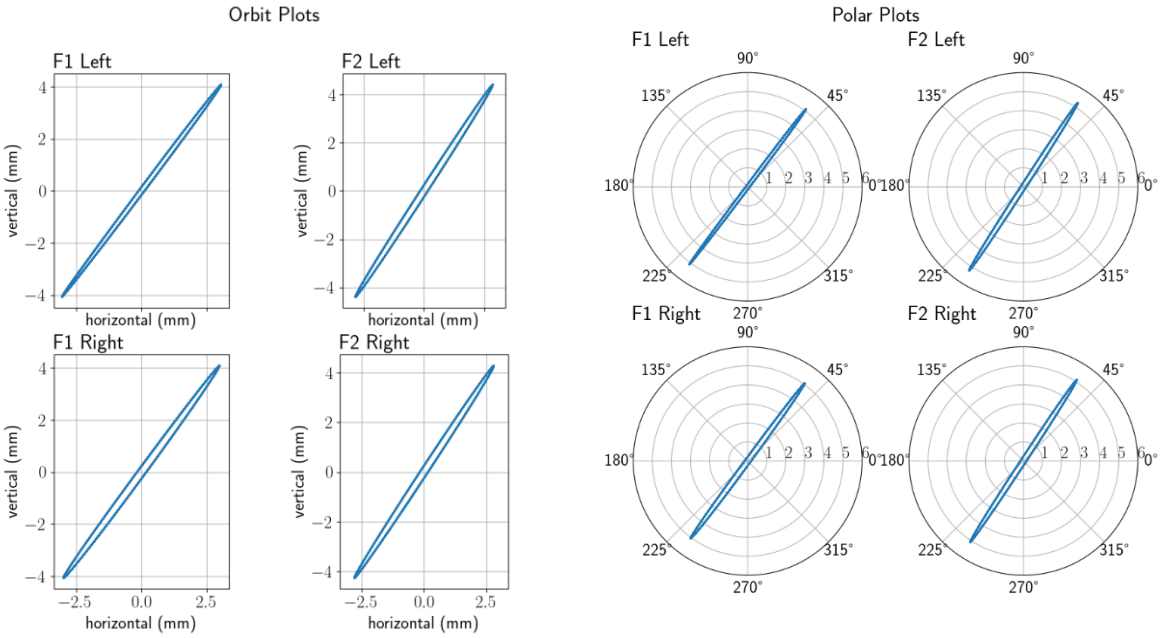

Figure 76: Vibrating screen orbits plotted on a) rectangular axes and b) polar axes

3.9.4 Operational measurement processing

Considering that the sensor measurements contain the start, steady operation, and stop phases, each phase need to be processed individually to obtain the relevant features. The flow diagram shown in Figure 77 illustrates the high-level signal processing procedure followed. A description of the steps are as follows:

1. The operational measurements, in the form of acceleration and rpm data, are divided into the respective operating phases using the RPM sensors as the que for when each phase begins and ends. This allows the data to be split into two streams of signal processing, one for the transient starts and stops and one for the stationary steady operations.

Starting with the '*T*ransient' stream the following process is followed,

2. Compute rigid body motion – the difference between selected acceleration measurements provides signals relevant to specific rigid body modes (excluding a bounce mode). Any phase shift or amplitude difference in between two signals' results in a large difference which is an indicator of a specific type of motion being excited. The following rigid body motion is calculated:
    a. Pitch motion – the difference between F2 and F1 sensors measuring in the vertical direction indicates when an out of phase pitching occurs.
    b. Rolling motion – the difference between left and right sensors measuring in the vertical direction indicates when an out of phase roll occurs.
    c. Yaw motion - the difference between left and right sensors measuring in the horizontal direction indicates when an out of phase yaw occurs.

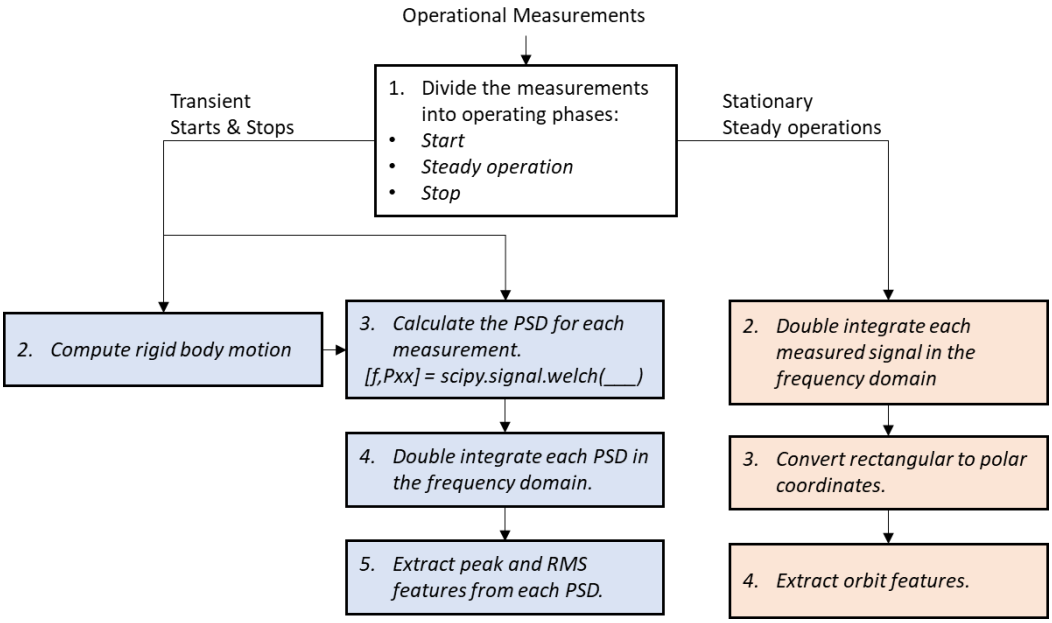

Figure 77: Operational measurements signal processing procedure

3. The acceleration PSD is calculated for both the original transient signals and the computed rigid body motion signals. The PSDs are calculated using a Python package Scipy function called 'signal.welch.py' which estimates the PSD using Welch's method. Within the Python script the function takes the following form:

```
f,Pzz=signal.welch(z,fs,'hann',block_size,int(block_size*overlap_ratio),nfft,scaling='density')
```

The function inputs are as follows,

   a. Vibration signal (*z*) – either the transient startup or coast down.
   b. Sampling rate (*fs*) – 1200hz
   c. Window type (*'hann'*) – the Hanning window is chosen for our application.
   d. Block or segment size (*blocksize*) – this was chosen to be 2^{11} or 2048 which equates to approximately 1.7 seconds in the time domain. This value was chosen as it allowed for a reasonable number of averages to be produced particularity for a start phase which is only ± 4 seconds long. This produced a very smooth PSD.
   e. Number of samples to overlap (*int(block_size*overlap_ratio)*) – this was calculated as shown based on an overlap ratio which is 0.75 representing a 75% overlap between segments. This high percentage of overlap was chosen to avoid the loss of information due to the window type used.
   f. Number of FFT bins – this was chosen to be 2^{13} or 8192. Effectively the windowed segment is zero padded until the number of FFT bins is satisfied. Zero padding is a technique used to increase the frequency resolution of the response by adding zeros to the end of the measurement segment until the desired frequency resolution is attained [58]. The resulting frequency resolution is ~0.15Hz.
   g. Scaling (*scaling='density'*) – chosen to be 'density' to ensure the magnitude is normalized to the frequency resolution.

4. After the PSDs are calculated they are double time integrated in the frequency domain to obtain the units of displacement (millimetres). The time integration is performed by simply dividing the magnitude of the PSD by $((i\omega)^2)^2$. This is because the units of the acceleration PSD are $[(m/s^2)^2/Hz]$. The final units of the displacement PSD is $[mm^2/Hz]$. Time domain

integration was considered, but the high pass filter used to remove the amplified <1Hz frequencies had a noticeable influence on frequencies below 5Hz. For frequencies above 5Hz the time and frequency domain integration gave the same PSDs.

5. The shape of the PSD is best described by its peaks. The PSD can contain multiple peaks. For this study only the largest 3 peaks are considered. Each peaks magnitude $[mm^2/Hz]$, width $[Hz]$, RMS (within the peak band width) $[mm]$ and frequency $[Hz]$ are extracted. Also, the integral of the PSD over the frequency band $[1.5, 20]Hz$ gives the mean square value of the PSD which is used to compute the resultant RMS displacement $[mm]$. The integral is limited within the selected band to avoid integration errors below $1.5Hz$. Also, no energy is introduced to frequencies above the operating speed of $\approx 16.5Hz$.
   In short 4 features are extracted per peak, for up to 3 peaks in a PSD, as well as 1 additional feature per PSD. There are 8 sensor measurements (for a sensor type) per test and 6 additional rigid body motions derived from the measurements. This adds up to a maximum of 182 features extracted from the PSDs for one start or stop phase and a total of 364 features per test.

An important note on the transient signals: the unbalanced motors of the vibrating screen synchronize through a dynamic phenomenon. This is a non-linear phenomenon and results in unpredictable behaviour when the motors are not synchronized. There is a short portion while the motors start up and a longer portion while the motors coast down where the motors are not synchronized. To avoid unpredictable results, these portions of the time signals are ignored during the calculation of the PSDs. The portions ignored are where the motor RPM was less than 200rpm (3.33Hz).

Now considering the '*Stationary*' stream the following process is followed:

1. The steady operating phases are double time integrated to get the displacement (in millimetres). The integration is performed in the frequency domain by taking the FFT of the time signal, diving the spectrum by $i\omega$ twice and taking the inverse FFT. Because only the operating phase is considered the inverse FFT is band limited or zoomed between 12 and 20Hz.
2. The vertical and horizontal displacement signals are now converted from rectangular to polar coordinates.
3. Finally, the orbit or elliptical features are extracted which comprise of the orbit length, width, and angle. There are 3 features per sensor measurement pair (vertical and horizontal) resulting in a total of 12 features per test.

3.10 Conclusion

From the preliminary results it can be concluded that the isolator type and test condition affect the transient envelopes considerably. This is most evident in the coast down times observed. For the different isolator types, it was shown that the coast down times for Resatec configurations were less than a quarter of the coast down times of the coil spring configurations. However, the coast down times for the rubber buffer configurations were nearly twice as long as those from the Resatec configurations. This implies a strong coupling between the exciter dynamics and the isolator type.

Now considering the test condition, it was shown that during the hot condition the coast down time was noticeably longer than during the cold condition. This occurred irrespective of the isolator used. The coil springs were the only isolator whose temperatures remained relatively unchanged from cold to hot conditions while all other isolators experienced a significant temperature increase. However, even for the coil springs the coast down times were longer during the hot condition. This implies that

the exciter temperature, which increased significantly from cold to hot conditions, was the primary contributor to this phenomenon.

Finally, for the evaluation of features there are three distinct techniques or classifications of feature extraction methods proposed in this study. The first is the extraction of natural frequency, damping and mode shapes from EMA measurements by modal parameter extraction. The second considers the stationary orbit length, width and angle which are extracted from the steady operating vibration measurements in the X and Z directions. Finally, the shape of a PSD obtained from transient startup and coast down measurements is described by the peaks and their respective magnitude, width, area (RMS) and location on the frequency axis.

4 RESULTS AND DISCUSSIONS

In this section the necessary results pertaining to this study are presented and discussed. First the EMA results are presented which consider how sensitive the modal parameters are to changes in isolators. Secondly the results from the operation simulations using the numerical model are presented. This is followed by the results obtained from the operational measurements performed experimentally. The latter two sets of results consider how selected transient and stationary features are influenced by the isolators. Finally, the comparison between the results obtained by numerical simulation and experiment is discussed. The use of different accelerometers is also discussed towards the end of this section.

The feature(s) most sensitive to changes in isolator condition should satisfy the following criteria:

1. The feature must undergo a significant percentage change for a given change in isolator condition. If the change is not significant then the probability of "noise" added by other vibrating screen anomalies (such as ore material build up) could overwhelm the percentage change observed thereby reducing the effectiveness of the feature for isolator condition indication.

2. The feature's change must have a strong correlation with the change in isolator condition such that a reduction in isolator stiffness results in a reduction of the feature's magnitude. However, one should not expect all features to change directly proportional to the fault. The change of some features may be inversely proportional (i.e., negatively correlated) which is also considered to be strong correlation if it is consistent. This has to do with the predictability of the change, the more positively/negatively correlated with the fault, the more predictable the change is.

3. The change in the feature must be measurable. This implies that, irrespective of the change in percentage, the feature must also undergo significant change in its own units. This change should be relative to the percentage of the fault introduced thereby indicating how much the feature changes for a given change in isolator condition (i.e., sensitivity). The reason this is important is the same as that stipulated in criteria number 1.

An important consideration is that features portraying inconsistent results are not considered reliable for isolator condition monitoring. From the experimental results (both EMA and operational measurements) for each configuration (see Table 5) the following comparisons are made:

- Config. 1 and Config. 2 (baseline) – All isolators change.
- Config. 3 and Config. 2 (baseline) – F2R isolator changes.
- Config. 4 and Config. 5 (baseline) – All isolators change.
- Config. 7 and Config. 5 (baseline) – F2R isolator changes.

The "baseline" configuration is the healthy/new isolator configuration.

With Resatecs, configuration 2 is the "healthy" configuration. For the tests with Resatecs the percentage change from a healthy/new Resatec to an old/used Resatec is estimated to be a *10% stiffness increase*. With coil springs, configuration 5 is the "healthy" configuration. The estimated percentage change from the healthy to unhealthy coil spring is a *22% stiffness decrease*. The static compression of the isolators recorded during tests (see Table 6) are used to estimate these percentage stiffness changes from the respective graphs (see Figure 49 and Figure 50).

In the tabulated results, colours are used to emphasize magnitude differences between results. The colour coding for all tables in this section show a darker/sharper colour for the largest numbers in a row. A dark/sharp green is a large positive number, and a dark/sharp red is a large negative number.

4.1 EMA RESULTS

The process outline in Section 3.9.1 is used for the extraction of modal parameters from the FRFs obtained experimentally. FRFs obtained for different configurations differed considerably in the lower frequency range [0, 30] Hz. This required varied inputs to the MATLAB functions used to get the best fit for the rigid and flexible body modes. There were two considerations made during the modal analysis:

1. Zero-padding is used to ensure a consistent frequency resolution for all FRFs from all configurations tested. This allows for a more generic algorithm for modal analysis with consistent modal fitting rather than a unique modal fit per FRF set which is very time consuming. It was also noticed that increasing the frequency resolution allows for a higher order fit.
2. To improve the modal fit and avoid the overfitting of modes within the frequency range it is deemed necessary to split the frequency range in two. For rigid body modes (RBM) and flexible body modes (FBM) the frequency range is split between [1, 25] Hz and [25, 100] Hz respectively. A separate fit is then performed on the RBMs and FBMs and the order of the fit can be adjusted accordingly to improve the fit. This worked well when the RBMs are not tightly coupled to the FBMs. However, for configurations with Resatecs, the modal fit over the whole frequency range of interest (1-100Hz) sometimes gave the best fit. The effect of splitting the frequency range is most obvious for the tests with coil springs. Figure 78 shows a comparison of the stability diagrams and modal fits for full [1, 100] Hz frequency range and split frequency ranges. Referring to the FRFs (Figure 78b), the red line is the modal fit for the complete frequency range and the black dotted line is the fit from the split frequency range which shows an obvious improvement.

Although a good fit is desired for the entire frequency range, the modal fit of the RBMs is most relevant to this study as the isolators have negligible influence on the FBMs of the vibrating screen. Figure 79 shows how the isolator influences the FRFs. Notice the 25Hz vertical line above which the FBMs of the vibrating screen are seen. The FRFs are shown in a magnitude and phase plot along with the coherence. Notice that the coherence is also influenced by the type of isolator used which is most noticeable in the lower frequency range for Config. 5, with coil springs, where a low coherence is obtained.

Figure 79 shows the differences in FRFs obtained for tests 2, 5 and 9. Both the Z and X direction FRF are shown from the IFM sensor responses. The vertical dashed red line indicates where the split between RBMs and FBMs occurs; at 25Hz. The RBMs are where the major differences are seen. However, there is a strong coupling between the first FBM observed ($\pm 32Hz$) and the isolator type used which is obvious when comparing tests 2 and 5. The FBMs for tests 5 and 9 are similar concluding that the coil springs and rubber buffers have less influence on the FBMs than the Resatecs. The influence of the Resatecs may be higher on the FBMs as they are fastened/bolted to the isolation brackets and static structure.

Considering the coherence graphs shown in Figure 79, the coherence in the RBM region is highest for the Resatec tests followed by the rubber buffer tests and is considerably lower for the tests with coil springs. The low coherence in the RBM region is a concern as low coherence is an indication of low

statistical reliability. However, the stability diagrams do indicate that the RBM modes are consistently stable, and therefore may be useful for modal fitting. Nevertheless, the low coherence is a limitation and should be considered for future experiments. Also notice regions of low coherence occur at antinodes of the FRFs as expected.

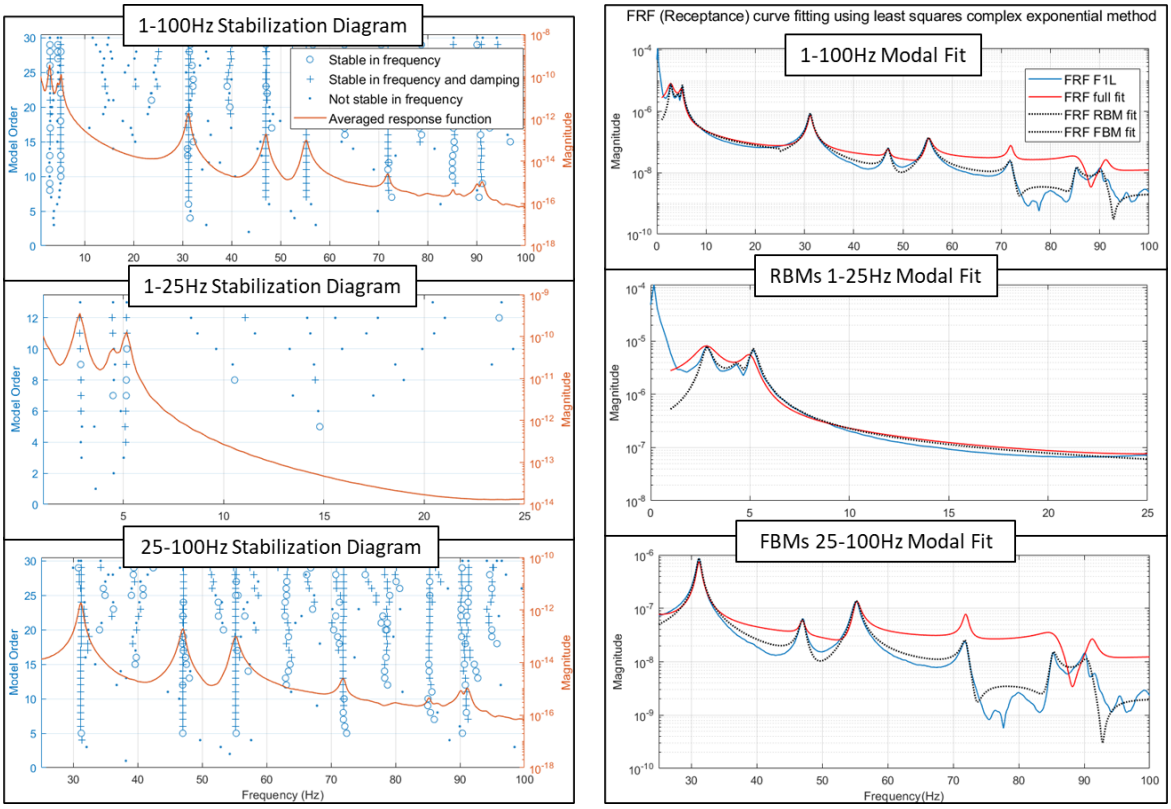

(a) *(b)*

Figure 78: (a) Stability diagram and (b) modal fit for Test 7's cold condition F1L IFM sensor in the z-direction

During the modal parameter extraction when comparing the quality of the modal fits for respective configurations, the resulting fits for coil spring and rubber buffer configurations are nearly indistinguishable from the actual FRFs with high correlation values. However, for the Resatec configurations, noticeable differences are apparent in peak positions and widths which result in lower correlation. These differences are most prevalent in the RBM region which is the region of interest. The differences in modal fits for tests 2, 5 and 9 can be seen in Appendix N Figure 112, Figure 113 and Figure 114 respectively.

The noticeable differences between the actual FRF and modal fit for the Resatec configurations could be attributed to non-linearities in stiffness of the Resatec. FRFs are inherently linear in computation and the model fits assume linearity in modal parameters which may limit their application. For Resatecs considerable non-linearity in stiffness results from the isolator's geometry and the rubber inserts of the torsional elements. The RBM damping ratios from the tests with Resatecs are higher than those for the other isolators tested. The higher damping may be attributed to the nonlinearity in stiffness which induces artificial damping. There is a strong coupling between the vertical, horizontal, and lateral stiffness of the Resatecs due to the torsional elements.

When performing a comparison of modal parameters between different configurations the mode shapes are used to identify and sort the modal parameters such that a like-for-like comparison can be made between the same modes. The natural frequencies and how they change between configurations are of primary concern because the natural frequency is directly influenced by changes in stiffness (i.e. isolator condition). There are two primary comparisons made, firstly how do the natural frequencies change between configurations and how do the natural frequencies change between hot and cold conditions.

To observe how the natural frequencies change between test conditions (cold/hot) each baseline's cold and hot conditions are compared to one another. Table 8 show the results of how the natural frequency changes.

Table 8: Natural frequency differences from ICP sensor Z direction responses

Conf. No.	Natural Frequencies (Hz)		Difference (Hot-Cold)	Difference All isolators fault		Difference F2R isolator fault		Mode
	Cold	Hot		Cold	Hot	Cold	Hot	
2: Resatecs	5.59	5.30	-5.18%	11.4%	1.1%	-1.7%	-1.3%	***RBM 1***
	9.17	8.97	-2.23%	16.7%	4.0%	0.7%	-1.3%	***RBM 2***
	19.37	19.46	0.46%	3.3%	-0.1%	1.2%	-1.3%	***RBM 3***
	33.96	33.86	-0.31%	2.7%	0.3%	0.5%	-0.3%	FBM 1
	47.61	47.68	0.15%	0.8%	-0.1%	0.3%	0.0%	FBM 2
	55.73	55.66	-0.12%	1.1%	0.2%	0.2%	0.0%	FBM 3
	72.47	72.51	0.06%	0.5%	0.0%	0.2%	0.0%	FBM 4
	85.20	85.36	0.18%	0.1%	-0.2%	0.1%	0.0%	FBM 5
	90.99	91.14	0.16%	0.3%	0.0%	0.1%	-0.1%	FBM 6
5: Coil Springs	2.82	2.82	-0.18%	-12.4%	-12.1%	-5.0%	-4.9%	***RBM 1***
	4.47	4.40	-1.43%	-10.3%	-8.1%	-4.0%	-3.2%	***RBM 2***
	5.16	5.16	-0.07%	-16.4%	-16.1%	-1.8%	-1.9%	***RBM 3***
	31.17	31.16	-0.03%	-0.5%	-0.6%	-0.2%	-0.1%	FBM 1
	46.99	46.98	-0.03%	-0.1%	-0.1%	-0.2%	-0.2%	FBM 2
	55.21	55.18	-0.05%	0.0%	0.0%	-0.1%	-0.1%	FBM 3
	71.88	71.81	-0.08%	-0.9%	-0.9%	-0.2%	-0.1%	FBM 4
	85.23	85.17	-0.08%	0.0%	0.0%	0.0%	0.0%	FBM 5
	90.55	90.46	-0.10%	0.3%	0.3%	-0.2%	-0.2%	FBM 6
9: Rubber buffers	5.06	4.75	-6.18%	***N/A***				***RBM 1***
	5.63	5.17	-8.16%					***RBM 2***
	8.34	7.82	-6.17%					***RBM 3***
	32.66	32.43	-0.71%					FBM 1
	47.37	47.29	-0.17%					FBM 2
	55.94	55.82	-0.22%					FBM 3
	72.31	72.23	-0.11%					FBM 4
	85.19	85.20	0.01%					FBM 5
	91.16	91.16	0.00%					FBM 6

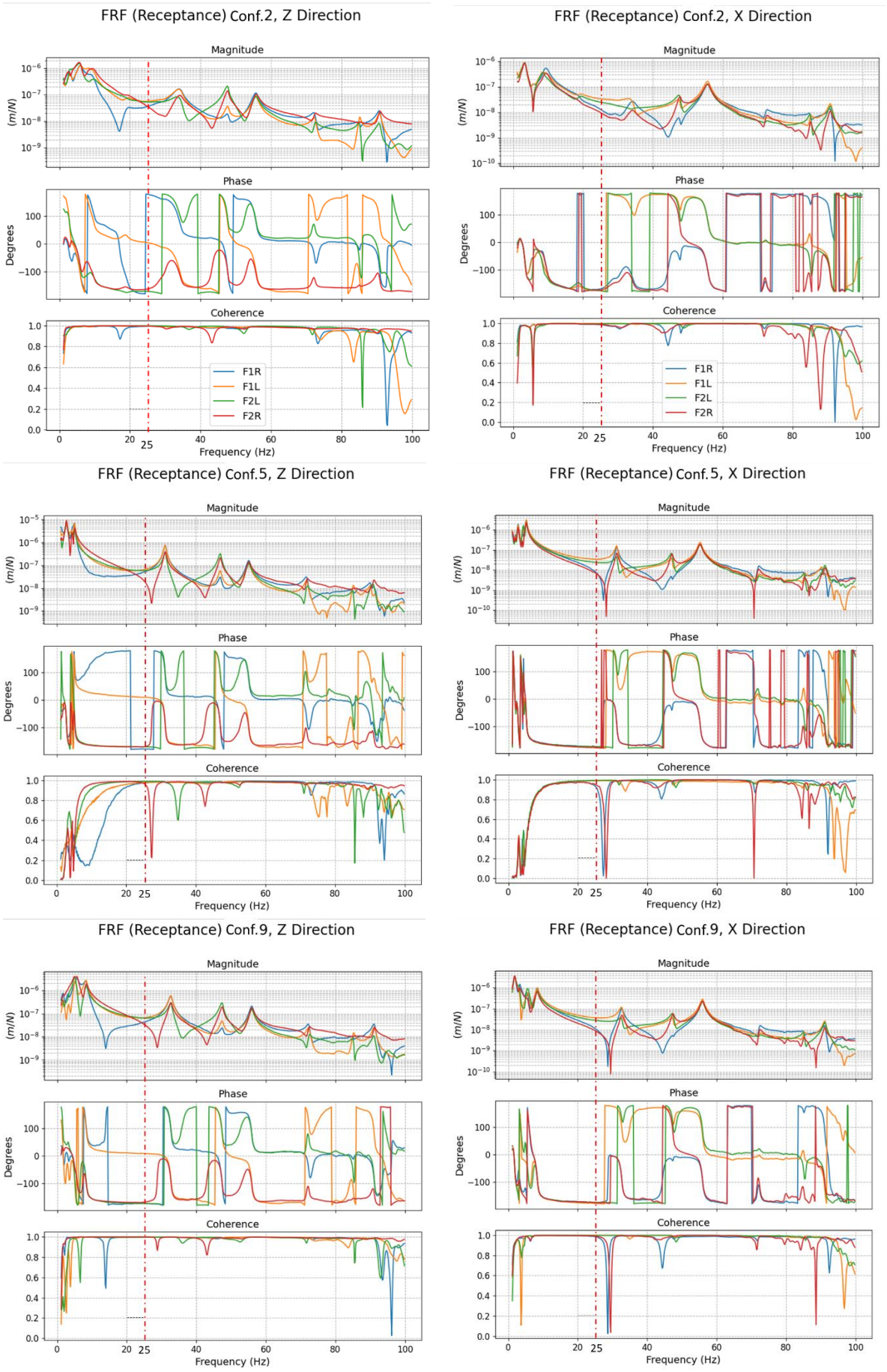

Figure 79: FRFs obtained from the IFM sensor responses for configurations 2 (Top), 5 (Middle) and 9 (Bottom) in the cold condition

4.2 EMA RESULTS DISCUSSION

From the results the following deductions are made:

- The test condition (cold/hot) influenced the RBM natural frequencies most significantly. Also, the influence is considerably higher for the Resatec and rubber buffer configurations. The reduction in natural frequencies correlates with the possible reduction in stiffness as the isolator's temperature increased. The changes in frequency for coil spring configurations based on test conditions are negligible.
- When all isolators are changed a noticeable difference in natural frequency occurs. This is clear for both coil spring and Resatec configurations where the natural frequencies of the RBMs decreased and increased respectively. This coincides with the predicted stiffness changes of the respective isolators (i.e., 10% stiffness increase for Resatecs and 22% stiffness reduction for coil springs). However, the test condition has a significantly larger influence on the Resatec configurations and has a negligible influence on the coil spring configurations. For the Resatec configuration the hot condition resulted in a smaller difference in natural frequency than the cold condition.
- When only changing one isolator the change in natural frequency is considerably less than when all the isolators are changed. A higher difference is shown for the coil spring than for the Resatec configuration. For the coil spring the change coincides with the change in stiffness of the isolator. The change in frequency for the Resatecs is small at less than 2%. Also, the test condition affects the change in natural frequency, but this is not significant.
- A less relevant observation is the influence of the isolator type on the first FBM natural frequency which differs by nearly 3Hz between coil spring and Resatec configurations. Once again, this can be attributed to the rigid connection between the Resatec and the vibrating screen.

RBM 3 for config. 2 in Table 8 occurs at what is considered a high frequency for a rigid mode at approximately 20Hz. Considering RBM 3's mode shapes in the X and Z directions (seen in Appendix K Figure 105) it is apparent that a yaw or lateral y-direction motion occurs. The Resatecs design causes it to be very stiff in the lateral y-direction which is the reason for this mode occurring at such high a frequency. Also, its presence in the Z and X directions is not as prevalent as the other modes (seen at approximately 20Hz in the top FRF in Figure 79) suggesting that the Z and X directions are not the primary directions of motion for this mode. However, the presence of this mode in both the Z and X direction responses is further justification of a strong coupling between vertical lateral and horizontal stiffnesses of the Resatec Isolator.

Considering the damping, Table 29 in Appendix K shows how the damping changes in a graphical representation for each respective mode and configuration. These differences are negligibly small and illogical for condition monitoring. Also, to illustrate what each mode looks like Figure 103, Figure 104 and Figure 105 in Appendix K shows the mode shapes obtained during modal analysis.

The damping ratios attained from each test are typical of lightly damped structures [19]. There is not a significant difference in damping ratios from cold to hot conditions. However, the damping ratios for the RBMs are observably higher than those obtained from FBMs. The FBMs appear to consistently have the same damping ratio. The RBMs are easily discernible from the FBMs based on the damping ratios obtained.

The mode shapes for the RBMs and FBMs shown are only for the Z responses as they are the most significant and obvious to interpret compared to the X response mode shapes. The RBMs occur in the

following order, first vertical bounce then rolling followed by pitching. For the Resatecs the rolling mode also exhibits some pitching and was not purely rolling as seen with the coil springs and rubber buffer tests. The FBMs shown in Figure 104 occur consistently for all tests performed irrespective of the isolators and sensors used.

4.3 OPERATING ENVELOPE RESULTS

The operational results refer to the features obtained from the full operating envelope (start, steady operation, and coast down) of the vibrating screen. A description of the features and how they are calculated is discussed in Sections 3.9.2, 3.9.3 and 3.9.4. There are a maximum of 376 individual features extracted from each test. There were 5 tests performed for 8 configurations and for each configuration there were 2 conditions (cold and hot) considered. Therefore, a total of 80 tests were performed. Clearly a large amount of data was collected, however it is not practical to evaluate each feature individually for its sensitivity. There are means available for such a comparison, but they fall outside the scope of this study. Rather, a reasonable assumption is made that the sensitivity to change for a feature may be the same or similar to the sensitivity to change of related features. In other words, if the magnitudes of peaks in the PSD of a sensor measurement change due to a change in isolator condition, then it is likely that the magnitude of peaks in other PSDs calculated from other sensor measurements will also change.

Data reduction can be achieved by grouping the calculated changes of related features into bins. The bins used can be seen in in Figure 80 which shows 23 feature bins representing individual features evaluated for their sensitivity. Notice that the PSD features calculated from the sensor measurements are kept apart from those obtained from the calculated rigid body motion(s). This is because the calculated rigid body motion(s) are also considered as features of the sensor measurements and are therefore evaluated separately.

Operating Envelope Feature Bins		
Start	**Steady operation**	**Stop**
Sensor measurements: a. Peak frequency b. Peak magnitude c. Peak width d. Peak RMS e. PSD RMS	Sensor measurements: a. Orbit angle b. Orbit width c. Orbit length	Sensor measurements: a. Peak frequency b. Peak magnitude c. Peak width d. Peak RMS e. PSD RMS
From calculated rigid body motion(s): a. Peak frequency b. Peak magnitude c. Peak width d. Peak RMS e. PSD RMS		From calculated rigid body motion(s): a. Peak frequency b. Peak magnitude c. Peak width d. Peak RMS e. PSD RMS

Figure 80: Feature bins

To evaluate how each feature changes from the baseline an excel spread sheet is used to extract the following information:

1. For the whole range of faults introduced the average of the absolute percentage differences ($Avg|\Delta\%|$) of each feature is taken. The feature comparisons or changes are captured, grouped into their respective bins, their magnitude/absolute value is taken, and the average calculated per bin. This gives an indication of the magnitude of change of each feature.
2. How each feature changes is correlated with the change caused by the introduction of a fault. For the simulated results a normalized cross correlation algorithm [69] is used which outputs

values ranging from [-1; 1]. The normalized cross correlation (γ_{xy}) between two signals (x and y) is calculated as follows,

$$\gamma_{xy} = \frac{\sum_{i=1}^{n}[x_i - \overline{x}][y_i - \overline{y}]}{\{\sum_{i=1}^{n}[x_i - \overline{x}]^2 \sum_{i=1}^{n}[y_i - \overline{y}]^2\}^{0.5}} \quad \textit{Eq. 35}$$

The value returned indicates whether the change of the feature has either positive correlation with (is in phase with) the change in stiffness, negative correlation (out of phase) with the change in stiffness or has no correlation with the change in stiffness.

For the experimental results a simple comparison is made of the sign of the feature's change and the sign of the stiffness change (i.e. fault). If the signs are the same, then the feature's change has a positive correlation with the fault and vice versa.

3. The magnitude in change of a feature expected for a percentage change in fault is an indication of how sensitive the features are to the fault. The sensitivity (s) is the ratio of the change in feature (in the features units) (Δf_i) to the magnitude of the fault (i.e. isolator stiffness Δk expressed as a percentage). This is illustrated in the following equation,

$$s = \frac{\Delta f_i}{|\Delta k|} \quad \textit{Eq. 36}$$

4.3.1 Numerical simulation

The full operating envelope (start, steady operation, and coast down) is simulated using the developed numerical model with the parameters relevant for the vibrating screen used for the experiments shown in Appendix I. "Faults" are introduced in the form of stiffness changes from -25% to +25% in increments of 5%. As with the experiments the numerical faults are first introduced to all the isolators simultaneously before only applying the fault to the F2R isolator. The simulated measurements are passed through the same signal processing algorithms as used to process the experimental measurements and to extract features. All simulations are compared to a baseline simulation where no faults were introduced.

Starting with the steady operation features, the average of the absolute percentage differences, percentage correlation and sensitivity ratio of each feature are shown in *Table 9*.

Table 9: Numerical simulation orbit feature results from steady operation

	Fault	Angles	Width	Length	
Avg|Δ%|	**All isolators**	0.49%	2.32%	0.96%	
	F2R isolator	0.42%	1.31%	0.45%	
% corr.	**All isolators**	99.99%	99.93%	99.99%	
	F2R isolator	-0.05%	0.00%	7.41%	
Δ feat./% fault	**All isolators**	16.62	0.47	7.18	$\times 10^{-3}$
	F2R isolator	14.12	0.27	3.36	$\times 10^{-3}$
	Units	°	mm	mm	per % fault

The same evaluations of the features from the starts and coast downs are shown in Table 10. For brevity only the results from the vertical (z) vibrations for the start and coast down envelops are reported. However, it was observed that similar results were obtained from the horizontal (x) vibrations from which the same conclusions can be drawn. An important consideration when comparing PSD features is that the peaks from two PSDs should be near one another if they are to be compared. This means that only peaks within similar frequency ranges should be compared to one another. This requires some sorting of the peak features to align them with all comparable peaks from other PSDs. If not done correctly the features have no meaning.

Table 10: Start and coast down PSD feature results from simulated Z responses

		SIMULATED VIBRATION MEASUREMENT					CALCULATED PITCHING MOTION					CALCULATED ROLLING MOTION					
	Fault	Freq.	Mag.	Width	RMS_{Peak}	RMS_{PSD}	Freq.	Mag.	Width	RMS_{Peak}	RMS_{PSD}	Freq.	Mag.	Width	RMS_{Peak}	RMS_{PSD}	
		FEATURE FROM VIBRATING SCREEN STARTS															
Avg|Δ%|	All	7.9%	24.2%	3.1%	14.3%	11.8%	7.8%	24.6%	6.6%	17.7%	16.5%	5.4%	20.2%	4.6%	11.2%	12.2%	
	F2R	2.9%	33.4%	10.2%	14.4%	10.6%	1.9%	21.2%	4.1%	9.8%	7.3%	3.8%	28898%	5.2%	1452%	1109%	
% corr.	All	99.3%	99.2%	45.1%	93.7%	100.0%	99.3%	99.4%	95.3%	96.9%	100.0%	24.6%	79.6%	21.8%	60.8%	100.0%	
	F2R	93.9%	-19.8%	35.1%	22.7%	0.7%	46.9%	-10.0%	10.9%	-14.1%	-95.6%	93.4%	-19.0%	61.7%	-8.7%	-11.2%	
Δ feat. /% fault	All	26.37	320.81	5.88	36.59	50.12	23.44	74.13	6.91	21.15	39.12	22.18	0.34	18.05	1.29	1.86	$\times 10^{-3}$
	F2R	10.18	324.79	18.18	33.45	38.61	5.13	51.23	7.86	17.80	16.50	11.72	697.01	2.11	102.76	164.08	$\times 10^{-3}$
	Units	Hz	mm^2/Hz	Hz	mm	mm	Hz	mm^2/Hz	Hz	mm	mm	Hz	mm^2/Hz	Hz	mm	mm	per % fault
		FEATURES FROM VIBRATING SCREEN COAST DOWNS															
Avg|Δ%|	All	5.4%	23.5%	3.4%	14.1%	13.0%	8.2%	13.5%	7.1%	5.7%	7.5%	8.5%	14.3%	0.9%	9.8%	5.6%	
	F2R	1.5%	18.5%	6.4%	9.1%	7.1%	2.5%	14.2%	18.9%	12.2%	6.6%	3.5%	15675%	7.1%	922.2%	838.8%	
% corr.	All	97.1%	99.5%	-20.4%	48.6%	99.0%	99.2%	100.0%	-95.3%	61.8%	99.9%	98.9%	100.0%	-51.0%	79.2%	100.0%	
	F2R	80.0%	-9.4%	12.9%	48.2%	5.4%	94.4%	-88.0%	38.3%	-42.6%	-97.4%	90.5%	-16.8%	48.7%	-5.8%	-10.1%	
Δ feat. /% fault	All	20.51	342.14	5.92	50.64	54.82	74.71	132.78	23.06	46.80	19.38	20.51	0.32	1.60	2.33	0.91	$\times 10^{-3}$
	F2R	6.02	222.90	15.29	27.79	29.24	41.02	96.37	52.92	61.14	15.93	11.72	446.46	4.47	81.08	135.18	$\times 10^{-3}$
	Units	Hz	mm^2/Hz	Hz	mm	mm	Hz	mm^2/Hz	Hz	mm	mm	Hz	mm^2/Hz	Hz	mm	mm	per % fault

Table 11: Start and coast down PSD feature results from ICP sensors Z response

	Cond.	Fault	ICP SENSOR VIBRATION MEASUREMENT					CALCULATED PITCHING MOTION					CALCULATED ROLLING MOTION					
			Freq.	Mag.	Width	RMS_{Peak}	RMS_{PSD}	Freq.	Mag.	Width	RMS_{Peak}	RMS_{PSD}	Freq.	Mag.	Width	RMS_{Peak}	RMS_{PSD}	
			FEATURE FROM VIBRATING SCREEN STARTS															
Avg|Δ%|	Cold	All	13.0%	57.7%	11.8%	28.3%	9.8%	15.1%	195.0%	7.7%	41.5%	43.3%	6.4%	66.2%	23.3%	27.4%	34.5%	
		F2R	5.3%	18.1%	5.2%	5.0%	3.5%	3.2%	75.4%	36.5%	61.2%	2.2%	8.2%	165.0%	18.8%	36.2%	45.1%	
	Hot	All	10.6%	37.5%	5.4%	16.2%	6.4%	11.6%	107.8%	15.5%	24.2%	13.3%	9.4%	56.1%	18.5%	36.3%	26.5%	
		F2R	3.8%	12.4%	5.6%	9.2%	3.4%	1.7%	45.4%	27.0%	44.0%	1.6%	4.2%	310.4%	18.5%	71.8%	79.3%	
% corr.	Cold	All	75.0%	43.8%	0.0%	9.4%	66.7%	83.3%	0.0%	16.7%	-8.3%	100.0%	72.9%	70.8%	-70.8%	25.0%	100.0%	
		F2R	59.6%	6.7%	-57.5%	10.8%	33.3%	33.3%	0.0%	-4.2%	-8.3%	-75.0%	-20.8%	-25.0%	4.2%	-25.0%	-12.5%	
	Hot	All	70.3%	17.7%	-2.1%	8.3%	50.0%	100.0%	-33.3%	-75.0%	-66.7%	75.0%	50.0%	33.3%	45.8%	62.5%	62.5%	
		F2R	62.5%	80.0%	-22.5%	75.0%	93.8%	20.4%	-26.7%	5.8%	-19.2%	-50.0%	-14.6%	12.5%	8.3%	4.2%	0.0%	
Δ feat. /% fault	Cold	All	45.40	218.09	54.95	27.51	34.91	38.02	78.39	8.68	9.09	50.40	36.87	2.57	24.70	1.38	6.27	$\times 10^{-3}$
		F2R	13.29	150.64	13.18	6.53	13.08	11.72	78.03	19.13	36.97	5.14	34.17	14.47	28.67	4.05	12.88	$\times 10^{-3}$
	Hot	All	27.10	242.27	22.21	16.29	25.88	31.02	81.86	20.21	9.40	28.10	31.43	4.34	13.87	4.65	7.31	$\times 10^{-3}$
		F2R	7.14	236.74	14.69	11.46	13.45	5.43	95.71	17.82	35.85	3.32	17.33	38.69	12.02	8.94	21.73	$\times 10^{-3}$
		Units	Hz	mm^2/Hz	Hz	mm	mm	Hz	mm^2/Hz	Hz	mm	mm	Hz	mm^2/Hz	Hz	mm	mm	per % fault
			FEATURES FROM VIBRATING SCREEN COAST DOWNS															
Avg|Δ%|	Cold	All	10.7%	20.2%	58.5%	31.8%	6.8%	11.5%	143.5%	12.8%	56.8%	30.1%	5.4%	24.8%	14.8%	15.0%	27.3%	
		F2R	4.9%	18.6%	44.1%	14.0%	4.5%	6.5%	110.2%	19.4%	40.4%	10.8%	4.5%	65.4%	12.4%	33.4%	13.0%	
	Hot	All	9.8%	18.4%	16.5%	11.2%	4.7%	1.3%	60.3%	12.9%	21.6%	7.3%	5.8%	97.7%	19.2%	28.3%	15.6%	
		F2R	4.9%	25.5%	25.6%	11.5%	8.6%	2.9%	34.6%	12.7%	17.9%	2.3%	8.4%	161.8%	23.1%	32.9%	26.2%	
% corr.	Cold	All	80.5%	36.9%	-23.9%	17.6%	100.0%	40.6%	100.0%	31.3%	100.0%	100.0%	75.0%	-25.0%	0.0%	-37.5%	0.0%	
		F2R	71.9%	59.4%	-29.2%	12.5%	75.0%	-18.8%	50.0%	-18.8%	0.0%	100.0%	34.4%	-50.0%	81.3%	-25.0%	-50.0%	
	Hot	All	72.7%	16.8%	26.7%	14.2%	68.8%	-6.3%	50.0%	-18.8%	31.3%	50.0%	-3.1%	-50.0%	93.8%	-25.0%	-75.0%	
		F2R	29.7%	43.8%	-30.2%	37.5%	68.8%	-18.8%	12.5%	-25.0%	0.0%	-50.0%	-43.8%	-50.0%	87.5%	-12.5%	0.0%	
Δ feat. /% fault	Cold	All	34.62	34.64	75.59	31.18	15.89	25.46	72.74	18.25	21.76	43.09	18.05	31.14	11.58	12.78	41.21	$\times 10^{-3}$
		F2R	18.13	36.86	38.56	13.65	9.29	20.28	120.30	21.15	21.43	17.71	8.17	109.28	7.97	18.73	19.05	$\times 10^{-3}$
	Hot	All	27.35	36.21	16.45	9.96	9.32	6.98	10.79	18.65	4.16	9.73	9.48	104.16	13.90	13.15	21.04	$\times 10^{-3}$
		F2R	16.50	55.31	20.01	10.02	17.86	20.81	1.43	18.24	6.42	2.97	14.77	237.73	13.37	19.93	35.79	$\times 10^{-3}$
		Units	Hz	mm^2/Hz	Hz	mm	mm	Hz	mm^2/Hz	Hz	mm	mm	Hz	mm^2/Hz	Hz	mm	mm	per % fault

Table 12: Steady operation orbit feature results from ICP sensors

	Cond.	Fault	Angles	Width	Length	
Avg|Δ%|	Cold	All isolators	0.5%	4.5%	1.0%	
		F2R isolator	0.9%	4.0%	0.8%	
	Hot	All isolators	0.5%	1.7%	0.5%	
		F2R isolator	1.1%	2.4%	0.7%	
% corr.	Cold	All isolators	-12.5%	25.0%	100.0%	
		F2R isolator	0.0%	68.8%	25.0%	
	Hot	All isolators	-50.0%	18.8%	50.0%	
		F2R isolator	-25.0%	43.8%	0.0%	
Δ feat./% fault	Cold	All isolators	21.23	0.70	9.12	$\times 10^{-3}$
		F2R isolator	35.21	0.56	5.97	$\times 10^{-3}$
	Hot	All isolators	19.11	0.44	3.17	$\times 10^{-3}$
		F2R isolator	30.95	0.62	4.00	$\times 10^{-3}$
		Units	°	mm	mm	per % fault

4.3.2 Experimental results

As described in Section 3.6 each configuration was tested 5 times for each condition (cold/hot). Rather than comparing each test from each configuration to one another, the minimum, mean, median and maximum feature values for each set of 5 tests from a configuration are computed. These values are then compared to corresponding values from other related configurations. The average absolute percentage differences, correlation percentage and feature sensitivities are computed from the differences in minimum, mean, median and maximum values. An example of this process is shown in Figure 115 in Appendix O. All computed values are grouped into the respective bins where an average is taken. The results are shown in Table 12, for the steady operation orbit features and Table 11 for the start and coast down envelope features. For start and coast down envelopes only features computed form the z-direction are considered. Also, the PSD features were sorted based on their respective frequency bands so that a like for like comparison is made.

A comparison between the respective test conditions (cold vs hot) is shown in Table 13, Table 14 and Table 15. The absolute percentage difference is shown as it provides a measure of the impact of the test condition on the features. This is sufficient to indicate the influence of the test condition on the features extracted.

4.3.3 Results interpretation

As mentioned, there are three criteria used to evaluate the features. Below is a description of how each criterion is computed as well as how it is interpreted:

1. The average of the absolute percentage difference (Avg|Δ%|).
   a. Computed by grouping the percentage differences for each feature into bins shown in Figure 80. Thereafter the absolute value of the percentage difference is taken, and the average of each group is computed. The simple interpretation of this result is the higher the value the more suitable the feature is for fault detection.
   b. Taking the average is not entirely representative of how each feature changes. However, an average value allows for a "general" comparison. Where practical (i.e., where there are 4 features or more in a bin) a box and whisker plot is taken which indicates the minimum, interquartile range, mean, median and maximum values of each bin. This provides more statistical insight into the interpretation of this result by illustrating the spread of the data.
2. The correlation percentage between the change in the features and the introduced fault.

a. For the simulated results the correlation percentage is a normalized cross correlation between the change in the feature and the change in the isolator stiffness. For the experimental results a simple check is done to see if the sign of the feature's percentage change has the same or opposite sign to that of the estimated stiffness change. The sign of the minimum, mean, median and maximum values of each features change are considered. A positive correlation is assigned the value of '1' and a negative correlation a value of '-1'. The values are all sorted into their respective bins and the average is calculated.
b. From observation, the following descriptions can be used to interpret the correlation percentage:
    - 0% to ± 30% indicates that there is no correlation between the feature and the developing fault.
    - ± 30% to ± 70% indicates that there is a partial positive or negative correlation (depending on the sign) between the feature and the developing fault.
    - ± 70% to ±100% indicates that there is a positive or negative correlation (depending on the sign) between the feature and the developing fault.

    The correlation percentage is an indication of how the feature changes with a change in isolator stiffness as opposed to the other criteria which only consider how each feature's magnitude changes. A positive 100% indicates the feature changes correlate positively with the isolator stiffness changes, and a negative 100% indicates the feature correlates negatively (i.e., if the isolator stiffness decreases, the features change will do the opposite). Approaching a 0% correlation, the feature's change does not correlate with or is uncorrelated with the fault.

3. The sensitivity of a feature is the ratio of the feature's change to the percentage fault, which is a change in stiffness, ($\Delta feat./\%fault$).
    a. Calculated by taking the differences of features between related configurations and dividing the difference by the percentage change in stiffness of the isolators. The absolute values are taken so as too only look at the magnitude of the change, similar to the absolute percentage difference.
    b. The assumption of this metric is that the feature changes linearly with the isolator stiffness. Under this assumption the metric gives an estimate of what the expected change would be if the stiffness were to increase or decrease. The higher the sensitivity value the more suitable the feature is for fault detection.

4.4 Operational results Discussion

First the simulation results are considered, there after the experimental results. Also, discussions on the statistical spread of the results, how the test condition influences the results and how the different sensors and data acquisition systems compared is presented.

4.4.1 Numerical simulation

The simulation results should be a good predictor of what to expect from the experimental results. From the steady orbit features the orbit width undergoes the higher percentage change and the orbit angle undergoes the largest change (in its units) for a given stiffness change (i.e., is the most sensitive). When all the isolators change in stiffness all the orbit features change with a positive correlation to the stiffness change. However, when only one isolator's stiffness is changed, the orbit features have no correlation with the faults. An important observation is that the steady orbit features change considerably less than most PSD features from the start and coast down envelopes. This is true of the percentage difference and the feature sensitivities.

Considering the start and coast down envelope features from the numerical simulation the features that undergo the largest changes are the magnitudes of the peaks in the PSDs. This is the case for the vibration measurements as well as the computed rigid body motions. The RMS of the peaks as well as the PSD RMS change considerably more than the peak frequency and width. The rolling rigid body motion shows a significant percentage change in PSD peak magnitude, RMS and PSD RMS when only the F2R isolator is changed. This can be attributed to the imbalance in stiffness introduced, but it is important to consider that the pitching motion is significantly less influenced by the imbalance compared to the rolling motion.

When all the isolators change, the majority of features from the start up and coast down envelopes have a positive correlation with the fault introduced. The PSD peak width features are either not correlated, partially positively or negatively correlated, or are negatively correlated with the fault. The peak width is an indicator of the shape of the PSD. If the peak width decreases while the peak magnitude increases this indicates that the peak is more prominent. If the peak width increased with the peak magnitude, this is indicative of the PSD RMS (i.e. the overall energy) increasing proportionally with the peak, so the peak's prominence changes less or reduces.

When only the F2R isolator changes, most features do not correlate with the fault. Only the peak frequency changes have a positive correlation with the fault. This is consistent with the EMA results which also show a positive correlation between the change in natural frequency and the change in isolator stiffness. From the coast down envelope the pitching motion's peak magnitude, RMS as well as PSD RMS have a negative correlation with the fault. This implies that when the fault increases, the pitching motion decreases. In contrast with the rolling motion's peak magnitude, RMS and PSD RMS which are uncorrelated with the fault. Closer inspection reveals that the rolling motion's peak magnitude, RMS and PSD RMS only increase irrespective of a positive or negative changes in stiffness.

Finally, considering the feature sensitivities, when all isolators are changed the peak magnitudes show the highest sensitivity to change except for the peak magnitudes derived from the rolling motion. Even though its percentage change is comparable to the pitching motion RMS of the PSD (which is the area of the PSD) is considerably smaller for the rolling motion than for the pitch motion. However, when only one isolator is changed, the rolling motions peak magnitude is more than twice as sensitive to change than that of the vibration measurement and pitch motion.

4.4.2 Experimental measurements

Considering the steady operation orbit features, similarly to that of the numerical simulation, the orbit width undergoes the largest percentage change whereas the orbit angle is the most sensitive to the change with a higher change in its units for a given fault. This is true for both hot and cold conditions as well as both fault types. When all isolators are changed only the change in orbit length has a positive correlation with the fault whereas the change in orbit width and angle are uncorrelated. This is true only in the cold condition. In the hot condition the changes in orbit length and angle are partially positively and negatively correlated respectively. When only one isolator is changed the change in orbit width correlates partially with the fault, but the change in orbit length and angle are uncorrelated with the fault.

Considering the start and coast down envelope features, the results are not as conclusive as the simulated results, with differing results for the start and coast down envelopes. This is not the case for the simulated results where the start and coast down envelopes gave very similar results. Therefore, first considering the start envelope, whose results are comparable to those from the simulation. The feature undergoing the highest percentage change is the peak magnitudes. This is true for the vibration measurements as well as the derived pitch and roll motions. The rolling motion's

peak magnitudes change considerably more when only one isolator is changed as opposed to when all the isolators change. This is in contrast with the vibration measurement's and pitching motion's peak magnitudes whose percentage change becomes less when only one isolator is changed. When all isolators are changed, the pitch motion's peak magnitudes undergo the highest percentage change which decreases considerably from cold to hot conditions.

When all isolators are changed, the change of most features either correlate positively or partially correlate with the fault. This is clearly the case for the peak frequency and PSD RMS in both cold and hot conditions. In the hot condition the peak magnitude, width and RMS for the pitch motion have a negative correlation with the faults but have a partially positive correlation for the rolling motion. Important to note, there is a significant correlation percentage discrepancy between cold and hot conditions. When only the F2R isolator changes the peak magnitudes, RMS and PSD RMS from the vibration measurements are positively correlated with the fault, but only in the hot condition. The peak frequencies from the vibration measurements are only partially positively corelated with the fault. All other correlation percentages change considerably between hot and cold conditions or are uncorrelated.

The sensitivity of the features for the start envelope shows the peak magnitudes for the vibration measurement and pitch motion to be the most sensitive. For the rolling motion, the change in peak frequency is the most sensitive except for when the F2R isolator is changed, and the test condition is hot. Then the rolling motions peak magnitude is considerably more sensitive to faults. The peak magnitudes from vibration measurements have the highest sensitivity to change for all conditions and faults. This is linked to the fact that the PSDs from the vibration measurements have the highest RMS (i.e., overall energy). The PSDs of the rolling motion have the lowest RMS which is the same for those from the simulated results. It is important to note that there is a correlation between the rolling motion's peak magnitudes from the experimental and simulated results, however the percentage changes and sensitivities from the experiments are nowhere near what is predicted by the numerical simulation. This is the case for both the start and coast down envelopes.

Now, considering the coast down envelope, the first observation is the large percentage change of the peak widths from the vibration measurements. This is most prevalent for the cold condition results and when all isolators are changed. As mentioned before, the peak width is an indicator of the peak shape. If the width changes considerably it implies the shape of the peak changes. Also, the percentage correlation of the peak widths are mostly uncorrelated with the fault. From the rigid body motions, the peak magnitudes have the largest percentage change. In the cold condition the pitch motion's peak magnitude undergoes the highest percentage change. Whereas, in the hot condition the rolling motion's peak magnitude undergo the highest percentage change. The rolling motions peak magnitude's percentage change is higher when only one isolator is changed, and the opposite is true for the pitch motion.

When all the isolators are changed, most of the features correlate either positively or partially with the fault. The features that have the highest positive correlation with the faults are the peak frequencies and PSD RMSs from the vibration measurements. Feature changes tend to be more negatively correlated for hot test conditions than for cold. Irrespective of the fault type, the feature changes from the rolling rigid body motion are more negatively than positively correlated with the faults whereas most features from the vibration measurements and pitching motion have positive correlation with the faults. When only one isolator is changed there are a similar number of positively and negatively correlated features, but the correlation percentages differ considerably between cold and hot conditions.

From the sensitivity of each feature in the coast down envelope, the peak magnitudes and widths are the most sensitive. However, their sensitivity is influenced by the test condition as well as the type of isolator. It was observed that the for the coil spring configurations the peak magnitudes were the most sensitive, and for the Resatec configurations the peak widths were more sensitive. From the vibration measurements the sensitivity of the peak widths reduces considerably from cold to hot conditions and for the pitch motion the sensitivity of the peak magnitudes also decreases from cold to hot. The sensitivity of the rolling motions peak magnitudes increased considerably from cold to hot conditions and the peak magnitudes are more than twice as sensitive when only one isolator is changed as opposed to all the isolators.

The changes of frequencies from the EMA and operational experiments are similar. This is clear by considering the absolute percentage change for the PSD peak frequencies which shows values up to 15% and 8% when all isolators or only one isolator is changed respectively. These values are comparable to the natural frequency changes shown for the EMA results in Table 8 of approximately 17% and 5% when all isolators or only one isolator is changed respectively. Also, the actual frequency values obtained from the EMA and operational experiments are comparable to one another.

4.5 STATISTICAL SPREAD OF THE FEATURE CHANGES

As mentioned, because the results presented thus far are highly averaged, a clear picture is not shown of how each feature changes. Box and whisker plots are a simple method of visualizing the spread of data by plotting the minimum, mean, median and maximum values. The first and third quartiles are also indicated and are used to calculate any outliers. Box and whisker plots of the absolute percentage change of start envelope features from vibration measurements for the simulated and experimental results can be seen in Figure 81 and Figure 82 respectively.

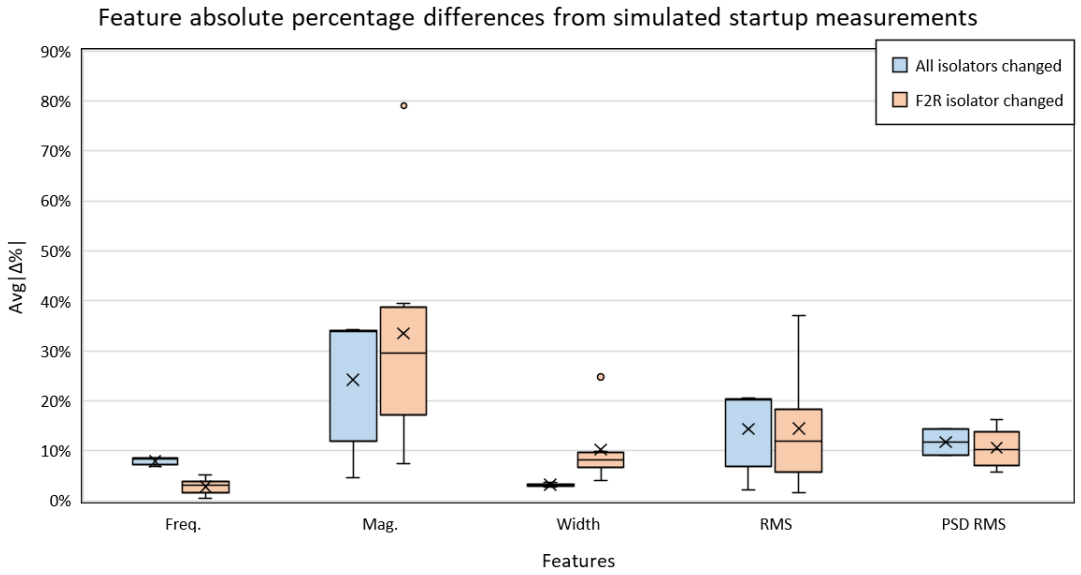

Figure 81: Box and whisker plot for features from simulated startup measurements

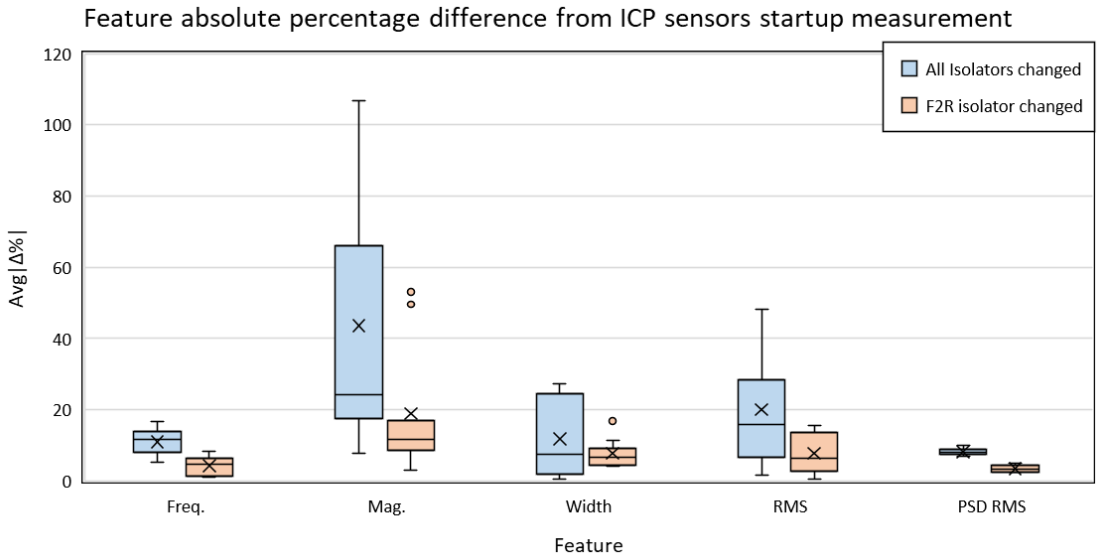

Figure 82: Box and whisker plot for features from ICP sensor startup measurements

Note that only features from the vibration measurements are considered as they have enough data per feature to represent statistically. The rigid body motion features often only had features from two peaks. Also, box and whisker plots of the absolute percentage change of coast down envelope features from vibration measurements for the simulated and experimental results can be seen in Figure 83 and Figure 84 respectively.

The plots reveal the largest spread for the PSD peak magnitude and RMS. From the experimental results the peak frequencies and PSD RMS have significantly less statistical spread than the simulated results, but their magnitudes are comparable, particularly for the startup features. The largest discrepancy between the experimental and simulated results are those for the peak widths which indicates a difference in the peak shapes in the PSDs. From the simulate results the peak widths appear not to change as much as the experimental results.

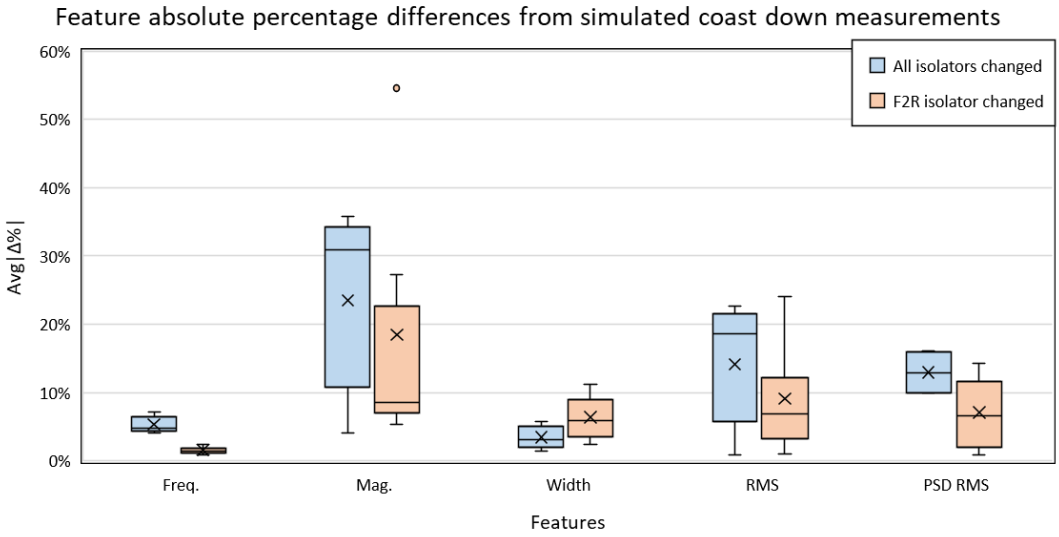

Figure 83: Box and whisker plot for features from simulated coast down measurements

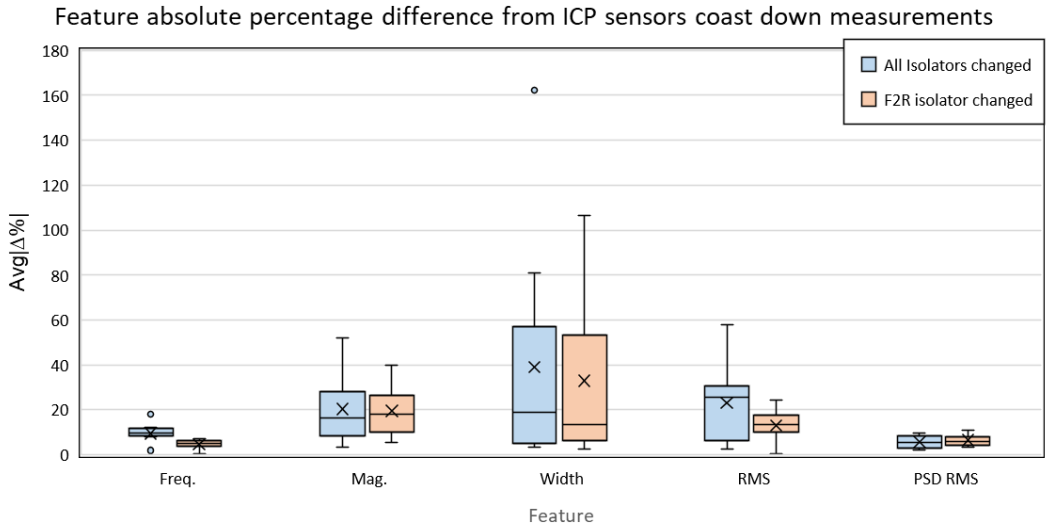

Figure 84: Box and whisker plot for features from ICP sensor coast down measurements

The plots indicate the minimum (bottom line), mean (X marker), median (middle horizontal line in box), maximum values (top line) as well as outliers (points/dots). Interestingly, most outliers came from measurements at isolator positions F1L and F1R. No outliers are traced back to the F2R isolator position, not even when only this isolator was changed. This is true for both the experimental and simulated results. Position of the median and mean values are an indication of how skewed the data is. The peak features describing its shape (i.e., magnitude, width and RMS) have the highest spread and skewness. The reason for this is that there is often a handful of peaks at one or two isolator positions which undergo significant change, whereas all the other peaks undergo changes which are considerably smaller. From the spread of the experimental results, the most reliable features are the peak frequencies and PSD RMS as their changes are least spread out making their change less dependent on the sensor location. However, their magnitude of change is significantly less than the other features. The highest magnitude of change and sensitivity is seen with the peak magnitudes. However, the magnitude of the percentage change and sensitivity are dependent on the sensor location.

4.5.1 Effect of test condition

From the EMA results it was seen that the test condition had a significant effect on the natural frequencies for the Resatecs and rubber buffers. Its effect was negligible for the coil spring configurations. However, this was not the case with the results from the experimental operational measurements where all the results were influenced by the test condition. As mentioned in the preliminary results section, during the hot condition tests, the coast down times were considerably higher than during the cold condition tests. This had less to do with the isolator temperature and more to do with the temperature of the motors. This was most clearly shown during the coil spring configurations where the coil springs temperature remained constant but the coast down times increased. Because of the coupling between the vibrating screen dynamics and the motor temperature the features are not expected to remain constant for hot and cold conditions.

The influence of the test condition on the percentage change of orbit features can be seen in Table 13. Although the influence is small in magnitude (less than 2%), the average percentage change of the orbit features was 4.5% between configurations. The most noticeable changes are seen in the startup and coast down features as shown in Table 14 and Table 15 respectively. The percentage change of these features is significant, and they occurred irrespective of the type of isolator being used. Upon closer examination it was revealed that the rubber buffer configuration underwent the highest

percentage change of PSD features with changes in test conditions. However, changes in PSD features from the derived rigid body motions were comparable between isolator configurations and in some cases the coils spring configurations indicated the largest percentage change.

Clearly the startup and coast down of the vibrating screen is significantly influenced by the test conditions. An explanation for this is that when the vibrating screen starts up and coasts down it passes through its rigid body modes. The development of the motion of each mode is influenced by the amount of energy introduced at that mode. The energy introduced to each mode is proportional to the amount of time spent at each mode. Therefore, a longer start up or coast down will result in more energy transferred to each mode and vice versa. This is clearly captured in the PSD features.

Table 13: Percentage difference from cold to hot condition of orbit features

	Fault	**Angles**	**Width**	**Length**
Avg|Δ%|	**Cold to Hot**	0.1%	1.7%	0.4%

Table 14: Percentage difference from cold to hot condition of startup PSD features

	Fault	**Freq.**	**Mag.**	**Width**	**RMS$_{Peak}$**	**RMS$_{PSD}$**
Avg|Δ%|	**From ICP sensor vibration measurements**					
	Cold to Hot	4.4%	15.8%	17.8%	14.0%	3.1%
	From calculated pitching motion					
	Cold to Hot	4.1%	42.8%	11.6%	21.2%	10.6%
	From calculated rolling motion					
	Cold to Hot	8.4%	81.3%	16.6%	24.2%	18.0%

Table 15: Percentage difference from cold to hot condition of coast down PSD features

	Fault	**Freq.**	**Mag.**	**Width**	**RMS$_{Peak}$**	**RMS$_{PSD}$**
Avg|Δ%|	**From ICP sensor vibration measurements**					
	Cold to Hot	4.0%	25.0%	13.8%	12.9%	4.8%
	From calculated pitching motion					
	Cold to Hot	5.5%	70.6%	6.8%	21.9%	10.4%
	From calculated rolling motion					
	Cold to Hot	2.9%	77.3%	6.4%	26.3%	19.8%

4.5.2 Sensor and DAQ comparisons

A qualitative comparison is made between the different sensors and data acquisition systems used. It was observed during the signal processing and reviewing of the results that similar conclusions could be drawn irrespective of the sensor selected. However, only the ICP sensor data is presented in this section. The experimental results from the Dysinet and IFM sensors are shown in Appendix J and Appendix K. Unfortunately, during the operational measurements, the measured ICP sensor responses during configurations 4 and 5 (i.e., before a 'mechanical' filter was introduced) showed signs of saturation during some starts and coast downs. This inevitably resulted in the deletion of important features which would have skewed the results considerably. Unfortunately, their deletion has also skewed the results slightly which is clearly seen when comparing the shutdown results from each respective sensor. The Dysinet and IFM sensors gave the same results whereas the ICP sensor data differed significantly particularly with the sensitivity values.

There are some practical advantages and disadvantage for using a specific sensor. Table 16 describes the major advantages and disadvantages of each sensor. Each of the three sensors were mounted differently using either bolted clamps, magnets, or super glue. From the results it was clear that the mounting method had negligible effect. Therefore, any mounting method would be suitable, only the

magnetic or bolted methods are preferred as the ICP sensors fastened with super glue tended to come loose during long term use.

Table 16: Practical considerations for sensor selection

Sensor	ICP	Dysinet	IFM
Advantages	Is a calibrated sensor which is easy to integrate into most existing data acquisition architectures.	Considerably cheaper than the other two sensors and can be purchased as a single, bi or triaxial sensor. Able to measure DC acceleration. Very small, compact sensor.	With a current output this sensor is less susceptible to electrical interference and signal loss due to the length of the wire. Small, easy to mount and robust.
Disadvantages	Sensor saturation due to high frequency impulsive structural behaviour can occur during startups and coast downs with coil spring isolators. The sensor is large and requires even more space when a cable is attached.	Being a DC sensor requires each sensing directions reasonably accurate calibration and zeroing for its orientation. If not done correctly, the results are not useful.	The sensor architecture is designed for an IFM diagnostic module and requires some additional work to integrate into other data acquisition architectures.

Considering the data acquisition systems, the HBM Quantum X DAQs are best suited for laboratory tests. These are robust and highly versatile DAUs able to measure a large variety of sensors from numerous suppliers. The IFM diagnostic module is made to interface with IFM sensors only. It is not designed for custom testing. It is flashed with IFM proprietary firmware which allows for some customization of sampling duration and other parameters. A limitation of the IFM diagnostic modules was found during the signal processing of the IFM sensor measurements. The following two anomalies were identified:

1. The sampling rate of 100kHz is not precise. The actual sampling rate is closer to 99 974Hz.
2. After approximately 30 seconds of recording an anomaly in the time signal occurs whereby the time signal is warped such that the frequency and amplitude of the signal being measured changes significantly for less than a second.

Both anomalies were considered in the signal processing as their effect on the result is far from negligible. More details regarding these anomalies and how they present themselves are given in Appendix M. The IFM DAQ used is responsible for this behaviour. The anomalies only occurred on the measured IFM sensor responses. Also, the anomalies occur at the same times for all measurements on all IFM sensors including the inductive sensors for motor speed pickup. The predictability of the anomalies made it easier to correct, remove or avoid during signal processing. The reason for these anomalies is most likely related to the hardware and firmware of the VSE modules. There were no issues observed during the use of the HBM Quantum X DAQs.

4.6 CONCLUSION

From the EMA result the following conclusions are made,

- The test condition had significant influence on the natural frequencies for the Resatec and rubber buffer configurations. The implications of the test condition having a major influence on the calculated changes in natural frequency is that the condition (i.e. temperature) of the isolators is another independent variable which should be considered for future condition monitoring projects.
- When all isolators are changed the change in natural frequency of the RBMs is significant at $\pm$17%. And the changes in natural frequency correlate positively with the changes in stiffness introduced.
- When only one isolator is changed, the natural frequencies changed considerably less with a maximum magnitude of 5% from the configurations with coil springs. The configurations with Resatecs showed very small changes of less than $\pm$2%.

Considering both the simulated and experimental operating measurements the following conclusions are made:

- The orbit features that undergo the largest percentage change and are the most sensitive are the orbit width and angle respectively.
- The largest discrepancy between the simulated and experimental orbit features occurs in the correlation percentages whereas the magnitude of the percentage change and the feature sensitivities are comparable. However, the experimental results show higher changes and sensitivities.
- The orbit features undergo a significantly smaller percentage change and are considerably less sensitive than most of the PSD features from the start and coast down envelopes.
- From the startups the features that undergo the largest percentage change are the magnitudes of the peaks in the PSDs from the vibration measurements and the calculated rigid body motions.
- From the startup and coast downs the calculated rolling rigid body motion's PSD peaks change considerably more in magnitude when only one isolator is changed as opposed to when all the isolators are changed. This is not the case for PSD peak magnitudes from vibration measurements and pitching motions.
- From the startup and coast downs the peak magnitudes from the pitching motion were less when only one isolator was changed as opposed to when all the isolators are changed.
- When all isolators are changed, the majority of features correlated positively with the faults. Whereas when only one isolator is changed, most features indicate a similar number of positively and negatively correlated features. For the experiments the correlation percentages changed considerably between test conditions.
- The peak frequencies from the vibration measurements indicated a positive correlation with the fault which is consistent with the results from the EMA.
- For the start envelope the sensitivity of the features shows that the peak magnitudes for the vibration measurement and pitch motion to be the most sensitive irrespective of the type of fault or test condition. However, for the rolling motion, the change in peak frequency is the most sensitive except for when the F2R isolator is changed in the hot test condition where the peak magnitude is the most sensitive.
- The sensitivity of the rolling motions peak magnitudes is significantly more sensitive when one isolator is changed as opposed to when all isolators are changed.

Generally, it was observed that the simulation results correlated the best with the experimental results in the hot condition. This was true of all percentage differences and sensitivities. However, for the correlation percentage the results from the simulation compared the best with the cold condition experimental results. The percentage changes obtained from the experiments are considerably higher than those obtained from the numerical simulations. The only exception is the rolling motion, which underwent a significant percentage change when only one isolator was changed, but the simulations significantly overestimated the changes.

From the results it was clear that when the stiffnesses of all the isolators changes simultaneously the feature that experiences the highest percentage change is the PSD peak magnitude from the pitching motion. And when the stiffness of only one isolator changes the feature that experienced the highest percentage change is the PSD peak magnitude from the rolling motion. Also, the largest discrepancy between the simulated and experimental orbit features occurs in the correlation percentages whereas the magnitude of the percentage change and the feature sensitivities are comparable.

The test condition is a critically important consideration when monitoring how the features change. This was clear for most features from experimental results where large discrepancies are observed between feature difference in the cold condition compared to the hot condition. Not monitoring or controlling the test condition can lead to erroneously interpreted feature changes. Practically, for a vibrating screen the monitoring of startup features may occur primarily in the cold condition whereas the monitoring of coast down features may occur primarily in the hot condition.

Most features identified changed significantly enough to be measurable. Also, the feature changes showed some correlation with the fault making them predictable. It was shown that the features extracted can be used generically irrespective of the type of isolator used. Although it was noticed that sensitivity values of some features were more influenced by the isolator installed, a change can still be expected when a fault is introduced. The statistical spread of the change of each feature indicated that some features change with similar magnitudes irrespective of the sensing positions. However, other features, which undergo the highest percentage change, are shown to be the most dependent on the sensor locations.

Regarding the sensors used, each sensor type used has some practical considerations and trade-offs. The ICP sensors are the most common type of sensor used in this application, however the other sensor types proved as useful for this application. Although the ICP sensors did saturate, this does not limit their application as a simple mechanical filter may be utilized to mitigate this phenomenon. An application of ICP sensors involves impact or shock testing, so there may also be scope for ICP sensors to evaluate how the impulse responses from coil spring isolators can be used to assess their condition. This will require a sensor with a suitable range to be selected.

Lastly, the use of wooden blocks as mechanical filters was successful in mitigating the ICP sensor saturation for test configuration 7. Unfortunately, the mechanical filters were not present during the configuration 4 and 5 tests which made some of the sensor measurements non-useful. The mechanical filters were shown to have negligible effect on the dynamic results which is seen in the results presented in Appendix L.

5 CONCLUSION AND RECOMMENDATIONS

5.1 CONCLUSION

In this study the behaviour of identified features and how they change is evaluated for changes in isolator condition. This is done using a model-based approach and experimental results for validation. The deterioration of an isolator's condition is presumed to present itself as a stiffness change. First, an MBD numerical model is developed and validated for the entire operating envelope of a vibrating screen. The model is then used to perform a sensitivity analysis of the identified features. The results from simulation are finally compared to results obtained by experiment. During the experiment the entire operating envelope is measured for different isolator types and configurations. Also, EMA measurements are performed to evaluated changes in modal parameters. Signal processing techniques are used to extract the same features from the simulated and experimental operating measurements.

For the evaluation of features there are three distinct techniques or classifications of feature extraction methods proposed in this study. The first is the extraction of natural frequency, damping and mode shapes from EMA measurements by modal parameter extraction. The second considers the stationary orbit length, width and angle which are extracted from the steady operating vibration measurements in the X and Z directions. It is known that during startup and coast down a vibrating screen's rigid body modes are excited. Using vibration measurements, the rigid body motion of each mode can be calculated by taking the difference between relevant measurements. Finally, the shape of a PSD obtained from transient startup, coast down measurements and calculated rigid body motions is described by the peaks and their respective magnitude, width, area (RMS) and location on the frequency axis. All the features mentioned above are considered in this study.

Based on the development and validation of the numerical model it is concluded that both the linear and non-linear (referring to large or small angle approximation) models represent the dynamics of a real vibrating screen. Both models gave answers which are comparable to experimental results with negligible differences between the two models. Therefore, the argument that a non-linear angle must be considered for vibrating screen models, particularly for the transient startup and coast down envelopes, is not compelling and small angle approximations are suitable. Discrepancies in magnitudes between the models and experiments were observed, however this does not obviate the model's usefulness. The most important consideration is that the model can simulate responses with reasonable accuracy and that the responses predicted are as interpretable as real measurements.

From preliminary experimental results presented it can be concluded that the isolator type and test conditions affect the transient envelopes considerably. This is most evident in the coast down times observed. The tests with coil springs had coast down durations of more than twice of those observed when other isolators were installed. This implies a strong coupling between the exciter dynamics and the isolator type. Also, the coast down times during the hot condition were noticeably longer in duration than during the cold condition. This occurred irrespective of the isolator type installed. Therefore, the temperature of the exciters is the primary contributor to this phenomenon.

Considering the modal parameters, and in particular the natural frequencies obtained from EMA measurements, it can be concluded that a change in natural frequency of RBMs can be expected when the stiffness of the isolators changes. For stiffness changes of approximately 10% to 20% some natural frequencies changed by up to 17%. This conclusion is reiterated in the results from the operating envelope features which include how the frequencies of peaks from a PSD of the transient

measurement change. The changes in natural frequency also correlate positively with the stiffness changes, meaning that if the stiffness increased, the natural frequency would also increase and vice versa.

Finally, considering the features extracted from both the simulated and experimental operating measurements it can be concluded that the features which undergo the highest percentage change, behave in a predictable manner and are the most sensitive to changes in isolator stiffness are the features extracted from the transient startup and coast down PSDs. The features describing the shape of the PSD (i.e., the peak magnitude, width and RMS) were significantly more sensitive than other features. The PSD feature that consistently experienced large percentage changes with reasonable predictability in its behaviour is the peak magnitude. However, it was noticed that the PSD shape features are sensitive to the location of the sensors whereas the peak frequency and resultant PSD RMS show consistent changes irrespective of the sensor position.

The stationary orbit features are substantially less sensitive than the majority of transient PSD features which is clear from the experimental results where the maximum average percentage change experienced by an orbit feature is 4.5% (for the orbit width) and by a PSD feature is 310% (for the PSD peak magnitude from the rolling motion). This does not imply that the orbit feature is not useful, but it can be concluded that features from the entire operating envelope of a vibrating screen should be considered for isolator condition monitoring.

The test condition is an important consideration when monitoring how features change. This was clear for most features from experimental results where large discrepancies are observed between feature difference in the cold condition compared to the hot condition. Not monitoring or controlling the test condition can lead to erroneously interpreted feature changes. The practical implication of the influence of the test condition is that for a vibrating screen the monitoring of startup features may occur primarily in the cold condition whereas the monitoring of coast down features may occur primarily in the hot condition. This can and should be managed accordingly.

Considering the discrepancies between simulated and experimental results, generally, it was observed that the simulation results compared the best with the experimental results in the hot condition. This was true of all percentage differences and sensitivities. However, for the correlation percentage the results from the simulation compared the best with the cold condition experimental results. Also, the average percentage changes obtained from the experiments are considerably higher than those obtained from the numerical simulations. The only exception is the rolling motion, which underwent a significant percentage change when only one isolator was changed, but the simulations significantly overestimated the changes.

As an added evaluation, the qualitative assessment of different vibration sensors showed that a cheaper MEMS sensor captures the same dynamic changes in the vibration signature of a vibrating screen when isolator conditions deteriorate. Other sensor technology such as the common ICP accelerometer and high-end MEMS accelerometers gave comparable results however there are practical considerations such as sensor saturation, size, durability and ease of use which require cognisance when performing a sensor selection. The conclusions made during this study would remain the same irrespective of the sensor data selected to present which is an indicator of how well the sensors compared to one another.

5.2 RECOMMENDATION

The following recommendations should be considered for future work in the modelling of vibrating screens in an MBD form, as well as studying the features relating to the condition of the isolators:

- A significant amount of data with many dimensions was captured during the experiments. Besides the actual fault introduced, some other dimensions which prove important are the sensor locations, the isolator type as well as the tests conditions (i.e. isolator and motor temperatures). It is proposed that the data be classified using an appropriate classification (machine learning) algorithm such as SVM. This is the obvious next step from this study as the results shown are indicative of the most promising features.
- The development of the numerical model as well as the planning of the experiments neglected other faults and conditions typical for a vibrating screen. It is proposed that the MBD numerical model be integrated with a DEM model (similar to that of M. M. Moncada and C. G. Rodriguez [39]) where the influence of the material on the deck of a vibrating screen can also be considered. Similarly, the experiments should be repeated with the inclusion of static weight or moving mass on the decks to simulate material buildup and on the deck and compare the results to the numerical model.
- The developed MBD numerical model is a simple linear, low-cost model which was able to predict trends in dynamic features when faults are introduced with relative reliability. It is proposed that two forms of non-linearities be introduced to the model in order to improve its correlation with real life results. The first is the inclusion of non-linear self-synchronization exciter models which are coupled to the modes of the vibrating screen. This is useful to simulate unbalanced motors which rely on the kinematics of the vibrating screen to synchronize their motion. Secondly, the exciter model should consider variations with operating temperatures which has been shown to considerably influence the dynamics of a vibrating screen.
- From the features extracted, some of the most sensitive features were derived from the computed rigid body motions. There exist sensors able to directly measure motions such as the pitch and roll angles. Therefore, it is recommended that other sensor technology should be explored, such as inertial measurement units, which are capable of measuring both the vibrations and changes in angle associated with rigid body motion. This may prove beneficial in reducing the number of sensors required while retaining valuable features for condition monitoring purposes.
- Lastly it is recommended that further exploration be performed in the direction of feature extraction and evaluation for isolator condition monitoring. Time-frequency based methods may be the most effective for transient vibration envelopes. However, considering the “stationary” operating environment, time domain methods may not be sensitive enough to changes in isolator condition to be of practical use. The possibility of exploring frequency domain methods and features may pave the way forward.

6 REFERENCES

[1] Multotec, "Industry Flow Sheets," Multotec, 2019. [Online]. Available: https://www.multotec.com/products/gallery/files/industry-flow-sheets. [Accessed 01 09 2022].

[2] K. Frolov and I. Goncharevich, Vibration Technology Theory and Practice, Moscow: Mir Publishers: CRC Press, 1992, pp. 96-112.

[3] Kwatani, "Kwatani Products," 2022. [Online]. Available: https://kwatani.com/products/. [Accessed 22 February 2022].

[4] ThyssenKrupp, *Brochure: Linear Vibrating Screens,* Beckum: ThyssenKrupp, 2022.

[5] P. Gackowiec, "General overview of maintenance strategies - concepts and approaches," *MAPE,* vol. 2, no. 1, pp. 126-139, 2019.

[6] R. B. Randall, "Vibration-Based Condition Monitoring : industrial, aerospace and automotive applications," Chichester, West Sussex: John Wiley & Sons Ltd, 2011.

[7] N. Standish, A. K. Bharadwaj and G. Hariri-Akbari, "A study of the effect of operating variables on the efficiency of a vibrating screen," *Powder Technology,* vol. 48, pp. 161-172, 1986.

[8] P. W. Cleary, M. D. Sinnott and R. D. Morrison, "Separation performance of double deck banana screens - Part 1: Flow and separation for different accelerations," *Mineral Engineering,* vol. 22, pp. 1218-1229, 2009.

[9] P. W. Cleary, M. D. Sinnott and R. D. Morrison, "Separation performance of double deck banana screens - Part 2: Quantitative predictions," *Minerals Engineering,* vol. 22, pp. 1230-1244, 2009.

[10] A. Davoodi, G. Asbjörnsson, E. Hulthén and E. Magnus, "Application of Discrete Element Method to Study the Effects of Stream Characteristics on Screening Performance," *Minerals,* vol. 9, pp. 1-13, 2019.

[11] C. G. Rodriguez, M. A. Moncada, E. E. Dufeu and M. I. Razeto, "Nonlinear model of vibrating screen to determine permissible spring deterioration for proper separation.," *Shock and Vibration,* 2016.

[12] Z. Makua, M. J. Lencwe, R. O. Kene and S. D. Chowdhury, "Design of a monitoring and protection system for a vibrating coal sizing screen," *IEEE PES/IAS Power Africa,* vol. 19, pp. 334-340, 2019.

[13] Vibramech, "Inclined Screens," 2017. [Online]. Available: https://www.vibramechglobal.com/inclined-screens.html. [Accessed 24 August 2022].

[14] Schenk Process Holding GmbH, "Double Banana Screen LinaClass SLD," 2022. [Online]. Available: https://www.schenckprocess.com/technologies/screening/screens/linaclass-sld-double-banana-screens. [Accessed 24 August 24].

[15] K. Shah, "Construction, Working and Maintenance of Electric Vibrators and Vibrating Screens," March 2018. [Online]. Available: www.practicalmaintenance.net. [Accessed 21 February 2022].

[16] P. R. Fry and D. M. E. Greenway, "An approach to assessing structural integrity and fatigue failures in vibrating equipment," Johannesburg, 1984.

[17] Kwatani, "Exciter Gearbox: JEG Series User Manual," May 2022. [Online]. Available: https://kwatani.com/. [Accessed 24 August 2022].

[18] Kwatani, "Unbalanced motors: JUD series user manual," May 2022. [Online]. Available: https://kwatani.com/. [Accessed 24 August 2022].

[19] S. S. Roa, Mechanical Vibrations Fifth Edition, Upper Saddle River: Pearson Education, 2011.

[20] G. Ene and N. Sporea, "Approaches regarding the calculus of the elastic system of the initial vibrating screens.," *Revista de Chimie (Bucharest),* vol. 67, no. 2, pp. 308-313, 2016.

[21] Persson, "On the theory of rubber friction.," *Surface science,* vol. 401, no. 3, pp. 445-454, 1998.

[22] S. Kayacı and A. K. Serbest, "Comparison of constitutive hyper-elastic material models in finite element theory.," *In 6 th Automotive Technologies Congress,* pp. 1-11, 2012.

[23] J. Steyn, "Fatigue failure of deck support beams on a vibrating screen," *Int. J. Pres. Ves. & Piping,* vol. 61, pp. 315-327, 1995.

[24] X. Guanghui, Z. Guorui, Z. Shigang, l. Hui and W. Miao, "Quick crack detection of the large vibrating screen lower beam based on combination technical method of MMMT and ET," *IEEE,* vol. 10, pp. 330-335, 2010.

[25] X. Guanghui and Z. Guorui, "Transfer function law and diagnosis method of large vibrating screen lower beam with crack flaw," *IEEE,* vol. 11, pp. 1044-1047, 2011.

[26] C. Liu, L. Peng and F. Li, "Survey of signal processing methods and research on vibrating screen fault diagnosis," *In 2011 Second International Conference on Mechanic Automation and Control Engineering ,* pp. 1709-1712, 2011.

[27] L.-p. Peng, C.-s. Liu, J. Li and H. Wang, "Static-deformation based fault diagnosis for damping spring of large vibrating screen," *Journal of Central South University,* vol. 21, no. 4, pp. 1313-1321, 2014.

[28] Y. Liu, S. Suo, G. Meng, D. Shang, L. Bai and J. Shi, "A theoretical rigid body model of vibrating screen for spring failure diagnosis," *Mathematics,* vol. 7, no. 3, p. 246, 2019.

[29] Y. Liu, G. Meng, S. Suo, D. Li, A. Wang and X. Cheng, "Spring failure analysis of mining vibrating screens: Numerical and experimental studies," *Applied Sciences,* vol. 9, no. 16, p. 3224, 2019.

[30] M. L. Chandravanshi and A. K. Mukhopadhyay, "Analysis of variations in vibration behaviour of vibratory feeder due to change in stiffness of helical springs using FEM and EMA methods.," *Journal of the Brazilian Society of Mechanical Sciences and Engineering,* vol. 39, no. 9, pp. 3343-3362, 2017.

[31] P. Krot and R. Zimroz, "Methods of Springs Failures Diagnostics in Ore Processing," in *In IOP Conference Series: Earth and Environmental Science.*, IOP Publishing., 2019.

[32] P. Krot, R. Zimroz, A. Michalak, J. Wodecki, S. Ogonowski, M. Drozda and M. Jach, "Development and verification of the diagnostic model of the sieving screen.," *Shock and Vibration,* p. 14, 2020.

[33] K. Gąsior, H. Urbańska, A. Grzesiek, R. Zimroz and A. Wyłomańska, "Identification, decomposition and segmentation of impulsive vibration signals with deterministic components—A sieving screen case study.," *Sensors,* vol. 20, no. 19, p. 5648, 2020.

[34] A. Michalak, J. Wodecki, M. Drozda, A. Wyłomańska and R. Zimroz, "Model of the vibration signal of the vibrating sieving screen suspension for condition monitoring purposes.," *Sensors,* vol. 21, no. 1, p. 213, 2020.

[35] N. Duda-Mróz, S. Anufriiev and P. Stefaniak, "Application of Wavelet Filtering to Vibrational Signals from the Mining Screen for Spring Condition Monitoring.," *Minerals,* vol. 11, no. 10, p. 1076, 2021.

[36] J. Parlar, *Vibration Analysis & Vibrating Screens: Theory & Practice, PhD Thesis.,* Ontario: McMaster University, 2010.

[37] K. J. Dong, A. B. Yu and I. Brake, "DEM simulation of particle flow on a multi-deck banana screen," *Minerals Engineering,* vol. 22, pp. 910-920, 2009.

[38] Z. Wang, C. Liu, J. Wu, H. Jiang and Y. Zhoa, "Impact of screening coals on screen surface and multi-index optimization for coal cleaning production," *Journal of Cleaner Products,* vol. 187, pp. 562-575, 2018.

[39] M. M. Moncada and C. G. Rodriguez, "Dynamic Modelling of a Vibrating Screen Considering the Ore Inertia and Force of the Ore over the Screen Calculated with Discrete Element Method," *Shock and Vibration,* p. 13, 2018.

[40] C. Warren, C. Niezrecki, P. Avitabile and P. Pingle, "Comparison of FRF measurements and mode shapes determined using optically image based, laser, and accelerometer measurements," *Mechanical Systems and Signal Processing,* vol. 25, pp. 2191-2202, 2011.

[41] J. Baqersad, P. Poozesh, C. Niezrecki and P. Avitabile, "Photogrammetry and Optical Methods in Structural Dynamics -A Review," *Mechanical Systems and Signal Processing,* vol. 86, pp. 17-34, 2017.

[42] Schenk Process, "CONIQ Monitor iQ you condition," Schenck Process Holding GmbH, 2022. [Online]. Available: https://www.schenckprocess.com/next/solutions/coniq-monitor. [Accessed 03 September 2022].

[43] Parker Lords, "G-Link-200 Rugged Wireless Accelerometer, 3-Axis," Parker Hannifin Corp, 2022. [Online]. Available: https://www.microstrain.com/wireless-sensors/G-Link-200. [Accessed 03 09 2022].

[44] Schenk Process Group, "Vibrating Screen & Feeder Condition Monitoring in Mineral Processing CONiQ," 12 01 2018. [Online]. Available: https://www.youtube.com/watch?v=CzMNssCSJMY. [Accessed 03 09 2022].

[45] Haver & Boecker Niagara, "Pulse Condition Monitoring," [Online]. Available: https://haverniagara.com/product/pulse-condition-monitoring/. [Accessed 03 09 2022].

[46] IFM, "ifm Solutions for Vibration Screen / Feeder Monitoring," [Online]. Available: https://www.ifm.com/binaries/content/assets/pdf-files/en/catalogues/application-package_screen-monitoring_en_low.pdf. [Accessed 03 09 2022].

[47] PCB Piezotronics , "Sensors for Monitoring Vibratory Screens and Feeders," 2022. [Online]. Available: https://www.pcb.com/applications/pdm-process-monitoring/vibratory-screens-and-feeders. [Accessed 03 09 2022].

[48] D. Volante, *Condition Monitoring for Rotational Machinery, Masters Thesis.,* Ontario: McMaster University, 2011.

[49] ReVibe Energy, "the ReLog," ReVibe Energy, [Online]. Available: https://revibeenergy.com/product-overview-relog/#detailed. [Accessed 03 09 2022].

[50] M. Varanis, A. Silva, A. Mereles and R. Pederiva, "MEMS accelerometers for mechanical vibration analysis: a comprehensive review with applications," *Journal of the Brazilian Society of Mechanical Science and Engineering,* p. 40:527, 2018.

[51] I. Koene, *Vibration measurement of large rotating machinery with MEMS accelerometer-based Internet of Things measurement device,* PHD Thesis ed., Helsinki: Aalto University, 2022.

[52] PCB Piezotronics, "Introduction to MEMS Accelerometers," 2022. [Online]. Available: https://www.pcb.com/resources/technical-information/mems-accelerometers. [Accessed 20 August 2022].

[53] A. Albarbar, S. Mekid, A. Starr and R. Pietruszkiewicz, "Suitability of MEMS accelerometers for Condition Monitoring: An experimental study," *Sensors,* vol. 8, no. 1, pp. 784-799, 2008.

[54] Y.-J. Park, S.-K. S. Fan and C.-Y. Hsu, "A review on fault detection and process diagnostics in industrial processes.," *Processes,* vol. 8, no. 9, p. 1123, 2020.

[55] C. Zhang, A. A. Mousavi, S. F. Masri, G. Gholipour, K. Yan and X. Li, "Vibration feature extraction using signal processing techniques for structural health monitoring: A review," *Mechanical Systems and Signal Processing,* vol. 177, p. 109175, 2022.

[56] A. P. Daga and L. Garibaldi, "Machine vibration monitoring for diagnostics through hypothesis testing.," *Information,* vol. 10, no. 6, p. 204, 2019.

[57] H. Yang, J. Mathew and L. Ma, "Vibration feature extraction techniques for fault diagnosis of rotating machinery: a literature survey.," in *Asia-pacific vibration conference*, Gold Coast, Australia, 2003.

[58] D. J. Ewins, Modal Testing: Theory, Practice and Application (Second Edition), Hertfordshire: Research Studies Press LTD. , 2000.

[59] R. O. Harat, "Dynamic investigation of vibratory screen response in a FEM environment.," *Masters, University of Pretoria,* 2020.

[60] D. J. Inman, Engineering Vibration, Essex: Pearson, 2014.

[61] J. A. Snyman and P. J. Vermeulen, "The mathematical modelling of the motion of a horizontal vibrating screen supported by ROSTA oscillating mountings," *R&D Journal,* pp. 25-33, 1992.

[62] G. Ciepok, K. Wójcik, K. Michalczyk and W. Sikora, "Equivalent Parameters of Metal-Elastomer Vibroinsulators," *Vibrations in Physical Systems,* vol. 31, pp. 1-13, 2020.

[63] W. Sikora, K. Michalczyk and T. Machniewicz, "A study of the preload force in metal-elastomer torsional springs," *ACTA Mechanica et Automatica,* vol. 10, no. 4, pp. 300-305, 2016.

[64] Persson, "On the theory of rubber friction," *Surface science,* vol. 401, no. 3, pp. 445-454, 1998.

[65] D. Ewins, Modal Testing: Theory, Practice and Application, 2nd ed., Hertfordshire: Research Studies Press Ltd., 2000.

[66] Siemens, "Getting Started with Modal Curvefitting," 21 September 2020. [Online]. Available: https://community.sw.siemens.com/s/article/getting-started-with-modal-curvefitting. [Accessed 26 July 2023].

[67] MathWorks, "modalfit," 2023. [Online]. Available: https://www.mathworks.com/help/signal/ref/modalfit.html. [Accessed 26 July 2023].

[68] L. H. Manring, J. F. Schultze, S. J. Zimmerman and B. P. Mann, "Improving magnitude and phase comparison metrics for frequency response functions using cross-correlation and log-frequency shifting.," *Journal of Sound and Vibration,* vol. 539, p. 117255, 2022.

[69] J. P. Lewis, "Fast template matching," *Vision Interface,* pp. 120-123, 1995.

[70] A. Pikovsky, M. Rosenblum and J. Kurths, Synchronization: A universal concept in nonlinear science, Cambridge: Cambridge University Press, 2001.

[71] A. Albarbar, A. Badri, J. Sinha and A. Starr, "Performance evaluation of MEMS accelerometers," *Measurement,* vol. 42, no. 5, pp. 790-795, 2009.

[72] Kwatani, "Kwatani," May 2022. [Online]. Available: https://kwatani.com/. [Accessed 12 August 2022].

[73] C. G. Rodriguez, M. A. Moncada, E. E. Dufeu and M. I. Razato, "Nonlinear model of vibrating screen to determine permissible spring deterioration for proper separation," *Shock and Vibration,* 2016.

1 APPENDIX A

1.1 MOTOR NAME PLATE AND DATA FROM CATALOGUE

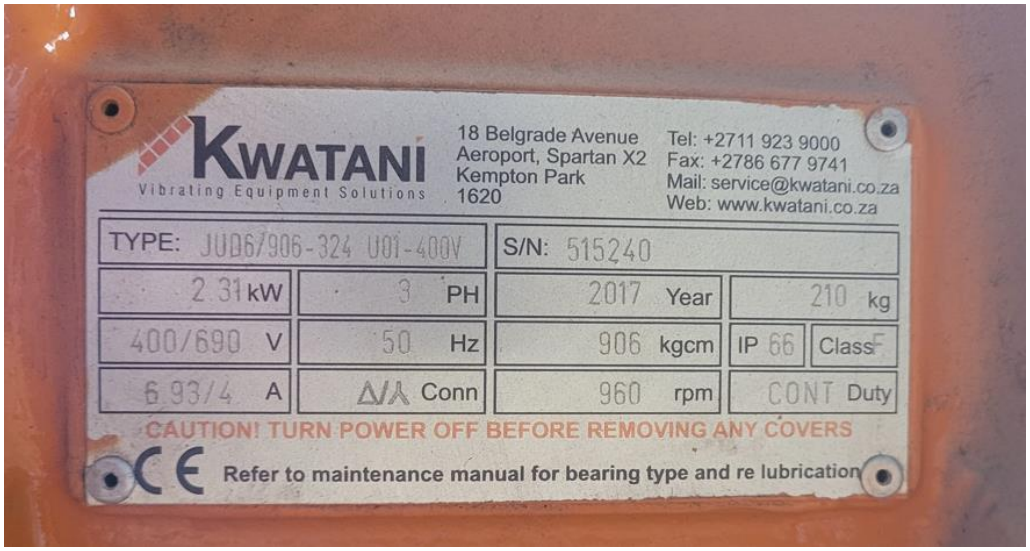

Figure 85: JUD 6/906 motor plate

DESCRIPTION	MECHANICAL SPECIFICATION				ELECTRICAL SPECIFICATION							
Type	Centrifugal Force		**Working Moment	Mass	Power [kW]		Full Load Current [A]			Starting Current [A]		
	[kg]	[kN]	[Kg.cm]	[Kg]	Input	Output	400V *Δ28	690V *Y28	525V *Y03	400V *Δ28	690V *Y28	525V *Y03
4 POLE | 1470rpm | 50Hz												
JUD 4/100 214 UO1	1159	11.37	100	56	0.68	0.5	1.43	0.83	1.14	9.4	5.5	7
JUD 4/140 274 UO1	1623	15.92	140	88	1.33	1.15	2.62	1.51	2.1	25	14.5	19
JUD 4/200 274 UO1	2318	22.74	200	93	1.33	1.15	2.62	1.51	2.1	25	14.5	19
JUD 4/300 274 UO1	3542	34.75	300	132	2.15	1.8	3.86	2.23	2.89	33	19.3	24.3
JUD 4/210 294 UO1	2434	23.88	210	114	1.33	1.15	2.62	1.51	2.1	25	14.5	19
6 POLE | 980rpm | 50Hz												
JUD 6/190 214 UO1	979	9.6	190	67	0.75	0.51	1.7	0.99	1.33	7.4	4.3	5.6
JUD 6/270 274 UO1	1391	13.64	270	98	1.17	0.9	3.2	1.85	2.5	16	9.3	12
JUD 6/470 294 UO1	2421	23.75	470	140	2.29	1.8	5.4	3.1	4.3	27	15.6	20
JUD 6/570 294 UO1	2936	28.8	570	148	2.29	1.8	5.4	3.1	4.3	27	15.6	20
JUD 6/763 324 UO1	3930	38.56	763	201	2.69	2.31	6.9	4	5.5	49	28	35
JUD 6/906 324 UO1	4667	45.78	906	210	2.69	2.31	6.9	4	5.5	49	28	35
JUD 6/1140 384 UO1	5872	57.61	1140	267	4.53	4	9.3	5.3	7.4	64	37	49
JUD 6/1400 404 UO1	7212	70.75	1400	347	6.0	5.5	13.3	7.7	10.2	83	48	64
JUD 6/1750 404 UO1	9014	88.43	1750	366	6.0	5.5	13.3	7.7	10.2	83	48	64
JUD 6/2050 404 UO1	10560	103.59	2050	381	6.0	5.5	13.3	7.7	10.2	83	48	64
8 POLE | 735rpm | 50Hz												
JUD 8/1800 384 UO1	5215	51.16	1800	312	3.78	3.3	9.5	5.5	7.6	55	32	44
**Working moment = 2x static moment												

Figure 86: JUD motor specifications (JUD 6/906 highlighted yellow)

2 APPENDIX B

2.1 RESATEC CATALOGUE

Belastungswerte/load values, **max. Einsatzparameter/**capacity limits

Typ type	Art. Nr. art. no.	Belastung load		Belastung load		Eigenfrequenz fe natural frequency fe	Dynam. Federrate cd dynam. spring ratio cd 960 min⁻¹		max. Einsatzparameter/capacity limits*											
							sw amplitude		720 min⁻¹ (12 Hz)				960 min⁻¹ (16 Hz)				1440 min⁻¹ (24 Hz)			
		min. N	max. N	min. Hz	max. Hz	verti. N/mm	peak to peak mm	hori. N/mm	sw mm	K –	W %	Vm m/min.	sw mm	K –	W %	Vm m/min.	sw mm	K –	W %	Vm m/min.
CH 3 – 40	556 403 02	50	160	4.5	2.4	10	11	13	13.5	3.9	95.4	16	11	5.7	97.4	17	8	9.3	99	18
CH 4 – 50	556 404 02	120	350	4	2.3	19	12	15	16	4.9	96.8	18	14	7.7	98.3	19	8	9.3	99	18
CH 5 – 60	556 105 02	240	800	3.8	2.2	35	14	18	17	4.9	96.6	20	14	8.8	98.1	24	8	9.3	99	18
CH 6 – 80	556 106 02	600	1 600	3.0	1.9	56	17	26	20	5.8	97.3	24	17	8.8	98.5	27	8	9.3	99	18
CH 7 – 110	556 107 02	1300	3 300	2.8	1.9	107	17	38	20	5.8	97.5	24	17	9.3	98.5	27	8	9.3	99	18
CH 8 – 120	556 108 01	2 400	5 800	2.4		194		84			97.5									
CH 8 – 160	556 108 02	3 200	8 000	2.4		266		138			97.5									
CH 8 – 200	556 108 03	4 000	9 800	2.4	1.9	327	18	149	22	6.4	97.5	26	18	9.3	98.5	28	8	9.3	99	18
CH 8 – 240	556 108 04	5 000	12 000	2.3		399		209			97.5									
CH 8 – 320	556 108 05	7 000	16 000	2.2		533		277			97.5									
CH 8 – 400	556 108 06	8 500	20 000	2.3		666		344			97.8									

*sw = Schwingweite/amplitude (peak to peak)
K = Schwingmaschinenkennzahl/oscillating machine factor
W = Schwingisolation/isolation efficiency
Vm = theo. Material-Fördergeschwindigkeit/theo. conveying speed (Winkel/angle 45°)

Figure 87: Resatec catalogue extract (CH8-160 highlighted yellow)

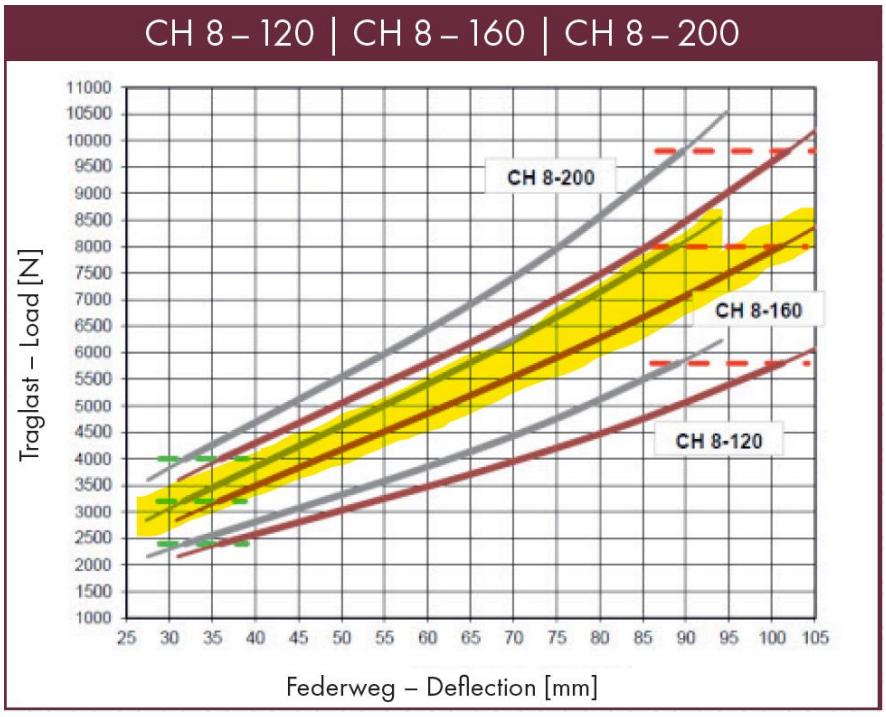

Figure 88: Resatec load deflection graph from catalogue (CH8-160 highlighted yellow)

3 APPENDIX C

3.1 PHOTOS OF QUASI-STATIC TESTING AT DELTA RUBBER

Figure 89: Resatec CH8-160 in parallel for quasi-static testing

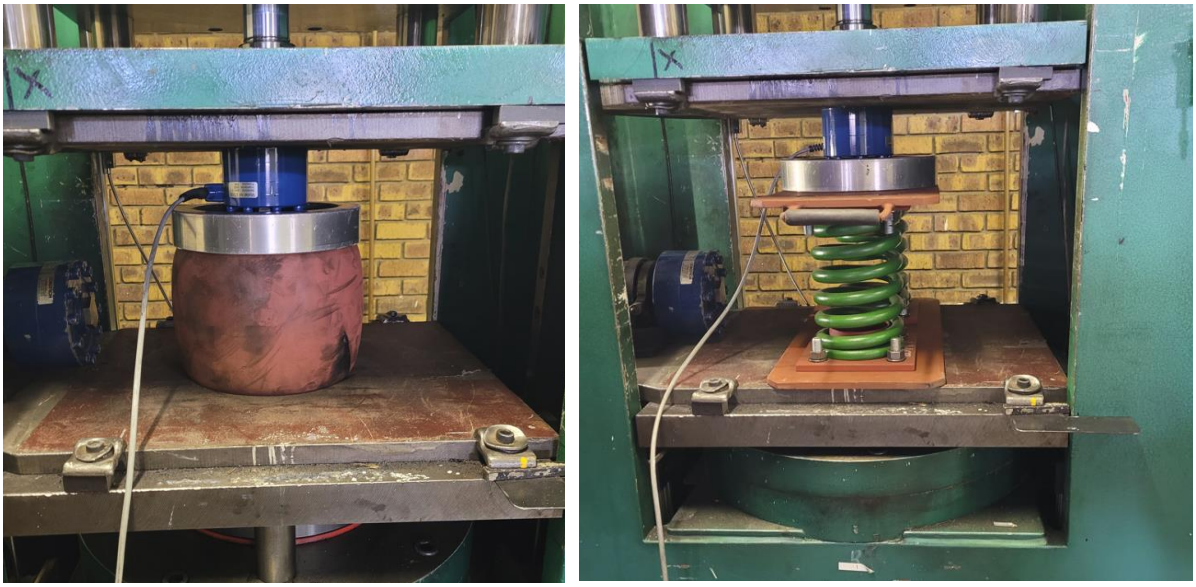

(a) *(b)*

Figure 90: Quasi-static testing of (a) a rubber isolator and (b) coil springs at Delta Rubber

4 APPENDIX D

4.1 SENSOR SPECIFICATIONS

Table 17: Accelerometers used during experiments

METRIC	SENSOR TYPES		
SENSOR LABEL	Dysinet DA 2202-050	IFM VSA 004	Piezoelectric ICP
RANGE	$\pm 50g$	$\pm 25g$	$\pm 50g$
NON-LINEARITY	0.3% F.S.	0.2% F.S.	1% F.S.
BANDWIDTH	0…400Hz, $\pm 3dB$	1…10kHz	0.33Hz…10kHz
RMS NOISE	<±0.2% F.S.	No Information given	1mg
OPERATING TEMP.	-55…+125°C	-20…80°C	-54…121°C
OVERRANGE	$\pm 4000g$	$\pm 500g$	5000g shock limit
OUTPUT IMPEDANCE	500Ohm	300Ohm	<100Ohm
SENSOR TYPE	MEMS	Capacitive/MEMS	ICP
OUTPUT	Voltage (±1.8V F.S.)	Current (0…10mA F.S.)	Voltage
SENSITIVITY	Estimate: ±18mV/g	142μA/g	100mV/g
NUMBER OF AXES	2	1	1
NO. SENSORS USED	4	8	8
SERIAL NUMBER(S)	1231, 5561, 5562, 5563	/	12247, 13329, 11990, 12250, 11991, 13331, 17181, 17179

Table 18: Inductive sensor specifications

SENSOR NAME →	IFM IGW 200
METRICS:	
SWITCHING FREQUENCY	2000Hz
SENSING RANGE	5mm ±10%
OPERATING DISTANCE	0…4.05mm
OPERATING TEMPERATURE	-25…70°C
SWITCHING OUTPUT	2.5V

Table 19: Modal hammer specifications

SENSOR NAME →	ICP IMPACT HAMMER
METRICS:	
SENSITIVITY (±15%)	0.23mV/N
MEASUREMENT RANGE	±22 240N pk
OUTPUT IMPEDANCE	<100Ohm
NON-LINEARITY	≤ 1%
HAMMER MASS	5.5kg

4.2 DATA ACQUISITION SPECIFICATIONS

Table 20: DAQs comparison

DAQ →	HBM QUANTUMX MX840B	IFM VSE002
INPUTS	8 Sensors or Analogue/Digital	4 Sensors + 2 Analogue/Digital
RESOLUTION	24 bits	16 bits Sensors/12 bits Analogue
SAMPLE RATE (MAX)	19200Hz	100kHz
FREQUENCY RANGE	0…6667Hz	0…12000Hz
OTHER	Allows for different sampling rates per channel.	Sample rate chosen is for all sensor channels.
	Multiple DAQs can be synchronized using a firewire connection between DAQs.	Synchronization of multiple modules can be performed by concurrently triggering measurements from the PC.

5 APPENDIX E

5.1 MODAL HAMMER POSITION TEST

Six modal hammer tests were performed where the impact responses to hammer impacts at 6 different positions are evaluated. The rationale behind these tests being that the position of the sensors and impact will determine the modes being measured and excited. Three different accelerometer types are used for this test, but for brevity only the ICP sensor results are displayed.

5.1.1 Description of modal positions evaluated.

1. Centre of Traverse Beam – at an angle to the horizontal.
2. RHS of Traverse Beam – at an angle to the horizontal.
3. RHS of Perimeter Stiffener – at an angle to the horizontal.
4. LHS of Perimeter Stiffener – at an angle to the horizontal.
5. F2 Left Isolation bracket - vertically.
6. F1 Left Isolation bracket – vertically.

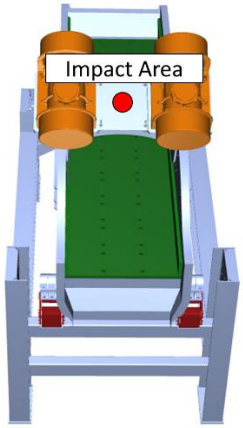

(1)

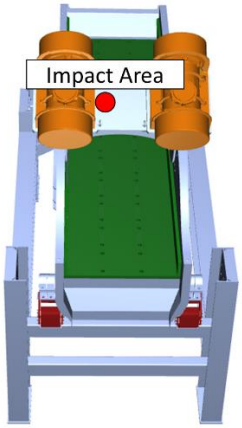

(2)

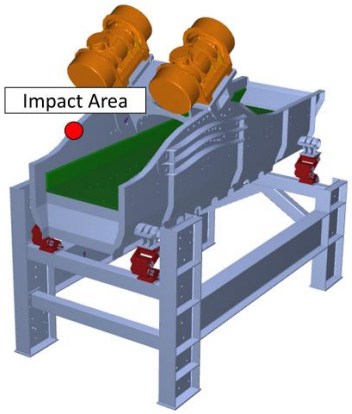

(3)

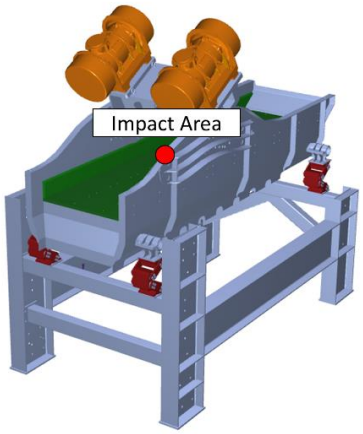

(4)

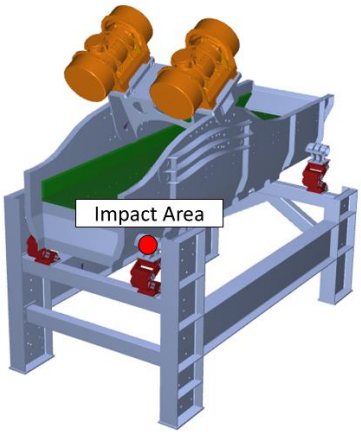

(5)

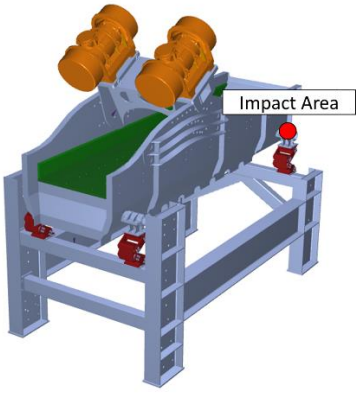

(6)

5.1.2 Description of apparatus

The apparatus used for this experiment is as follows:

- 1x Modal hammer
- 4x Dysinet biaxial accelerometers
- 8x IFM VSA 004 accelerometers
- 8x ICP Industrial accelerometers
- 2x Quantum DAQs

The accelerometers were positioned such that the vertical (up/down) and horizontal (feed direction) directions are measured. Therefore, 1x Dysinet sensor, 2x IFM and 2x ICP sensors are mounted per corner of the machine on the isolation brackets.

The three types of accelerometers used are compared to each other for usefulness and consistency in measured results. For the modal hammer test all three sensors should give the same results.

5.1.3 Modal Results

5.1.3.1 Centre of Traverse Beam

ICP Sensor X Response

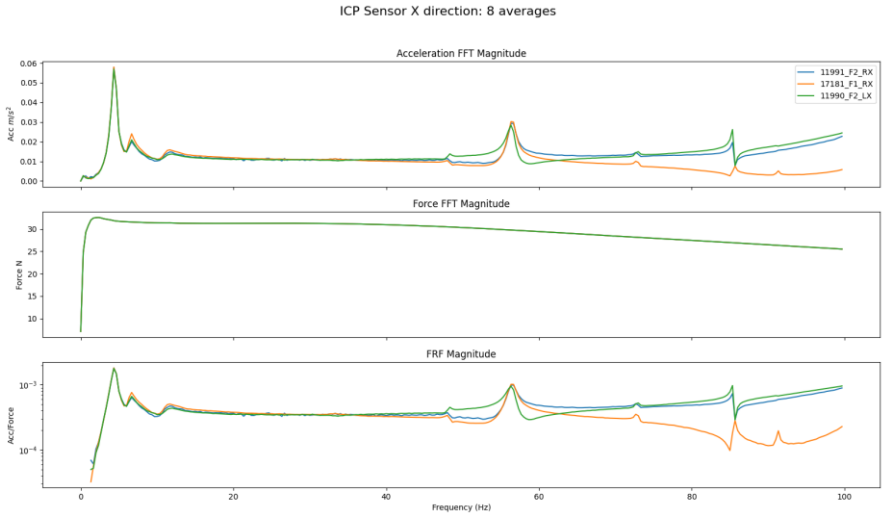

ICP Sensor Z Response

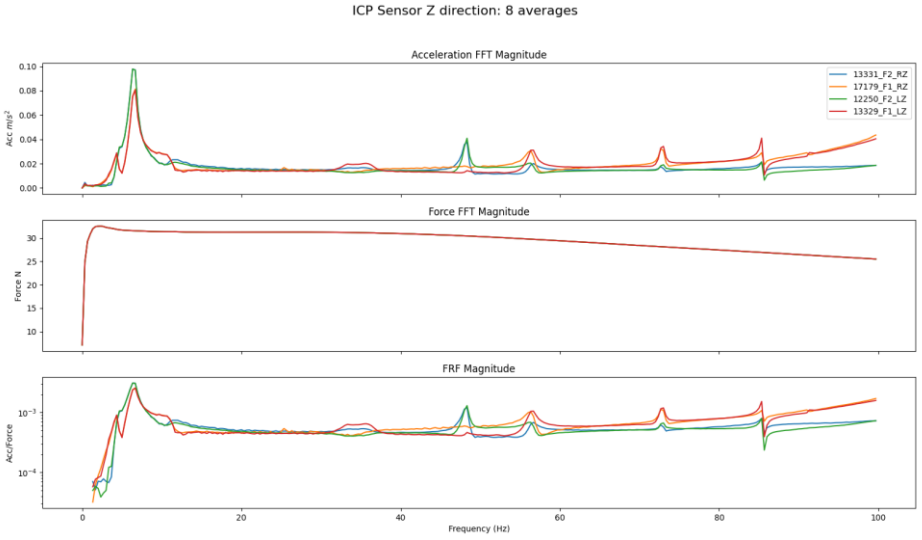

5.1.3.2 RHS of Traverse Beam

ICP Sensor X Response

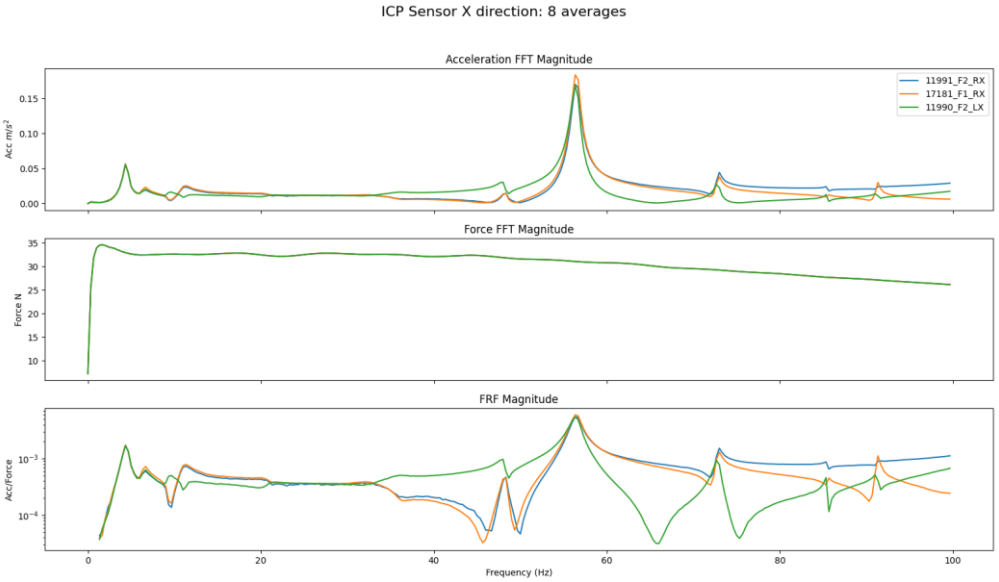

ICP Sensor Z Response

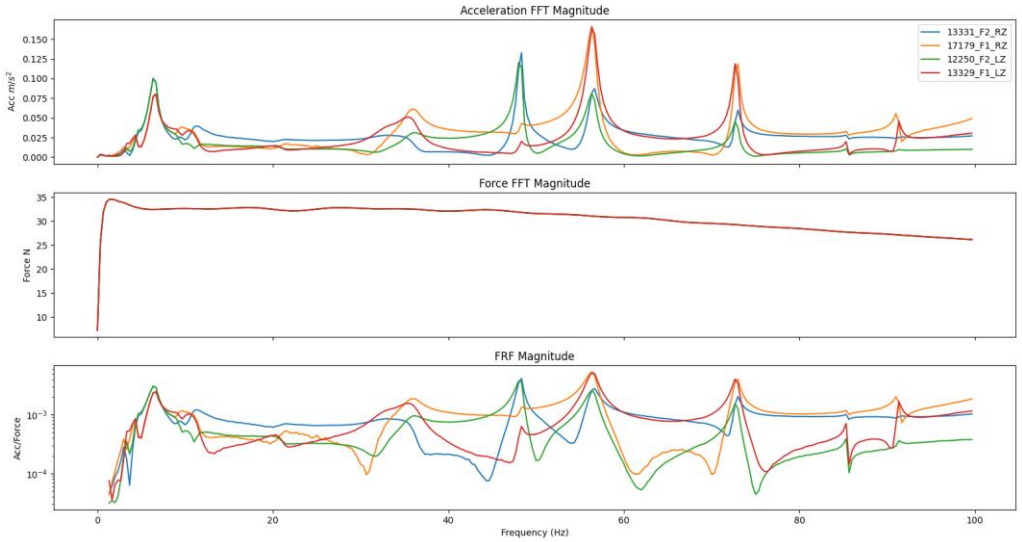

5.1.3.3 RHS Perimeter Stiffener

ICP Sensor X Response

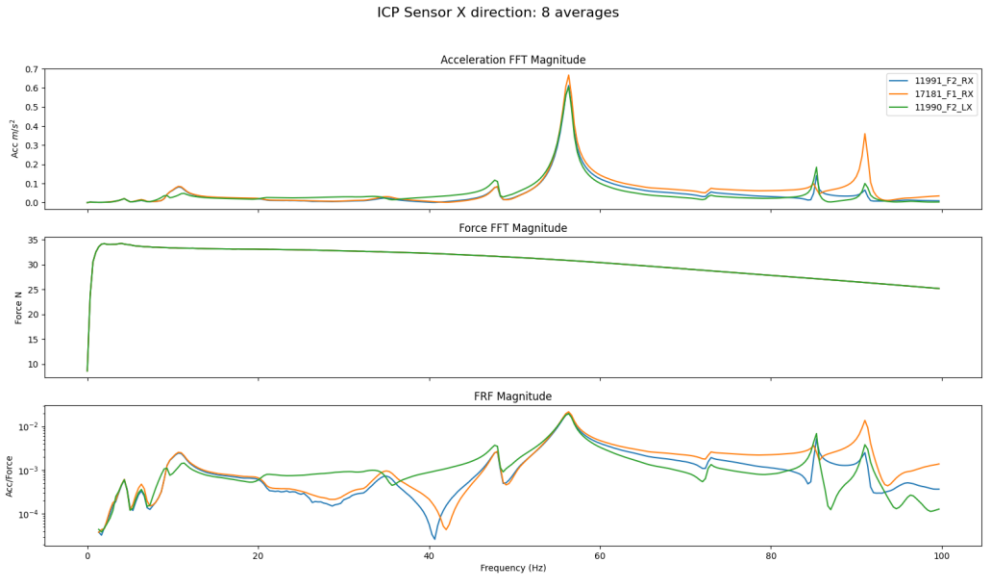

ICP Sensor Z Response

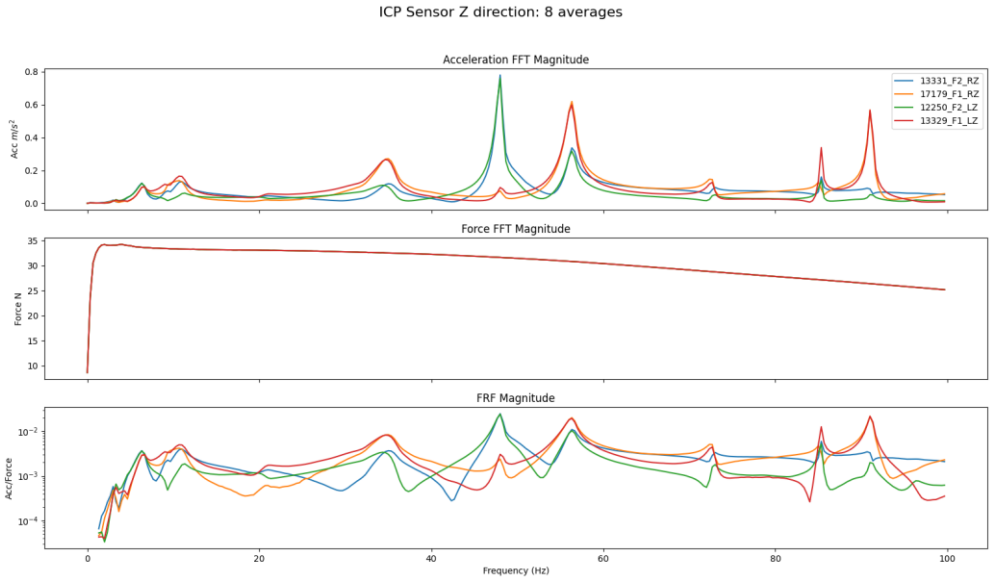

5.1.3.4 LHS Perimeter Stiffener

ICP Sensor X Response

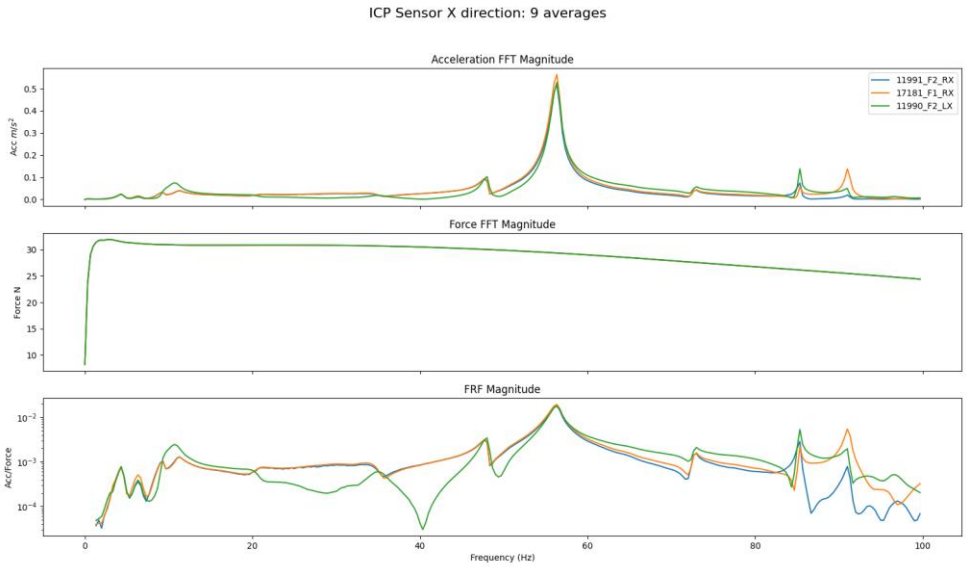

ICP Sensor Z Response

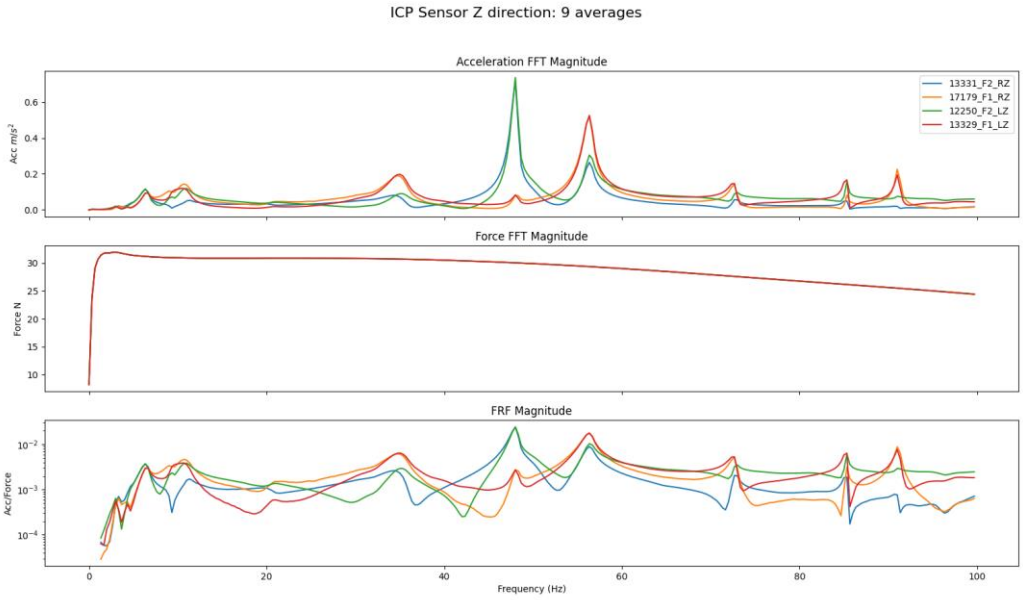

5.1.3.5 F2 Left

ICP Sensor X Response

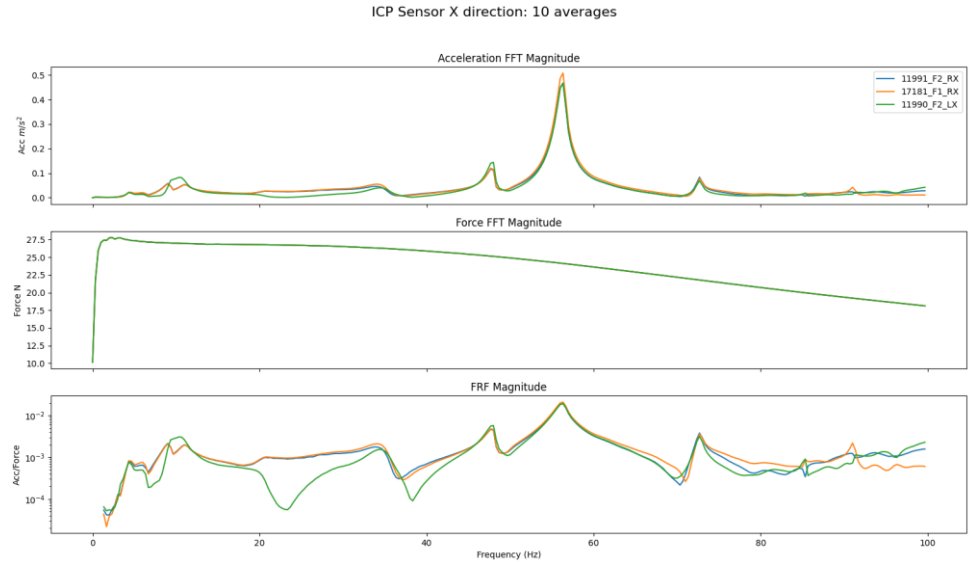

ICP Sensor Z Response

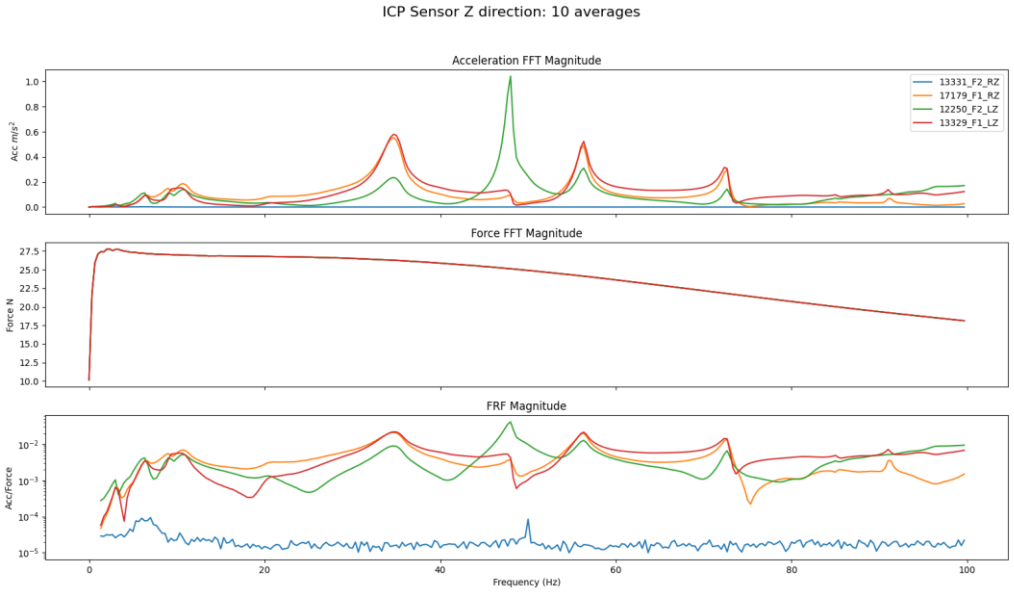

Notice ICP sensor 13331 at F2R was not measuring correctly as it had disconnected.

5.1.3.6 F1 Left

ICP Sensor X Response

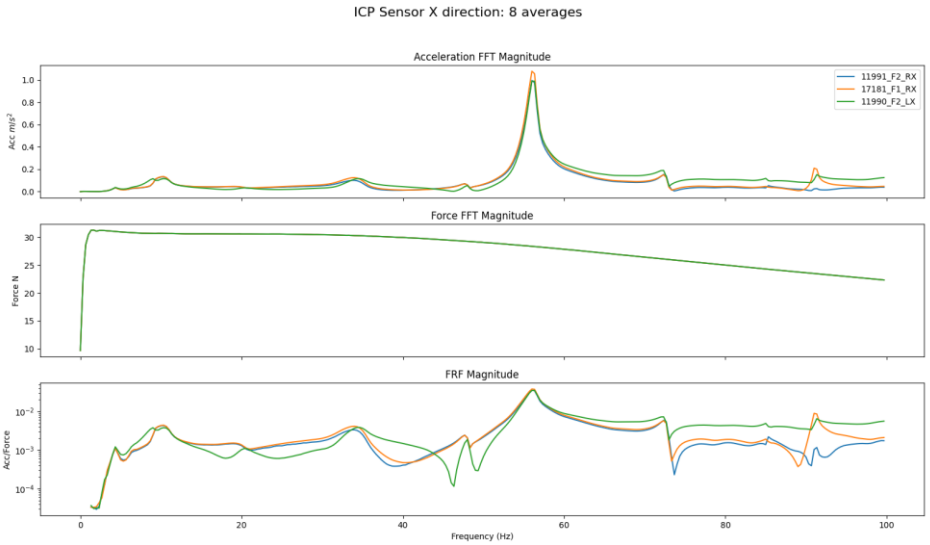

ICP Sensor Z Response

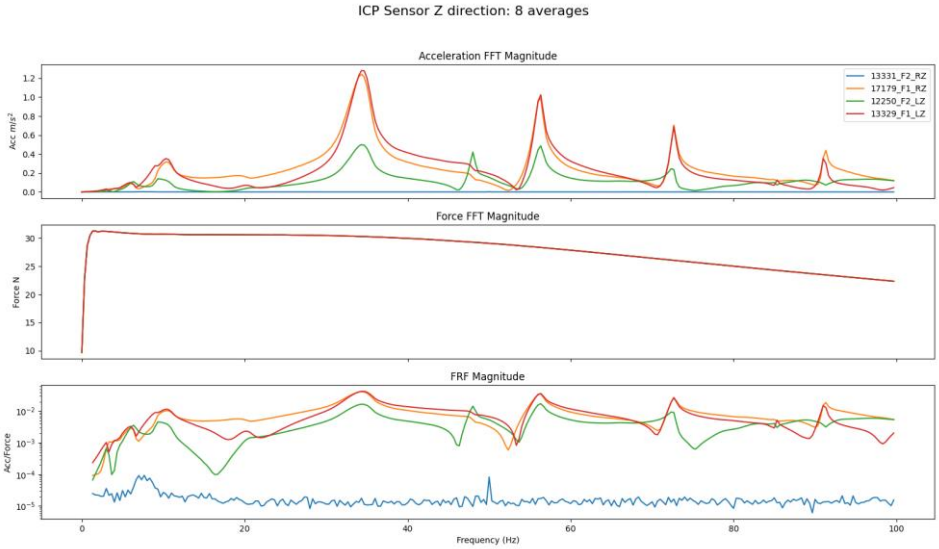

Notice again that ICP sensor 13331 at F2R was not measuring correctly as it had disconnected.

6 APPENDIX F

6.1 LINEARIZED NUMERICAL MODEL EQUATIONS

For the linearized case the displacements and velocities in equations Eq. 10 and Eq. 12 are simplified to,

$$\begin{aligned} x_{F1} &= x_{CG} + \theta \cdot B \\ x_{F2} &= x_{CG} + \theta \cdot D \\ z_{F1} &= z_{CG} - \theta \cdot A \\ z_{F2} &= z_{CG} - \theta \cdot C \end{aligned} \qquad \textit{Eq. 37}$$

, and

$$\begin{aligned} \dot{x}_{F1} &= \dot{x}_{CG} + \dot{\theta} \cdot B \\ \dot{x}_{F2} &= \dot{x}_{CG} + \dot{\theta} \cdot D \\ \dot{z}_{F1} &= \dot{z}_{CG} - \dot{\theta} \cdot A \\ \dot{z}_{F2} &= \dot{z}_{CG} - \dot{\theta} \cdot C \end{aligned} \qquad \textit{Eq. 38}$$

The final linearized vertical displacement equations per corner combine the linearized equations (Eq. 37) and linearized equations Eq. 14 and Eq. 15. z_{F1} and z_{F2} are expanded to the following,

$$\begin{aligned} z_{F1R} &= z_{F1} - \frac{w}{2} \cdot \phi \\ z_{F1L} &= z_{F1} + \frac{w}{2} \cdot \phi \\ z_{F2R} &= z_{F2} - \frac{w}{2} \cdot \phi \\ z_{F2L} &= z_{F2} + \frac{w}{2} \cdot \phi \end{aligned} \qquad \textit{Eq. 39}$$

And the respective linearized velocities are,

$$\begin{aligned} \dot{z}_{F1R} &= \dot{z}_{F1} - \frac{w}{2} \cdot \dot{\phi} \\ \dot{z}_{F1L} &= \dot{z}_{F1} + \frac{w}{2} \cdot \dot{\phi} \\ \dot{z}_{F2R} &= \dot{z}_{F2} - \frac{w}{2} \cdot \dot{\phi} \\ \dot{z}_{F2L} &= \dot{z}_{F2} + \frac{w}{2} \cdot \dot{\phi} \end{aligned} \qquad \textit{Eq. 40}$$

Finally, equations Eq. 16 and Eq. 17 are also linearized for small angles θ and ϕ,

$$\begin{aligned} a' &= A + B \cdot \theta \\ b' &= C + D \cdot \theta \\ c_1' &= -B + D \cdot \theta \end{aligned} \qquad \textit{Eq. 41}$$

$$c_2' = -D + C \cdot \theta$$

$$w_L' = \frac{w}{2} - c \cdot \phi$$

$$w_R' = -\frac{w}{2} - c \cdot \phi$$

Eq. 42

6.2 SIDE MOUNTED UNBALANCED MOTOR MODEL

Motors mounted on either side of a vibrating screen, as see in Figure 91, exert force in the x and z directions when the motors synchronize in the operating direction. However, should the motors synchronize in the lateral direction then large rolling moments are expected.

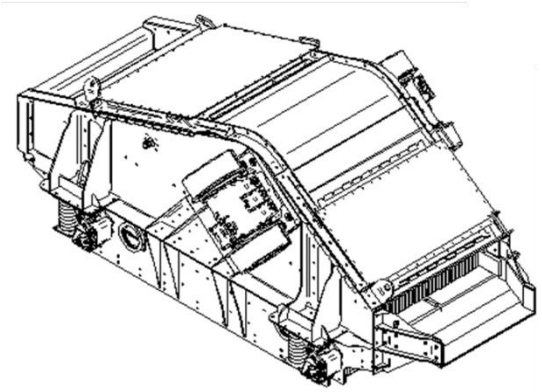

Figure 91: Vibrating screen with side mounted motors

Figure 92 shows the Freebody diagram of a rigid body vibrating screen model with side mounted unbalanced motors. Note that forces F_{1y} and F_{2y} act in opposite directions as the motors rotate in opposite directions. Variable d is calculated using equation Eq. 27.

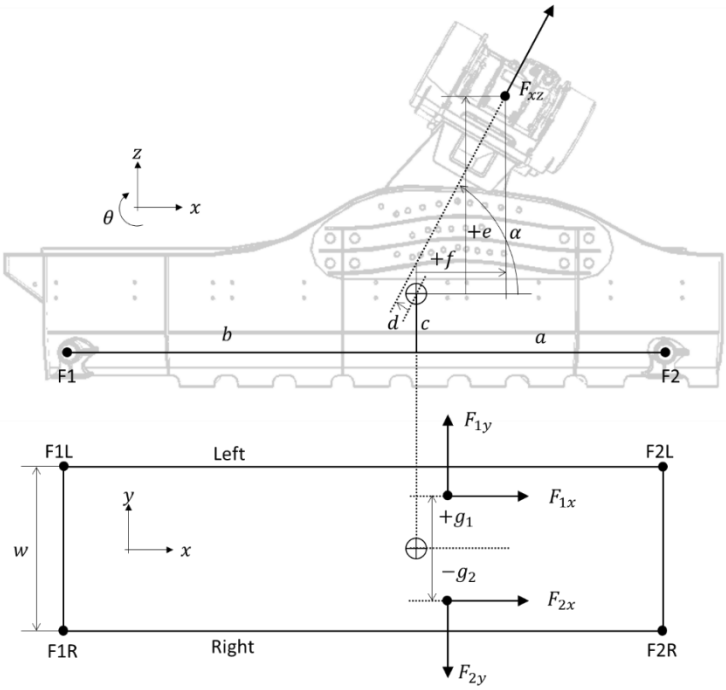

Figure 92: Freebody diagram of rigid screen with side mounted unbalanced motors

The motors are not mechanically coupled and rely on the self-synchronization phenomena to rotate in phase together in the operating direction. The unbalanced motors are mounted such that they have the greatest likelihood of synchronizing in the α direction.

The equations for the forces are as follows,

$$F_{xz1} = WM \cdot \omega_1^2 \cdot \sin(\omega_1 \cdot t)$$

$$F_{y1} = WM \cdot \omega_1^2 \cdot \cos(\omega_1 \cdot t)$$

$$F_{xz2} = WM \cdot \omega_2^2 \cdot \sin(\omega_2 \cdot t) \qquad \textit{Eq. 43}$$

$$F_{y2} = -WM \cdot \omega_2^2 \cdot \cos(\omega_2 \cdot t)$$

Where ω_1 and ω_2 are the rotating speeds of the left and right motors respectively. F_{y1} and F_{y2} are the lateral y direction force components due to motors being side mounted. The moments exciting the pitch (θ) and roll (ϕ) degrees of freedom are calculated as follows,

$$M_\theta = F_{xz} \cdot d$$

$$M_\phi = F_y \cdot e + F_{xz1} \cdot \sin(\alpha) \cdot g_1 + F_{xz2} \cdot \sin(\alpha) \cdot g_2 \qquad \textit{Eq. 44}$$

Where $F_{xz} = F_{xz1} + F_{xz2}$ and $F_y = F_{y1} + F_{y2}$.

6.3 TOP MOUNTED UNBALANCED MOTOR MODEL

Two unbalanced motors mounted on the top of a vibrating screen used to exert forces in the z and x directions. The two motors are not synchronized mechanically (with gears, couplings, or pulleys) but instead rely on a phenomenon known as self-synchronization during start-up and operation. The ability of the unbalanced motors to synchronize in a particular motion or directions depends on the coupling strength, or interaction between the two independent oscillators and the dynamic motion, and "frequency detuning" which refers to the mechanical differences between the two oscillators [70].

The two motors are mounted in the width wise centre of the vibrating screen. Figure 93 shows and example of screen with top mounted unbalanced motors. In this example the motors are mounted on base plates that are orthogonal to one another.

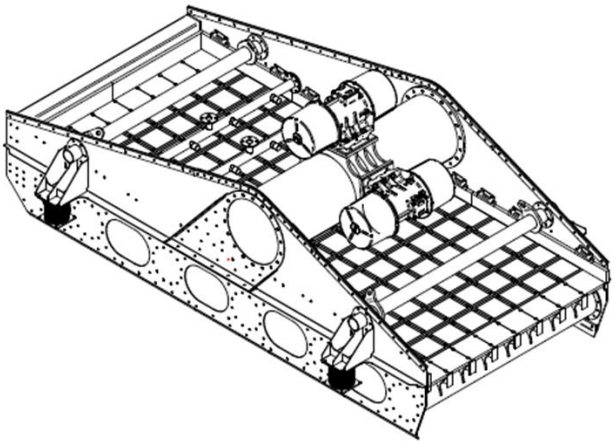

Figure 93: Vibrating screen with top mounted unbalanced motors

Figure 94 shows the Freebody diagram of this configuration. The unbalanced motors are positioned such that they synchronize in the drive angle (α) direction. An offset angle is also allowed in the model which accounts for motor mounting imperfections resulting in the excitation of the rolling degree of freedom. Because there are now two independent motors more variables are required to position the motors geometrically within the model. There are now two e, and f variables as well as four d variables (split between d and $d1$).

The d variables are calculated by rotating the x and z axes about the CG by α. They are calculated as follows,

$$d_1 = e_1 \cdot \cos(\alpha) - f_1 \cdot \sin(\alpha)$$

$$d_2 = e_2 \cdot \cos(\alpha) - f_2 \cdot \sin(\alpha)$$

$$d1_1 = f_1 \cdot \cos(\alpha) + e_1 \cdot \sin(\alpha) \qquad \text{Eq. 45}$$

$$d1_2 = f_2 \cdot \cos(\alpha) + e_2 \cdot \sin(\alpha)$$

The $d1$ variables are there to account for the moment created by the forces perpendicular to the drive angle. The perpendicular forces are balanced during operating due to the motors being synchronized in the drive angle direction. This results in a linear reciprocating force. However, when the motors are not perfectly in sync, then a net unbalanced force results which excites the pitching mode of the screen.

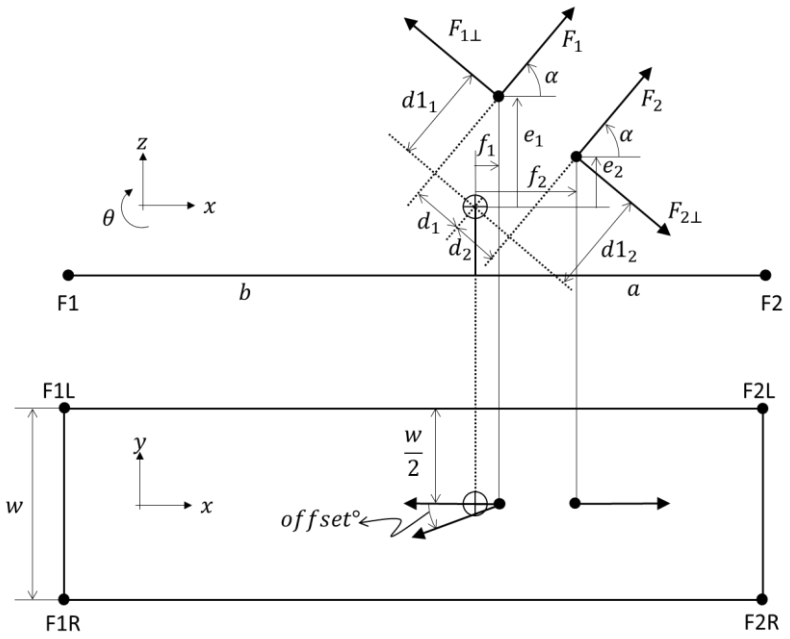

Figure 94: Freebody diagram of rigid screen with two unbalanced motors top mounted

The force components are calculated as follows,

$$F_1 = WM \cdot \omega_1^2 \cdot \sin(\omega_1 \cdot t)$$

$$F_2 = WM \cdot \omega_2^2 \cdot \sin(\omega_2 \cdot t)$$

$$F_{1\perp} = WM \cdot \omega_1^2 \cdot \cos(\omega_1 \cdot t)$$

$$F_{2\perp} = -WM \cdot \omega_2^2 \cdot \cos(\omega_2 \cdot t)$$

Eq. 46

$$F_y = F_1 \cdot \cos(\alpha) \cdot \sin(\text{offset°}) - \mathrm{F}_{1\perp} \cdot \cos(90° - \alpha) \cdot \sin(offset°) + F_2 \cdot \sin(\alpha) \cdot \sin(offset°) - F_{2\perp} \cdot \cos(\alpha) \cdot \sin(offset°)$$

Where ω_1 and ω_2 are the rotating speeds of the top and bottom motors respectively and F_y is the force in the lateral y direction due to the offset angle. Also note the sign difference of $F_{2\perp}$ as this force acts in the opposite direction to that of $F_{1\perp}$.

The moments acting on the pitch and roll degrees of freedom are calculated as,

$$M_\theta = F_1 \cdot d_1 - F_{1\perp} \cdot d1_1 + F_2 \cdot d_2 + F_{2\perp} \cdot d1_2$$

$$M_\phi = F_1 \cdot \cos(\alpha) \cdot \sin(offset°) \cdot e_1 + F_2 \cdot \sin(\alpha) \cdot \sin(offset°) \cdot e_2 - F_{1\perp} \cdot \cos(90° - \alpha) \cdot \sin(offset°) \cdot e_1 - F_{2\perp} \cdot \cos(\alpha) \cdot \sin(offset°) \cdot e_2$$

Eq. 47

7 APPENDIX G

7.1 FEA MODAL RESULTS OF VIBRATING SCREEN FOR MODEL VALIDATION

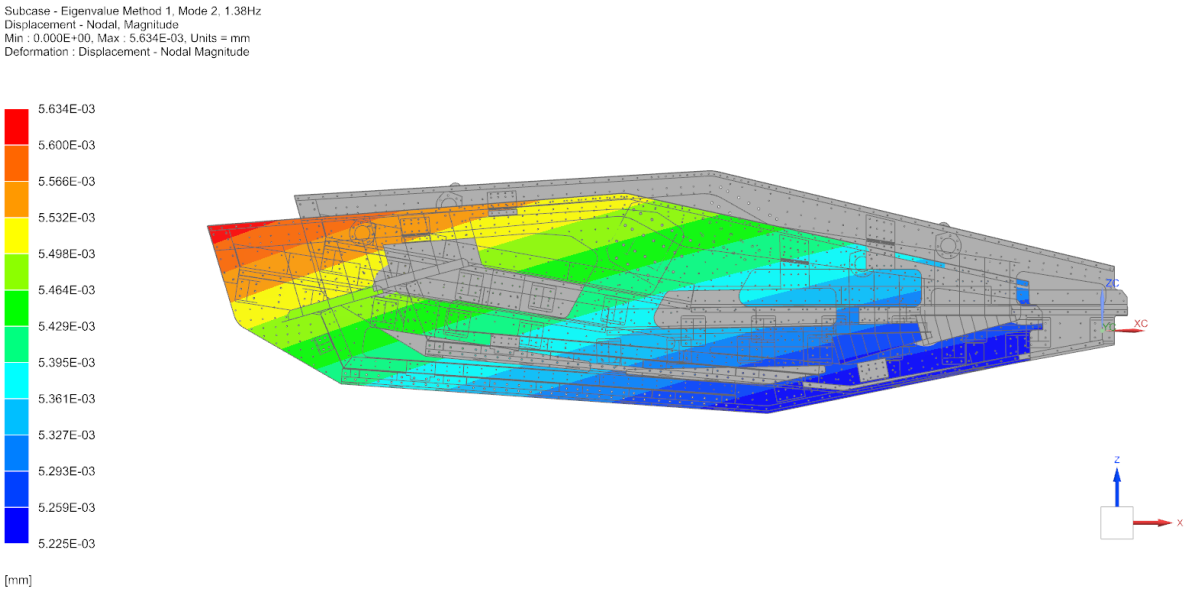

Figure 95: Horizontal bounce at 1.38Hz

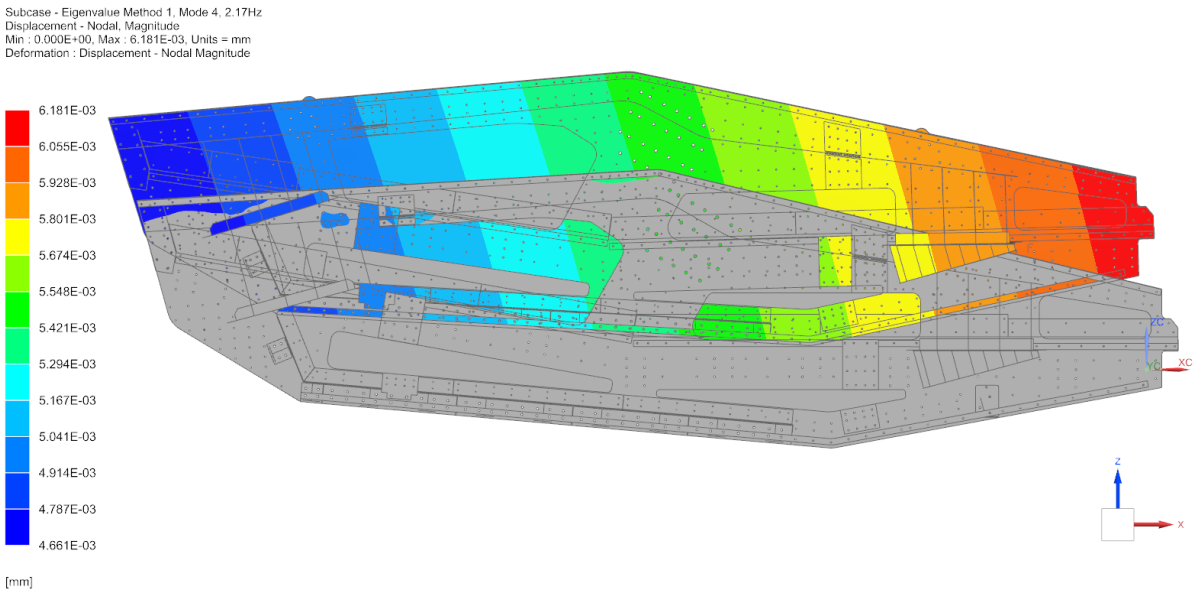

Figure 96: Vertical Bounce at 2.17Hz

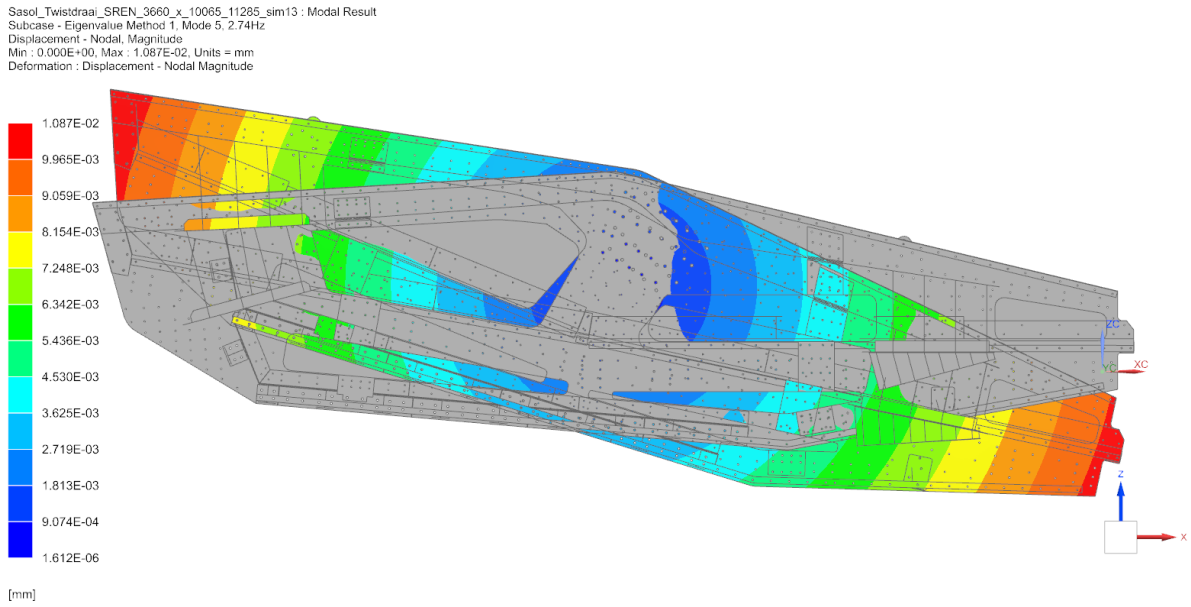

Figure 97: Pitch about lateral axis at 2.74Hz

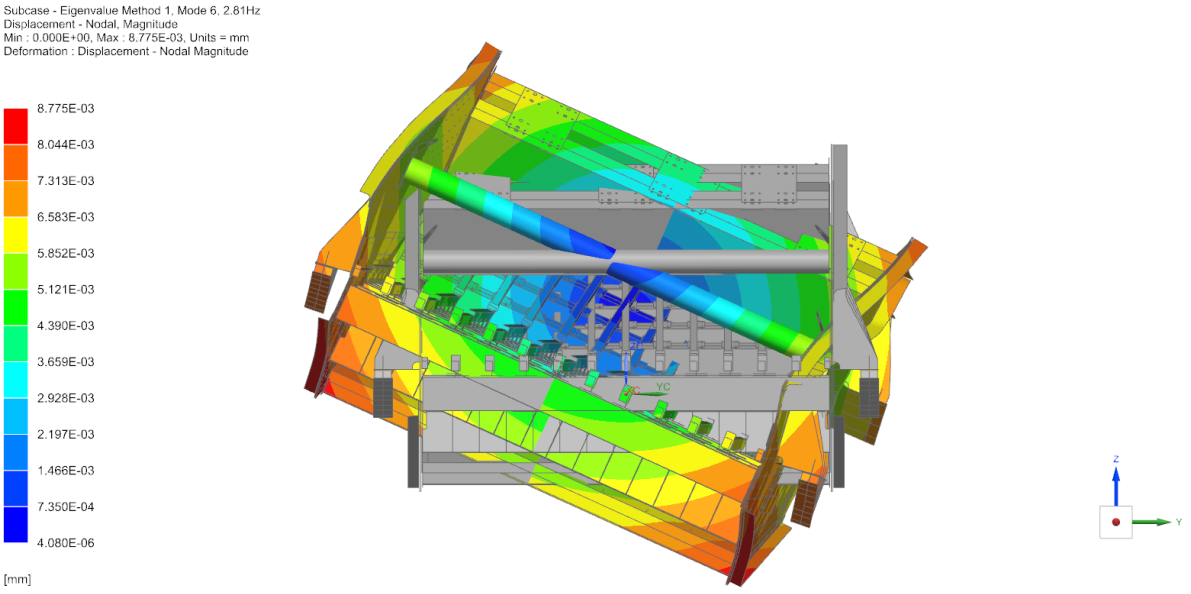

Figure 98: Rolling about the horizontal axis at 2.81Hz

8 APPENDIX H

8.1 EXPERIMENTS TEST CARD

The following page shows a sample of the test card document used during tests. This document ensures that no tests are missed and that all information relevant to the test is recorded.

Test NO: 11
Date: 06/06/2022
Test Description: Rubber Buffers Φ 120×50×140 (263 N/mm)
NO wooden blocks

Static Compression	F1 - R	F1 - L	F2 - R	F2 - L
Free Length				
Compressed Length	129	126	123	~~126~~ 127

Static Compression	F1 - R	F1 - L	F2 - R	F2 - L
Free Length				
Compressed Length	130	126	123	128

Modal Test Cold Time: 09:57 & 10:29 Results Checked: ✓
Modal Test Cold Time: 12:~~28~~ Results Checked: ✓

COLD

Test	Time	Comment	Temperature of Motors Before Start (°C)		Temperature of Isolators Before Start (°C)				VSD Motor Current (A)	Running Time (S)	Test Saved
			Motor left	Motor Right	F1 Left	F2 Left	F1 Right	F2 Right			
1	10:37		10,4	9,6	12,1	12,6	11,6	10,4	10,8	60	✓
2	10:43								10,8	60	✓
3	10:49								10,8	60	✓
4	10:53								10,8	60	✓
5	11:00								10,8	60	✓
			15,4	15,2	15,4	15,6	15,1	18,2			

WARM

Test	Time	Comment	Temperature of Motors Before Start (°C)		Temperature of Isolators Before Start (°C)				VSD Motor Current (A)	Running Time (S)	Test Saved
			Motor left	Motor Right	F1 Left	F2 Left	F1 Right	F2 Right			
1	12:41	ICP sensor F.-x having knocks	~~10,4~~	31,1	33,8	30,6	27,9	31,1	10,6	60	✓
2	12:51		32,6						10,8	60	✓
3	13:00								10,8	60	✓
4	13:05								10,8	60	✓
5	13:11								10,8	60	✓
	13:17			30,8	25,3	23,3	25,5	23,1	10,8	60	✓

9 APPENDIX I

9.1 NUMERICAL MODEL PARAMETERS

Table 21: Numerical model parameters for the vibrating screen used during experiments

Variables	Symbol	Units	Value
Distance CG to F2	a	m	1.144
Distance CG to F1	b	m	1.886
Perpendicular distance CG to line F1-F2	c	m	0.676
Vertical distance CG to exciter(s)	e	m	0.614
Horizontal distance CG to exciter(s)	f	m	0.527
Lateral distance CG to exciter(s)	g_1, g_2	m	0, 0
Distance F1L to F1R (= distance F2L to F2R)	w	m	1.125
Mass moment of inertia about pitching (y) axis	J_y	$kg.m^2$	1698.5006
Mass moment of inertia about pitching (x) axis	J_x	$kg.m^2$	673.8299
Mass of vibrating screen	m	kg	1720
Drive angle	α	°	50
Screen angle	β	°	0
Gravitational Acceleration	g_{acc}	m/s^2	9.81
Number of exciters	$N_{exciters}$		2
Working moment (unbalance $(\boldsymbol{m} \cdot \boldsymbol{r})$) per exciter	WM	Kg.cm	906
Weight setting	WS	%	100
Vertical Stiffness Per Corner	K_z	N/m	1x 330000
Horizontal Stiffness Per Corner	K_x	N/m	7x 165 000
Vertical Damping per corner	C_z	$\frac{N}{m}/s$	1650
Horizontal Damping per corner	C_x	$\frac{N}{m}/s$	825
Zeta (damping scaling factor)			1

Table 22: Parameters for the Runge-Kutta solver and exciter rpm calculator

Variables	Symbol	Units	Value
Time step	h	s	0.00083333
Initial time	t_0	s	0
Total time	T	s	110
Ramp up time	T_{up}	s	4
Coast down time	T_{down}	s	30
Machine stationary time	T_{stat}	s	5
Operating Speed	rpm_{op}	rpm	960

10 APPENDIX J

10.1 OTHER SENSOR RESULTS

The experiment results displayed in the body of this dissertation are from the ICP sensor. To perform a like for like comparison, Table 23 and Table 25 show the results from the Dysinet sensors and Table 24 and Table 26 show the results from the IFM sensors. Also, the box and whisker diagrams showing the statistical spread of the absolute percentage differences obtained from the measured sensor's responses are shown in Figure 99 and Figure 100 for the startups and Figure 101 and Figure 102 for the coast down measurements.

Table 23: Steady operation orbit feature results from Dysinet sensors

	Cond.	Fault	Angles	Width	Length	
Avg|Δ%|	Cold	All isolators	0.5%	3.1%	0.9%	
		F2R isolator	0.4%	3.7%	0.5%	
	Hot	All isolators	0.4%	3.1%	0.4%	
		F2R isolator	0.4%	3.1%	0.3%	
% corr.	Cold	All isolators	-18.8%	12.5%	56.3%	
		F2R isolator	-18.8%	43.8%	18.8%	
	Hot	All isolators	-25.0%	81.3%	50.0%	
		F2R isolator	-43.8%	48.4%	89.1%	
Δ feat./% fault	Cold	All isolators	20.94	0.70	7.42	$\times 10^{-3}$
		F2R isolator	19.37	0.66	4.01	$\times 10^{-3}$
	Hot	All isolators	15.66	0.62	2.86	$\times 10^{-3}$
		F2R isolator	13.56	0.66	2.03	$\times 10^{-3}$
		Units	°	mm	mm	per % fault

Table 24: Steady operation orbit feature results from IFM sensors

	Cond.	Fault	Angles	Width	Length	
Avg|Δ%|	Cold	All isolators	0.6%	17.6%	0.7%	
		F2R isolator	0.4%	8.8%	0.4%	
	Hot	All isolators	0.5%	8.5%	0.6%	
		F2R isolator	0.3%	7.5%	0.3%	
% corr.	Cold	All isolators	0.0%	93.8%	100.0%	
		F2R isolator	0.0%	56.3%	31.3%	
	Hot	All isolators	0.0%	18.8%	75.0%	
		F2R isolator	-37.5%	-75.0%	37.5%	
Δ feat./% fault	Cold	All isolators	31.30	4.11	6.97	$\times 10^{-3}$
		F2R isolator	20.82	2.59	3.44	$\times 10^{-3}$
	Hot	All isolators	22.98	1.85	4.03	$\times 10^{-3}$
		F2R isolator	13.36	3.66	2.15	$\times 10^{-3}$
		Units	°	mm	mm	per % fault

Table 25: Start and coast down results from Dysinet sensors Z response

			DYSINET SENSOR VIBRATION MEASUREMENT					CALCULATED PITCHING MOTION					CALCULATED ROLLING MOTION					
	Cond.	Fault	Freq.	Mag.	Width	RMS_{Peak}	RMS_{PSD}	Freq.	Mag.	Width	RMS_{Peak}	RMS_{PSD}	Freq.	Mag.	Width	RMS_{Peak}	RMS_{PSD}	
			FEATURE FROM VIBRATING SCREEN STARTS															
Avg|Δ%|	Cold	All	13.2%	54.4%	9.5%	24.1%	8.4%	16.2%	224.5%	6.9%	49.5%	42.6%	9.4%	51.8%	34.4%	25.0%	17.5%	
		F2R	5.5%	25.7%	5.5%	8.4%	5.1%	5.7%	95.8%	24.5%	54.6%	3.9%	11.0%	253.3%	22.7%	47.9%	33.7%	
	Hot	All	10.1%	37.6%	6.5%	15.9%	6.0%	10.9%	116.6%	15.2%	25.0%	11.7%	10.3%	106.0%	22.4%	51.0%	21.1%	
		F2R	3.9%	12.4%	3.5%	8.0%	3.1%	2.9%	49.4%	18.7%	39.7%	2.1%	5.5%	329.1%	22.7%	84.9%	60.2%	
% corr.	Cold	All	75.0%	35.0%	-0.6%	-5.6%	50.0%	87.5%	0.0%	-25.0%	-8.3%	100.0%	70.8%	50.0%	-37.5%	25.0%	75.0%	
		F2R	57.5%	15.0%	-60.0%	37.5%	50.0%	54.2%	16.7%	-16.7%	-16.7%	-50.0%	-45.8%	20.8%	-18.8%	-2.1%	-62.5%	
	Hot	All	65.6%	15.0%	25.0%	15.0%	50.0%	97.9%	-33.3%	-50.0%	-41.7%	50.0%	60.0%	30.0%	-23.8%	40.0%	50.0%	
		F2R	61.3%	80.0%	-30.0%	70.0%	75.0%	25.0%	-16.7%	-4.2%	-12.5%	-25.0%	11.3%	40.0%	-3.8%	15.0%	0.0%	
Δ feat. /% fault	Cold	All	44.52	221.19	44.27	22.24	30.00	40.90	78.74	7.76	11.05	48.39	37.95	3.40	24.19	1.56	6.27	$\times 10^{-3}$
		F2R	14.35	242.23	15.74	9.98	19.42	16.73	119.14	16.39	32.80	7.11	56.46	21.03	21.65	6.32	12.51	$\times 10^{-3}$
	Hot	All	22.51	274.37	29.60	16.74	24.51	29.47	83.53	19.13	9.33	26.69	27.44	6.49	13.21	4.25	8.73	$\times 10^{-3}$
		F2R	8.16	207.96	10.03	9.66	12.08	6.89	99.20	13.74	26.96	3.64	23.30	38.16	18.02	8.79	22.20	$\times 10^{-3}$
		Units	Hz	mm^2/Hz	Hz	mm	mm	Hz	mm^2/Hz	Hz	mm	mm	Hz	mm^2/Hz	Hz	mm	mm	per % fault
			FEATURES FROM VIBRATING SCREEN COAST DOWNS															
Avg|Δ%|	Cold	All	11.1%	21.0%	24.1%	22.1%	5.3%	12.2%	132.7%	12.5%	49.9%	29.5%	13.3%	37.4%	16.5%	25.0%	27.4%	
		F2R	6.3%	18.7%	37.5%	11.4%	3.4%	6.9%	74.5%	12.6%	36.7%	10.6%	5.7%	65.4%	12.9%	34.6%	12.1%	
	Hot	All	10.2%	17.7%	12.6%	13.3%	4.4%	6.9%	93.3%	21.5%	33.9%	27.4%	8.1%	89.3%	22.5%	26.4%	16.3%	
		F2R	4.2%	25.3%	35.3%	11.9%	7.2%	11.3%	58.9%	25.2%	44.8%	13.9%	4.2%	168.7%	24.5%	36.4%	26.7%	
% corr.	Cold	All	79.5%	29.8%	-7.7%	19.0%	93.8%	96.9%	100.0%	18.8%	100.0%	100.0%	100%	25.0%	0.0%	-37.5%	0.0%	
		F2R	64.1%	47.9%	-44.8%	-7.3%	62.5%	-18.8%	50.0%	-31.3%	0.0%	100.0%	81.3%	-47.5%	65.0%	-42.5%	-37.5%	
	Hot	All	62.5%	12.2%	-6.3%	15.9%	75.0%	-18.8%	100.0%	-56.3%	56.3%	100.0%	71.9%	-50.0%	87.5%	-25.0%	-75.0%	
		F2R	16.1%	39.6%	-40.6%	34.4%	50.0%	-25.0%	75.0%	-50.0%	0.0%	12.5%	43.8%	-37.5%	87.5%	-12.5%	0.0%	
Δ feat. /% fault	Cold	All	33.25	34.75	38.58	23.37	12.50	36.78	96.57	18.47	19.81	39.94	36.97	39.91	11.77	15.74	44.86	$\times 10^{-3}$
		F2R	26.84	36.51	36.45	12.07	7.12	16.38	100.97	16.45	19.73	15.91	23.85	129.93	14.32	22.75	19.32	$\times 10^{-3}$
	Hot	All	29.54	35.19	24.48	13.20	9.20	17.63	141.20	19.97	14.49	47.50	15.18	140.20	16.34	15.37	23.88	$\times 10^{-3}$
		F2R	15.21	55.90	34.34	12.11	14.65	29.54	108.48	18.62	24.97	25.87	9.45	288.52	15.45	21.60	40.22	$\times 10^{-3}$
		Units	Hz	mm^2/Hz	Hz	mm	mm	Hz	mm^2/Hz	Hz	mm	mm	Hz	mm^2/Hz	Hz	mm	mm	per % fault

Table 26: Start and coast down results from IFM sensors Z response

			IFM SENSOR VIBRATION MEASUREMENT					CALCULATED PITCHING MOTION					CALCULATED ROLLING MOTION					
	Cond.	Fault	Freq.	Mag.	Width	RMS_{Peak}	RMS_{PSD}	Freq.	Mag.	Width	RMS_{Peak}	RMS_{PSD}	Freq.	Mag.	Width	RMS_{Peak}	RMS_{PSD}	
			FEATURE FROM VIBRATING SCREEN STARTS															
Avg|Δ%|	Cold	All	12.5%	41.6%	7.3%	19.1%	7.0%	17.0%	181.9%	8.4%	44.8%	41.7%	11.9%	147.0%	16.7%	46.8%	34.5%	
		F2R	4.9%	17.9%	4.5%	7.3%	3.4%	6.5%	93.3%	18.0%	53.3%	2.6%	8.5%	141.8%	14.2%	36.4%	32.1%	
	Hot	All	9.8%	31.8%	5.6%	14.0%	6.0%	11.4%	93.4%	12.2%	28.0%	12.0%	11.1%	58.7%	32.5%	36.6%	25.9%	
		F2R	3.5%	14.1%	4.5%	8.7%	3.6%	2.3%	55.1%	21.1%	49.5%	2.3%	6.7%	235.8%	19.8%	55.6%	65.8%	
% corr.	Cold	All	75.0%	75.0%	-12.5%	37.5%	75.0%	85.4%	50.0%	2.1%	45.8%	100.0%	79.2%	83.3%	-8.3%	58.3%	100.0%	
		F2R	55.6%	15.0%	-60.0%	25.0%	50.0%	58.3%	4.2%	18.8%	-12.5%	-25.0%	-1.0%	14.6%	12.5%	18.8%	-62.5%	
	Hot	All	68.8%	55.0%	5.0%	58.1%	100.0%	100.0%	16.7%	-50.0%	-22.9%	100.0%	62.5%	33.3%	29.2%	33.3%	50.0%	
		F2R	55.6%	77.5%	-27.5%	77.5%	93.8%	33.3%	4.2%	8.3%	16.7%	37.5%	3.1%	20.8%	39.6%	4.2%	0.0%	
Δ feat. /% fault	Cold	All	41.46	202.18	32.41	19.10	26.30	38.04	66.25	8.00	11.15	39.10	43.12	4.60	12.53	3.06	7.61	$\times 10^{-3}$
		F2R	12.74	146.94	11.55	7.99	12.81	16.80	104.70	11.22	25.95	2.16	30.70	11.58	12.76	3.51	9.56	$\times 10^{-3}$
	Hot	All	20.44	261.59	26.18	16.53	24.58	25.19	72.87	10.58	8.63	18.05	31.14	5.72	19.43	5.19	8.98	$\times 10^{-3}$
		F2R	6.30	174.33	14.96	10.63	13.20	4.96	93.13	9.93	28.70	2.57	19.42	26.53	12.97	5.94	17.38	$\times 10^{-3}$
		Units	Hz	mm^2/Hz	Hz	mm	mm	Hz	mm^2/Hz	Hz	mm	mm	Hz	mm^2/Hz	Hz	mm	mm	per % fault
			FEATURES FROM VIBRATING SCREEN COAST DOWNS															
Avg|Δ%|	Cold	All	10.2%	19.3%	57.7%	28.1%	5.9%	7.3%	145.1%	28.3%	63.5%	37.4%	20.2%	43.5%	17.1%	38.0%	36.4%	
		F2R	5.7%	15.7%	36.8%	10.2%	3.0%	7.3%	86.8%	26.8%	38.6%	13.4%	4.6%	56.1%	8.4%	31.3%	14.3%	
	Hot	All	8.7%	13.9%	13.9%	8.0%	4.8%	7.3%	91.8%	26.1%	45.0%	26.4%	9.0%	82.7%	29.6%	16.7%	18.3%	
		F2R	5.8%	18.6%	36.3%	11.9%	6.4%	8.7%	60.7%	24.4%	44.1%	16.0%	5.0%	162.9%	31.4%	23.0%	24.8%	
% corr.	Cold	All	57.3%	45.8%	-25.0%	27.1%	100.0%	43.8%	87.5%	-6.3%	93.8%	100.0%	100%	31.3%	6.3%	-31.3%	0.0%	
		F2R	35.5%	37.1%	-15.3%	0.2%	56.3%	6.3%	50.0%	-12.5%	6.3%	100.0%	78.1%	-25.0%	75.0%	-25.0%	-75.0%	
	Hot	All	51.3%	41.6%	-15.6%	52.0%	93.8%	6.3%	100.0%	-37.5%	31.3%	100.0%	75.0%	-50.0%	81.3%	31.3%	-75.0%	
		F2R	-12%	43.8%	-6.1%	21.8%	81.3%	-6.3%	50.0%	-43.8%	0.0%	0.0%	50.0%	-50.0%	87.5%	0.0%	0.0%	
Δ feat. /% fault	Cold	All	36.54	27.43	86.35	30.62	15.05	18.67	79.44	35.09	20.04	47.97	48.28	42.64	10.42	21.65	52.58	$\times 10^{-3}$
		F2R	26.44	26.10	34.87	10.91	6.14	22.36	93.43	26.41	16.95	19.18	9.83	86.11	5.63	16.21	21.21	$\times 10^{-3}$
	Hot	All	28.09	24.58	14.21	8.44	10.25	15.77	98.27	29.17	16.44	41.32	16.89	91.94	23.50	8.30	24.22	$\times 10^{-3}$
		F2R	25.27	34.13	30.50	11.77	14.21	29.57	80.74	22.75	21.26	26.24	11.19	205.31	21.40	12.15	30.99	$\times 10^{-3}$
		Units	Hz	mm^2/Hz	Hz	mm	mm	Hz	mm^2/Hz	Hz	mm	mm	Hz	mm^2/Hz	Hz	mm	mm	per % fault

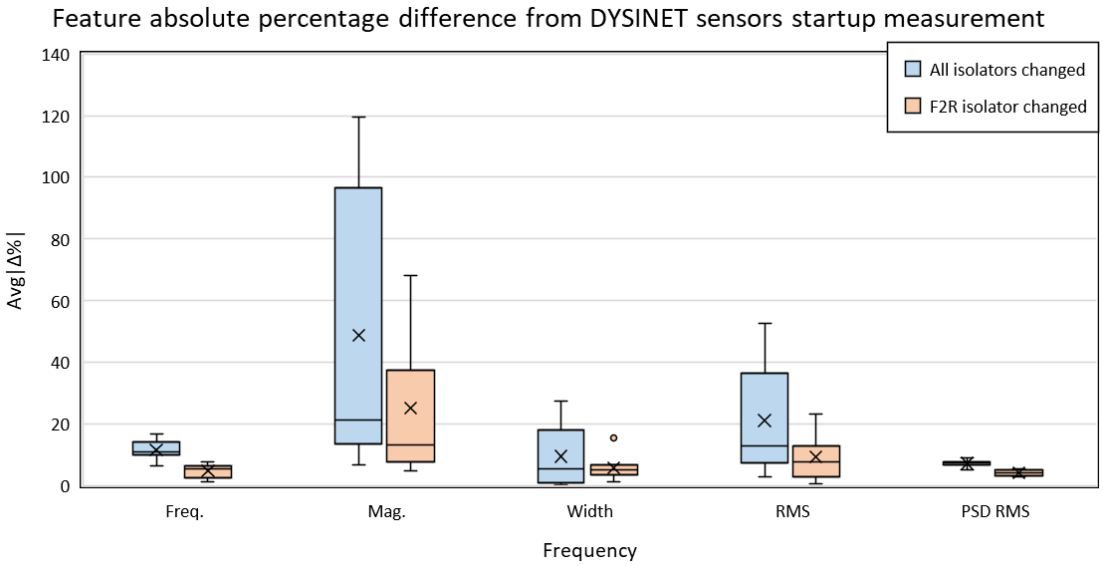

Figure 99: Box and whisker plot for features from Dysinet sensor startup measurements

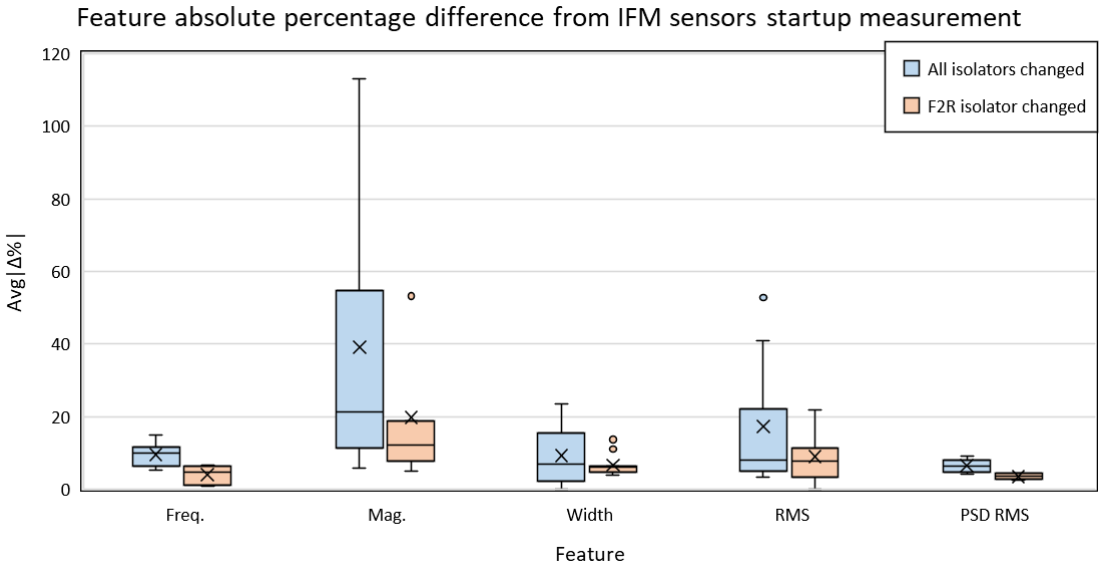

Figure 100: Box and whisker plot for features from IFM sensor startup measurements

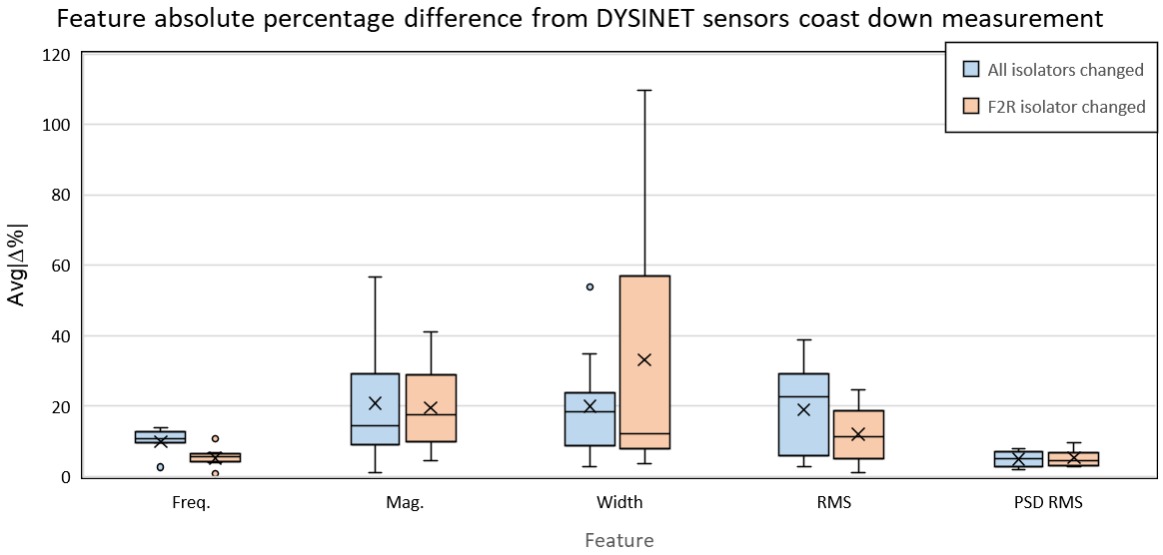

Figure 101: Box and whisker plot for features from Dysinet sensor coast down measurements

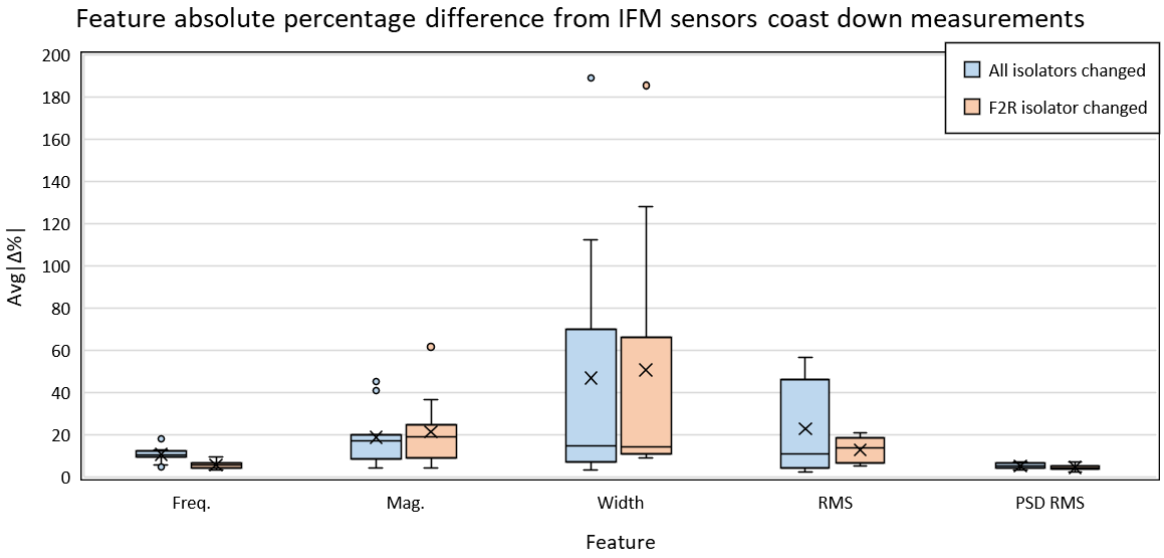

Figure 102: Box and whisker plot for features from IFM sensor coast down measurements

11 APPENDIX K

11.1 MODAL RESULTS FROM OTHER SENSORS

Table 27: Differences in natural frequencies from Dysinet sensor Z responses

Conf. No.	Natural Frequencies (Hz)		Difference (Hot-Cold)	Difference All Isolators		Difference F2R isolator		Mode
	Cold	Hot		Cold	Hot	Cold	Hot	
2: Resatecs	5.59	5.30	-5.40%	11.5%	0.9%	-1.6%	-0.7%	***RBM 1***
	9.17	8.97	-2.36%	15.8%	3.6%	0.3%	-1.5%	***RBM 2***
	19.37	19.46	1.99%	3.4%	-0.9%	2.7%	-1.1%	***RBM 3***
	33.96	33.86	-0.34%	2.7%	0.3%	0.5%	-0.4%	FBM 1
	47.61	47.68	0.15%	0.8%	-0.1%	0.3%	0.0%	FBM 2
	55.73	55.66	-0.12%	1.1%	0.2%	0.2%	0.0%	FBM 3
	72.47	72.51	0.06%	0.5%	0.0%	0.2%	0.0%	FBM 4
	85.20	85.36	0.22%	0.1%	-0.2%	0.2%	-0.1%	FBM 5
	90.99	91.14	0.15%	0.3%	0.0%	0.1%	-0.1%	FBM 6
5: Coil Springs	2.82	2.82	-0.16%	-11.3%	-11.3%	-5.0%	-4.7%	***RBM 1***
	4.47	4.40	-0.20%	-7.2%	-6.5%	-2.7%	-3.2%	***RBM 2***
	5.16	5.16	-0.17%	-16.9%	-16.7%	-1.8%	-1.9%	***RBM 3***
	31.17	31.16	-0.05%	-0.6%	-0.6%	-0.2%	-0.1%	FBM 1
	46.99	46.98	-0.03%	-0.1%	-0.1%	-0.2%	-0.2%	FBM 2
	55.21	55.18	-0.05%	0.0%	0.0%	-0.1%	-0.1%	FBM 3
	71.88	71.81	-0.10%	-1.0%	-0.9%	-0.2%	-0.1%	FBM 4
	85.23	85.17	-0.09%	0.0%	0.0%	-0.1%	0.0%	FBM 5
	90.55	90.46	-0.05%	0.3%	0.3%	-0.2%	-0.2%	FBM 6
9: Rubber buffers	5.06	4.75	-5.65%	***N/A***				***RBM 1***
	5.63	5.17	-8.69%					***RBM 2***
	8.34	7.82	-5.98%					***RBM 3***
	32.66	32.43	-0.69%					FBM 1
	47.37	47.29	-0.15%					FBM 2
	55.94	55.82	-0.22%					FBM 3
	72.31	72.23	-0.12%					FBM 4
	85.19	85.20	0.04%					FBM 5
	91.16	91.16	-0.02%					FBM 6

Table 28: Differences in natural frequencies from IFM sensor Z responses

Conf. No.	Natural Frequencies (Hz)		Difference (Hot-Cold)	Difference All Isolators		Difference F2R isolator		Mode
	Cold	Hot		Cold	Hot	Cold	Hot	
2: Resatecs	5.59	5.30	-5.12%	11.1%	0.8%	-1.3%	-0.9%	***RBM 1***
	9.17	8.97	-2.23%	17.8%	4.1%	0.7%	-1.2%	***RBM 2***
	19.37	19.46	0.91%	4.2%	-0.5%	1.4%	-1.2%	***RBM 3***
	33.96	33.86	-0.32%	2.7%	0.3%	0.5%	-0.3%	FBM 1
	47.61	47.68	0.16%	0.8%	-0.1%	0.3%	-0.1%	FBM 2
	55.73	55.66	-0.11%	1.1%	0.1%	0.2%	0.0%	FBM 3
	72.47	72.51	0.06%	0.4%	0.0%	0.2%	0.0%	FBM 4
	85.20	85.36	0.23%	0.1%	-0.2%	0.1%	-0.1%	FBM 5
	90.99	91.14	0.16%	0.3%	0.0%	0.1%	-0.1%	FBM 6
5: Coil Springs	2.82	2.82	-0.54%	-11.7%	-12.1%	-5.2%	-5.0%	***RBM 1***
	4.47	4.40	-1.30%	-7.6%	-8.3%	-3.9%	-3.0%	***RBM 2***
	5.16	5.16	-0.26%	-16.0%	-16.0%	-2.0%	-2.0%	***RBM 3***
	31.17	31.16	-0.03%	-0.5%	-0.6%	-0.2%	-0.1%	FBM 1
	46.99	46.98	-0.03%	-0.1%	-0.1%	-0.2%	-0.2%	FBM 2
	55.21	55.18	-0.05%	0.0%	0.0%	-0.1%	-0.1%	FBM 3
	71.88	71.81	-0.09%	-1.0%	-0.9%	-0.2%	-0.1%	FBM 4
	85.23	85.17	-0.06%	0.1%	0.0%	-0.1%	-0.1%	FBM 5
	90.55	90.46	-0.17%	0.1%	0.2%	-0.2%	-0.2%	FBM 6
9: Rubber buffers	5.06	4.75	-6.70%	***N/A***				***RBM 1***
	5.63	5.17	-8.53%					***RBM 2***
	8.34	7.82	-6.01%					***RBM 3***
	32.66	32.43	-0.69%					FBM 1
	47.37	47.29	-0.18%					FBM 2
	55.94	55.82	-0.22%					FBM 3
	72.31	72.23	-0.14%					FBM 4
	85.19	85.20	-0.04%					FBM 5
	91.16	91.16	-0.03%					FBM 6

11.2 Damping Ratios graphical results

Table 29 shows the damping ratios obtained for all modal analyses from the Z responses. The damping ratios obtained from each sensor's response is shown in each respective vertical axis. The order of the graphs in rows are for all Resatec, coil spring and rubber buffers tests respectively. The y axis for each graph has the same tick marks so visual comparisons are easily made. The damping ratios obtained from the Resatec configurations are almost 100% more than the damping ratios from the other configurations.

Table 29: Damping ratios for each test's sensor Z responses

ICP Accelerometers	Dysinet Accelerometers	IFM Accelerometers
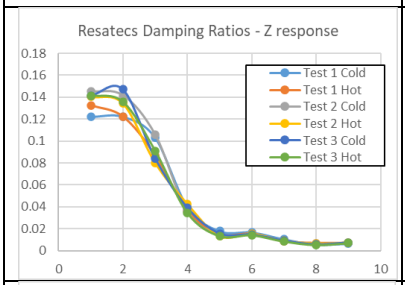	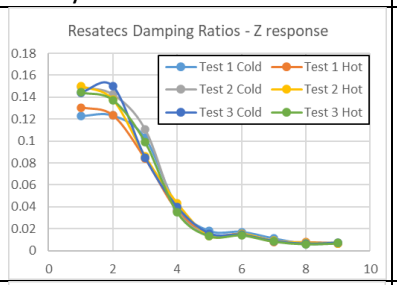	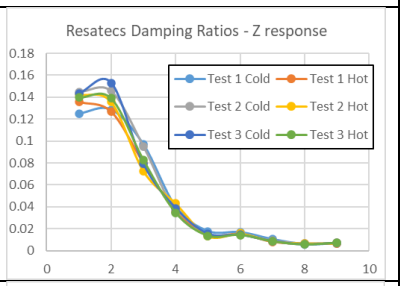
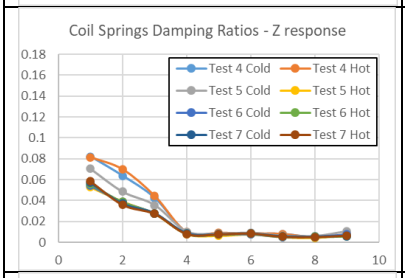	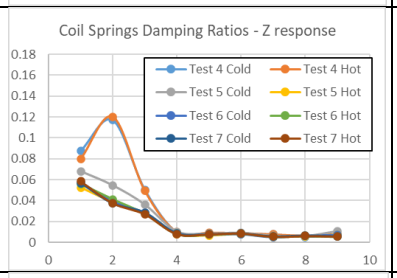	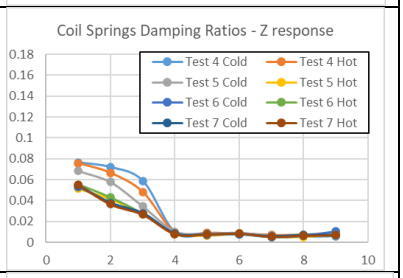
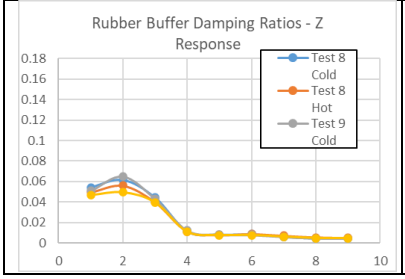	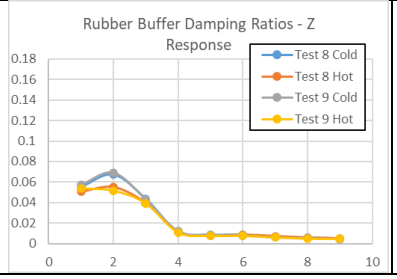	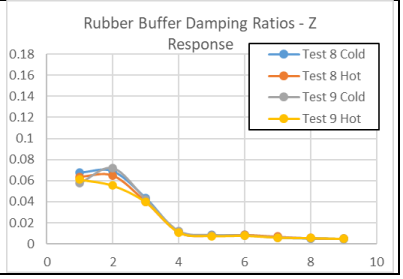

11.3 Mode shapes for RBMs and FBMs

See the next pages for RBM and FBM mode shapes.

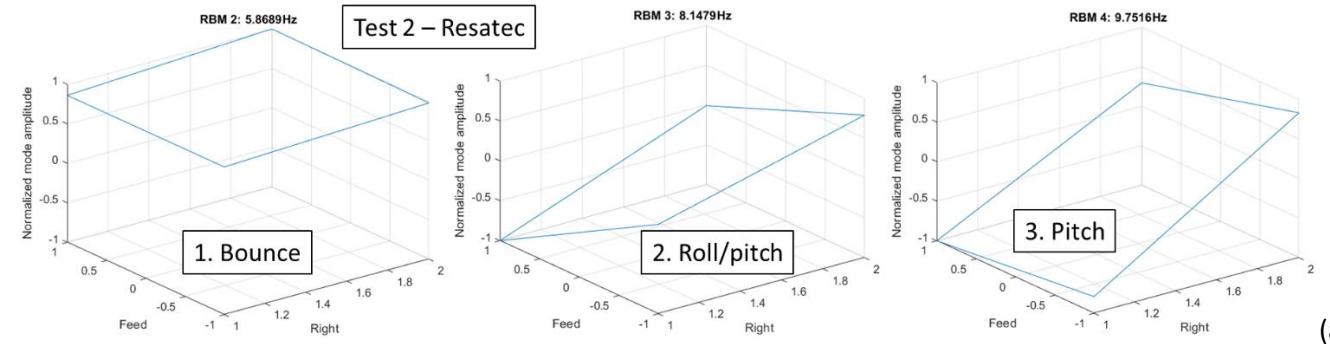

(a)

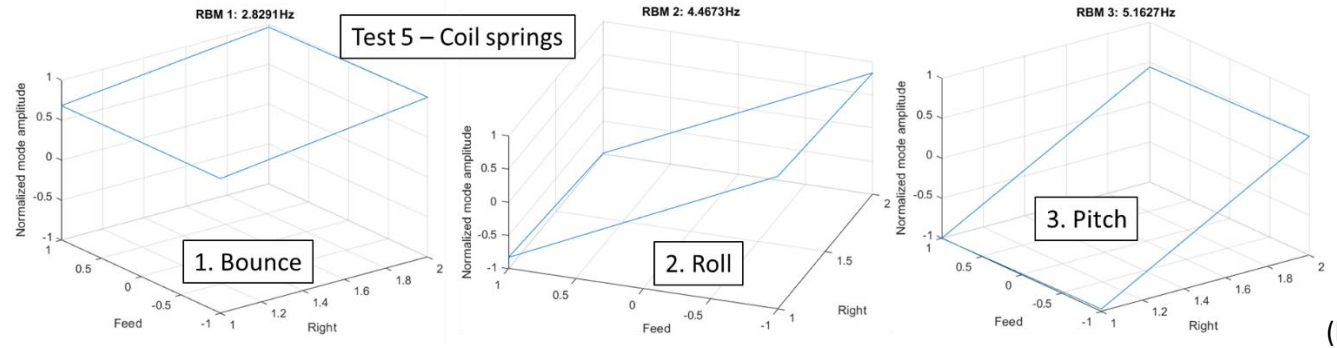

(b)

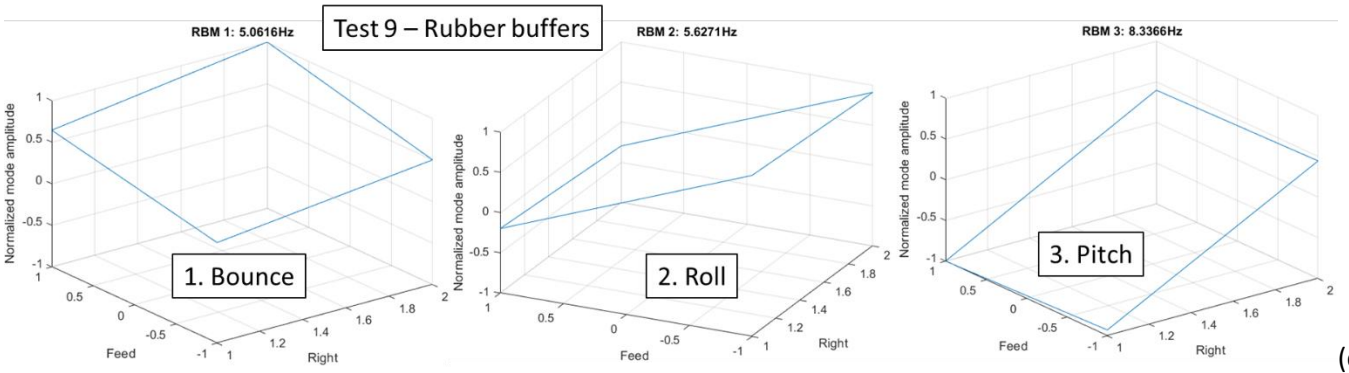

(c)

Figure 103: RBM Z-direction mode shapes for a) Test 2, b) Test 5 and c) Test 9

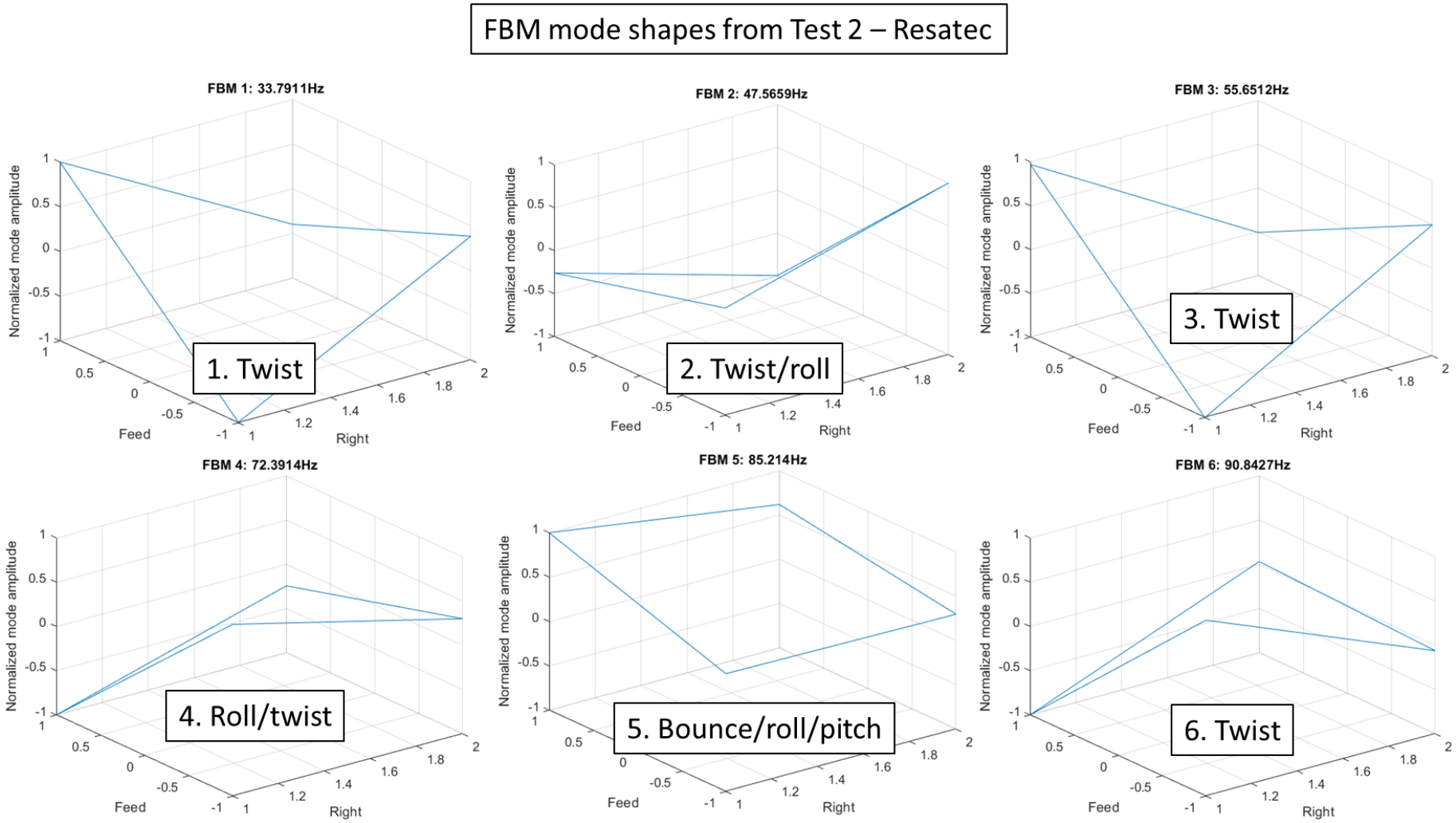

Figure 104: FBM mode shapes for test 2 Z response

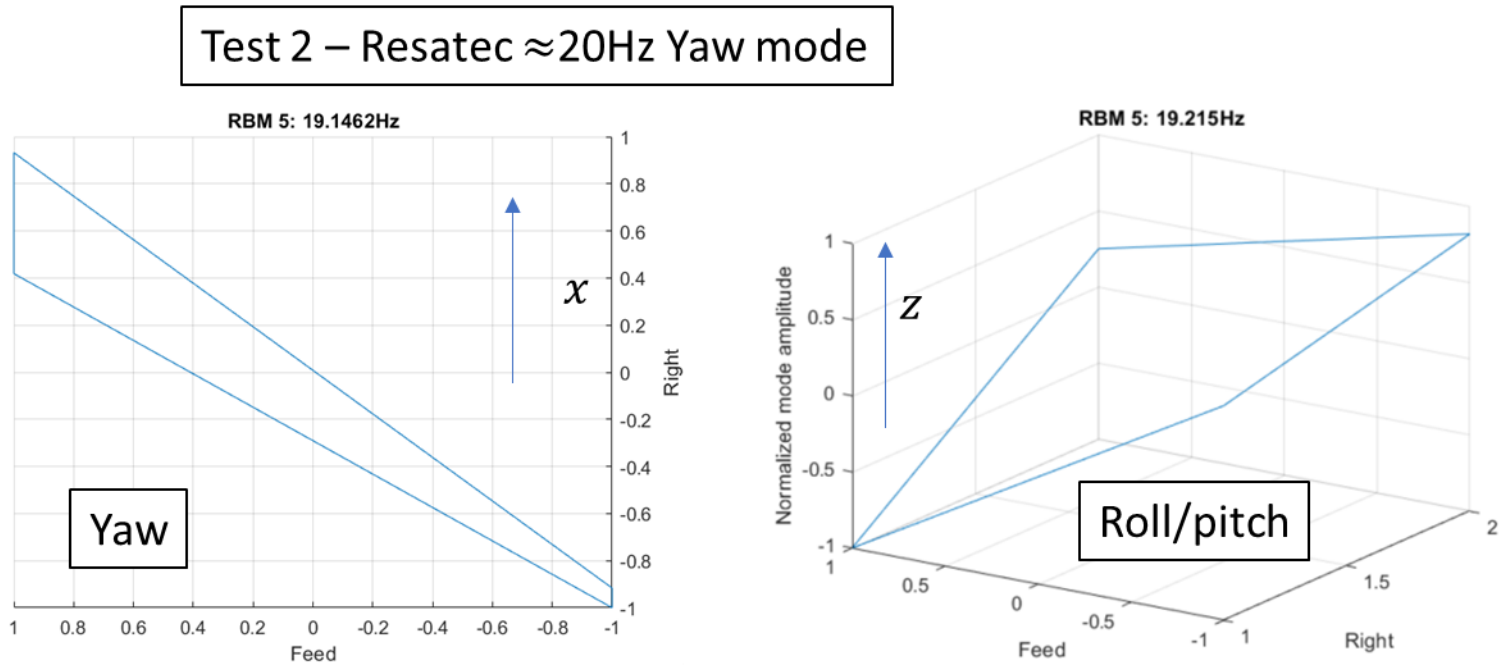

Figure 105: Yaw RBM mode shapes for test 2

Notice in Figure 105 that the X direction mode shape is on the left and the Z direction mode shape is on the right. The yaw shape is more distinct in the X direction mode shape.

12 APPENDIX L

12.1 ANALYSIS OF MECHANICAL FILTER

Differences between tests 6 and 7 as well as between tests 8 and 9 are used to evaluate the effects of wooden blocks as mechanical filters. Table 30 shows the differences in natural frequencies obtained for tests before and after the mechanical filter is introduced on the ICP sensors only. Greater differences in natural frequency are observed for the rubber buffers tests in cold conditions. The ambient temperatures differed between the cold condition test for tests 8 and 9 and therefore the rubber temperatures also differed which may have influenced the results. However, the behaviour of the ICP sensor results is the same as those obtained from the Dysinet and IFM sensors. The introduction of wooden blocks as a mechanical filter does not influence the modal results and also mitigates ICP sensor saturation successfully. In addition, the difference in damping ratios is negligible as seen in Table 29.

Table 30: Comparison of tests before and after mechanical filter is introduced on ICP sensor

Sensor and Mode		Difference Test 7 – Test 6				Difference Test 9 – Test 8			
		Cold	%	Hot	%	Cold	%	Hot	%
ICP	***RBM 1***	***0.006***	***0.24***	***0.003***	***0.11***	***-0.194***	***-3.82***	***-0.026***	***-0.54***
	RBM 2	***-0.007***	***-0.16***	***0.019***	***0.46***	***-0.254***	***-4.50***	***-0.032***	***-0.62***
	RBM 3	***0.002***	***0.05***	***-0.002***	***-0.04***	***-0.290***	***-3.48***	***-0.026***	***-0.34***
	FBM 1	0.001	0.00	-0.010	-0.03	-0.130	-0.40	-0.042	-0.13
	FBM 2	-0.024	-0.05	-0.035	-0.07	-0.048	-0.10	-0.018	-0.04
	FBM 3	0.000	0.00	-0.024	-0.04	-0.226	-0.40	-0.127	-0.23
	FBM 4	0.040	0.06	0.014	0.02	-0.099	-0.14	-0.067	-0.09
	FBM 5	-0.056	-0.07	-0.053	-0.06	-0.043	-0.05	-0.030	-0.04
	FBM 6	-0.038	-0.04	0.080	0.09	-0.064	-0.07	-0.058	-0.06
Dysinet	***RBM 1***	***0.000***	***0.01***	***0.002***	***0.06***	***-0.172***	***-3.40***	***-0.029***	***-0.61***
	RBM 2	***-0.035***	***-0.82***	***0.015***	***0.35***	***-0.279***	***-4.93***	***-0.024***	***-0.46***
	RBM 3	***0.000***	***-0.01***	***-0.003***	***-0.06***	***-0.281***	***-3.38***	***-0.025***	***-0.32***
	FBM 1	0.001	0.00	-0.015	-0.05	-0.124	-0.38	-0.039	-0.12
	FBM 2	-0.022	-0.05	-0.033	-0.07	-0.047	-0.10	-0.018	-0.04
	FBM 3	-0.002	0.00	-0.024	-0.04	-0.225	-0.40	-0.123	-0.22
	FBM 4	0.055	0.08	0.009	0.01	-0.090	-0.12	-0.065	-0.09
	FBM 5	-0.067	-0.08	-0.021	-0.02	-0.045	-0.05	-0.065	-0.08
	FBM 6	-0.054	-0.06	0.066	0.07	-0.063	-0.07	-0.063	-0.07
IFM	***RBM 1***	***-0.001***	***-0.04***	***0.002***	***0.06***	***-0.199***	***-3.93***	***-0.006***	***-0.14***
	RBM 2	***-0.005***	***-0.12***	***0.016***	***0.37***	***-0.281***	***-4.98***	***-0.032***	***-0.61***
	RBM 3	***0.002***	***0.03***	***0.003***	***0.05***	***-0.279***	***-3.35***	***-0.026***	***-0.33***
	FBM 1	0.002	0.01	-0.012	-0.04	-0.126	-0.39	-0.040	-0.12
	FBM 2	-0.026	-0.06	-0.033	-0.07	-0.048	-0.10	-0.012	-0.03
	FBM 3	0.001	0.00	-0.027	-0.05	-0.230	-0.41	-0.125	-0.22
	FBM 4	0.039	0.05	0.012	0.02	-0.099	-0.14	-0.049	-0.07
	FBM 5	-0.001	0.00	0.009	0.01	-0.042	-0.05	-0.003	0.00
	FBM 6	-0.113	-0.12	0.069	0.08	-0.048	-0.05	-0.044	-0.05

13 APPENDIX M

13.1 IFM DAQ ANOMALY SUMMARY

13.1.1 Introduction

This short document shows some observations made during tests performed using IFM's VSE 002 diagnostic modules with AnReSa firmware flashed (version unknown). The anomalies detected could be a combination of firmware and hardware as the AnReSa firmware is not a commercial IFM product and the version of the firmware is not the latest. Upgrading to the latest version could alleviate the anomalies. Also, the hardware of the IFM VSE 002 module is an older version and an updated version of the hardware is available.

13.1.2 Test Description

A vibrating screen was instrumented with 8 Accelerometers (VSA 004) and 2 Inductive sensors (IGW 200) for speed pickup on separate two unbalanced motors. In conjunction with the VSA 004 accelerometers, Industrial ICP and MEMS sensors are used to measure the acceleration on the 4 corners of the screen in the vertical and horizontal directions.

The VSA 004, and IGW 200 sensors were sampled using two VSE 002 modules that received the same trigger from a computer in Kwatani's laboratory. AnReSa is configured to measure at its default sampling rate (100kHz).

The Industrial ICP and MEMS sensors are sampled using an HBM DAQ (Quantum X) which is suitable for lab testing. The Quantum is set to sample at 1200Hz. It is therefore necessary to filter and down sample the IFM sensors during post processing.

Due to the VSE 002 module and the HBM Quantum receiving different triggers it is also necessary to cross correlate the IFM sensor with the others to synchronize measurements for comparisons.

Two types of tests were performed:

1. Impact Hammer Test – the vibrating screen is hit with a rubber hammer to determine natural frequencies of the vibrating screen.
2. Transient Test – the vibrating screen is started, left to run for a few seconds and then coast down to a complete stop.

13.1.3 Test 1 Impulse Hammer Results

Figure 106 below shows the time domain results obtained during the tests. The screen was hit 8 times with the rubber hammer. The IFM measurement is filtered and down sampled to 1200Hz. The cross-correlated result is also shown, this is where the IFM sensor is synchronized with the other sensor measurements. A more detailed description of the time domain comparison will be discussed in the next section, however there are magnitude differences, which is a direct result of the sampling rates, filtering and down sampling algorithms used. The frequency content is the most important information.

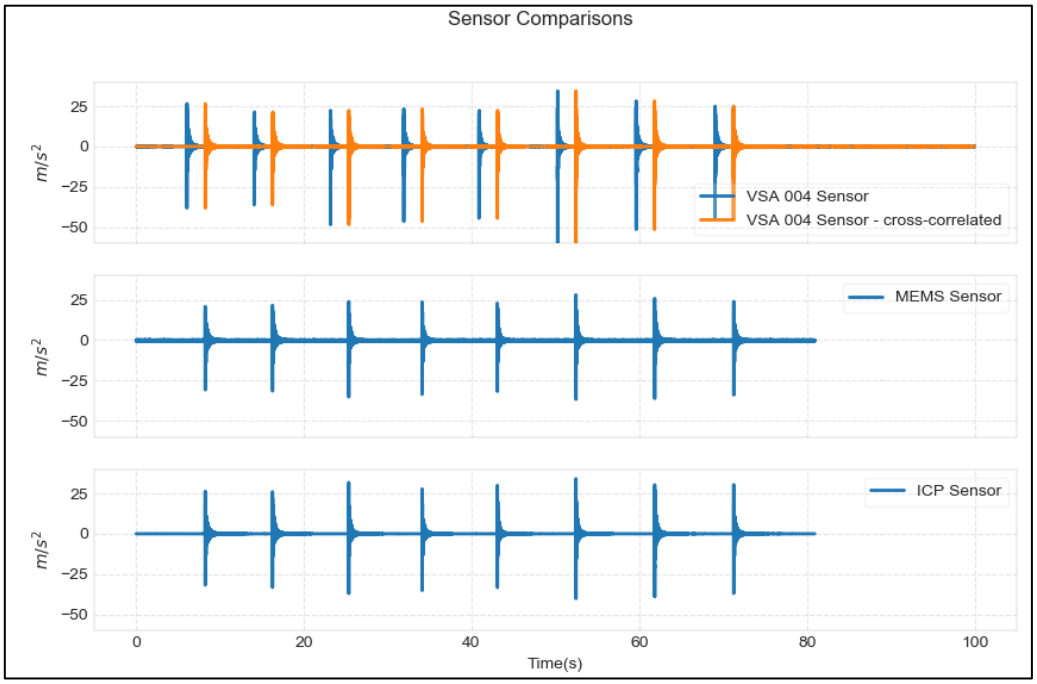

Figure 106: Hammer Test Time Domain Comparison

Figure 107 shows the frequency domain results obtained for the tests. All the sensors contain the same frequency content (i.e. peaks at the same frequencies) within the frequency range shown with changes in amplitude observed. These differences in amplitude are reduced by using averages of several measured impulse responses.

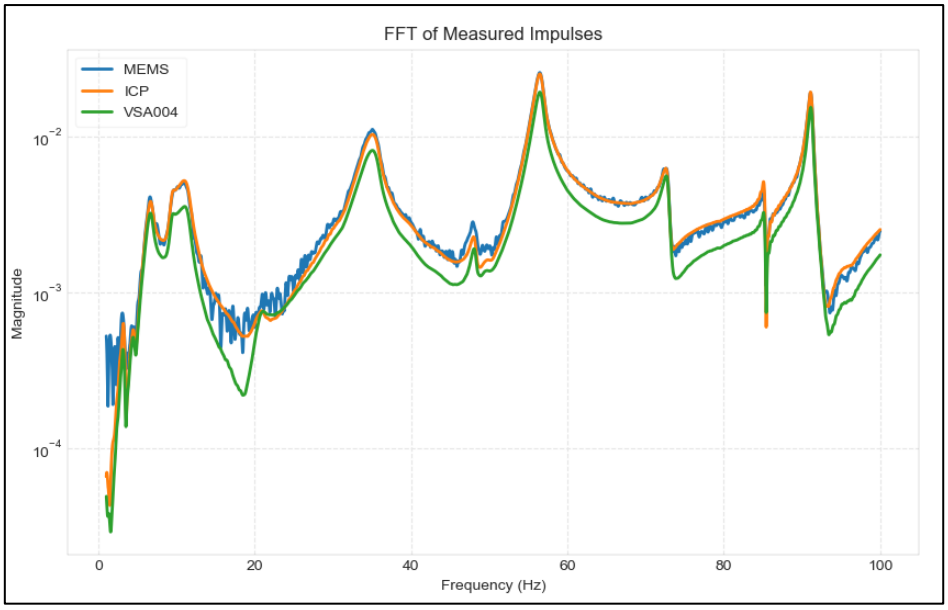

Figure 107: Frequency Domain comparison of hammer test impulses

13.1.4 Test 1 Observations

During cross-correlation the IFM sensor is offset by N number of samples to align/synchronize the IFM sensor measurement with the other sensor measurements. An impulse event is used to cross-correlate and calculate the offset. Figure 106 above shows the IFM measurement offset by the cross-correlation of the first impulse. The offset obtained for the first impulse was not the same as the offset obtained for the other impulses. Assuming a sample rate of 100kHz for the IFM sensors and 1.2kHz for the other sensors the following offsets were obtained per impulse:

- The offset for the IFM sensor impulse 1: -2628 samples
- The offset for the IFM sensor impulse 2: -2631 samples
- The offset for the IFM sensor impulse 3: -2633 samples
- The offset for the IFM sensor impulse 4: -2636 samples
- The offset for the IFM sensor impulse 5: -2644 samples
- The offset for the IFM sensor impulse 6: -2647 samples
- The offset for the IFM sensor impulse 7: -2685 samples
- The offset for the IFM sensor impulse 8: -2687 samples

The negative offset means that the IFM sensor leads the other sensor measurements and therefore $N = |offset|$ samples need to be added at the start of the IFM measurement. The offset appears to increase incrementally. An explanation for this change in offset is that the assumption that the IFM sensors are sampled at exactly 100kHz is incorrect.

Figure 108 below shows the time domain comparison along with some close ups of impulse observed early in the signal as well as towards the end of the signal. As mentioned, the entire measured signal is offset using the offset computed for the first impulse only. It is clear the first pulse is completely synchronized whereas the third pulse is not, and the last pulse is also completely out of sync.

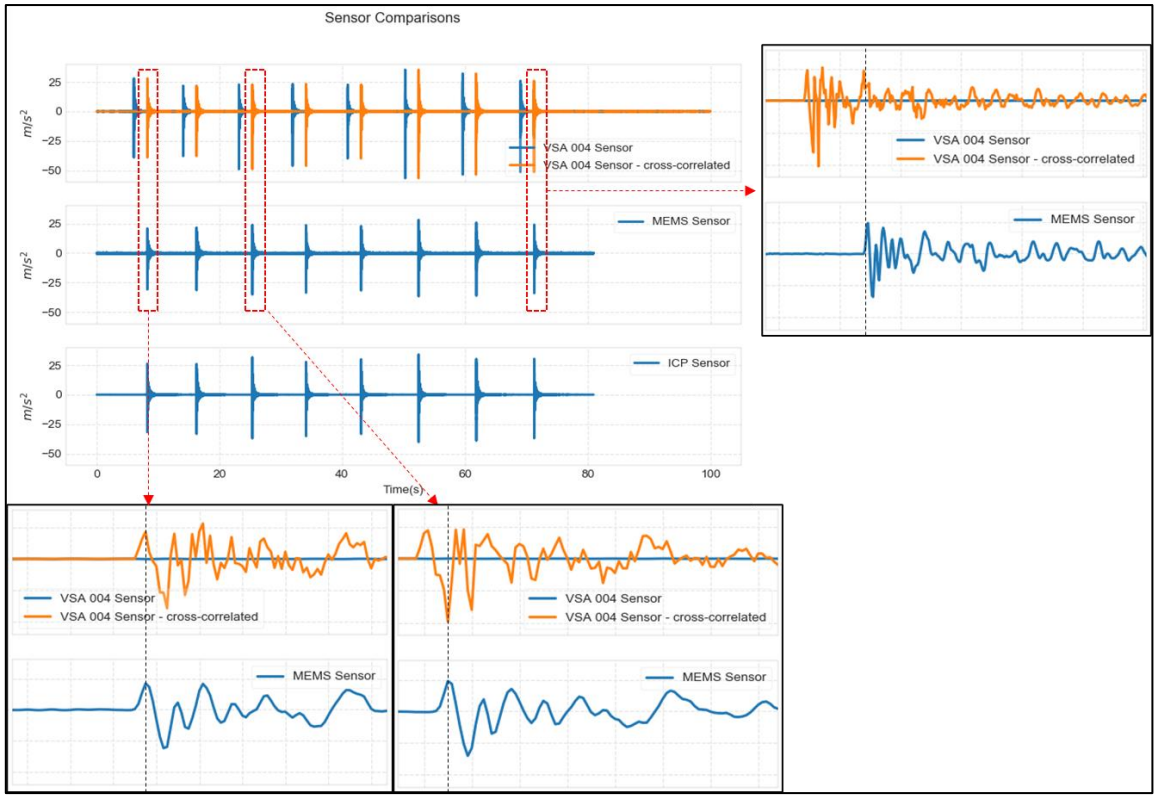

Figure 108: Sensor Offset comparison

To get more consistent offsets between impulses the sampling rate of the IFM sensor measurements was varied in the postprocessing algorithm until the "best fit" was observed. The sample rate of 99 974Hz gave the following offsets:

- The offset for the IFM sensor impulse 1: -2626
- The offset for the IFM sensor impulse 2: -2626
- The offset for the IFM sensor impulse 3: -2626
- The offset for the IFM sensor impulse 4: -2626
- The offset for the IFM sensor impulse 5: -2631
- The offset for the IFM sensor impulse 6: -2631
- The offset for the IFM sensor impulse 7: -2666
- The offset for the IFM sensor impulse 8: -2666

From the offsets shown above the first 4 impulses are synchronized whereas impulses 5 and 6 are in sync and impulses 7 and 8 are in sync. The sampling rate of 99 974Hz is a 0.026% difference from the 100kHz assumption.

A reason for the differences in offsets obtained above is clearly seen in the transient test data and has to do with the time at which the impulses occurred.

13.1.5 Test 2 Transient Results

Figure 109 and Figure 110 shows the transient results obtained for the ICP and IFM sensors respectively. Once again there is a difference in magnitude but overall, the sensors compare very well. These measurements are not yet cross correlated.

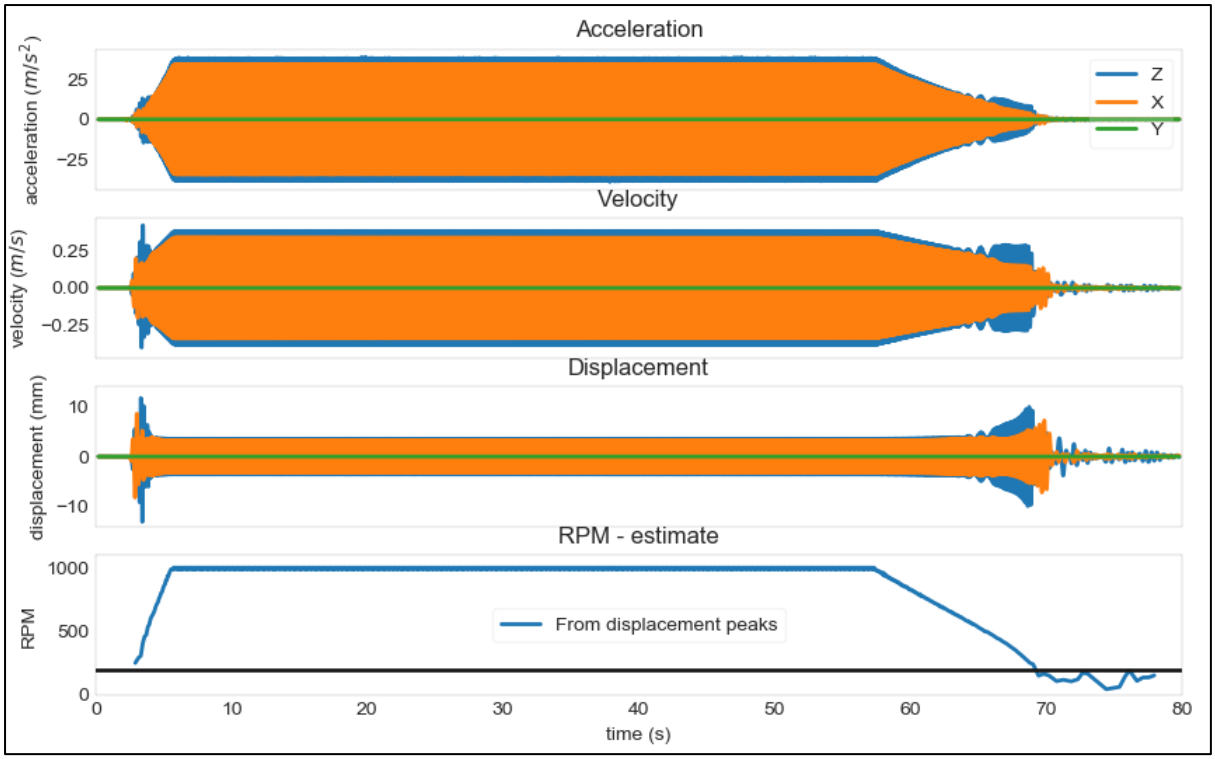

Figure 109: Transient Measurement for ICP sensors

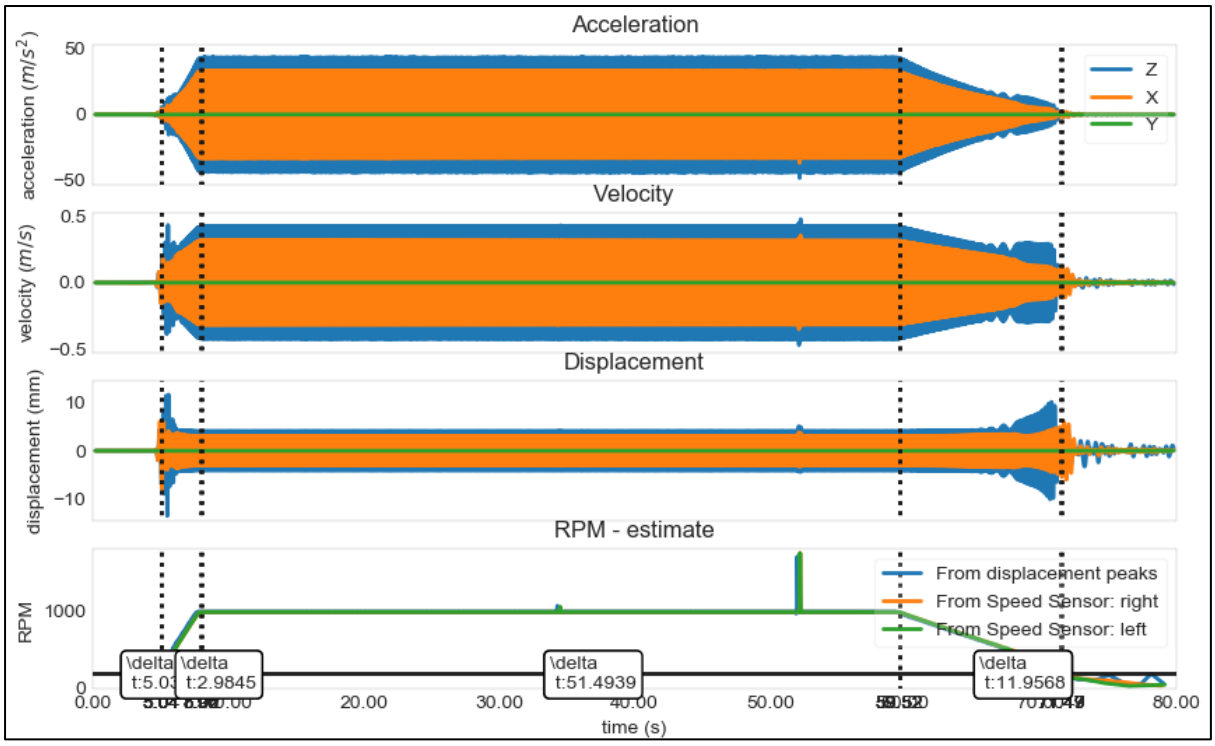

Figure 110: Transient Measurement for IFM sensors

13.1.6 Test 2 Observations

As seen in Figure 110, there are two events that occur consistently at approximately 35 seconds and 53 seconds after a measurement is started. These events were not observed with the other sensors and is therefore assumed to be something to do with the VSE 002 AnReSa module.

Figure 111 shows the events as well as closeups to show what exactly is happening at the event locations.

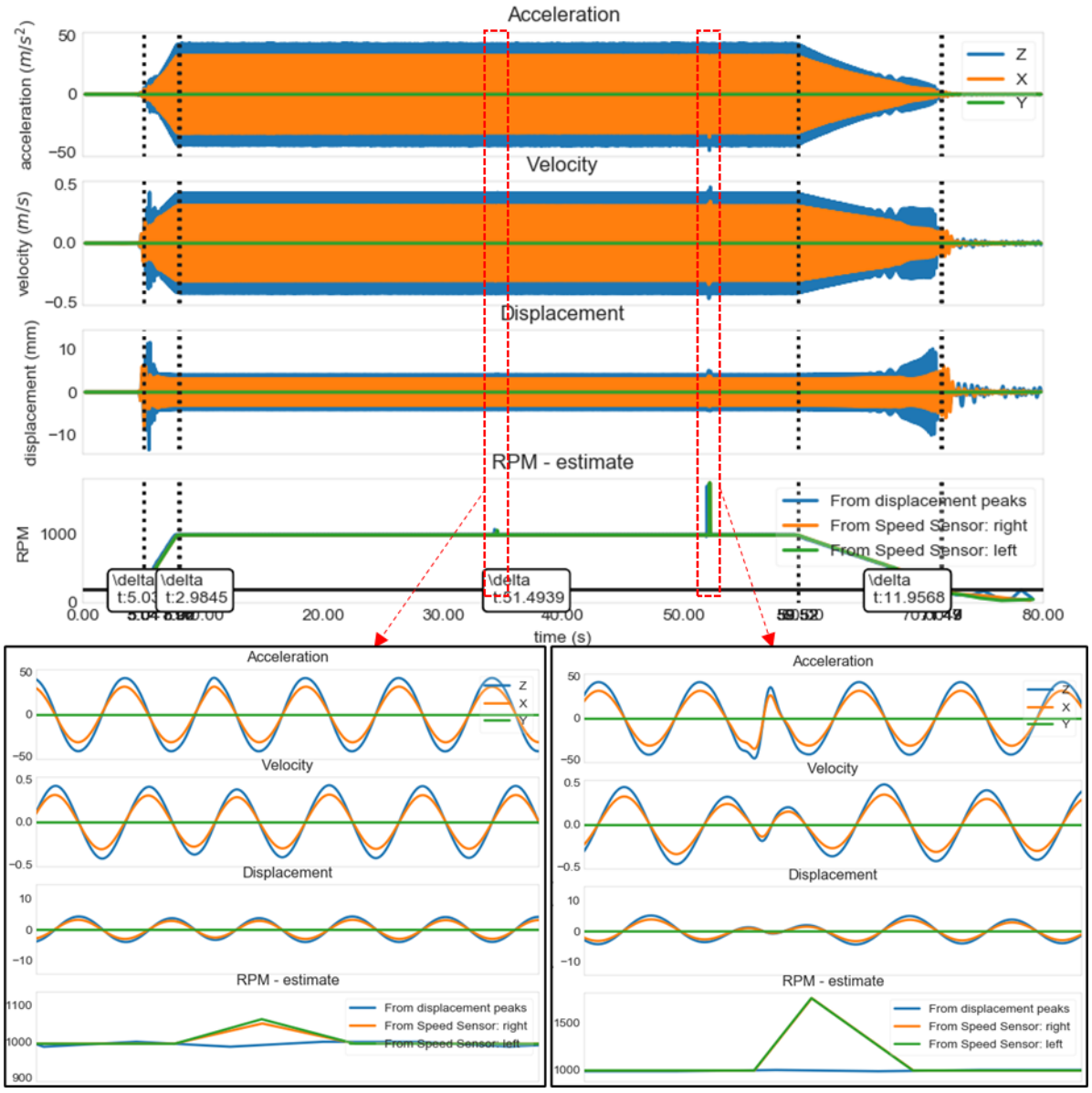

Figure 111: Transient events

The explanation as to what exactly happens at these events is not known, but its occurrence at the time of ≈35 seconds and ≈53 seconds explains why the offsets discovered in the hammer test are synchronized for the first 4 impulses as well as impulse 5 with 6 and 7 with 8. The first 4 impulses occurred before 35 seconds, impulses 5 and 6 occur between 35 and 53 seconds and the last two impulses occurred after 53 seconds.

14 APPENDIX N

14.1 MODAL FIT COMPARISONS FOR TESTS 2, 5 AND 9

Figures shown on the next 3 pages are from tests 2, 5 and 9 respectively and only consider the Dysinet accelerometer's Z response.

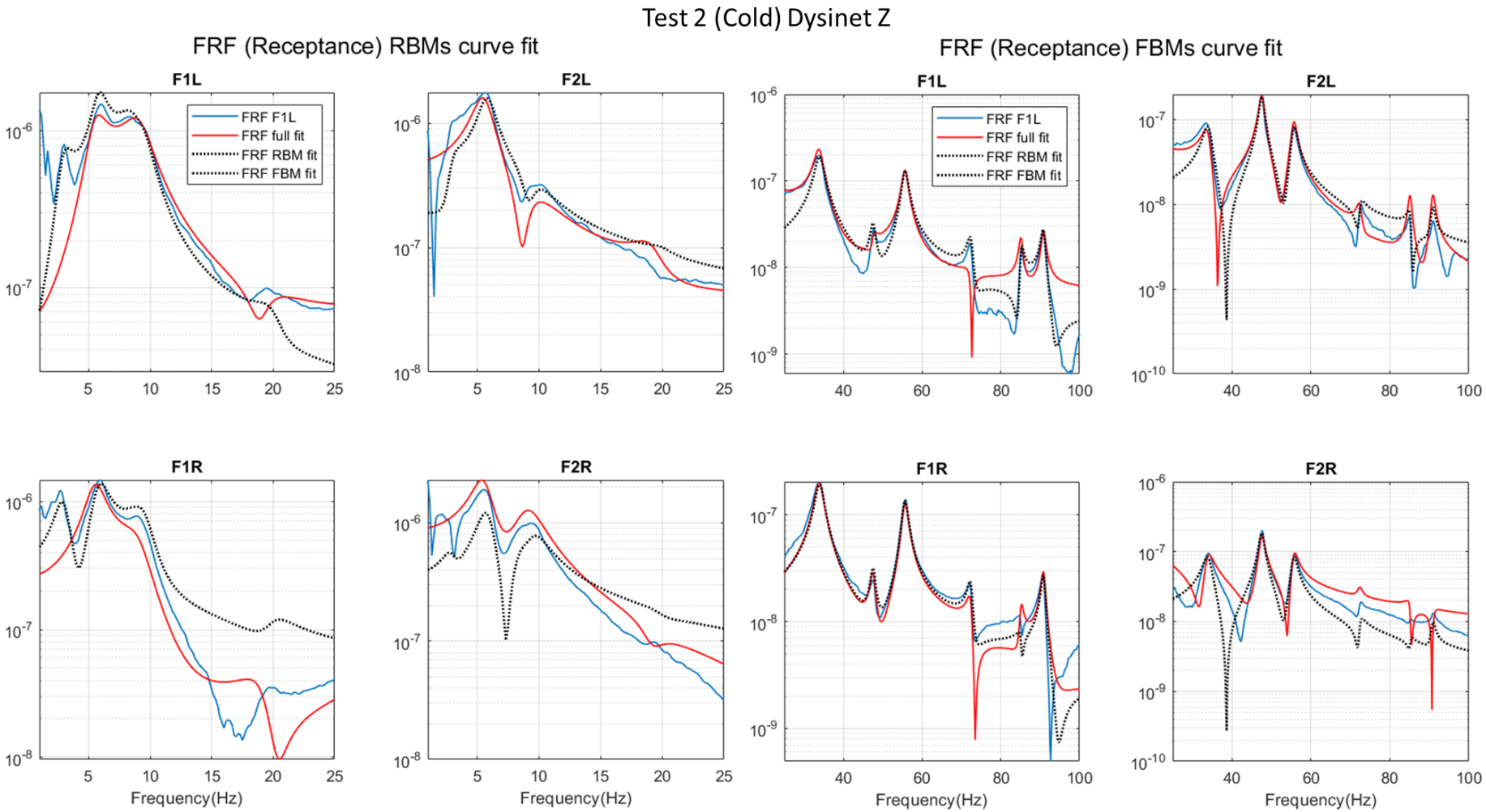

Figure 112: Modal fits for test 2 Dysinet Z response

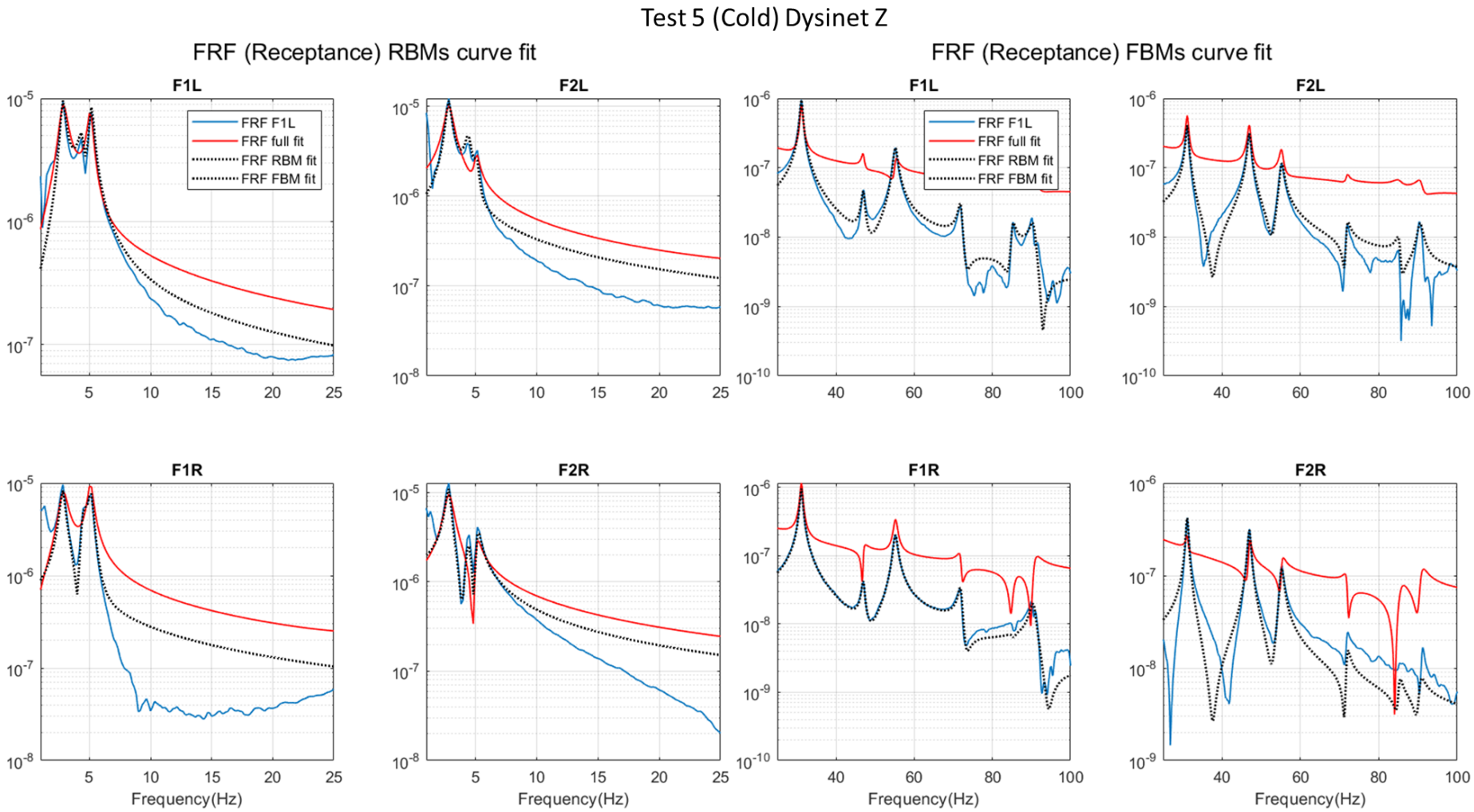

Figure 113: Modal fits for test 5 Dysinet Z response

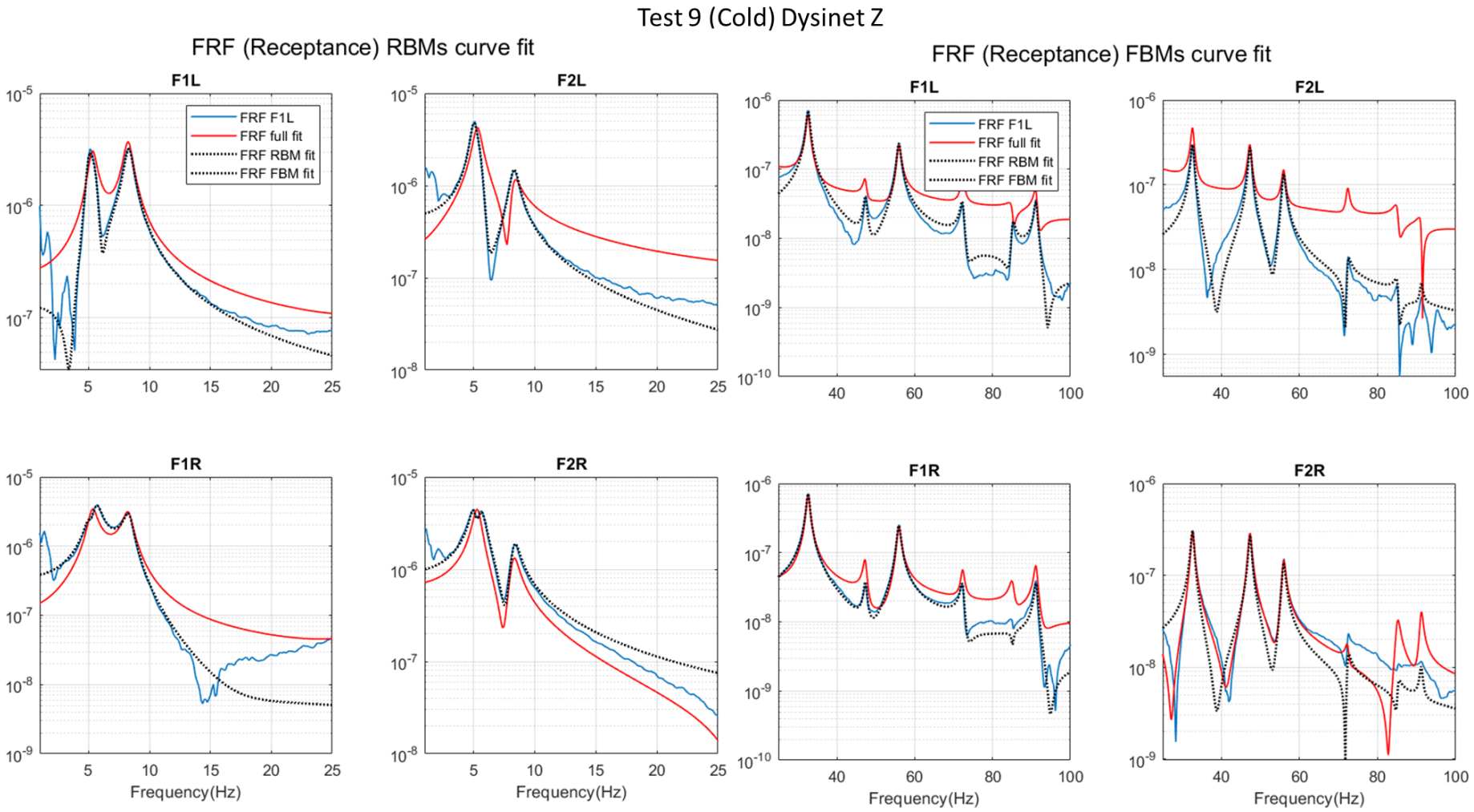

Figure 114: Modal fits for test 9 Dysinet Z response

15 APPENDIX O

15.1 RESULTS COMPARISON ALGORITHM DESCRIPTION

An example of how the comparisons is made between configurations for the experimental results can be seen in Figure 115.

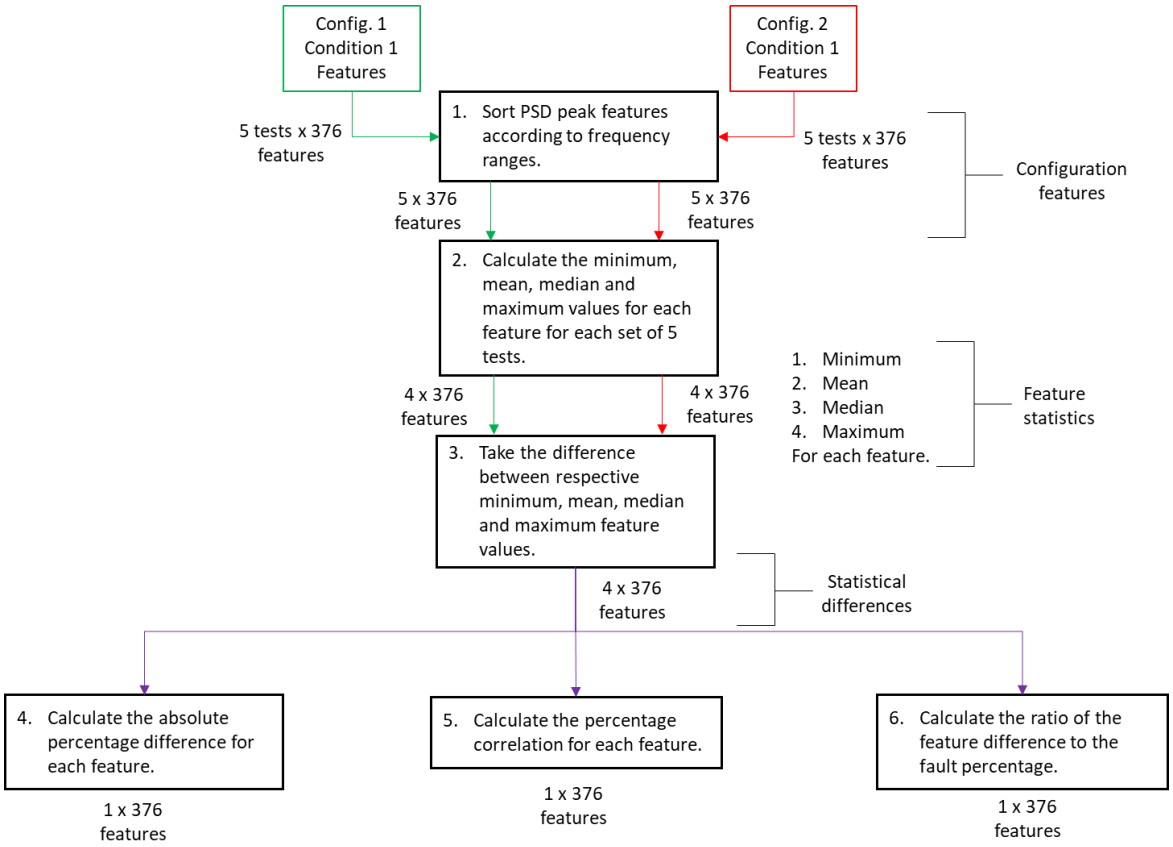

Figure 115: Example flow diagram for a comparison of experimental features